Mass spectrometry-guided molecular omics approaches for the study of lipid metabolism connected with the peroxisome/PPAR system

Cumulative dissertation

by

Vannuruswamy Garikapati

Submitted to the

Faculty of Biology and Chemistry

Prepared at the

Institute of Inorganic and Analytical Chemistry

For the degree of

Doctor rerum naturalium (*Dr. rer. nat.*)

Justus Liebig University Giessen, Germany

Giessen 2024

This thesis is accepted as a doctoral dissertation in fulfillment of the requirements for the degree of *Doctor rerum naturalium (Dr. rer. nat.)* by the Faculty of Biology and Chemistry, Justus Liebig University Giessen, Germany.

Members of the examination committee

Prof. Dr. Bernhard Spengler

Prof. Dr. Eveline Baumgart-Vogt

Prof. Dr. Richard Göttlich

Prof. Dr. Martin Rühl

Referee Prof. Dr. Bernhard Spengler

Institute of Inorganic and Analytical Chemistry, Justus Liebig University Giessen, 35392 Giessen, Germany

Referee Prof. Dr. Eveline Baumgart-Vogt

Institute for Anatomy and Cell Biology II, Division of Medical Cell Biology, Justus Liebig University Giessen, 35392 Giessen, Germany

DECLARATION

I declare that I have completed this dissertation without the unauthorized help of a second party and only with the assistance acknowledged therein. I have appropriately acknowledged and referenced all text passages that are derived from published scientific literature, and all information that relates to verbal communications. I have abided by the principles of good scientific conduct laid down in the charter of the Justus Liebig University Giessen in carrying out the investigations described in the dissertation.

Place, Date

Signature

Ich erkläre: Ich habe die vorgelegte Dissertation selbständig und ohne unerlaubte fremde Hilfe und nur mit den Hilfen angefertigt, die ich in der Dissertation angegeben habe. Alle Textstellen, die wörtlich oder sinngemäß aus veröffentlichten Schriften entnommen sind, und alle Angaben, die auf mündlichen Auskünften beruhen, sind als solche kenntlich gemacht. Bei den von mir durchgeführten und in der Dissertation erwähnten Untersuchungen habe ich die Grundsätze guter wissenschaftlicher Praxis, wie sie in der „Satzung der Justus-Liebig-Universität Gießen zur Sicherung guter wissenschaftlicher Praxis“ niedergelegt sind, eingehalten.

Ort, Datum

Unterschrift

CONTENTS

ACKNOWLEDGMENTS

I would like to convey my warm gratitude to Prof. Dr. Bernhard Spengler for his supervision, constructive suggestions, motivation, and freedom during this journey. I am indebted to him for introducing me to the fields of mass spectrometry imaging, lipidomics, top-down proteomics, and for encouraging me to work on diverse and challenging research projects.

I owe my sincere appreciation to Prof. Dr. Eveline Baumgart-Vogt for her supervision, enthusiasm, support, and valuable guidance from the very early stage of this journey. I am thankful to her for teaching me the basics of human and laboratory mouse anatomy, and for sharing her immense knowledge and experience in the field of peroxisome biology.

I thank all my collaborators Prof. Dr. Sven Heiles, Prof. Dr. Srikanth Karnati, Prof. Dr. Christoph Rummel, Prof. Dr. Gerd Schmitz, Prof. Dr. Karl-Heinz Kogel, Prof. Dr. Aline Koch, PD. Dr. Gerhard Liebisch, Dr. Claudia Colasante, Dr. Dhaka Ram Bhandari, Dr. Sabine Schulz, Dr. Xuelu Ding, Dr. Eistine Boateng, Dr. Vijith Vijayan, Dr. Stefanie Gerbig, Dr. Fabian Pflieger, and Dr. Parviz Ghezellou. I am delighted to have the opportunity to work with all these brilliant people on interdisciplinary collaborative research projects.

Sincere thanks to Dr. Yashwant Kumar (THSTI, India) for providing access to Progenesis QI (Waters Corporation) software for metabolomics data analysis. I also thank Dr. David Peake and Dr. Elena Sokol (Thermo Fisher Scientific, USA) for assisting in lipidomics data analysis with LipidSearch (Thermo Fisher Scientific) software. I gratefully acknowledge Prof. Dr. Lingjun Li and Dr. Kellen Delaney (University of Wisconsin-Madison, USA) for hosting me as a visiting research scholar and introducing me to the fields of peptidomics and glycomics.

I am very grateful to Prof. Dr. Richard Göttlich and Prof. Dr. Martin Rühl for their time and willingness to be members of the dissertation examination committee.

I would like to thank all my colleagues for their exciting scientific discussions, appreciable support, and timely help. Sincere thanks to Bianca Pfeiffer, Andrea Textor, and Lilli Walz for their outstanding technical support.

I am grateful to the International Giessen Graduate Centre for the Life Sciences (GGL), the German Society for Mass Spectrometry (DGMS), and Anatomische Gesellschaft (AG). I owe my deep sense of gratitude to the German Academic Exchange Service (DAAD) for financial support and four months of integrated course on German language and culture.

Finally, I am thankful to my parents, siblings, and friends for their moral support and unconditional love.

PUBLICATIONS

This thesis is based on the following publications in peer-reviewed scientific journals.

Publications (included in this thesis)

1. **Garikapati V**, Colasante C, Baumgart-Vogt E, Spengler B. Sequential lipidomic, metabolomic, and proteomic analyses of serum, liver, and heart tissue specimens from peroxisomal biogenesis factor 11α knockout mice.

   Analytical and Bioanalytical Chemistry. 2022;414(6):2235-2250.

   DOI: 10.1007/s00216-021-03860-0

2. **Garikapati V**, Karnati S, Bhandari DR, Baumgart-Vogt E, Spengler B. High-resolution atmospheric-pressure MALDI mass spectrometry imaging workflow for lipidomic analysis of late fetal mouse lungs.

   Scientific Reports. 2019;9(1):3192.

   DOI: 10.1038/s41598-019-39452-3

3. Karnati S[*], **Garikapati V[*]**, Liebisch G, Van Veldhoven PP, Spengler B, Schmitz G, Baumgart-Vogt E. Quantitative lipidomic analysis of mouse lung during postnatal development by electrospray ionization tandem mass spectrometry.

   PLOS ONE. 2018;13(9):e0203464 ([*]contributed equally to this work).

   DOI: 10.1371/journal.pone.0203464

Publications (not included in this thesis)

4. Ghezellou P, Albuquerque W, **Garikapati V**, Casewell N, Kazemi SM, Ghassempour A, Spengler B. Integrating top-down and bottom-up mass spectrometric strategies for proteomic profiling of Iranian saw-scaled viper, *Echis carinatus sochureki*, venom.

   Journal of Proteome Research. 2021;20(1):895-908.

   DOI: 10.1021/acs.jproteome.0c00687

5. Koch A, Schlemmer T, Höfle L, Werner BT, Presusser C, Hardt M, Möbus A, Biedenkopf D, Claar M, Perlet C, Jelonek L, Goesmann A, **Garikapati V**, Spengler B, Busche T, Kalinowski J, Kogel KH. Host-induced gene silencing involves transfer of dsRNA-derived siRNA via extracellular vesicles.

   bioRxiv (an open-access preprint), 2020.

   DOI: 10.1101/2020.02.12.945154

6. Ghezellou P, **Garikapati V**, Kazemi SM, Strupat K, Ghassempour A, Spengler B. A perspective view of top-down proteomics in snake venom research.

   Rapid Communications in Mass Spectrometry. 2019;33(S1):20-27.

   DOI: 10.1002/rcm.8255

7. Ding X, **Garikapati V**, Spengler B, Heiles S. Analysis of ketone-based neurosteroids by reactive low-temperature plasma mass spectrometry.

   Rapid Communications in Mass Spectrometry. 2018;32(16):1439-1450.

   DOI: 10.1002/rcm.8180

8. Vijayan V, Srinu T, Karnati S, **Garikapati V**, Linke M, Kamalyan L, Mali SR, Sudan K, Kollas A, Schmid T, Schulz S, Spengler B, Weichhart T, Immenschuh S, Baumgart-Vogt E. A new immunomodulatory role for peroxisomes in macrophages activated by the TLR4 ligand lipopolysaccharide.

   Journal of Immunology. 2017;198(6):2414-2425.

   DOI: 10.4049/jimmunol.1601596

Publications (manuscripts under preparation & not included in this thesis)

9. Colasante C, Chen J, **Garikapati V**, Spengler B, Schlüter K-D, Baumgart-Vogt E. Heart recovery after ischemia/reperfusion injury is impaired by a mild peroxisome biogenesis defect induced by the knockout of the peroxin PEX11α.

10. Boateng E, Bonilla-Martinez R, Ahlemeyer B, **Garikapati V**, Alam MR, Trompak O, Oruqaj G, El-Merhie N, Seimetz M, Ruppert C, Günther A, Spengler B, Karnati S, Baumgart-Vogt E. Role of peroxisome proliferator-activated receptor beta/delta and catalase in pulmonary fibrosis.

11. Pflieger FJ, **Garikapati V**, Bhandari DR, Bredehöft J, Peek V, Roeb E, Roderfeld M, Hernandez J, Schulz S, Culmsee C, Laye S, Mayer K, Roth J, Spengler B, Rummel C. Combined lipidomics in a multimodal pathway analysis revealed alterations of brain lipid mediator metabolism during the progression of LPS-induced systemic inflammation in wild type and fat-1 mice.

    Conference abstracts were published in (i) Brain, Behavior, and Immunity. Vol 98, Supplement, November 2021, Page 43. (ii) Neuroimmunomodulation. Vol 29, Supplement 1, March 2022, Page 35.

    DOI: (i) 10.1016/j.bbi.2021.08.162 & (ii) 10.1159/000524082

ABBREVIATIONS

AA	Arachidonic acid
AcCa	Acylcarnitine
ACN	Acetonitrile
AP	Atmospheric pressure
ARSD	Area relative standard deviation
BiNGO	Biological network gene ontology
CAR	Carnitine ester
CE	Cholesteryl ester
Cer	Ceramide
ChE	Cholesterol
CID	Collisional induced dissociation
CL	Cardiolipin
Da, kDa	Dalton, Kilodalton
DAVID	Database for annotation, visualization, and integrated discovery
DAP	Differentially abundant proteins
DDA	Data-dependent acquisition
DG	Diglyceride
DHA	Docosahexaenoic acid
DHB	2,5-dihydroxybenzoic acid
DIA	Data-independent acquisition
DPA	Docosapentaenoic acid
DPPC	Dipalmitoylphosphatidylcholine
DPPG	Dipalmitoylphosphatidylglycerol
DTT	Dithiothreitol
EPA	Eicosapentaenoic acid
E19	Late fetal stage at day 19 of gestation
FA	Fatty acyls and/or fatty acid
FDR	False discovery rate
g	Relative centrifugal force
GL	Glycerolipids
GP	Glycerophospholipids or phospholipids
HCA	Hierarchical clustering analysis

HCD	Higher-energy collisional dissociation
HESI	Heated electrospray ionization
HexCer	Hexosylceramide
HMDB	Human metabolome database
IAA	Iodoacetamide
IPA	Isopropyl alcohol or 2-propanol
KEGG	Kyoto encyclopedia of genes and genomes
KO	Knockout
LFQ	Label-free quantification
LIPID MAPS	Lipid metabolites and pathways strategy
LPA	Lysophosphatidic acid
LPC	Lysophosphatidylcholine
LPE	Lysophosphatidylethanolamine
LPG	Lysophosphatidylglycerol
LPI	Lysophosphatidylinositol
LPS	Lysophosphatidylserine
MALDI	Matrix-assisted laser desorption/ionization
MeOH	Methanol
MG	Monoglyceride
MS	Mass spectrometry
MS/MS	Tandem mass spectrometry
MSI	Mass spectrometry imaging
MTBE	Methyl *tert*-butyl ether
MUFA	Monounsaturated fatty acid
m/z	Mass-to-charge-number ratio
NCE	Normalized collision energy
PA	Phosphatidic acid
PANTHER	Protein analysis through evolutionary relationships
PBD	Peroxisomal biogenesis disorders
PC	Phosphatidylcholine
PCA	Principal component analysis
PC O- / PC P-	Ether-linked phosphatidylcholine
PD	Peroxisomal disorders
PE	Phosphatidylethanolamine

PED	Peroxisomal enzyme deficiencies
PE O- / PE P-	Ether-linked phosphatidylethanolamine
PEX	Peroxisomal biogenesis factor (protein) or peroxin
Pex	Peroxisomal biogenesis factor (gene)
PG	Phosphatidylglycerol
PI	Phosphatidylinositol
pNA	4-nitroaniline or *para*-nitroaniline
ppm	Parts per million
PS	Phosphatidylserine
PTS	Peroxisomal targeting signal
PUFA	Polyunsaturated fatty acid
P1	Newborn
P15	15-day-old
P84	12-week-old
RMSE	Root-mean-square error
ROS	Reactive oxygen species
RP	Reversed-phase
RT	Retention time
SD	Standard deviation
SHexCer	Sulfatide
SM	Sphingomyelin
sn	Stereospecific numbering
SP	Sphingolipids
SPH	Sphingosine
TFA	Trifluoroacetic acid
TG	Triglyceride
TIC	Total ion count
UHPLC	Ultra-high-performance liquid chromatography
VLCFA	Very long-chain fatty acid
WT	Wild type
ZS	Zellweger syndrome
ZSD	Zellweger spectrum disorders

ABSTRACT

Multi-layered molecular (i.e. lipids, metabolites, and proteins) read-outs can provide deeper insights into biochemical cascades and disease mechanisms. Mass spectrometry (MS) has emerged as an invaluable and elemental analytical tool to study these molecular components in biological systems. Peroxisomes are small, omnipresent subcellular organelles that perform a wide range of functions in human health and disease. They participate in numerous degradative and biosynthetic processes, including lipid metabolism. Peroxisomal dysfunction leads to devastating genetic human disorders, namely peroxisomal biogenesis disorders (PBDs) and single peroxisomal enzyme deficiencies (PEDs). PBDs arise from mutations in *Pex* genes that encode peroxisomal biogenesis proteins (also named peroxins, PEX). The PEX11 protein family (α, β, and γ isoforms) regulates fission and proliferation of peroxisomes. However, detailed physiological and molecular functions of PEX11 protein isoforms, pathological and metabolic consequences owing to their defects are still being discovered.

In this thesis, MS-guided molecular omics (i.e. lipidomics, metabolomics, and proteomics) workflows were developed and employed to ascertain the molecular compositional changes occurring due to *Pex11α* and *Pex11*β deficiencies, as well as during the postnatal lung development. The cutting-edge analytical technologies used for this purpose were ultra-high-performance liquid chromatography coupled with high-resolution tandem mass spectrometry (UHPLC-HRMS/MS), atmospheric pressure scanning microprobe matrix-assisted laser desorption/ionization mass spectrometry imaging (AP-SMALDI MSI), and direct flow injection electrospray ionization tandem mass spectrometry (ESI-MS/MS).

In the first article, altered molecular species and metabolic pathways were depicted in serum, liver, and heart tissues of untreated *Pex11α* knockout adult mice in comparison to the wild type controls. Primarily, a single-step liquid-liquid extraction (MTBE/MeOH/H_2O) method was utilized and optimized for the parallel extraction of lipids (upper organic phase), polar metabolites (lower aqueous phase), and proteins (sediment pellet) from the same and limited amount of biological specimens. Later, the dried lipid, polar metabolite, and protein extracts were quantitatively analyzed using a reversed-phase UHPLC-MS/MS system individually in positive- and negative-ion mode. In addition, extensive data filtering and manual curation strategies were implemented and high-confidence molecular annotations were reported by removing/minimizing the false positives. Furthermore, comprehensive specimen-specific multiple molecular species and related metabolic pathway changes were uncovered in distinct biological specimens of *Pex11α* knockout mice.

In the second article, MALDI MS imaging was used to characterize the full lipidome of late fetal mouse lungs at day 19 of gestation (E19) followed by semi-quantitative analysis of lipids in E19 WT and *Pex11β*

knockout mice lung tissue sections. Sample preparation protocol including tissue handling, sectioning of E19 mouse lungs without embedding material, homogenous deposition of matrices, instrumental and data processing framework were optimized. MS imaging experiments were carried out at a high resolution in mass (140,000 @ *m/z* 200) and space (10 µm per pixel) using an AP-SMALDI10 ion source. E19 mouse lung full lipidome was characterized based on accurate mass (≤ 2 ppm) and on-tissue tandem mass spectrometry experiments in both positive- and negative-ion mode. Additionally, data handling and analysis strategies including different normalization approaches were tested and optimized for direct comparison of relative signal intensities of lipids and endogenous metabolites among different tissue sections. Furthermore, the developed MSI workflow was employed and illustrated the molecular changes in *Pex11β* knockout mouse lung tissues in comparison to the E19 WT controls.

In the third article, direct flow injection quantitative lipidomic analysis (also called shotgun lipidomics) was carried out to monitor the compositional changes in mouse lung lipidome during the postnatal development process, from birth to adulthood. Lipids were extracted from whole lung tissue homogenates of newborn (P1), 15-day-old (P15), and 12-week-old (P84) adult mice using $CHCl_3$/MeOH/H_2O liquid-liquid extraction (Bligh and Dyer method). Then, the extracted lipids were quantified using electrospray ionization tandem mass spectrometry in positive-ion mode. Overall, an extensive quantitative (molar abundances) lipidome of mouse lung and significant stage-specific alterations of lipid classes and individual lipid molecular species were presented during the postnatal pulmonary development process.

ZUSAMMENFASSUNG

Mehrschichtige molekulare Daten (z. B. Lipide, Metaboliten und Proteine) können tiefere Einblicke in biochemische Abläufe und Krankheitsmechanismen geben. Die Massenspektrometrie (MS) hat sich als unschätzbares und elementares Analyseinstrument zur Untersuchung dieser molekularen Komponenten in biologischen Systemen erwiesen. Peroxisomen sind kleine, allgegenwärtige subzelluläre Organellen, welche eine Vielzahl von Funktionen erfüllen, die bei Gesundheit und Krankheit des Menschen in Erscheinung treten. Sie sind an zahlreichen Abbauprozessen und biosynthetischen Prozessen beteiligt, einschließlich des Lipidstoffwechsels. Peroxisomale Funktionsstörungen führen zu verheerenden genetischen Störungen beim Menschen, nämlich zu Peroxisomen-Biogenese-Störungen (PBDs) und zu Defiziten einzelner peroxisomaler Enzyme (PEDs). PBDs entstehen durch Mutationen in *Pex*-Genen, die für peroxisomale Biogeneseproteine (auch Peroxine, PEX genannt) kodieren. Die PEX11-Proteinfamilie (α-, β- und γ-Isoformen) steuert die Spaltung und Vermehrung von Peroxisomen. Die detaillierten physiologischen und molekularen Funktionen der PEX11-Protein-Isoformen sowie die pathologischen und metabolischen Folgen ihrer Defekte sind Gegenstand der aktuellen Forschung.

In dieser Arbeit wurden MS-gestützte molekulare „Omics-Workflows“ (d. h. Lipidomics, Metabolomics und Proteomics) entwickelt und eingesetzt, um die molekularen Veränderungen in der Zusammensetzung zu ermitteln, die aufgrund von *Pex11α*- und *Pex11β*-Mangel sowie während der postnatalen Lungenentwicklung auftreten. Zu diesem Zweck wurden modernste Analysetechnologien eingesetzt: Ultra-Hochleistungs-Flüssigkeitschromatographie gekoppelt mit hochauflösender Tandem-Massenspektrometrie (UHPLC-HRMS/MS), Atmosphärendruck-Scanning-Mikrosonden-Matrix-unterstützte Laser-Desorptions/Ionisations-Massenspektrometrie-Bildgebung (AP-SMALDI MSI) und Direktfluss-Injektions-Elektrospray-Ionisations-Tandem-Massenspektrometrie (ESI-MS/MS).

Im ersten Artikel wurden veränderte molekulare Spezies und Stoffwechselwege in Serum, Leber und Herzgewebe von unbehandelten erwachsenen *Pex11α*-Knockout-Mäusen im Vergleich zur Wildtyp-Kontrolle verglichen. Im ersten Schritt wurde eine einstufige Flüssig-Flüssig-Extraktionsmethode (MTBE/MeOH/H_2O) für die gleichzeitige Extraktion von Lipiden (obere organische Phase), polaren Metaboliten (untere wässrige Phase) und Proteinen (Sedimentpellet) aus derselben, minimalen Menge an biologischen Proben verwendet und optimiert. Anschließend wurden die getrockneten Lipid-, polaren Metabolit- und Proteinextrakte mit einem Umkehrphasen-UHPLC-MS/MS-System einzeln im Positiv- und Negativ-Ionen-Modus quantitativ analysiert. Darüber hinaus wurden umfangreiche Strategien zur Datenfilterung und manuellen Kuratierung implementiert und molekulare Annotationen mit hoher Konfidenz generiert, indem falsch positive Ergebnisse entfernt bzw. minimiert wurden. Darüber hinaus wurden in verschiedenen biologischen Proben von *Pex11α*-Knockout-Mäusen multiple probenspezifische

molekulare Spezies und damit zusammenhängende Veränderungen in den Stoffwechselwegen aufgedeckt und beschrieben.

Im zweiten Artikel wurde die MALDI-MS-Bildgebung zur Charakterisierung des gesamten Lipidoms der spätfetalen Mäuselunge am 19. Tag der Trächtigkeit (E19) verwendet, gefolgt von einer semiquantitativen Analyse der Lipide in E19-Lungengewebeschnitten von WT- und *Pex11β*-Knockout-Mäusen. Das Probenvorbereitungsprotokoll, einschließlich der Handhabung des Gewebes, des Schneidens von E19-Mauslungen ohne Einbettungsmaterial, der homogenen Ablagerung von Matrizen sowie der instrumentellen und datenverarbeitenden Rahmenbedingungen wurden optimiert. MS-Bildgebungsexperimente wurden mit einer hohen Auflösung in Bezug auf Masse (140.000 @ *m/z* 200) und Raum (10 µm pro Pixel) unter Verwendung einer AP-SMALDI10-Ionenquelle durchgeführt. Das vollständige Lipidom der E19-Mauslunge wurde auf der Grundlage präziser Massen- (≤ 2 ppm) und On-Tissue-Tandem-Massenspektrometrie-Experimente sowohl im Positiv- als auch im Negativ-Ionen-Modus charakterisiert. Darüber hinaus wurden Datenverarbeitungs- und Analysestrategien, einschließlich verschiedener Normalisierungsansätze, getestet und für den direkten Vergleich der relativen Signalintensitäten von Lipiden und endogenen Metaboliten zwischen verschiedenen Gewebeschnitten optimiert. Zusätzlich wurde der entwickelte MSI-Workflow vielfach angewandt und veranschaulichte die molekularen Veränderungen im Lungengewebe von *Pex11β*-Knockout-Mäusen im Vergleich zu den E19-WT-Kontrolle.

Im dritten Artikel wurde eine quantitative Lipidomanalyse mittels direkter Durchflussinjektion (auch Shotgun-Lipidomik genannt) durchgeführt, um die Veränderungen in der Zusammensetzung des Lungenlipidoms von Mäusen während des postnatalen Entwicklungsprozesses von der Geburt bis zum Erwachsenenalter zu verfolgen. Die Lipide wurden aus Homogenaten des gesamten Lungengewebes von neugeborenen (P1), 15 Tage alten (P15) und 12 Wochen alten (P84) erwachsenen Mäusen mittels $CHCl_3$/MeOH/H_2O Flüssig-Flüssig-Extraktion (Bligh und Dyer Methode) extrahiert. Anschließend wurden die extrahierten Lipide mittels Elektrospray-Ionisations-Tandem-Massenspektrometrie im Positiv-Ionen-Modus quantifiziert. Insgesamt wurden ein umfangreiches, quantitatives Lipidprofil der Mauslunge und signifikante stadienspezifische Veränderungen der Lipidklassen und einzelner Lipidmolekülspezies während der postnatalen Lungenentwicklung dargestellt.

CHAPTER I

1.1 An introduction to systems biology

Systems biology is deep-rooted with an understanding of a large variety of molecular components within a cell and of interactions between cells that allow assembly of a multicellular organism. Approximately, 75-80% of the living matter by weight is composed of water, inorganic ions, and numerous small organic molecules, specifically lipids, vitamins, amino acids, peptides, nucleotides, cofactors, carbohydrates, etc. The remaining 20-25% consist of macromolecules namely deoxyribonucleic acid (DNA), ribonucleic acid (RNA), and proteins [1]. The "central dogma of molecular biology" enunciated by Francis Crick elucidates the residue-by-residue transfer of genetic information and the relationship between these bio-macromolecules [2]. Concisely, the pattern of genetic inheritance comprises three important phases including (i) replication, (ii) transcription, and (iii) translation. In the replication step, a double-stranded DNA is replicated to give identical copies, which preserves genetic information (DNA → DNA). In transcription, the genetic information encoded in the section of DNA is transcribed into small portable RNA messages (DNA → RNA; mRNA). During translation, mRNAs travel from the nucleus into the cytoplasm (ribosomes), where they are read to make a protein and/or a small group of proteins (RNA → proteins) [1, 2]. The unique structural, biochemical, and functional properties of these macromolecules (i.e. DNA/gene, RNA/transcript, and proteins/enzymes) make them the principal components of the cell. Whereas, metabolites/lipids are often referred to as end products of the complex biochemical processes catalyzed by enzymes and connected with genes, transcripts, and proteins and represent the most downstream stage within the systems biology framework (Fig. 1) [3].

Over the past decades, high-throughput technological advancements (e.g. instrumentation, sample handling strategies, robust bioinformatics, and computational tools) have revolutionized modern biology and enabled systems biology methodologies for a better understanding of complex biochemical pathways. "Omics" is a branch of science that showcase a comprehensive or global assessment of chemical constituents that make up the cell, tissue, organ, and/or organism. Primarily, omics studies aim at the collective characterization and quantification of the molecular components present in a particular biological specimen to stipulate the current state (e.g. healthy or disease, normal or mutant) of the biological system [4]. This suite of technologies mainly encompasses genomics, transcriptomics, proteomics, metabolomics, and lipidomics. In addition, several other approaches such as epigenomics, glycomics, peptidomics, ionomics, microbiomics, exposomics, phenomics, fluxomics, metagenomics, and interactomics exist and are listed under the umbrella term "omics" (Fig. 1). Specialized and individual applications of all these omics approaches have been demonstrated to be beneficial in understanding and characterization of numerous biological processes. Nonetheless, integration of multi-level molecular omics data that are associated with

the genotype (e.g. genomics and transcriptomics) and those connected with the phenotype (e.g. proteomics, metabolomics, and lipidomics) along with the other omics data, spatial and temporal information, clinical data, advanced machine learning, mathematical modeling, and statistical approaches conceivably result in accurate prediction of health and disease states and also provide insights for effective therapeutic interventions (Fig. 1) [5, 6].

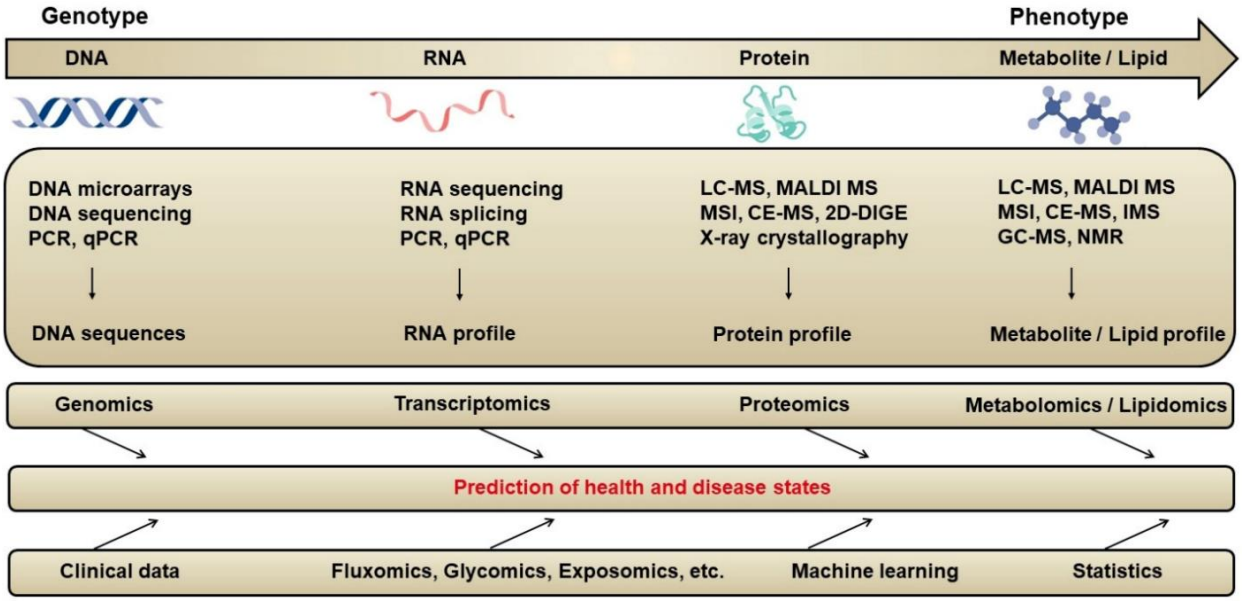

Fig. 1 Snapshot of systems biology approaches. The figure is prepared based on the collective scientific literature on different omics technologies.

1.2 Mass spectrometry-guided molecular omics

Mass spectrometry (MS) has turned out to be a valued and fundamental analytical technique in understanding the role of biologically active components at a cellular and molecular level. Simplified below are the MS-guided molecular omics (i.e. proteomics, metabolomics, and lipidomics) approaches that are frequently applied in biomedical research in a non-biased/non-targeted and/or targeted manner.

1.2.1 Proteomics

Proteins are the most versatile and imperative class of bioactive molecules that execute numerous biochemical reactions. In 1994, Marc Wilkins proposed the term “proteome” in analogy to the genome, with a native meaning (protein complement expressed by a genome) which implies the study of the total set of identifiable proteins in a given sample, at a particular time, under specified conditions [7]. The third downstream omics discipline in systems biology is proteomics (Fig. 1), and the current inclusive definition of proteomics deals with the identification, quantification, characterization of post-translational

modifications (PTMs), interactions, and cellular localization of proteins using high-throughput analytical approaches [8, 9].

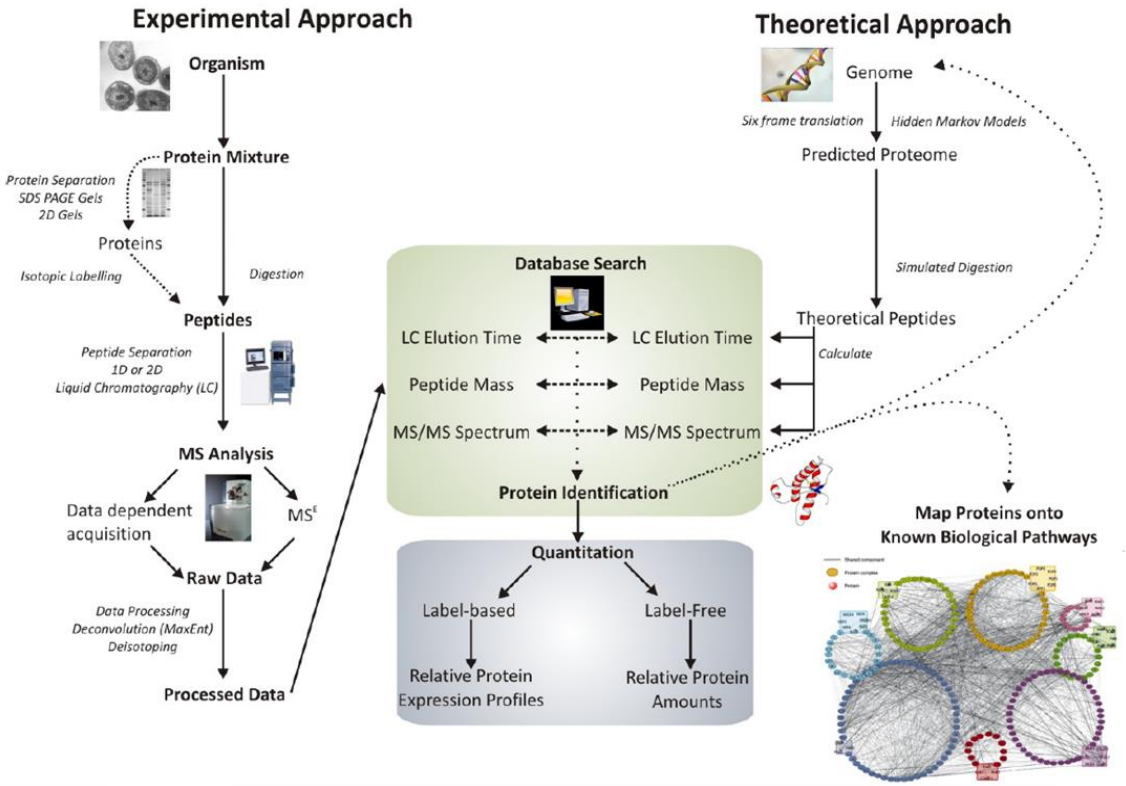

Fig. 2 A classical workflow of mass spectrometry-guided bottom-up proteomics. The figure is obtained from a tutorial presentation listed in reference [10].

The proteomics field has progressed from two-dimensional electrophoresis (2-DE) visualization of a small group of proteins from a complex biological mixture [11] to the characterization of several thousands of proteins from a single cell [12, 13]. With the rapid technological developments, MS has arisen as a potential and universal analytical method of choice for high-throughput large-scale proteomics studies (Fig. 1 & 2). Depending on the scheme of the protein characterization, MS-based proteomics is sub-classified into three diverse analytical workflows; (i) top-down, (ii) bottom-up, and (iii) middle-down proteomics. In the case of top-down proteomics, proteins are identified and characterized by the fragmentation of intact proteins (i.e. no proteolysis before MS data acquisition). This approach has potential benefits to locate and illustrate PTMs, proteoforms, and access nearly complete protein sequence coverage [14]. However, the applicability of this method is confined to a single and/or a small number of purified proteins due to several technical challenges such as fractionation, purification, ionization, and fragmentation of intact proteins [15]. In contrast, peptides from the enzymatically digested proteins (i.e. proteolysis prior to the MS data acquisition) are identified and quantified in bottom-up proteomics (also called shotgun proteomics) (Fig. 2) [10, 16].

The shotgun approach is largely adopted by the researchers in the proteomics community due to the fact that digested peptides are easier to separate (high-resolution) and analyze (high-sensitivity) than intact proteins with less sophisticated instrumentation, expertise, and well-established bioinformatics tools [17]. Recently, the middle-down approach has evolved as a novel scheme by linking the key features of bottom-up and top-down methodologies, where relatively larger peptide fragments (preferably above 3 kDa) are analyzed with restricted proteolysis of proteins [18].

Based on the biological rationale, proteomics experiments aim at (i) the large-scale screening of proteins including PTMs (proteome profiling), (ii) quantitative analysis of proteins between multiple conditions (differential proteomics), (iii) localization, compartmentalization, conformations, and interactions with proteins and/or other biomolecules (structural proteomics), and (iv) biological networks, pathways, and disease mechanisms (functional proteomics) [16].

The routinely used MS-based bottom-up proteomics (particularly differential proteomics) workflow can be broken down into several steps (Fig. 2). In short, (i) appropriate sample collection and storage, (ii) protein extraction with MS-compatible lysis buffers and protein estimation (e.g. Bradford, Bicinchoninic acid, Lowry protein assays), (iii) optional fractionation/enrichment/depletion of proteins via 2-DE, size exclusion, and affinity chromatographic methods, (iv) enzymatic digestion (usually with trypsin or other proteases) of proteins into peptides, (v) peptide cleanup (e.g. ZipTip) and separation using liquid chromatography followed by MS data acquisition (e.g. targeted, DDA, DIA), (vi) peptide and protein identification with a database (e.g. species-specific proteome sequence from UniProt, https://www.uniprot.org/) search using search engines (e.g. SEQUEST HT, Mascot, Andromeda), (vii) labeling (e.g. chemical, metabolic) and/or label-free quantification (LFQ) of proteins, (viii) bioinformatics analyses such as mapping differentially abundant proteins (DAPs) onto known biological pathways and network analysis using various functional categorization tools including DAVID (https://david.ncifcrf.gov/), STRING (https://string-db.org/), Cytoscape (https://cytoscape.org/), BiNGO (https://www.psb.ugent.be/cbd/papers/BiNGO/Home.html), PANTHER (http://pantherdb.org/), and (ix) validation of certain DAPs with antibody-based methods (e.g. Western blot) and/or with targeted MS (MRM/PRM) approaches [8, 10, 19, 20]. Furthermore, in MS imaging workflows (where intact proteins and/or digested peptides are identified, quantified, and imaged directly from the biological specimens), additional antigen retrieval and washing steps are implemented to remove lipids, salts, and other ionic compounds [21, 22].

During the preparation of this thesis, LC-MS/MS-based label-free quantitative bottom-up proteomics (publications 1 & 5), a combination of bottom-up and top-down proteomics (publications 4 & 6) workflows were optimized and employed in diverse research projects.

1.2.2 Metabolomics

Although metabolomics is regarded as a comparatively new branch in the omics disciplines, the basic idea of studying metabolites for potential biomedical applications is not new. For instance, in ancient Greek and China, urine sweetness (i.e. high levels of glucose in the urine) with the help of ants was used as a method to diagnose diabetes [23]. In the late 1960s, Dalgliesh et al. utilized gas chromatography together with a flame ionization detector for the identification of a broad spectrum of metabolites [24]. Later in 1971, Horning and colleagues utilized mass spectrometry (GC-MS) for the first time to characterize metabolites in urine and tissue homogenates [25] and proposed the term "metabolic profile". Generally, these studies exemplified the beginning of the development of modern metabolomics. Thereafter in 1998, Steven Oliver coined the word "metabolome" in analogy to genome, transcriptome, and proteome [26]. Shortly after, Jeremy Nicholson introduced "metabonomics" and Oliver Fiehn used "metabolomics" to denote the comprehensive quantitative assessment of all possible metabolites in a given biological system [27, 28]. The synonyms metabolomics, metabonomics, metabolome analysis, metabolic profiling/profile, and metabolite profiling/profile are often used intertwined; nonetheless, the term "metabolomics" is most widely adopted by the community (https://metabolomicssociety.org/).

Metabolites (small chemical entities, typically ≤1000 Da molecular weight) are the substrates, intermediates, and/or end products of the cellular metabolism that provide a functional readout (e.g. phenotype) of the biological system [29, 30]. Metabolomics is an uprising field of omics science, which can deliver absolute and/or relative quantities of numerous endogenous and exogenous compounds for example lipids, sugars, peptides, toxins, nucleotides, amino acids, vitamins, polyamines, organic acids, pharmaceuticals, dietary compounds, microbial metabolites, and environmental chemicals from a large variety of sample types including biological fluids (e.g. serum, saliva, urine, BALF, and CSF), cells, tissues, feces, and/or entire organism [5, 31]. Metabolomics studies have widely been applied in diverse domains such as clinical research (e.g. biomarker discovery), disease diagnosis (e.g. screening of inborn metabolic disorders including peroxisomal disorders) and treatment, drug discovery (e.g. pharmacokinetics and dynamics), animal, plant, nutritional, microbial, and environmental research [32].

Based on the study hypothesis, metabolomics workflows are broadly categorized into (i) untargeted (discovery), and (ii) targeted (validation) approaches [29]. Untargeted or global metabolomics is a powerful strategy that allows unbiased measurement of as many as possible metabolites from a given biological sample without any prior knowledge, which can unveil novel and unforeseen results. Targeted metabolomics, on the other hand, focuses on a set of specific, predefined metabolites and/or metabolic pathways, which can provide higher sensitivity, reproducibility, and lower false-positive rates than the untargeted approach [33]. The two-tiered or hybrid approach also exists, in which targeted metabolomics

(hypothesis-driven) is employed to validate the results derived from an untargeted metabolomics workflow (hypothesis generation).

In principle, frequently employed analytical technologies in metabolomics experiments are nuclear magnetic resonance spectroscopy (e.g. ^{1}H, ^{13}C, and ^{31}P NMR), and mass spectrometry (Fig. 1). NMR is a non-destructive method that offers fast and reproducible qualitative and quantitative results, while MS is more cost-effective and provides higher sensitivity towards a wide range of metabolites than NMR. Further, separation methodologies, especially liquid chromatography (LC), gas chromatography (GC), capillary electrophoresis (CE), and ion mobility spectrometry (IMS) hyphenated to MS can deliver higher sensitivity and comprehensive coverage of the metabolome. Furthermore, it is feasible to attain both the qualitative and quantitative molecular and spatial information of the metabolites directly within biological specimens (e.g. tissues, cells) using mass spectrometry imaging (MSI) approaches [22].

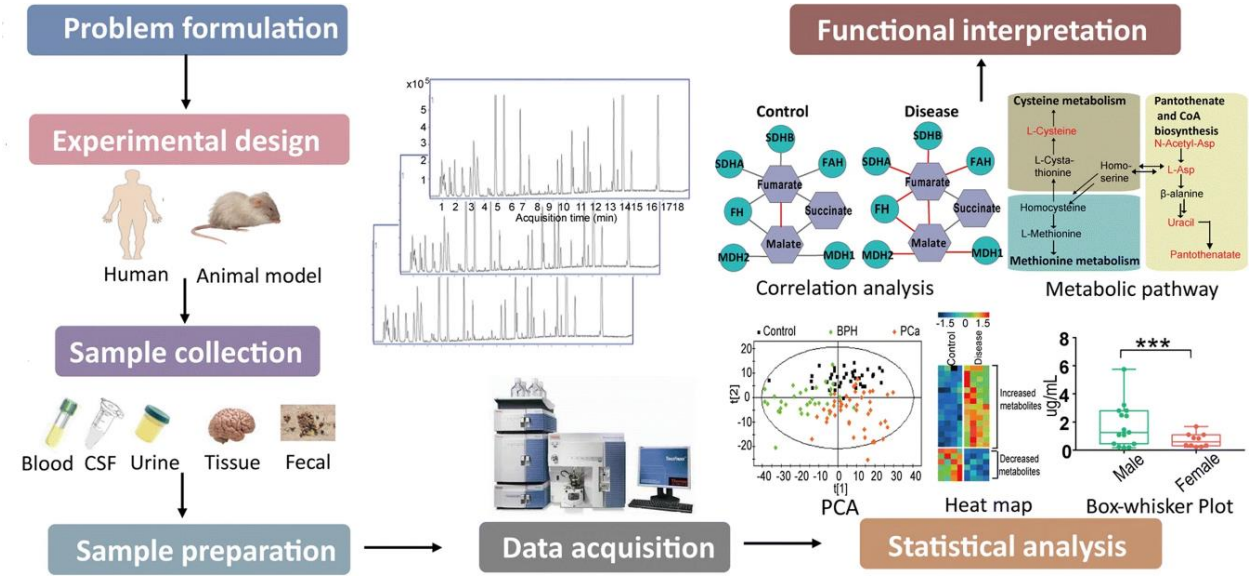

Fig. 3 A schematic representation of the mass spectrometry-guided metabolomics workflow [31].

Regardless of the approach and analytical setup, basic steps of the metabolomics workflow include (i) biological question formulation, (ii) suitable experimental design, (iii) appropriate sample collection and storage, (iv) sample preparation (comprises stopping/quenching of the metabolism/enzyme activity, tissue sectioning, homogenization, metabolite extraction, reconstitution of extracts, and optional chemical derivatization, etc.), (v) data acquisition using either NMR or MS (with or without separation techniques, MS imaging), (vi) data analysis (e.g. data import and alignment, peak picking, filtering, normalization, image generation, statistical analysis, metabolite annotation and structural elucidation), (vii) functional interpretation (e.g. correlation analysis, pathway mapping, network analysis) using several visualization tools and databases such as MetPA (http://metpa.metabolomics.ca/), iPath (https://pathways.embl.de/),

KEGG (https://www.genome.jp/kegg/pathway.html), Reactome (https://reactome.org/), MetScape (http://metscape.ncibi.org/), and BioCyc (https://biocyc.org/) (Fig. 3) [20, 31]. All these steps are uniquely valuable and the high-quality metabolomics data depends on the selection and implementation of the right choice.

During the preparation of this thesis, LC-MS/MS-based untargeted semi-quantitative metabolomics (publications 1, 10 & 11), and targeted quantitative (publication 7) workflows were optimized and utilized in various research projects.

1.2.3 Lipidomics

Lipids are a key class of biologically active "metabolites", which play a central role in numerous pathophysiological processes. The dysregulation of lipids and lipid metabolism are interlinked with several diseases, for instance diabetes, cancer, Alzheimer's, pulmonary diseases, and several metabolic disorders that are related to peroxisome, mitochondria, and lysosome organelles [34, 35]. Lipidomics is a sub-branch of "metabolomics" that deals with large-scale profiling, quantitation and structural elucidation of lipid species in a given sample at a stipulated point of time and condition.

- **Lipid definitions**

Historically, the word lipid has matured from "lipine, lipin, lipoid, and lipide" and there is no satisfactory or universally accepted definition to date [36]. Some educational aids such as biochemistry textbooks and the International Union of Pure and Applied Chemistry (IUPAC) described lipids as "a group of naturally occurring substances that are soluble in non-polar and/or organic solvents". But, the definition provided in terms of solubility is ambiguous and does not suit lipids (e.g. gangliosides, bile acid conjugates) which are soluble in water and/or other polar solvents [37]. Christie et al. proposed that "lipids are fatty acids and their derivatives, and substances related biosynthetically or functionally to these compounds" [38]. However, this definition does not cover isoprenoids, steroid hormones, and polyketides. Lately, Fahy and colleagues from the LIPID MAPS consortium broadly defined lipids as "hydrophobic or amphipathic small molecules that may originate entirely or in part by carbanion-based condensations of ketoacyl thioesters (i.e. fatty acyls, glycerolipids, glycerophospholipids, sphingolipids, saccharolipids, polyketides) and/or by carbocation-based condensations of isoprene units (i.e. prenols, sterols)" [39].

- **Lipid classification, nomenclature, and functions**

Bloor classified lipids (by then lipoids) into simple, complex, and derived lipids. Whereas, biochemists segregated them into the membrane, energy, and bioactive lipids according to their functions (Table 1) [36].

In 2005, the LIPID Metabolites and Pathways Strategy (LIPID MAPS; https://www.lipidmaps.org/) consortium and the International Lipid Classification and National Nomenclature Committee (ILCNC) classified lipids into eight well-defined categories based on their chemical and biochemical properties (Table 2, 3 & Fig.4), which were further reviewed and updated in 2009 and 2020 [39-42].

Table 1 An overview of important functions of various lipid classes [36, 43].

Functions	Lipid classes
Membrane components	PC, PE, PI, PS, PG, PA, SM, CL, GluCer, GalCer, ChE, ST, glycolipids, and gangliosides
Energy storage & metabolism	FA, MG, DG, TG, and AcCa
Signaling	Lysophospholipids, MG, DG, FA, AcCa, eicosanoids, Cer, SPH, and oxidized lipids
Antioxidant Lipid (fatty acid) transport Mitochondrial respiration	Plasmalogens Carnitine esters or acylcarnitines Cardiolipins

Table 2 Lipid classification according to LIPID MAPS. Shown are the eight lipid categories, the number of lipid classes with a few examples, and the number of lipid structures for each lipid category compiled within the LIPID MAPS structure database [39, 40].

S. No	Lipid categories	Lipid classes	A few examples of lipid classes	Abbreviation (No. of lipid structures in LMSD)
1	Fatty acyls	14	Fatty acids, AcCa	FA (10761)
2	Glycerolipids	08	MG, DG, TG	GL (7739)
3	Glycerophospholipids	26	PC, PE, PG, PS, PI	GP (10097)
4	Sphingolipids	10	SM, Cer, HexCer	SP (4989)
5	Sterol lipids	06	Cholesterol, Bile acids	ST (3899)
6	Prenol lipids	05	Isoprenoids	PR (2485)
7	Saccharolipids	06	Acylaminosugars	SL (1345)
8	Polyketides	16	Linear polyketides	PK (7178)

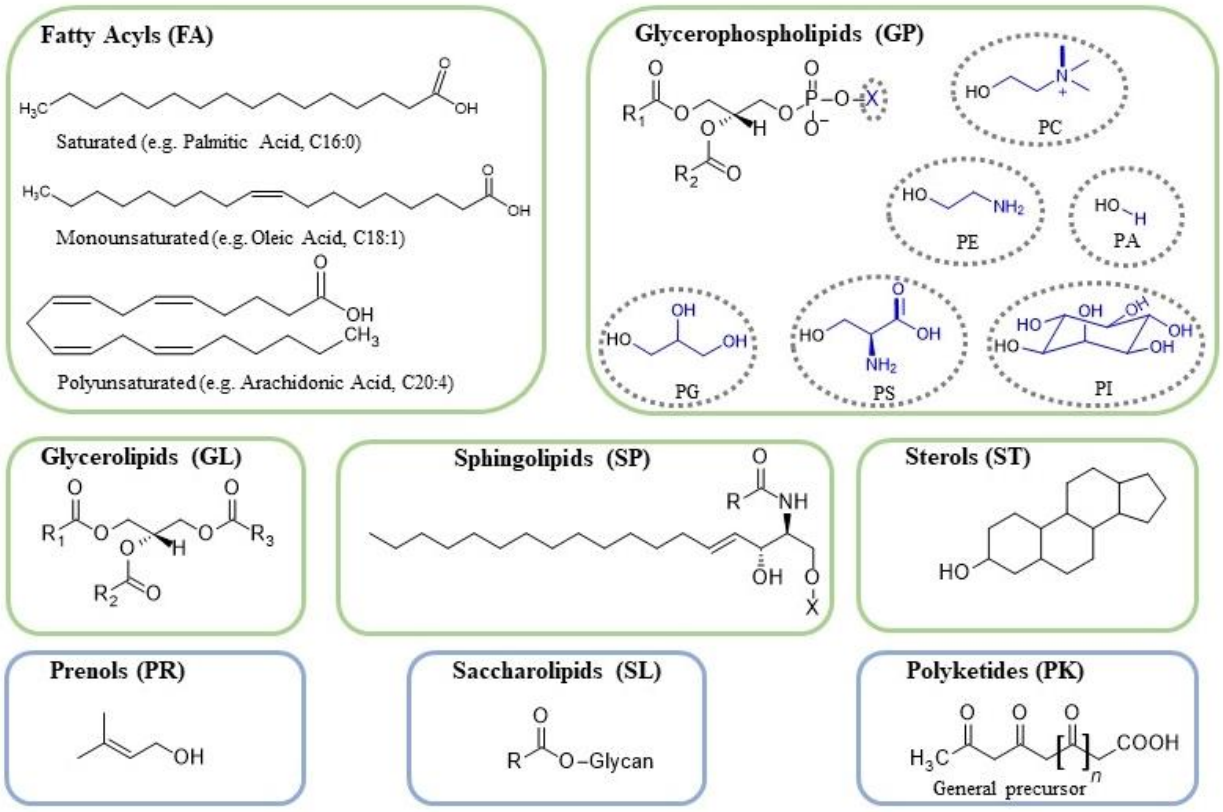

Fig. 4 Representative structures of the eight lipid categories. Fatty acyls (activated fatty acids) and/or fatty acids (FA) are the simplest lipid categories and act as building blocks for several complex lipids. Fatty acids differ by carbon chain length (e.g. short-, medium-, long-, and very long-chain) and degree of unsaturation (e.g. saturated, monounsaturated, and polyunsaturated). Glycerolipids (GL) are fatty acid esters of glycerol in which either one, two, or three fatty acids are bound to a glycerol backbone via an ester linkage (e.g. mono-, di-, and triacylglycerol). Whereas, glycerophospholipids (GP; also termed as phospholipids) consist of an additional phosphate group and are subdivided into various classes based on polar headgroup (X; choline, ethanolamine, glycerol, serine, inositol, etc.). Lysoglycerophospholipids (e.g. LPC, LPE, LPG, LPS, and LPI) consist of a single fatty acid chain along with the polar head group. Sphingolipids (SP) contain a sphingosine backbone with a fatty acid chain (R) and vary by polar fraction (X). Sterols (ST) are tetracyclic ring structures (e.g. cholesterol, bile acids) [39-42, 44, 45]. These five (i.e. FA, GL, GP, SP, ST) are the frequently analyzed lipid categories (highlighted in light green color boxes) in conventional lipidomics studies. The above representative chemical structures are drawn using the ACD/ChemSketch program.

Each of these lipid categories is further divided into main classes, subclasses, and substructures. In total (as of January 2024), 48,493 unique lipid structures (26,426 curated and 22,067 computationally generated) are covered in the LIPID MAPS Structure Database (LMSD). The LIPID MAPS In-Silico Structure

Database (LMISSD), on the other hand, consists of over 1.13 million lipid structures (among which roughly 25,000 overlap with LMSD), created by the computational expansion of head groups and side chains of frequently occurring lipids including fatty acyls (1,795), glycerolipids (787,670), glycerophospholipids (304,139), and sphingolipids (38,886). In theory, the total number of lipid species is possibly far from those compiled in the LIPID MAPS and/or any other databases such as LipidSearch, Metlin, HMDB, SwissLipids, etc.

Table 3 The hierarchy of lipid classification, shorthand notation, and characterization of lipid species, explained with an example of PC(P-34:1). The standard rules for shorthand nomenclature of lipid structures derived from mass spectrometric approaches are detailed in references [41, 46].

Nomenclature level	**Description**	**Shorthand notation [Preferred analysis]**
Category	Glycerophospholipid	GP
Main class	Glycerophosphocholine (Phosphatidylcholine)	PC
Subclass	1-O-alkenyl-acylglycerophosphocholine	PC(P-XX:YY)
Sum composition	Total number of carbon atoms and double bonds in the fatty acyl chains	PC(P-34:1) [Full scan MS]
Molecular composition	Without *sn*-position confirmation (underscore separator)	PC(P-16:1_18:0) [Tandem MS]
Molecular composition	With *sn*-position confirmation (slash separator)	PC(P-16:1/18:0) [separation MS, MS3]
Structurally defined lipid	Double bond position confirmation	PC(P-16:1(9Z)/18:0) [OzID, PB, UVPD]

- **Lipidomics workflow**

Although several strategies (including fluorescent dyes, enzyme kits, thin layer chromatography, NMR, etc.) have been employed in lipidomics, the field has greatly advanced with the developments in MS methodologies. Similar to polar metabolomics, the conventional lipidomics workflow comprises experimental design, sample collection and storage, sample preparation, MS data acquisition, data processing, and biological interpretation (Fig. 5) [35, 47, 48]. A draft of minimal guidelines and

recommendations for MS-guided lipidomics (covering pre-analytics, lipid extraction, lipid ion monitoring, lipid species identification and quantitation, quality controls, normalization, validation, and reporting of the lipidomics data, etc.), resources related to potential difficulties (such as isomeric overlap, isobaric overlap, and in-source fragmentation), and diagnostic fragment ions for various lipid classes and molecular species are concisely described in the Lipidomics Standards Initiative (https://lipidomics-standards-initiative.org/) web portal [49]. The utmost important steps of the lipidomics workflow are briefly described in the following sections.

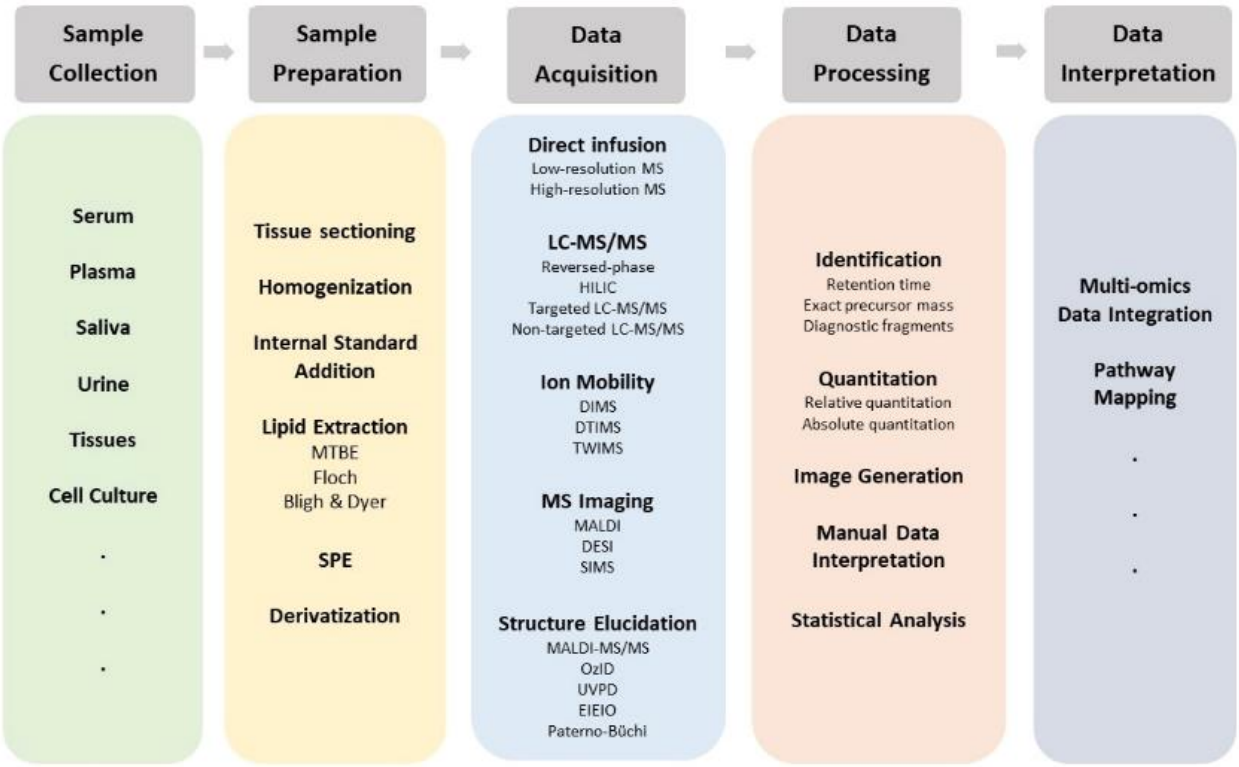

Fig. 5 An overview of mass spectrometry-guided lipidomics. The figure is modified from the original figure listed in reference [47].

Pre-analytics (measures prior to the actual lipidomics) include (i) study design, (ii) nature and origin of the study samples, (iii) sample collection (e.g. sample amount, collection tubes, collection time, number of cell passages, demographic and clinical data), (iv) sample quality (e.g. hemolysis, lipemia), (v) storage conditions, (vi) freeze-thaw cycles, (vii) fixative agents and MS-compatible embedding material in the case of tissue specimens, (vii) selection and optimization of MALDI matrices, and (viii) prevention of artefactual generation (e.g. hydrolysis, oxidation, peroxidation products), etc., are crucial which can influence the data quality and should be documented properly for the interpretation of lipidomics data [50].

In general, direct infusion, direct flow injection, and LC-MS/MS-guided lipidomics studies utilize lipid extracts from biological matrices (e.g. serum/plasma, saliva, urine, cell pellets, tissues, feces), whereas MS imaging experiments mostly use non-extracted matrices such as intact tissue slices, whole organism, and/or single cells [35]. In sample preparation, homogenization (utilizing mortar and pestle, pebble mill with beads, etc.) is an important step to extract lipids from biological specimens such as tissues and cell pellets. To extract lipids, researchers have developed and optimized several extraction protocols depending on the analytes of interest (e.g. general lipid classes, polar lipids, eicosanoids, and fatty acids), biological matrices, and experimental conditions. To mention a few, liquid-liquid extraction (LLE) methods based on chloroform/methanol/water ($CHCl_3$/MeOH/H_2O) mixture such as Bligh & Dyer [51] and Folch methods [52], alternatively heptane/isopropanol/water (Heptane/IPA/H_2O) mixture [53], and more recently less toxic methyl *tert*-butyl ether/methanol/water (MTBE/MeOH/H_2O) [54], butanol/methanol/water (BuOH/MeOH/H_2O) mixture [55] based LLE methodologies have been developed for global lipidomics analysis (Fig. 5). On the other hand, solid-phase extraction (SPE) and derivatization protocols (e.g. Girard's Reagent P, methylation) were also demonstrated for specialized applications [47, 56]. Notably, none of the above-mentioned and/or any other protocols are capable of extracting all possible lipid classes and molecular lipid species in a single experiment due to the wide polarity range and diversity of the lipidome. Furthermore, the addition of appropriate internal standards (for instance naturally or biologically not occurring lipids, odd-chain fatty acid-containing lipids, isotopically labeled lipid internal standard mixtures such as SPLASH and UltimateSPLASH LIPIDOMIX) to the homogenates before the extraction step (in the case of shotgun and LC-MS/MS) [57], spotting of stable isotopically labeled internal standards, and/or serial dilutions of calibration standards on tissue sections (in the case of MS imaging) [22] is vital in quantitative lipidomics workflows. The added internal standards are then used to compensate inheritance variations in sample preparation and ionization efficiencies and to assist in the estimation of absolute and/or relative quantitative values of lipid classes/molecular lipid species [58].

In MS data acquisition, lipidomic datasets can be acquired either directly from the intact biological specimens using MS imaging methods (e.g. MALDI MSI, DESI MSI, SIMS, and NIMS) or by using crude lipid extracts with the help of organic solvents. The latter one includes direct infusion or direct flow injection analysis (also called shotgun lipidomics) and separation methodologies (e.g. normal-phase LC, reversed-phase LC, HILIC, GC, CE, and IMS) coupled to MS [48, 59]. As a subsection of metabolomics, lipidomics also uses similar analytical strategies depending on the study hypothesis. For instance, full MS or tandem MS (MS/MS) or both can be employed simultaneously either in a targeted (hypothesis-driven; validation) or untargeted (hypothesis generation; discovery) manner using unit/low mass resolution (e.g. QqQ) and/or high-resolution and high-mass-accuracy MS instruments (e.g. Orbitrap, Q-TOF). Moreover, specific methodologies namely ozone-induced dissociation (OzID), Paternò-Büchi (PB) functionalization,

ultraviolet photodissociation (UVPD), and electron impact excitation of organic ions (EIEIO) were developed for the structural elucidation of the molecular lipid species (e.g. determination of double-bond positions) (Fig. 5).

A vast number of data processing and data analysis tools are available for qualitative and quantitative lipidomics data analysis, specific to the employed analytical strategies. Some of the frequently used data processing tools in lipidomics research are mentioned here for shotgun lipidomics (e.g. LipidXplorer, LipidPionner, LipidView, LipidProfiler, LipidQC, ALEX, LipidMatch, and LipidSearch), LC-MS/MS (e.g. LipidSearch, Progenesis QI, SimLipid, LipidMatch, LipidFinder, XCMS, MZmine, Lipidyzer, MS-DIAL, LIQUID, and Lipid Data Analyzer), and MS imaging (e.g. Mirion, MSiReader, METASPACE, Lipostar, BioMap, Mozaic, and ImageQuest) [60]. Lipid annotations can be attained by using customized precursor (MS) and diagnostic fragment ion (MS/MS) libraries derived from experimental or computational methods including vendor-specific databases (e.g. LipidSearch), or public respiratory databases such as LIPID MAPS (https://www.lipidmaps.org/), Metlin (https://metlin.scripps.edu/), Human Metabolome Database (https://hmdb.ca/), SwissLipids (https://www.swisslipids.org/), LipidBank (http://lipidbank.jp/), LipidHome (https://www.ebi.ac.uk/metabolights/lipidhome/), and LipidBlast (https://fiehnlab.ucdavis.edu/projects/LipidBlast). Although several automated data processing tools are available, an additional manual curation step is essential in lipidomics/metabolomics data analysis workflows to remove and/or minimize false-positive identifications that may arise due to isotopic, isomeric and isobaric overlap, in-source fragmentation, or contaminants. Furthermore, various statistical analyses including univariate (e.g. fold-change analysis, t-test, volcano plots, one-way ANOVA), multivariate (e.g. PCA, HCA, PLS-DA, OPLS-DA, MANOVA), and hierarchical clustering analysis (e.g. dendrogram and heat maps) are applied to reveal the differentially abundant lipids/metabolites among the study groups [20]. Lastly, integration of lipidomics data with other molecular-omics data, functional characterization, and pathway analysis is challenging but crucial to disclose the underlying molecular mechanisms associated with lipid metabolism in normal physiological and pathological conditions.

During the preparation of this thesis, (i) LC-MS/MS-based untargeted semi-quantitative lipidomics (publications 1, 10 & 11), (ii) MALDI MS imaging-guided qualitative and relatively quantitative lipidomics (publications 2, 9 & 11), (iii) direct flow injection quantitative lipidomics (publication 3), and (iv) LC-MS/MS-based targeted quantitative lipidomics (publications 8, 10 & 11) workflows were developed and employed in various research projects.

1.3 Mass spectrometry

1.3.1 History and basic principles

Mass spectrometry (MS) is an indispensable and sensitive analytical platform that provides qualitative, quantitative molecular and spatially-resolved information about compounds in a given sample. Regardless of the instrument configuration, a typical mass spectrometer comprises three basic components including (i) an ionization source, (ii) a mass analyzer, and (iii) an ion detector unit. The ionization source operates at atmospheric pressure (AP) or under vacuum conditions, whereas both the mass analyzer and ion detector units are operated under high-vacuum conditions (Fig. 6). Ions from various chemical compounds (i.e. organic or inorganic) are produced in the ionization source by different ionization mechanisms, including protonation, deprotonation, cationization, electron ejection, or electron capture, after transfer from the condensed phase into the gas phase. The generated ions are then electrostatically propelled into the mass analyzer where they are separated based on mass-to-charge-number (*m/z*) ratios. In tandem MS experiments, selected ions (precursor ions) are fragmented in a collision cell (e.g. HCD cell), and the fragment ions are then analyzed in a second mass analyzer and detected by a detector unit (e.g. electron multiplier). Finally, the data processing system generates a mass spectrum, which is a two-dimensional plot consisting of *m/z* values on the *x*-axis and relative abundances of the ions (i.e. signal intensities) on the *y*-axis (Fig. 6) [61-63].

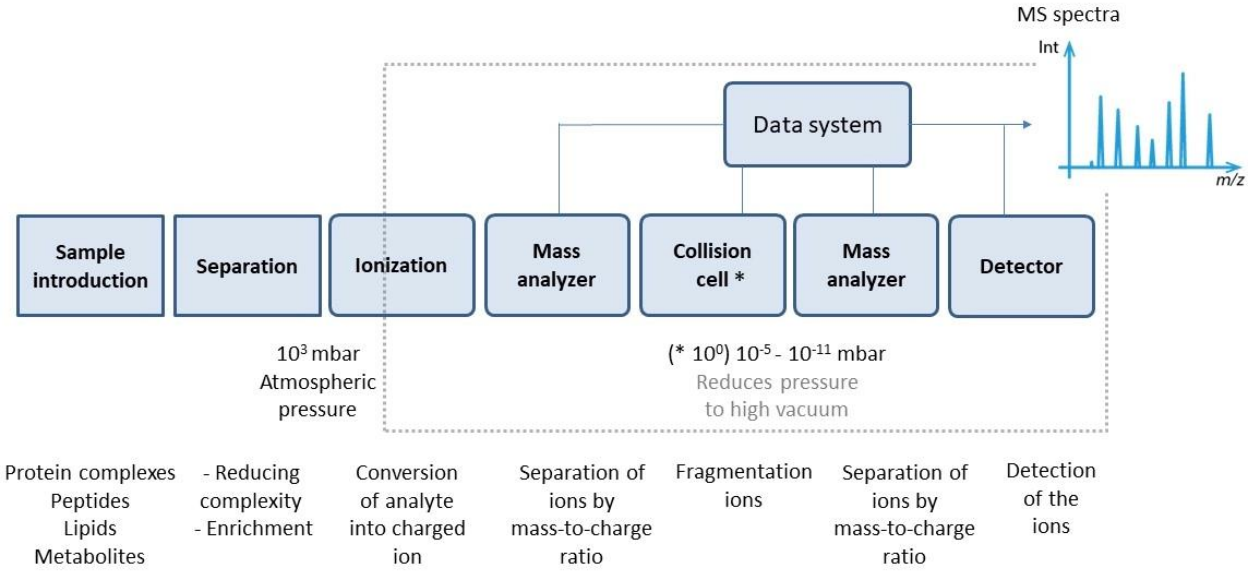

Fig. 6 Basic components of a typical mass spectrometer. The figure is prepared based on the information obtained from mass spectrometry textbooks listed in the reference [61-63].

In addition to the above-mentioned three basic components, mass spectrometers are also associated with a sample inlet system to introduce the sample (Fig. 6). For instance, the most frequently used methods are

direct insertion with a probe and/or plate usually in the case of MALDI MS, direct injection and/or infusion with the help of GC, LC, and CE separation techniques in EI, ESI, and APCI MS analyses [61, 62].

Mass spectrometry has undergone remarkable technological developments in the last decades and made a significant contribution as an analytical platform in many areas, particularly in biomedical research such as omics (e.g. proteomics, metabolomics, lipidomics, and glycomics), high throughput drug discovery, and drug metabolism [61]. The history of MS goes back to the early 1900's and commences with the inventive work of German physicist W. Wien (i.e. deflection of rays of positively-charged particles by magnetic fields) followed by J. J. Thomson (i.e. discovery of the electron and the isotopes of neon) and his protégé F. W. Aston (i.e. atomic characterization of numerous elements using mass spectrograph). Since then, several researchers contributed enormously to the advancement of the field by developing (i) various ionization techniques (e.g. EI, CI, DCI, FI, FAB/LSIMS, SIMS, FD, LIFDI, PD, MALDI, LDI, ESI, APCI, APPI, DESI, DART, REIMS, TI, SS, GD, ICP), (ii) instrumentation methodologies including different mass analyzers (e.g. electric sector, magnetic sector, quadrupole, ion trap, TOF, FT-ICR, Orbitrap), (iii) hybrid mass spectrometers (e.g. QqQ, QIT-TOF, TOF/TOF, Q-TOF, ion trap Orbitrap, Q-Orbitrap), (iv) numerous fragmentation methods (e.g. CID, HCD, SID, ECD, ETD, UVPD, IRMPD), (v) MS imaging modalities (e.g. MALDI-MSI, DESI-MSI, Nano-DESI MSI, LAESI-MSI, LA-ICP MSI, SIMS, NIMS, LTP-MSI), (vi) coupling of separation technologies to the MS (e.g. HPTLC-MS, LC-MS, GC-MS, CE-MS, IMS-MS, FAIMS), and (vii) different data acquisition strategies including DDA, DIA, SWATH, SRM, MRM, and PRM. A snapshot of major milestones (not a complete list) highlights the key individuals and their inventions in the history of mass spectrometry and allied research topics, as detailed in Fig. 7 [61-63].

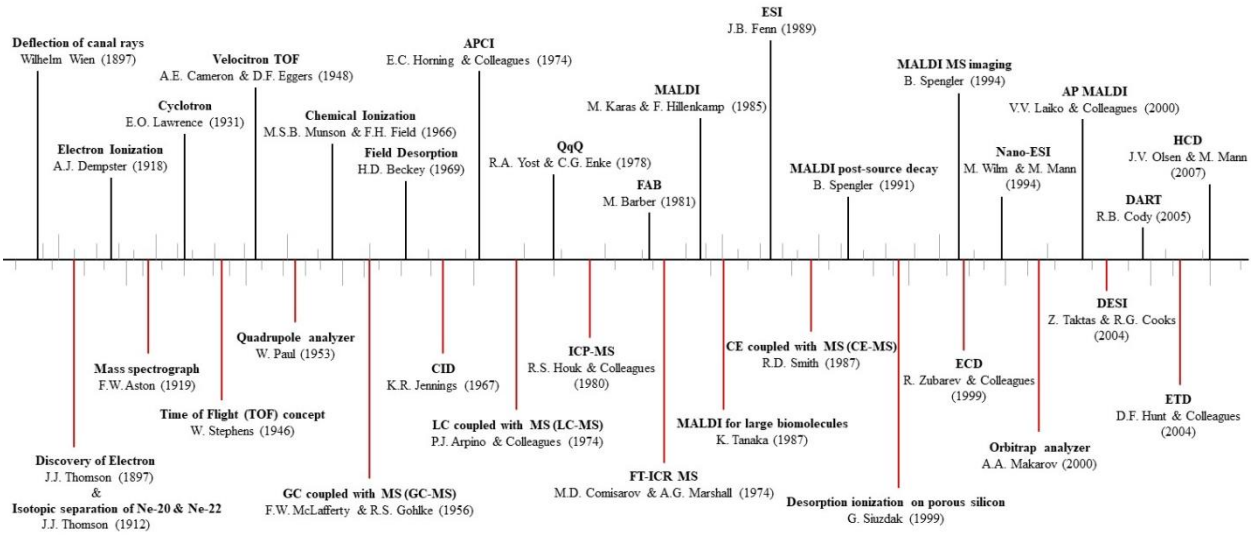

Fig. 7 Snapshot of major milestones in the field of mass spectrometry. The figure is prepared based on the collective information obtained from the scientific literature and mass spectrometry textbooks listed in reference [61-63].

Abbreviations: EI: electron ionization; CI: chemical ionization; DCI: desorption chemical ionization; FI: field ionization; FAB: fast atom bombardment; LSIMS: liquid secondary ion mass spectrometry; FD: field desorption; LIFDI: liquid injection field desorption/ionization; PD: plasma desorption; LDI: laser desorption/ionization; APCI: atmospheric pressure chemical ionization; APPI: atmospheric pressure photoionization; DART: direct analysis in real time; REIMS: rapid evaporative ionization mass spectrometry; TI: thermal ionization; SS: spark source; GD: glow discharge; ICP: inductively coupled plasma; TOF: time of flight; FT-ICR: Fourier-transform ion cyclotron resonance; QqQ: triple-quadrupole; QIT: quadrupole ion trap; SID: surface-induced dissociation; ECD: electron capture dissociation; ETD: electron transfer dissociation; IRMPD: infrared multiple photon dissociation; FAIMS: field-asymmetric ion mobility spectrometry; DIA: data-independent acquisition; SWATH: sequential window acquisition of all theoretical mass spectra, SRM/MRM/PRM: selected/multiple/parallel reaction monitoring; and remaining shortened forms are abbreviated in the main abbreviations list and/or respective sections in the text.

1.3.2 Mass spectrometry imaging

Mass spectrometry imaging (MSI) is a precise and informative bioanalytical technique that has clear advantages over other non-imaging MS and conventional imaging methods, since (i) labeling is not necessary (label-free), (ii) several hundreds of analytes are conceivably identified and quantified in a single experiment (untargeted), and (iii) spatial information of a wide range of endogenous and exogenous molecules including lipids, polar metabolites, peptides, proteins, glycans, toxins, pharmaceuticals in biological tissues (e.g. mammals, plants, insects, microorganisms) is provided [22, 34, 64]. Among the techniques are matrix-assisted laser desorption/ionization (MALDI), desorption electrospray ionization (DESI), nanostructure-initiator mass spectrometry (NIMS), secondary ion mass spectrometry (SIMS), laser ablation electrospray ionization (LAESI), laser ablation inductively coupled plasma (LA-ICP) MS imaging, and several others. Each method has its own merits and demerits, ranging from its applicability, achievable sensitivity, and resolution. To highlight a few, SIMS provides the highest spatial resolution down to the nanometer range but suffers from the severe fragmentation of molecular ions and lower sensitivity in the higher mass range [22]. A recently developed ambient ionization technique (i.e. DESI MSI) offers the advantage of little and/or no sample preparation but the spatial resolution is limited [65, 66]. MALDI MSI (introduced by Bernhard Spengler in 1994) offers high sensitivity and an outstanding lateral resolution for a large variety of compound classes, but the sample preparation and matrix application processes are laborious [22, 67]. Nevertheless, MALDI MSI has been the most commonly employed MS imaging methodology in the field of biomedical, clinical, and molecular biological research [64].

Sample preparation is the most essential step in any kind of MS imaging experiment. Parameters such as (i) biological specimens/tissue collection and storage, (ii) quenching of the enzyme activity to diminish delocalization and/or degradation of biomolecules (e.g. flash freezing, fixation), (iii) optional embedding with MS-compatible embedded material (e.g. gelatin, tragacanth, carboxymethylcellulose) in the case of

non-homogeneous, delicate, and/or fragile samples (e.g. insects, worms), (iv) sectioning (typically < 20 µm thick) and storage of the tissue slices, (v) washing, pre-spraying, and on-tissue proteolytic (e.g. trypsin) digestion in the case of protein/peptide analysis, (vi) thawing and matrix application (e.g. choice of the matrix, solvent, local matrix concentration, application method, homogeneity of the matrix on tissue surfaces, and matrix crystal size) are crucial and directly influence the MSI data quality [22, 34].

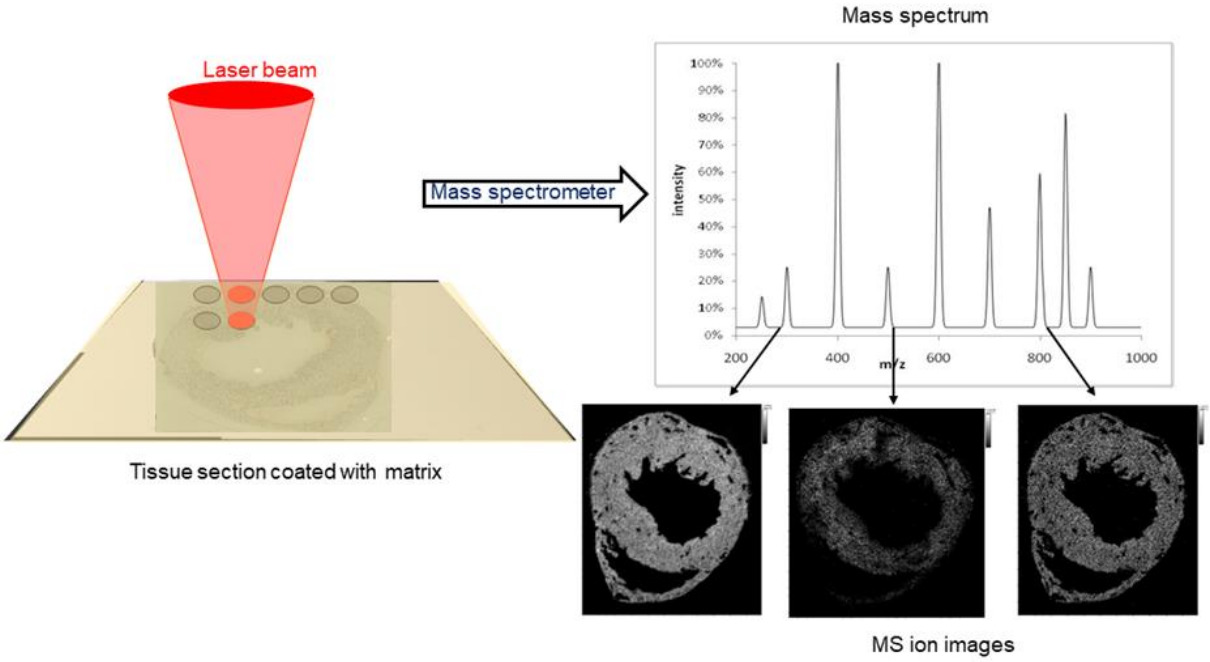

Fig. 8 A schematic representation of the MALDI MS imaging workflow. The figure is modified from the original figure listed in reference [64].

The basic workflow of the MALDI MS imaging experiment is depicted in Fig. 8. In brief, after carefully optimized sample preparation, the biological specimen is scanned with a pulsed laser (for instance nitrogen gas laser with a wavelength of 337 nm or a solid-state laser with 343 nm) in a grid array of fixed dimensions (i.e. ROI; region of interest), and the step size is defined and positioned over the section. For each pixel/spot, a single mass spectrum is recorded. Subsequently, spatial distribution and relative intensities of molecular ions can be visualized (i.e. MS ion images) using a color scale corresponding to the signal intensities of ions at each pixel (Fig. 8) [22, 64]. Diagnostic fragment ions resulting from on-tissue fragmentation (MS/MS) experiments can be used for compound identifications. Otherwise, molecular species annotations are based on high mass resolution (R > 100,000) MSI measurements and accurate mass matching with databases comprising of curated/computationally-generated molecules within a certain mass error range, typically root mean square error (RMSE) value ≤ 2 ppm [34].

Technological advancements, specifically (i) improvements in reproducible sample preparation and data processing workflow to enhance the reliable interpretation of quantitative MS imaging data (publication 2, current thesis) [34], (ii) developments in instrumentation such as lateral resolution close-to-physiological conditions (1.4 µm spot size, subcellular level) [68], molecular and topographical analysis of 3D surfaces [69], and (iii) easy-to-use bioinformatics and online respiratory tools for MSI data processing and evaluation [70] have further advanced the field. Furthermore, a combination of MSI with other analytical techniques including ion mobility MSI, LC-MS/MS, and/or complementary imaging modalities such as imaging with Raman spectroscopy, magnetic resonance imaging (MRI), positron emission tomography (PET), computed tomography (CT), microscopic and histological methods (e.g. H&E staining) possibly expand and validate the biological conclusions obtained from MS imaging.

1.4 Peroxisomes and peroxisomal biogenesis disorders

1.4.1 Background and general functions

Peroxisomes are ubiquitous, multifunctional, and single membrane-bound subcellular organelles that exist in nearly every eukaryotic cell. Initially, they were reported as "microbodies" in epithelial cells of proximal convoluted tubules of the mouse kidney [71], and then in rat liver parenchymal cells [72]. Successively after a decade, De Duve coined the name "peroxisomes" due to their functional involvement in the hydrogen peroxide (H_2O_2) metabolism [73]. Further to mention, the granular electron-lucent matrix of peroxisomes consists of a wide range of FAD-dependent oxidases (e.g. D-amino oxidase, sarcosine oxidase, acyl-CoA oxidases, pipecolic acid oxidase, urate oxidase) which produce H_2O_2 during the conversion of their substrates (such as D-proline, sarcosine, pipecolate, and uric acid) and the antioxidative enzyme catalase that decomposes H_2O_2 (Fig. 9) [74]. Furthermore, peroxisomes encompass many other antioxidant enzymes (for instance peroxiredoxin 1 and 5, Cu/Zn-superoxide dismutase, glutathione peroxidase, Mn-superoxide dismutase, and epoxide hydrolase) which participate in the reactive oxygen (ROS) and reactive nitrogen (RNS) species metabolism [75, 76].

Peroxisomes are very dynamic and differ in their abundance, size (0.1-1µm), shape (e.g. spherical, elongated, tubular and angular), protein and enzyme composition depending on the cell type, organ, organism as well as metabolic needs and response to the external and/or pharmacological stimuli such as nutritional fluctuations and inflammatory responses [74, 77]. Mammalian peroxisomal proteomics studies revealed that these versatile organelles possess more than 190 different proteins, which mediate several degradative (catabolic) and biosynthetic (anabolic) metabolic processes [78]. To mention (i) breakdown of very-long-chain fatty acids and bioactive secondary lipid mediators via β-oxidation, (ii) degradation of branched-chain fatty acids and carboxylates via α- and β-oxidation, (iii) biosynthesis of ether-linked

phospholipids (plasmalogens), retinoic acid, docosahexaenoic acid, cholesterol and dolichol, (iv) formation of primary and conjugated bile acids, (v) purine and polyamine catabolism, (vi) detoxification of glyoxylate, and (vii) regulation of acyl-CoA/CoA ratio (Fig. 9) [79, 80]. Utmost of these indispensable metabolic functions is unique for peroxisomes, although some require cooperation with other subcellular organelles such as mitochondria, endoplasmic reticulum (ER), lysosomes, and lipid droplets [81, 82]. Described below are the selected specific functions of peroxisomes that are associated with lipid metabolism.

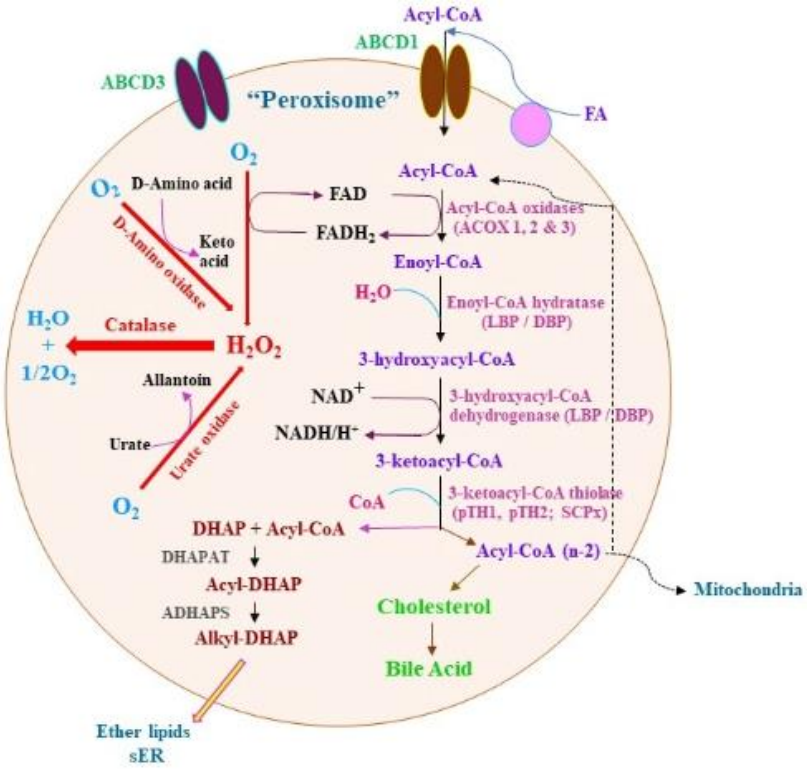

Fig. 9 Major metabolic functions of peroxisomes. The figure is modified from the original figure provided by Prof. Dr. Eveline Baumgart-Vogt.

- **Fatty acid β-oxidation**

Fatty acids (FAs) undergo degradation through several mechanisms (e.g. α-, β- and ω-oxidation), and among the most common route is β-oxidation. The peroxisomal beta-oxidation process was first noticed in plant cells [83], and then in mammalian cells [84]. In mammals, β-oxidation occurs in both peroxisomes and mitochondria, whereas in yeasts and plants takes place only in peroxisomes [75]. Though the mechanistic principles of β-oxidation processes are identical with four subsequent enzymatic reactions, there are few exceptions between these two organelle systems. For instance, the primary step of the β-oxidation process in peroxisomes is mediated by acyl-CoA oxidases (ACOX) in contrast to the acyl-CoA dehydrogenases (ACAD) in mitochondria. Another major difference is substrate specificity; as mentioned,

peroxisomes actively participate in the breakdown of very-long-chain fatty acids (VLCFAs, ≥ C22), long-chain dicarboxylic acids, eicosanoids (e.g. prostaglandins, leukotrienes), branched-chain fatty acids (e.g. pristanic acid), bile acid intermediates (e.g. DHCA, THCA), xenobiotics, vitamins E and K. Mitochondria, on the other hand, are mainly responsible for the degradation of short-, medium-, and long-chain fatty acids (≤ C20). Further, FAs are transported as activated fatty acids (i.e. acyl-CoAs) across the peroxisomal membrane (Fig. 9), whereas in mitochondria they are transported as acylcarnitines (also called carnitine esters) via the carnitine shuttle. Moreover, mitochondria completely oxidize FAs via the citric acid cycle, while peroxisomes merely shorten the fatty acyl chain length and the end products need to be transferred to the mitochondria for complete breakdown [80-82, 85].

As detailed in Fig. 9, four sequential cyclic steps of the peroxisomal β-oxidation process include (i) dehydrogenation of fatty acyl-CoAs → 2-trans-enoyl-CoAs mediated by acyl-CoA oxidases (i.e. ACOX1, ACOX2, and ACOX3), (ii) hydration of unsaturated intermediate enoyl-CoAs → 3-hydroxyacyl-CoAs catalyzed by bifunctional proteins (i.e. L-bifunctional protein; LBP and D-bifunctional protein; DBP), (iii) dehydrogenation of 3-hydroxyacyl-CoAs → 3-ketoacyl-CoAs exerted by bifunctional proteins, (iv) and thiolytic cleavage of terminal acetyl-CoA group leading to an acyl-CoA, which is two carbon atoms shorter than the precursor molecule mediated by thiolase enzymes (i.e. pTH1 and pTH2; SCPx).

- **Fatty acid α-oxidation**

Branched-chain fatty acids comprising methyl and/or other groups at the third carbon cannot undergo a straight β-oxidation process. Degradation of such FAs (e.g. phytanic acid) requires a prior oxidative decarboxylation (i.e. removal of carbon atom) to generate 2-methyl branched-chain fatty acids (e.g. pristanic acid), which can be degraded by peroxisomal β-oxidation. The phytanic acid α-oxidation process takes place via the consequent action of various peroxisomal enzymes including (i) very long-chain acyl-CoA synthetase (phytanic acid → phytanoyl Co-A), (ii) phytanoyl-CoA 2-hydroxylase (phytanoyl Co-A → 2-OH-phytanol-CoA), (iii) 2-hydroxyphytanoyl-CoA lyase (2-OH-phytanol-CoA → pristanal), and (iv) pristanal dehydrogenase (pristanal → pristanic acid). The resulting pristanic acid undertakes three cycles of peroxisomal β-oxidation, and then the end products are shuttled to mitochondria for a complete oxidation process [75, 80, 81, 85].

- **Ether-linked phospholipids biosynthesis**

Ether-linked phospholipids are a unique class of peroxisome-derived glycerophospholipids with an ether linkage at the *sn-1* position and an ester linkage at the *sn-2* position of the glycerol backbone [58]. They predominantly occur in two subgroups (i) 1-O-alkyl (plasmanyl phospholipids), and (ii) 1-O-alkenyl (plasmenyl phospholipids; plasmalogens) with ethanolamine and/or choline as head group, rarely inositol

and serine head groups have also been observed. In mammals, ether lipids constitute up to 18-20% of the phospholipid pool, and the highest levels were witnessed in the lung, heart, brain, spleen, kidney, white blood cells, skeletal muscles, and testis [81, 86].

Ether-linked phospholipid biosynthesis involves a series of enzymatic reactions in peroxisomes and ER. As shown in Fig. 9, the foremost step includes the esterification of dihydroxyacetone phosphate (DHAP) with fatty acyl-CoAs to produce acyl-DHAP by the action of peroxisomal enzyme dihydroxyacetone phosphate acyltransferase (DHAPAT). In the following step, acyl-DHAP is converted to alkyl-DHAP by fatty alcohol and the enzyme alkyl-DHAP synthase (ADHAPS) (Fig. 9). Further, the third step is processed in both peroxisomes and ER, where alkyl-DHAP is reduced to alkylglycerol-3-phosphate (alkyl-G3P) by a membrane-bound enzyme acyl/alkyl-DHAP reductase. Finally, alkyl-G3P undertakes subsequent reactions in the ER to synthesize various ether-linked phospholipid species [86-88].

- **Synthesis of docosahexaenoic acid, bile acids, and cholesterol metabolism**

Docosahexaenoic acid (C22:6; n-3, DHA) is an important polyunsaturated fatty acid, predominantly found in the brain, cerebral cortex, and retina. DHA is synthesized from an essential fatty acid α-linoleic acid (C18:3; n-3, ALA) via a sequence of desaturation and elongation phases followed by peroxisomal β-oxidation. As the last step in the biosynthetic pathway, docosapentaenoic acid (C22:5; n-3, DPA) is elongated to tetracosapentaenoic acid (C24:5, n-3) and desaturated to tetracosahexaenoic acid (C24:6; n-3, THA) in microsomes. Then, the THA undertakes one cycle of peroxisomal beta-oxidation to form DHA [89].

Cholesterol is transformed into primary bile acids through manifold enzymatic cascades in various subcellular compartments (Fig. 9). In peroxisomes, the bile acid intermediates such as 3α,7α-dihydroxy-5β-cholestanoic acid (DHCA) and 3α,7α,12α-trihydroxy-5β-cholestanoic acid (THCA) undertake one cycle of beta-oxidation to produce primary bile acids including chenodeoxycholic acid and cholic acid. Furthermore, the formed primary bile acids are then converted into taurine and/or glycine conjugates by bile acid-CoA: amino acid N-acyltransferase (BAAT), and subsequently exported from peroxisomes and excreted into bile [90, 91]. Besides cholesterol oxidation, several important enzymes such as HMG-CoA reductase (HMGCR; also localized in the ER), mevalonate kinase (MVK), phosphomevalonate kinase (PMVK), mevalonate diphosphate decarboxylase (MPD), isopentenyl diphosphate isomerase (IPP), and farnesyl diphosphate synthase (FPP) are localized in the peroxisomes and participate in the cholesterol/isoprenoid biosynthetic pathway (Fig. 9) [92].

1.4.2 Peroxisome biogenesis

Compelling evidence from different studies has shown that peroxisomes can form either (i) semi-autonomously by deriving the matrix proteins from the cytosol, membrane proteins and phospholipids from ER or (ii) autonomously from pre-existing organelles through growth and division (Fig. 10) [82]. Regardless of the process, a set of heterogeneous proteins named peroxins (PEX) encoded by genes (*Pex*) mediates (i) the formation of peroxisomal membrane assembly including import of membrane proteins, (ii) import of matrix proteins, and (iii) proliferation of the peroxisomes.

Thus far, more than 32 diverse peroxins have been recognized out of which at least 14 are well characterized in mammals, regulating various aspects of the peroxisomal biogenesis process (Fig. 10) [93]. The central phases of the peroxisomal biogenesis process are briefly described in the following sections.

- **Peroxisomal membrane assembly and import of PMPs**

Peroxisomal membrane proteins (PMPs) are translated on cytosolic polyribosomes and imported from the cytosol into the organelle membrane. Three peroxins (i.e. PEX3, PEX16, and PEX19) are known to be essential, facilitating the initial stages of biogenesis and being involved in the peroxisomal membrane assembly of various species including humans (Fig. 10) [94]. PEX19 is a major cytosolic protein, which forms a cargo complex with many different PMPs via an internal membrane protein targeting signal (mPTS) motif. PEX3 is situated at the peroxisomal membrane and serves as a membrane-anchoring site for the PEX19-PMPs cargo complex. Similarly, PEX16 is another peroxisomal membrane-bound protein that acts as a receptor for the PEX19 cargo protein complex loaded with PEX3 [75, 93, 94].

- **Import of peroxisomal matrix proteins**

Similar to PMPs, peroxisomal matrix proteins are synthesized on ribosomes in the cytoplasm and subsequently transported into import-component (pre)-peroxisomes [85]. The import is mediated by the peroxisomal targeting signal 1 (PTS 1) and 2 (PTS 2) and various receptor proteins (peroxins) (Fig. 10). Several peroxisomal matrix proteins consist of a carboxy-terminal tripeptide (PTS1) motif recognized by the soluble cytosolic receptor proteins PEX5S and PEX5L [95, 96], whereas a small subset of matrix proteins (e.g. 3-ketoacyl-CoA thiolase, phytanoyl-CoA hydroxylase, AGPS) conserved an amino-terminal nonapeptide (PTS2) motif, recognized by another cytosolic receptor protein PEX7 [97]. As stated, PEX5L and PEX5S receptors recognize the PTS1, and PEX7 recognizes the PTS2 signals of matrix proteins in the cytosol, forming a cargo complex upon binding and subsequently transporting them to the docking and translocation complex (PEX13 and PEX14) on the peroxisomal membrane [77, 85]. After docking, (i) the matrix proteins are delivered into the peroxisomal matrix (mediated by PEX2, PEX10, and PEX12), and

(ii) then the cytosolic receptors (PEX5 and PEX7) are released/recycled from the peroxisomal membrane into the cytoplasm for another import cycle (mono-ubiquitination, mediated by peroxisomal ATPase's and PEX1-PEX6-PEX26 complex) and/or degraded (poly-ubiquitination) by proteasomes [75, 77].

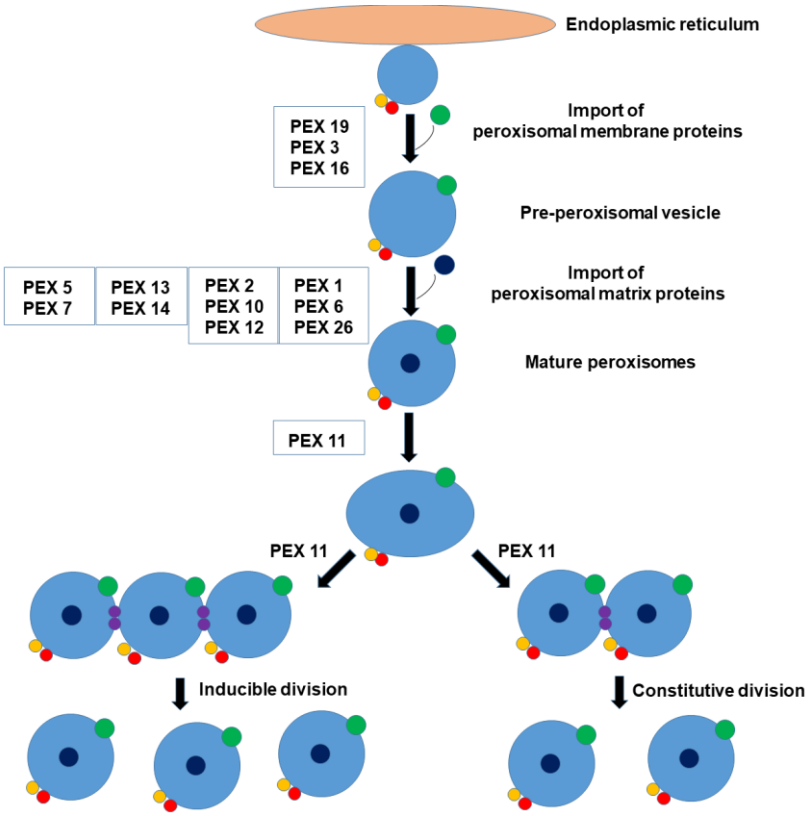

Fig. 10 A schematic representation of the peroxisomal biogenesis process. The figure is modified from the original figure listed in reference [77].

- **Proliferation of peroxisomes**

Peroxisomes are multiplied by the fission of pre-existing organelles (Fig. 10). Several studies on different model systems have revealed that the PEX11 protein family, dynamin-like proteins (DLP1/DRP1), mitochondrial fission 1 protein (Fis1), mitochondrial fission factor (Mff), and ganglioside-induced differentiation-associated protein 1 (GDAP1) collectively regulate the shape, size, and abundance of peroxisomes in a cell (Fig. 10) [98-101]. PEX11 is the highly conserved and most abundant peroxisomal membrane protein (α, β, and γ isoforms) that plays a key role in the elongation, tubulation, and constriction of pre-existing organelles, while DRP1/DLP1, Fis1, Mff, and GDAP1 are involved in the final fission event of peroxisomes as well as mitochondria [75, 77, 101].

1.4.3 Peroxisomal disorders

The functional importance of peroxisomes and their metabolism is emphasized by the discovery of numerous fatal peroxisomal disorders (PDs). The peroxisomal disorders are broadly categorized into (i) defects in specific metabolic pathways (i.e. peroxisomal enzyme deficiencies) and/or (ii) defects in functions and assembly of peroxisomes (i.e. peroxisomal biogenesis disorders).

- **Peroxisomal enzyme deficiencies**

Peroxisomal enzyme deficiencies (PEDs) are sub-classified according to the impairment of a specific metabolic pathway. For instance, PEDs are associated with defects in (i) fatty acid β-oxidation, (ii) fatty acid α-oxidation, (iii) glyoxylate metabolism, (iv) ether-linked phospholipid biosynthesis, (v) bile acid synthesis, (vi) H_2O_2 metabolism, and (vii) cholesterol biosynthesis [75, 80, 85, 102]. Table 4 provides an overview of PEDs along with the genes involved and the corresponding metabolic function abnormalities.

Table 4: List of peroxisomal enzyme deficiencies (http://www.peroxisomedb.org/)

Peroxisomal enzyme deficiencies (PEDs)	Mutant gene	Altered metabolic function
X-linked adrenoleukodystrophy (ALD)	*ABCD1*	β-oxidation
Acyl-CoA oxidase deficiency	*ACOX1*	
Acyl-CoA oxidase deficiency	*ACOX2*	
D-bifunctional protein deficiency	*HSD17B4*	
Sterol-carrier-protein X deficiency	*SCP2*	
2-methylacyl-CoA racemase deficiency	*AMACR*	
Acyl-CoA binding domain containing 5 deficiency	*ABCD5*	
Refsum disease	*PHYH/PAHX*	α-oxidation
Primary hyperoxaluria type 1	*AGXT*	Glyoxylate metabolism
Primary hyperoxaluria type 2	*GRHPR*	
Primary hyperoxaluria type 3	*HOGA1*	
Rhizomelic chondrodysplasia puncatata 2	*GNPAT*	Ether-linked phospholipid biosynthesis
Rhizomelic chondrodysplasia puncatata 3	*AGPS*	
Rhizomelic chondrodysplasia puncatata 4	*FAR1*	

ATP-binding cassette sub-family D member 3 (PMP70) deficiency	*ABCD3*	Bile acid synthesis
Bile acid-CoA: amino acid N-acyltransferase deficiency	*BAAT*	
Acatalasemia	*CAT*	H_2O_2 metabolism
Mevalonate kinase deficiency	*MVK*	Cholesterol biosynthesis

- **Peroxisomal biogenesis disorders**

Peroxisomal biogenesis disorders (PBDs) are a diverse group of multi-systemic genetic disorders that arise due to mutations in *Pex* genes, which encode PEX proteins required for the normal peroxisomal biogenesis process. Based on the clinical manifestations and biochemical abnormalities, PBDs are broadly categorized into (i) Zellweger spectrum disorders (ZSDs), (ii) rhizomelic chondrodysplasia puncatata type 1 and 5, and (iii) peroxisomal fission defects [103]. Table 5 summarizes the peroxisomal biogenesis disorders with information on the genes involved.

Table 5: List of peroxisomal biogenesis disorders (http://www.peroxisomedb.org/)

Peroxisomal biogenesis disorders (PBDs)	**Mutant genes**
Zellweger syndrome	*Pex1, Pex2, Pex3, Pex5, Pex6, Pex10, Pex11β, Pex12, Pex13, Pex14, Pex16, Pex19, Pex26*
Neonatal adrenoleukodystrophy	*Pex1, Pex3, Pex5, Pex6, Pex10, Pex12, Pex13, Pex26*
Infantile refsum disease	*Pex1, Pex2, Pex5, Pex6, Pex10, Pex12, Pex26*
Rhizomelic chondrodysplasia puncatata type 1	*Pex7*
Rhizomelic chondrodysplasia puncatata type 5	*Pex5L, Pex7*
Peroxisomal fission defects	*Pex11* (*α, β*), *DLP1/DLR1*, *Fis1*, *Mff*, *GDAP1*

Zellweger syndrome (ZS), neonatal adrenoleukodystrophy (NALD), and infantile refsum disease (IRD) with an overlap of clinical symptoms are referred to as ZSDs. Among ZSDs, ZS exhibit the most severe phenotype with craniofacial abnormalities (for instance high forehead, large anterior fontanel, microcepahaly, long filtrum), hypotonia, neuronal migration defects, hepatic, and renal insufficiency with which patients rarely survive, and die within their first year of life. While, NALD is intermediate in severity,

and patients with NALD suffer from hepatomegaly, retinitis pigmentosa, hypotonia, seizures, polymicrogyria, and absence of visual and auditory responses with which usually die in late infancy. In comparison to these two disorders, IRD is a less severe phenotype with vision problems, hearing loss, developmental delay, and some degree of intellectual disability that may survive into late childhood. Nonetheless, liver diseases, neurodevelopmental delay, retinopathy, and peripheral deafness with onset in the early months of life are common among the ZSDs [94, 104]. Mutations in at least 13 genes (Table 5) have been reported to cause ZSDs, among which the majority of the patients are diagnosed with defects in the *Pex1* [105].

Rhizomelic chondrodysplasia puncatata type 1 (RCDP1) is caused by defects in the *Pex7* which acts as a receptor for the PTS2-mediated matrix protein import. RCDP1 is the second most common PBD characterized by skeletal abnormalities, marked rhizomelia, mental retardation, congenital cataracts, neurological impairments, and respiratory problems [106]. RCDP5 (similar phenotype as RCDP1) is a recently reported disease caused by the loss of *Pex5*L [75].

Peroxisomal fission defects in which peroxisomal maintenance is compromised are manifested due to mutations in *Pex11*, *DLP1/DLR1*, *Fis1*, *Mff*, and *GDAP1* (Fig. 10). Mitochondrial encephalopathy, tubular peroxisomes and mitochondria in cells were observed in *DLP1* [107] and *Mff* mutant patients [108], whereas elongated peroxisomes and mitochondria were noticed in *GDAP1* deficient patients [109]. The *Pex11* gene encodes the PEX11 protein family, which consists of three homologous isoforms (α, β, and γ) with distinct functions. Among them, *Pex11β* is expressed constitutively throughout the tissues, while α and γ isoforms are tissue-specific and are evident majorly in the liver, heart, kidney, and testis [77, 110]. Li and Baumgart *et al*. generated a *Pex11β* knockout (KO) mouse model, in which a reduced number of peroxisomes, neonatal lethality (die immediately after birth), and severe pathological features of ZS such as developmental delay, hypotonia, and neuronal apoptosis were observed [111]. Similar to the *Pex11β* deficient mouse model, ZS phenotype features including congenital cataracts, mild intellectual disability, progressive hearing loss, gastrointestinal problems, and cells with elongated peroxisomes were observed in a human patient diagnosed with mutations in the *Pex11β* gene [112]. Further, Li and Baumgart *et al*. demonstrated that (i) overexpression of *Pex11α* by 4-phenyl butyric acid (a non-classical peroxisome proliferator) resulted in peroxisomal proliferation, and (ii) in contrast to *Pex11β*, *Pex11α* KO animals developed normally (adulthood) and displayed a mild phenotype [110]. Furthermore, in a recent study, reduced peroxisomal abundance, accumulation of triglycerides in the liver (nonalcoholic fatty liver disease) [113], and elevated levels of palmitic acid and other fatty acids in brown adipose tissue were observed in *Pex11α* deficient mice challenged with a high-fat diet [114]. Nevertheless, in-depth molecular and physiological functions of the PEX11 protein family and their isoforms (*Pex11α*, *β, γ*), metabolic and

molecular alterations due to their deficiencies in different cell types/organs/organisms, and their implications in peroxisomal disorders are still poorly understood.

1.4.4 Peroxisomal disorders – clinical and biochemical perspectives

In general, (i) elevated levels of VLCFAs, pristanic acid, phytanic acid, DHCA, THCA, pipecolic acid in plasma, (ii) reduced levels of plasmalogens and DHA in plasma and skin fibroblasts, (iii) elevated levels of LPC(26:0) and CAR(26:0) in dried blood spots are some of the biochemical parameters that are proposed for clinical suspicion of peroxisomal disorders [75, 81, 115]. Further, (i) individual enzyme activity assays and immunoblot analyses of various proteins (e.g. ACOX1, DBP, DHAPT, PHYH), (ii) presence or absence of peroxisomes with immunofluorescence microscopy using antibodies against membrane proteins (e.g. ABCD3/PMP70) and peroxisomal matrix proteins (e.g. catalase), and (iii) molecular genetic analysis (e.g. transfection complementation assays, next-generation sequencing) of the relevant implicated *Pex* genes provide more prognostic information on peroxisomal disorders [75, 105, 116, 117].

Currently, there is no curative treatment for peroxisomal disorders, and disease management is limited to surveillance and developmental assessments. Over several decades, pathogenesis and pathophysiological consequences of deadly peroxisomal disorders, and the role of peroxisomes in health and disease states have been investigated by using specific cell types (e.g. oligodendrocytes, fibroblasts, hepatocytes, and neural cells), yeast, and mouse models by selective disruption of genes encoding either peroxisomal biogenesis or the metabolic functions. For instance, PBD mouse models were generated with disruption of genes responsible for PTS-1 and PTS-2 dependent matrix protein import (e.g. *Pex5*, *Pex2*, *Pex13*), only PTS-2 dependent matrix protein import (e.g. *Pex7*), peroxisomal proliferation (e.g. *Pex11 α* and *β*), and specific metabolic pathways (including *Gnpat*, *Acox1*, *Hsd17B4*, *Scp2*, *Abcd1*, *Ehhadh*, *Slc27a2*, *Amacr*, *mThb,* and *cat*) [81, 110, 111, 118, 119]. Although vast progress has been made in understanding peroxisomal biology, several fine details concerning the metabolic functions, biogenesis, morphogenesis of peroxisomes, and underlying molecular pathophysiology mechanisms of different peroxisomal disorders remain to be resolved.

1.5 Summary and outline of the thesis

This thesis focuses on mass spectrometry-guided (LC-MS/MS, MALDI MS imaging, and direct flow injection ESI-MS/MS) molecular omics (lipidomics, metabolomics, and proteomics) performed in the distinct biological specimens of peroxisome biogenesis factor 11α (serum, liver, and heart), peroxisome biogenesis factor 11β (lung) knockout mouse models, and at different stages of mouse postnatal pulmonary development process. The first part of this thesis (**chapter I**) familiarizes with the systems biology, an overview of mass spectrometry-based molecular omics technologies including proteomics, metabolomics

and lipidomics, the history and basic principles of mass spectrometry, and mass spectrometry imaging methodologies. In addition, **chapter I** summarizes a brief review of the biochemistry of peroxisomes including the background of peroxisome organelles, major metabolic functions connected with lipid metabolism, peroxisomal biogenesis process, and diseases associated with peroxisome dysfunction, clinical and biochemical perspectives of the peroxisomal disorders.

The second part of the thesis (**chapter II, publication 1**) focuses on semi-quantitative lipidomic, metabolomic, and proteomic analyses of various biological specimens (i.e. serum, liver, and heart) from peroxisomal biogenesis factor 11α (*Pex11α*) deficient mice.

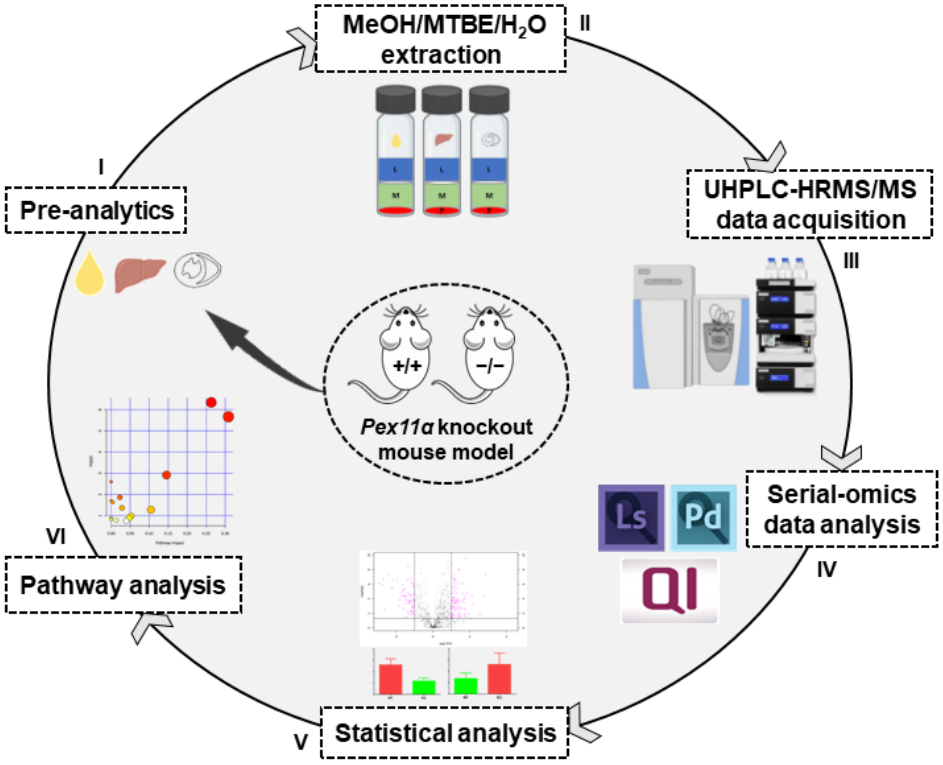

Fig. 11 Graphical representation of the sequential molecular-omics (lipidomics, polar metabolomics, and proteomics) analyses of distinct biological specimens from *Pex11α* knockout mice [20].

Briefly, serum and tissue homogenates (i.e. liver and heart) from adult three-month-old wild type (WT) and *Pex11α* knockout (KO) mice were subjected to MTBE/MeOH/H_2O liquid-liquid extraction and optimized an integrated workflow for the simultaneous extraction of lipids (upper organic phase), polar metabolites (lower aqueous phase), and proteins (sediment pellet) from the same and very minimal amount of sample. After extraction, distinct phases were processed and subjected to relative-quantitative molecular omics analyses using a reversed-phase ultra-high-performance liquid-chromatography coupled with high-resolution tandem mass spectrometry (UHPLC-HRMS/MS). Lipidomic datasets were obtained individually

in positive- and negative-ion mode in a data-dependent manner (Full MS/ddMS^2, Top15) and processed with LipidSearch software. Similarly, polar metabolomics datasets were attained independently in positive- and negative-ion mode (Full MS/ddMS^2, Top10) and analysed with Progenesis QI software, while bottom-up proteomics datasets were acquired in positive-ion mode (Full MS/ddMS^2, Top10) and processed with Proteome Discoverer software. Further, statistical and pathway interpretation of the molecular-omics data were performed with MetaboAnalyst, PANTHER, and BINGO bioinformatics tools (Fig. 11).

False-positive identifications are a major concern in regular untargeted lipidomics and metabolomics experiments. In this work, we optimized and used a series of filtering criteria and manual curation (i.e. accept, reject, or reassign) strategies to reduce false positives and provided unambiguous lipid/metabolite identifications. For instance, signal-to-noise ratio, peak shape and quality, number of data points per peak, mass accuracy, isotopic profile and fatty acid distribution pattern, lipid class and molecular species-specific diagnostic fragment ions, characteristic retention times based on the polarity, area relative standard deviation, confirmation in both-ion modes, etc. measures were cautiously monitored for each precursor ion. After minimizing several false positives, a total of 690, 908, and 939 lipid species were annotated in serum, liver, and heart tissue homogenates. Collectively, these lipid species represent 22 distinct lipid classes, and the majority of them are grouped into three main lipid categories, namely glycerophospholipids, sphingolipids, and glycerolipids. Among them, 102 (64 increased, 38 decreased) in serum, 145 (80 increased, 65 decreased) in liver, and 102 (12 increased, 90 decreased) lipid species in heart exhibited significant (FDR-adjusted p-value ≤ 0.05) differential abundances (ratio threshold ± 2) in the *Pex11α* KO mice, in comparison with their WT controls. Of note, a greater number of ether-linked and docosahexaenoic acid-containing lipid species exhibited lower abundances in the *Pex11α* KO mouse specimens. In the case of polar metabolomics, 123 (serum), 98 (liver), and 80 (heart) metabolites were annotated, and among 25, 12, and 11 metabolites revealed statistically significant differences in the abundances (FDR-adjusted p-value ≤ 0.05, ratio threshold ± 2) of *Pex11α* KO mice. Collectively, metabolic pathway enrichment analyses uncovered that these differentially abundant lipid species and metabolites are linked with lipid metabolism (glycerophospholipid, sphingolipid, glycerolipid, linolenic acid, α-linolenic acid and arachidonic acid metabolism, and fatty acid degradation), amino acid metabolism (tryptophan, purine, tyrosine, cysteine and methionine metabolism, and lysine degradation), carbohydrate and nucleotide metabolic pathways, etc. Furthermore, label-free relative quantitative proteomics data revealed significant changes in abundances (p-value threshold ≤ 0.05, ratio threshold ± 2) of 54 proteins (42 increased, 12 decreased) in liver and 29 proteins (14 increased, 15 decreased) in heart tissue homogenates of *Pex11α* KO mice. The gene ontology enrichment analysis of these differentially abundant proteins indicated that they were involved in translation, protein folding, amino acid metabolism, nucleotide metabolism, fatty acid processing, carbohydrate metabolism, steroid biosynthesis, electron transport chain, and ROS metabolism. Overall, an

integrated workflow was optimized for simultaneous molecular-omics analyses from the same sample and demonstrated significant specimen-specific changes in the relative abundances of lipids, polar metabolites, proteins, and metabolic pathways in different biological specimens of *Pex11α* KO adult mice. This comprehensive molecular omics study could serve as a reference for a better understanding of the roles of *Pex11α* and molecular mechanisms of peroxisomal disorders.

In the third part of this thesis (**chapter III, publication 2**), high-resolution in mass and space atmospheric-pressure scanning microprobe MALDI MS imaging (AP-SMALDI MSI) was employed for the first time to characterize the lipidome of late fetal mouse lungs at day 19 of gestation (E19). Further, an optimized sample preparation and data processing framework was developed for reliable relative comparison of the signal intensities of lipids and other endogenous metabolites directly from distinct (e.g. WT control and *Pex11β* KO) biological specimens (Fig. 12).

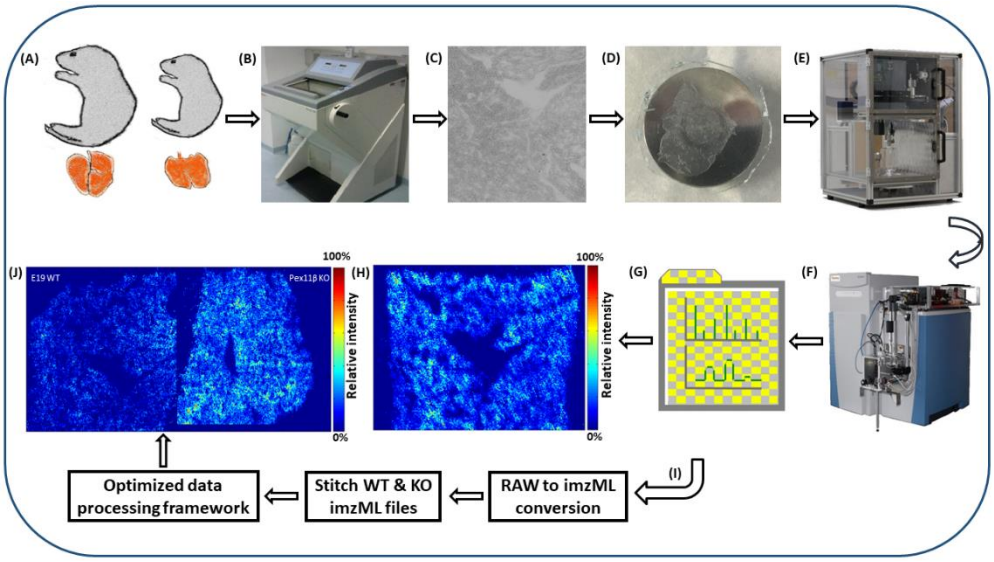

Fig. 12 Schematic representation of the optimized AP-SMALDI MS imaging workflow [34].

The most critical part of this study was the handling and cryosectioning of E19 mouse lung tissues due to their typical fetal structure and differences in consistency among divergent tissues. After several efforts, optimal tissue processing and cryosectioning procedures were optimized for E19 mouse lungs without using any tissue-embedding material. Then, 12-µm thick cryosections were obtained and scanned at a high mass resolution (140,000 @ *m/z* 200) and high spatial resolution (10 µm per pixel) using an AP-SMALDI10 imaging ion source coupled to an orbital trapping mass spectrometer (Q Exactive). Lipid species from different lipid classes (i.e. fatty acids, glycerophospholipids, lysoglycerophospholipids, sphingomyelins, ceramides, triglycerides, carnitine esters, sulfatides) and other endogenous metabolites (e.g. CDP-Choline) were identified with different charge carriers (i.e. protonated, sodiated and potassiated in positive-ion mode,

deprotonated in negative-ion mode). The lipid species were characterized based on accurate mass (RMSE ≤ 2 ppm) and on-tissue tandem mass spectrometry (lipid class and lipid species-specific diagnostic fragment ions) experiments in both positive- and negative-ion mode. In mammals, lung development (e.g. the alveolarization process) continues postnatally until adult age (publication 3, current thesis). However, in this study, late fetal mouse lungs at day 19 of gestation (E19, before birth) were used, in which the lungs are not completely developed, type I and type II cells in the alveolar region, as well as club cells in the bronchiolar region are not fully differentiated. Moreover, the tissue is not extended by inflation with "air" therefore it is still very dense and cells are very closely neighbouring to each other. Therefore, at this stage, it would be relatively difficult to resolve distinct cell types in the tissue, and thus the majority of the identified lipid species were ubiquitously distributed in the whole E19 mouse lung tissue sections.

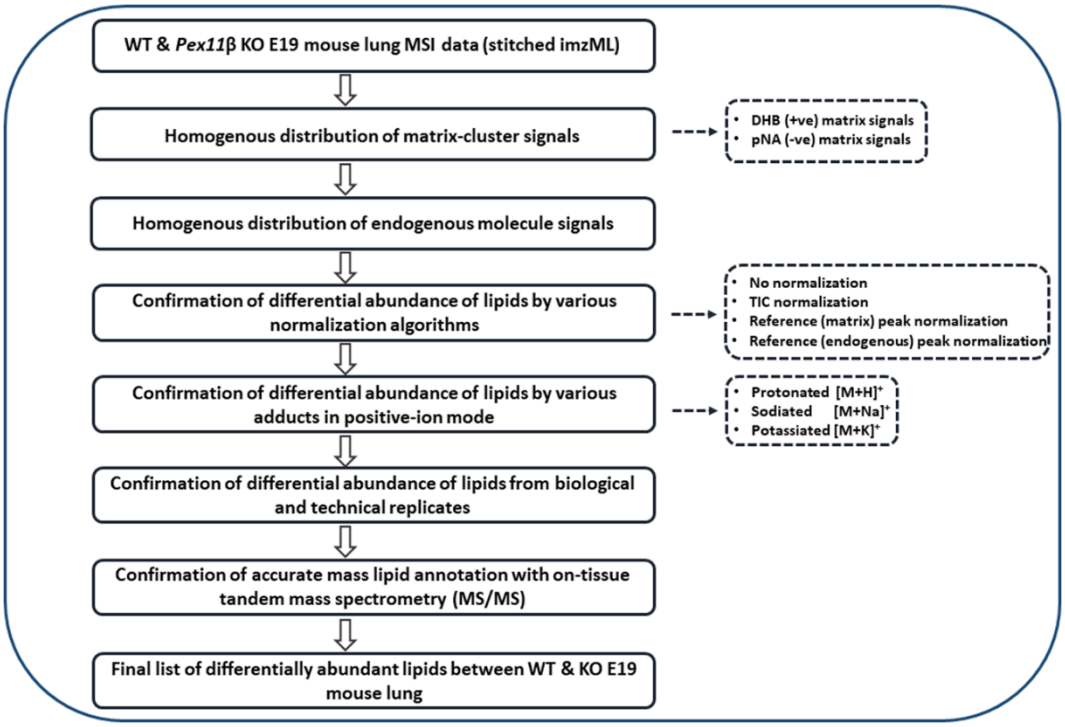

Fig. 13 An overview of the optimized MALDI MS imaging semi-quantitative data processing and evaluation framework [34].

It is worth mentioning that deficiencies of most peroxisomal biogenesis genes lead to early death of the pups after birth (e.g. *Pex 5*, *Pex11β*, etc.). Due to this reason, the E19 lung (gestation period of laboratory mice is 19-21, average 20 days) is an optimal model to study molecular differences occurring due to peroxisomal deficiency or any of the gene deficiency models leading to neonatal death of the pups. After characterization of the E19 mouse lung lipidome, a dedicated sample preparation strategy and data processing framework were optimized to compare the direct relative signal intensities of analytes among

different tissue sections (Fig. 13). Briefly, 12-µm thick tissue sections from WT control and *Pex11β* KO E19 mouse lung tissues were analysed successively with identical instrumental and experimental conditions in both positive- and negative-ion mode. Care was taken to spray homogenous distributions of matrix (i.e. 2,5-dihydroxybenzoic acid in positive-ion mode, para-nitroaniline in negative-ion mode) onto tissue surfaces. Sprayed matrix crystal sizes were monitored with an optical microscope before MS data acquisition, and the matrix homogenous distribution pattern was confirmed with matrix-cluster ion signals (MS ion images) across different tissue sections. Among the annotated species, several lipids (e.g. lysophospholipids, plasmalogens, sulfatides, and carnitine esters) and endogenous metabolites (e.g. UDP-N-acetyl glucosamine) showed differential abundances between WT and *Pex11β* KO E19 mouse lung tissue sections. To validate these biological findings, and to distinguish the technical and biological variances, differentially abundant lipid MS ion images were generated (i) without normalization, (ii) with TIC normalization, (iii) normalized with homogeneously spread matrix-cluster ion signals, and (iv) normalized with uniformly distributed endogenous signals. Regardless of the normalization approach, MSI data generated with the optimized sample preparation and instrumental setup showed consistent results and normalization did not induce any major changes in the differential abundance patterns of the lipids/metabolites across different tissue sections. Furthermore, differentially abundant molecular species were corroborated with different ion adducts in positive-ion mode, with biological and technical triplicates, and on-tissue tandem mass spectrometry experiments.

To address the lipid molecular changes, occurring over the course of postnatal pulmonary development (**chapter IV, publication 3**), a comprehensive quantitative lipidomic analysis of mouse whole lung tissue homogenates was carried out at different stages of the postnatal development process (Fig. 14A). Concisely, snap-frozen lungs from newborn (P1), 15-day-old (P15), and 12-week-old adult (P84) male mice were homogenized, two naturally not occurring lipid species for each lipid class (except for SM and PE P) and deuterated cholesterol were added as internal standards, and then the lipids were extracted, employing a chloroform/methanol/water ($CHCl_3$/MeOH/H_2O) mixture-based liquid-liquid extraction protocol (Bligh and Dyer method). After extraction, dried lipid extracts (i.e. chloroform phase) were subjected to direct flow injection (shotgun lipidomics) analysis using a triple-quadrupole mass spectrometer equipped with an electrospray ionization source in positive-ion mode. The diagnostic fragment ions (e.g. *m/z* 184 for PC, PCO, LPC, and SM; *m/z* 364, 390, and 392 for PE-based plasmalogens; *m/z* 264 for Cer; *m/z* 369 for cholesterol and CE lipid species) and neutral loss scans (e.g. *m/z* 141 and 185 for PE, PS; *m/z* 189 and 277 for PG and PI) were used for identification and quantitation of lipid species. The lipid species were quantified by plotting the standard calibration curves of naturally occurring lipid species.

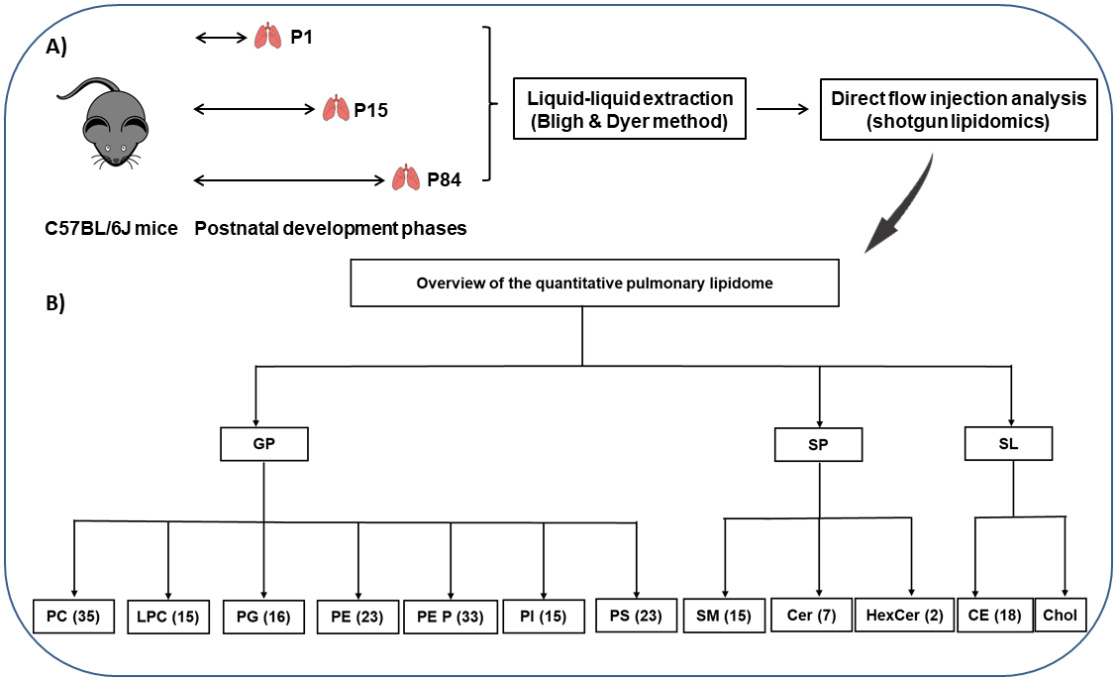

Fig. 14 Overview of the quantitative lipidomics analyses of mouse whole lung tissue homogenates during postnatal pulmonary development [58].

In total 203 lipid species spanning 160 glycerophospholipids (GP; 24 PC, 11 PC O, 23 PE, 33 PE P, 16 PG, 15 PI, 23 PS, 15 LPC), 24 sphingolipids (SP; 15 SM, 7 Cer, 2 HexCer), 18 cholesteryl esters (CE), and cholesterol from mouse lung whole tissue homogenates were quantified (Fig. 14B) and provided (i) total lipid quantity (nmol/mg wet weight), (ii) detailed overview and distribution patterns of analyzed lipid classes (mol%), (iii) molar abundances (nmol/mg wet weight) of individual lipid species, (iv) molar ratios of the selected lipid classes, and (v) distribution patterns of GPs according to carbon chain length (total number of carbon atoms) and degree of unsaturation (total number of double bonds). Briefly, total glycerophospholipid (sum of all analyzed GP species) and cholesterol levels were elevated during the development process from P1 to P84. Further, stage-specific variations were witnessed in the case of individual molecular species of various lipid classes (detailed in chapter IV). To mention a few, the majority of the monounsaturated (total number of double bonds = 1) lipid species were elevated in newborn lungs, and adult lungs exhibited high levels of polyunsaturated (total number of double bonds ≥2) lipid species. Whereas, high levels of myristic and palmitic acid containing lipid species were noticed in two-weeks-old mouse lungs. Collectively, this study provides a quantitative (molar concentrations) snapshot of mouse whole lung lipidome during postnatal development, which offers a unique resource for a better understanding of organ (lung) development and pulmonary diseases connected with lipid metabolism.

To sum up, with the help of mass spectrometry-guided molecular omics approaches, the results described in this dissertation revealed that several molecular signatures and metabolic pathways were altered in the distinct biological specimens of *Pex11α* and *Pex11β* KO mouse models. These results might serve as a unique reference for follow-up validation studies with independent large cohorts, which opens new avenues to identify diagnostic biomarkers and also facilitates understanding the molecular underpinnings of peroxisomal disorders. In addition, the optimized single-sample sequential molecular omics workflow could be seamlessly adapted to a large variety of other studies, particularly in disease models with limited sample availability such as inborn errors of metabolism. It is worth mentioning that, the developed workflow was used to comprehend the role of peroxisomes in idiopathic pulmonary fibrosis (unpublished data, manuscript 10), and modulation of immune-to-brain communication in systemic inflammation (unpublished data, manuscript 11). Similarly, the optimized semi-quantitative MALDI MS imaging workflow for direct comparison of signal intensities of analytes was utilized to unveil the molecular compositional changes in *Pex11α*$^{-/-}$ mouse heart (unpublished data, manuscript 9), and *organum vasculosum laminae terminalis* of fat-1 transgenic mouse brain under the influence of ω-3 fatty acids during systemic inflammation (unpublished data, manuscript 11).

1.6 References

1. Lodish H, B.A., Zipursky SL, Matsudaira P, Baltimore D, and Darnell J., *Molecular Cell Biology* 4th edition ed. 2000, New York.
2. Crick, F., *Central dogma of molecular biology.* Nature, 1970. **227**(5258): p. 561-3.
3. Rinschen, M.M., et al., *Identification of bioactive metabolites using activity metabolomics.* Nature Reviews Molecular Cell Biology, 2019. **20**(6): p. 353-367.
4. Blum, B.C., F. Mousavi, and A. Emili, *Single-platform "multi-omic' profiling: unified mass spectrometry and computational workflows for integrative proteomics-metabolomics analysis.* Molecular Omics, 2018. **14**(5): p. 307-319.
5. Misra, B.B., et al., *Integrated omics: tools, advances and future approaches.* Journal of Molecular Endocrinology, 2019. **62**(1): p. R21-R45.
6. Beale DJ, K.A., Ahmed W, *Beyond Metabolomics: A Review of Multi-Omics-Based Approaches*, in *Microbial Metabolomics*, K.K. Beale D, Palombo E, Editor. 2016, Springer: Cham.
7. Wilkins, M.R., et al., *From proteins to proteomes: large scale protein identification by two-dimensional electrophoresis and amino acid analysis.* Biotechnology (N Y), 1996. **14**(1): p. 61-5.
8. Aebersold, R. and M. Mann, *Mass spectrometry-based proteomics.* Nature, 2003. **422**(6928): p. 198-207.
9. Yates, J.R., C.I. Ruse, and A. Nakorchevsky, *Proteomics by mass spectrometry: approaches, advances, and applications.* Annu Rev Biomed Eng, 2009. **11**: p. 49-79.
10. Scrivens, P.J., *Practical Proteomics Course*, P. Presentation, Editor. 2013: Bangalore, India.
11. O'Farrell, P.H., *High resolution two-dimensional electrophoresis of proteins.* J Biol Chem, 1975. **250**(10): p. 4007-21.
12. Beck, M., et al., *The quantitative proteome of a human cell line.* Mol Syst Biol, 2011. **7**: p. 549.
13. Nagaraj, N., et al., *Deep proteome and transcriptome mapping of a human cancer cell line.* Mol Syst Biol, 2011. **7**: p. 548.

14. Chen, B., et al., *Top-Down Proteomics: Ready for Prime Time?* Anal Chem, 2018. **90**(1): p. 110-127.
15. Zhang, Y., et al., *Protein analysis by shotgun/bottom-up proteomics.* Chem Rev, 2013. **113**(4): p. 2343-94.
16. Gillet, L.C., A. Leitner, and R. Aebersold, *Mass Spectrometry Applied to Bottom-Up Proteomics: Entering the High-Throughput Era for Hypothesis Testing.* Annu Rev Anal Chem (Palo Alto Calif), 2016. **9**(1): p. 449-72.
17. Cox, J. and M. Mann, *Quantitative, high-resolution proteomics for data-driven systems biology.* Annu Rev Biochem, 2011. **80**: p. 273-99.
18. Cristobal, A., et al., *Toward an Optimized Workflow for Middle-Down Proteomics.* Anal Chem, 2017. **89**(6): p. 3318-3325.
19. Altelaar, A.F., J. Munoz, and A.J. Heck, *Next-generation proteomics: towards an integrative view of proteome dynamics.* Nat Rev Genet, 2013. **14**(1): p. 35-48.
20. Garikapati, V., et al., *Sequential lipidomic, metabolomic, and proteomic analyses of serum, liver, and heart tissue specimens from peroxisomal biogenesis factor 11alpha knockout mice.* Anal Bioanal Chem, 2022. **414**(6): p. 2235-2250.
21. Scupakova, K., et al., *Cellular resolution in clinical MALDI mass spectrometry imaging: the latest advancements and current challenges.* Clin Chem Lab Med, 2020. **58**(6): p. 914-929.
22. Spengler, B., *Mass spectrometry imaging of biomolecular information.* Anal Chem, 2015. **87**(1): p. 64-82.
23. Gowda, G.A. and D. Djukovic, *Overview of mass spectrometry-based metabolomics: opportunities and challenges.* Methods Mol Biol, 2014. **1198**: p. 3-12.
24. Dalgliesh, C.E., et al., *A gas-liquid-chromatographic procedure for separating a wide range of metabolites occuring in urine or tissue extracts.* Biochem J, 1966. **101**(3): p. 792-810.
25. Horning, E.C. and M.G. Horning, *Metabolic profiles: gas-phase methods for analysis of metabolites.* Clin Chem, 1971. **17**(8): p. 802-9.
26. Oliver, S.G., et al., *Systematic functional analysis of the yeast genome.* Trends Biotechnol, 1998. **16**(9): p. 373-8.
27. Nicholson, J.K., J.C. Lindon, and E. Holmes, *'Metabonomics': understanding the metabolic responses of living systems to pathophysiological stimuli via multivariate statistical analysis of biological NMR spectroscopic data.* Xenobiotica, 1999. **29**(11): p. 1181-9.
28. Fiehn, O., et al., *Metabolite profiling for plant functional genomics.* Nat Biotechnol, 2000. **18**(11): p. 1157-61.
29. Patti, G.J., O. Yanes, and G. Siuzdak, *Innovation: Metabolomics: the apogee of the omics trilogy.* Nat Rev Mol Cell Biol, 2012. **13**(4): p. 263-9.
30. Johnson, C.H., J. Ivanisevic, and G. Siuzdak, *Metabolomics: beyond biomarkers and towards mechanisms.* Nat Rev Mol Cell Biol, 2016. **17**(7): p. 451-9.
31. Shao, Y. and W. Le, *Recent advances and perspectives of metabolomics-based investigations in Parkinson's disease.* Mol Neurodegener, 2019. **14**(1): p. 3.
32. Yang, Q., et al., *Metabolomics biotechnology, applications, and future trends: a systematic review.* RSC Advances, 2019. **9**(64): p. 37245-37257.
33. Riekeberg, E. and R. Powers, *New frontiers in metabolomics: from measurement to insight.* F1000Res, 2017. **6**: p. 1148.
34. Garikapati, V., et al., *High-resolution atmospheric-pressure MALDI mass spectrometry imaging workflow for lipidomic analysis of late fetal mouse lungs.* Sci Rep, 2019. **9**(1): p. 3192.
35. Yang, K. and X. Han, *Lipidomics: Techniques, Applications, and Outcomes Related to Biomedical Sciences.* Trends Biochem Sci, 2016. **41**(11): p. 954-969.
36. Han, X., *Lipidomics: Comprehensive Mass Spectrometry of Lipids*. 2016: John Wiley & Sons, Inc.

37. *<[13653075 - Pure and Applied Chemistry] Glossary of class names of organic compounds and reactivity intermediates based on structure (IUPAC Recommendations 1995).pdf>.*
38. Christie, W.W., *High-performance liquid chromatography and Lipids: A Practical Guide*. 1987: Pergamon Press, Oxford.
39. Fahy, E., et al., *A comprehensive classification system for lipids.* J Lipid Res, 2005. **46**(5): p. 839-61.
40. Fahy, E., et al., *Update of the LIPID MAPS comprehensive classification system for lipids.* J Lipid Res, 2009. **50 Suppl**: p. S9-14.
41. Liebisch, G., et al., *Update on LIPID MAPS classification, nomenclature, and shorthand notation for MS-derived lipid structures.* J Lipid Res, 2020. **61**(12): p. 1539-1555.
42. Fahy, E., et al., *Lipid classification, structures and tools.* Biochim Biophys Acta, 2011. **1811**(11): p. 637-47.
43. Han, X., *Lipidomics for studying metabolism.* Nat Rev Endocrinol, 2016. **12**(11): p. 668-679.
44. Agrawal, I., et al., *Deciphering lipid dysregulation in ALS: from mechanisms to translational medicine.* Transl Neurodegener, 2022. **11**(1): p. 48.
45. Ward, A.V., S.M. Anderson, and C.A. Sartorius, *Advances in Analyzing the Breast Cancer Lipidome and Its Relevance to Disease Progression and Treatment.* J Mammary Gland Biol Neoplasia, 2021. **26**(4): p. 399-417.
46. Liebisch, G., et al., *Shorthand notation for lipid structures derived from mass spectrometry.* J Lipid Res, 2013. **54**(6): p. 1523-30.
47. Zullig, T., M. Trotzmuller, and H.C. Kofeler, *Lipidomics from sample preparation to data analysis: a primer.* Anal Bioanal Chem, 2020. **412**(10): p. 2191-2209.
48. Holcapek, M., G. Liebisch, and K. Ekroos, *Lipidomic Analysis.* Anal Chem, 2018. **90**(7): p. 4249-4257.
49. Lipidomics Standards Initiative, C., *Lipidomics needs more standardization.* Nat Metab, 2019. **1**(8): p. 745-747.
50. Burla, B., et al., *MS-based lipidomics of human blood plasma: a community-initiated position paper to develop accepted guidelines.* J Lipid Res, 2018. **59**(10): p. 2001-2017.
51. Bligh, E.G. and W.J. Dyer, *A rapid method of total lipid extraction and purification.* Can J Biochem Physiol, 1959. **37**(8): p. 911-7.
52. Folch, J., M. Lees, and G.H. Sloane Stanley, *A simple method for the isolation and purification of total lipides from animal tissues.* J Biol Chem, 1957. **226**(1): p. 497-509.
53. Hara, A. and N.S. Radin, *Lipid extraction of tissues with a low-toxicity solvent.* Anal Biochem, 1978. **90**(1): p. 420-6.
54. Matyash, V., et al., *Lipid extraction by methyl-tert-butyl ether for high-throughput lipidomics.* J Lipid Res, 2008. **49**(5): p. 1137-46.
55. Lofgren, L., et al., *The BUME method: a novel automated chloroform-free 96-well total lipid extraction method for blood plasma.* J Lipid Res, 2012. **53**(8): p. 1690-700.
56. Vijayan, V., et al., *A New Immunomodulatory Role for Peroxisomes in Macrophages Activated by the TLR4 Ligand Lipopolysaccharide.* J Immunol, 2017. **198**(6): p. 2414-2425.
57. Wang, M., C. Wang, and X. Han, *Selection of internal standards for accurate quantification of complex lipid species in biological extracts by electrospray ionization mass spectrometry-What, how and why?* Mass Spectrom Rev, 2017. **36**(6): p. 693-714.
58. Karnati, S., et al., *Quantitative lipidomic analysis of mouse lung during postnatal development by electrospray ionization tandem mass spectrometry.* PLoS One, 2018. **13**(9): p. e0203464.
59. Liebisch, G., et al., *Quantitative measurement of different ceramide species from crude cellular extracts by electrospray ionization tandem mass spectrometry (ESI-MS/MS).* J Lipid Res, 1999. **40**(8): p. 1539-46.

60. Zullig, T. and H.C. Kofeler, *High Resolution Mass Spectrometry in Lipidomics.* Mass Spectrom Rev, 2020.
61. Stroobant, E.d.H.a.V., *Mass Spectrometry: Principles and Applications, 3rd Edition*. 2007: Wiley. 502.
62. Siuzdak, G., *The Expanding Role of Mass Spectrometry in Biotechnology*. Second ed. 2006, San Diego: MCC Press.
63. Gross, J.H., *Mass Spectrometry A Textbook*. Third ed. 2017, Switzerland: Springer Nature.
64. Rompp, A. and B. Spengler, *Mass spectrometry imaging with high resolution in mass and space.* Histochem Cell Biol, 2013. **139**(6): p. 759-83.
65. Campbell, D.I., et al., *Improved spatial resolution in the imaging of biological tissue using desorption electrospray ionization.* Anal Bioanal Chem, 2012. **404**(2): p. 389-98.
66. Takats, Z., et al., *Mass spectrometry sampling under ambient conditions with desorption electrospray ionization.* Science, 2004. **306**(5695): p. 471-3.
67. Bernhard Spengler, M.H., Raimund Kaufmann, *MALDI Ion Imaging and Biological Ion Imaging with a new Scanning UV-Laser Microprobe*, in *Proceedings of the 42nd Annual Conference on Mass Spectrometry and Allied Topics*. 1994: Chicago, Illinois, United States of America.
68. Kompauer, M., S. Heiles, and B. Spengler, *Atmospheric pressure MALDI mass spectrometry imaging of tissues and cells at 1.4-mum lateral resolution.* Nat Methods, 2017. **14**(1): p. 90-96.
69. Kompauer, M., S. Heiles, and B. Spengler, *Autofocusing MALDI mass spectrometry imaging of tissue sections and 3D chemical topography of nonflat surfaces.* Nat Methods, 2017. **14**(12): p. 1156-1158.
70. Palmer, A., et al., *FDR-controlled metabolite annotation for high-resolution imaging mass spectrometry.* Nat Methods, 2017. **14**(1): p. 57-60.
71. Rhodin, J.A.G., *Correlation of ultrastructural organization: and function in normal and experimentally changed proximal convoluted tubule cells of the mouse kidney: an electron microscopic study*, in *Department of Anatomy,*. 1954, Karolinska Institute: Sweden.
72. Bernhard, W. and C. Rouiller, *Microbodies and the problem of mitochondrial regeneration in liver cells.* J Biophys Biochem Cytol, 1956. **2**(4 Suppl): p. 355-60.
73. Deduve, C. and P. Baudhuin, *Peroxisomes (Microbodies and Related Particles).* Physiological Reviews, 1966. **46**(2): p. 323-+.
74. Baumgart, E., *Application of in situ hybridization, cytochemical and immunocytochemical techniques for the investigation of peroxisomes. A review including novel data. Robert Feulgen Prize Lecture 1997.* Histochem Cell Biol, 1997. **108**(3): p. 185-210.
75. Waterham, H.R., S. Ferdinandusse, and R.J. Wanders, *Human disorders of peroxisome metabolism and biogenesis.* Biochim Biophys Acta, 2016. **1863**(5): p. 922-33.
76. Immenschuh, S. and E. Baumgart-Vogt, *Peroxiredoxins, oxidative stress, and cell proliferation.* Antioxid Redox Signal, 2005. **7**(5-6): p. 768-77.
77. Colasante, C., et al., *Peroxisomes in cardiomyocytes and the peroxisome / peroxisome proliferator-activated receptor-loop.* Thromb Haemost, 2015. **113**(3): p. 452-63.
78. Yifrach, E., et al., *Defining the Mammalian Peroxisomal Proteome.* Subcell Biochem, 2018. **89**: p. 47-66.
79. Cipolla, C.M. and I.J. Lodhi, *Peroxisomal Dysfunction in Age-Related Diseases.* Trends Endocrinol Metab, 2017. **28**(4): p. 297-308.
80. Wanders, R.J., *Metabolic functions of peroxisomes in health and disease.* Biochimie, 2014. **98**: p. 36-44.
81. Wanders, R.J.A. and H.R. Waterham, *Biochemistry of mammalian peroxisomes revisited.* Annual Review of Biochemistry, 2006. **75**: p. 295-332.

82. Lodhi, I.J. and C.F. Semenkovich, *Peroxisomes: a nexus for lipid metabolism and cellular signaling.* Cell Metab, 2014. **19**(3): p. 380-92.
83. Cooper, T.G. and H. Beevers, *Beta oxidation in glyoxysomes from castor bean endosperm.* J Biol Chem, 1969. **244**(13): p. 3514-20.
84. Lazarow, P.B. and C. De Duve, *A fatty acyl-CoA oxidizing system in rat liver peroxisomes; enhancement by clofibrate, a hypolipidemic drug.* Proc Natl Acad Sci U S A, 1976. **73**(6): p. 2043-6.
85. Van Veldhoven, P.P., *Biochemistry and genetics of inherited disorders of peroxisomal fatty acid metabolism.* J Lipid Res, 2010. **51**(10): p. 2863-95.
86. Dean, J.M. and I.J. Lodhi, *Structural and functional roles of ether lipids.* Protein Cell, 2018. **9**(2): p. 196-206.
87. Wanders, R.J., et al., *Peroxisomes, lipid metabolism and lipotoxicity.* Biochim Biophys Acta, 2010. **1801**(3): p. 272-80.
88. Wanders, R.J., *Peroxisomes, lipid metabolism, and peroxisomal disorders.* Mol Genet Metab, 2004. **83**(1-2): p. 16-27.
89. Ferdinandusse, S., et al., *Identification of the peroxisomal beta-oxidation enzymes involved in the biosynthesis of docosahexaenoic acid.* J Lipid Res, 2001. **42**(12): p. 1987-95.
90. Ferdinandusse, S. and S.M. Houten, *Peroxisomes and bile acid biosynthesis.* Biochim Biophys Acta, 2006. **1763**(12): p. 1427-40.
91. Wanders, R.J., H.R. Waterham, and S. Ferdinandusse, *Metabolic Interplay between Peroxisomes and Other Subcellular Organelles Including Mitochondria and the Endoplasmic Reticulum.* Front Cell Dev Biol, 2015. **3**: p. 83.
92. Faust, P.L. and W.J. Kovacs, *Cholesterol biosynthesis and ER stress in peroxisome deficiency.* Biochimie, 2014. **98**: p. 75-85.
93. Fujiki, Y., et al., *Peroxisome biogenesis in mammalian cells.* Front Physiol, 2014. **5**: p. 307.
94. Wanders, R.J. and H.R. Waterham, *Peroxisomal disorders I: biochemistry and genetics of peroxisome biogenesis disorders.* Clin Genet, 2005. **67**(2): p. 107-33.
95. Gould, S.J., et al., *A conserved tripeptide sorts proteins to peroxisomes.* J Cell Biol, 1989. **108**(5): p. 1657-64.
96. Smith, J.J. and J.D. Aitchison, *Peroxisomes take shape.* Nat Rev Mol Cell Biol, 2013. **14**(12): p. 803-17.
97. Rehling, P., et al., *The import receptor for the peroxisomal targeting signal 2 (PTS2) in Saccharomyces cerevisiae is encoded by the PAS7 gene.* EMBO J, 1996. **15**(12): p. 2901-13.
98. Kobayashi, S., A. Tanaka, and Y. Fujiki, *Fis1, DLP1, and Pex11p coordinately regulate peroxisome morphogenesis.* Experimental Cell Research, 2007. **313**(8): p. 1675-1686.
99. Koch, J. and C. Brocard, *PEX11 proteins attract Mff and human Fis1 to coordinate peroxisomal fission.* Journal of Cell Science, 2012. **125**(16): p. 3813-3826.
100. Koch, A., et al., *A role for Fis1 in both mitochondrial and peroxisomal fission in mammalian cells.* Molecular Biology of the Cell, 2005. **16**(11): p. 5077-5086.
101. Anthonio, E.A., et al., *Small G proteins in peroxisome biogenesis: the potential involvement of ADP-ribosylation factor 6.* Bmc Cell Biology, 2009. **10**.
102. Wanders, R.J. and H.R. Waterham, *Peroxisomal disorders: the single peroxisomal enzyme deficiencies.* Biochim Biophys Acta, 2006. **1763**(12): p. 1707-20.
103. Braverman, N.E., M.D. D'Agostino, and G.E. MacLean, *Peroxisome Biogenesis Disorders: Biological, Clinical and Pathophysiological Perspectives.* Developmental Disabilities Research Reviews, 2013. **17**(3-4): p. 187-196.
104. Konkolova, J., et al., *A novel mutation in the PEX12 gene causing a peroxisomal biogenesis disorder.* Mol Biol Rep, 2015. **42**(9): p. 1359-63.

105. Ebberink, M.S., et al., *Genetic classification and mutational spectrum of more than 600 patients with a Zellweger syndrome spectrum disorder.* Hum Mutat, 2011. **32**(1): p. 59-69.
106. Purdue, P.E., et al., *Rhizomelic chondrodysplasia punctata, a peroxisomal biogenesis disorder caused by defects in Pex7p, a peroxisomal protein import receptor: a minireview.* Neurochem Res, 1999. **24**(4): p. 581-6.
107. Waterham, H.R., et al., *A lethal defect of mitochondrial and peroxisomal fission.* N Engl J Med, 2007. **356**(17): p. 1736-41.
108. Shamseldin, H.E., et al., *Genomic analysis of mitochondrial diseases in a consanguineous population reveals novel candidate disease genes.* J Med Genet, 2012. **49**(4): p. 234-41.
109. Huber, N., et al., *Charcot-Marie-Tooth disease-associated mutants of GDAP1 dissociate its roles in peroxisomal and mitochondrial fission.* EMBO Rep, 2013. **14**(6): p. 545-52.
110. Li, X., et al., *PEX11alpha is required for peroxisome proliferation in response to 4-phenylbutyrate but is dispensable for peroxisome proliferator-activated receptor alpha-mediated peroxisome proliferation.* Mol Cell Biol, 2002. **22**(23): p. 8226-40.
111. Li, X.L., et al., *PEX11 beta deficiency is lethal and impairs neuronal migration but does not abrogate peroxisome function.* Molecular and Cellular Biology, 2002. **22**(12): p. 4358-4365.
112. Ebberink, M.S., et al., *A novel defect of peroxisome division due to a homozygous non-sense mutation in the PEX11beta gene.* J Med Genet, 2012. **49**(5): p. 307-13.
113. Weng, H., et al., *Pex11alpha deficiency impairs peroxisome elongation and division and contributes to nonalcoholic fatty liver in mice.* Am J Physiol Endocrinol Metab, 2013. **304**(2): p. E187-96.
114. Chen, C., et al., *Pex11a deficiency causes dyslipidaemia and obesity in mice.* J Cell Mol Med, 2019. **23**(3): p. 2020-2031.
115. Ferdinandusse, S., et al., *The important role of biochemical and functional studies in the diagnostics of peroxisomal disorders.* J Inherit Metab Dis, 2016. **39**(4): p. 531-43.
116. Gootjes, J., et al., *Biochemical markers predicting survival in peroxisome biogenesis disorders.* Neurology, 2002. **59**(11): p. 1746-9.
117. Krause, C., H. Rosewich, and J. Gartner, *Rational diagnostic strategy for Zellweger syndrome spectrum patients.* Eur J Hum Genet, 2009. **17**(6): p. 741-8.
118. Baes, M., et al., *A mouse model for Zellweger syndrome.* Nat Genet, 1997. **17**(1): p. 49-57.
119. Muller, C.C., et al., *PEX13 deficiency in mouse brain as a model of Zellweger syndrome: abnormal cerebellum formation, reactive gliosis and oxidative stress.* Dis Model Mech, 2011. **4**(1): p. 104-19.

CHAPTER II

Publication 1

Sequential lipidomic, metabolomic, and proteomic analyses of serum, liver, and heart tissue specimens from peroxisomal biogenesis factor 11α knockout mice

Vannuruswamy Garikapati, Claudia Colasante, Eveline Baumgart-Vogt, Bernhard Spengler

Published in Analytical and Bioanalytical Chemistry. 2022;414(6):2235-2250

DOI: 10.1007/s00216-021-03860-0

Supporting information: https://link.springer.com/article/10.1007/s00216-021-03860-0#Sec22

Analytical and Bioanalytical Chemistry (2022) 414:2235–2250
https://doi.org/10.1007/s00216-021-03860-0

RESEARCH PAPER

Sequential lipidomic, metabolomic, and proteomic analyses of serum, liver, and heart tissue specimens from peroxisomal biogenesis factor 11α knockout mice

Vannuruswamy Garikapati[1,2] · Claudia Colasante[2] · Eveline Baumgart-Vogt[2] · Bernhard Spengler[1]

Received: 30 December 2020 / Revised: 25 November 2021 / Accepted: 20 December 2021 / Published online: 27 January 2022

Abstract
Peroxisomes are versatile single membrane-enclosed cytoplasmic organelles, involved in reactive oxygen species (ROS) and lipid metabolism and diverse other metabolic processes. Peroxisomal disorders result from mutations in *Pex* genes-encoded proteins named peroxins (PEX proteins) and single peroxisomal enzyme deficiencies. The PEX11 protein family (α, β, and γ isoforms) plays an important role in peroxisomal proliferation and fission. However, their specific functions and the metabolic impact caused by their deficiencies have not been precisely characterized. To understand the systemic molecular alterations caused by peroxisomal defects, here we utilized untreated peroxisomal biogenesis factor 11α knockout (*Pex11α* KO) mouse model and performed serial relative-quantitative lipidomic, metabolomic, and proteomic analyses of serum, liver, and heart tissue homogenates. We demonstrated significant specific changes in the abundances of multiple lipid species, polar metabolites, and proteins and dysregulated metabolic pathways in distinct biological specimens of the *Pex11α* KO adult mice in comparison to the wild type (WT) controls. Overall, the present study reports comprehensive semi-quantitative molecular omics information of the *Pex11α* KO mice, which might serve in the future as a reference for a better understanding of the roles of *Pex11α* and underlying pathophysiological mechanisms of peroxisomal biogenesis disorders.

Keywords Lipidomics · Metabolomics · Proteomics · Mass spectrometry · Peroxisomes · Peroxisomal biogenesis disorders

Introduction

Peroxisomes are small (0.1–0.5 μm in diameter), single membrane bound, subcellular organelles present in almost every eukaryotic cell. They play a central role in a wide variety of vital metabolic functions, namely (i) β-oxidation of very long-chain fatty acids (e.g., VLCFAs, ≥C22) and of bioactive secondary lipid mediators (such as prostaglandins and leukotrienes), (ii) α- (e.g., phytanic acid) and β-oxidation (e.g., pristanic acid) of branched-chain fatty acids, (iii) biosynthesis of ether-phospholipids (e.g., plasmalogens), cholesterol, dolichol, and conjugated bile acids, (iv) glyoxylate detoxification, and (v) breakdown of polyamines and purines [1]. The granular matrix of peroxisomes contains a large variety of oxidases, producing not only hydrogen peroxide (H_2O_2) during the conversion of their substrates but also the antioxidative marker enzyme catalase that cleaves H_2O_2 into water and oxygen, and protects the cell from excessive ROS production [2, 3].

The abundance, size, shape, protein/enzyme composition, and functions of peroxisomes can differ based on the physiological condition and metabolic needs of the cell type, tissue, organ, and/or organism [3, 4]. Regulators of malleability and biogenesis of peroxisomes are a set of heterogeneous proteins referred to as peroxins (PEX proteins), located in the cytoplasm, the peroxisomal membrane as well as their matrix. They mediate all steps in peroxisomal biogenesis,

✉ Eveline Baumgart-Vogt
Eveline.Baumgart-Vogt@anatomie.med.uni-giessen.de

✉ Bernhard Spengler
Bernhard.Spengler@anorg.chemie.uni-giessen.de

Vannuruswamy Garikapati
Vannuruswamy.Garikapati@anorg.chemie.uni-giessen.de

Claudia Colasante
Claudia.Colasante@anatomie.med.uni-giessen.de

[1] Institute of Inorganic and Analytical Chemistry, Justus Liebig University Giessen, 35392 Giessen, Germany

[2] Institute for Anatomy and Cell Biology II, Division of Medical Cell Biology, Justus Liebig University Giessen, 35392 Giessen, Germany

such as (i) the formation of the peroxisomal membrane, (ii) the import of their membrane and matrix proteins, and (iii) the proliferation of the organelles. Hitherto, more than 32 distinct PEX proteins have been recognized (named with reference to their date of discovery), out of which at least 14 are conserved in mammalians [5, 6].

The functional importance of peroxisomal metabolism for health in humans is emphasized by the existence of numerous peroxisomal disorders. These devastating genetic human diseases are either resulting from mutations in *Pex* genes (peroxisomal biogenesis disorders, PBDs, or Zellweger spectrum disorders, ZSDs) or genes encoding single peroxisomal enzymes (peroxisomal enzyme deficiencies, PEDs) [1]. In both cases, the specific metabolic functions of multiple organs (such as brain, liver, kidney, adrenal gland, testis, bone, and many others) are severely disturbed, affecting the organism at a systemic level and often resulting in premature death. The processes that are usually affected are the fatty acid β- and α-oxidation, the plasmalogens biosynthesis, the glyoxylate metabolism, the bile acid synthesis, and the H_2O_2 metabolism [7, 8].

To study PBDs, Li and Baumgart et al. previously generated and bred *Pex11* (α and β) knockout mouse models and performed their basal characterization [9, 10]. Thereby, they also identified a third *Pex11* gene (*Pex11γ*). The three PEX11 protein isoforms (α, β, and γ) are responsible for peroxisome proliferation and fission by mediating elongation, tubulation, and constriction of pre-existing peroxisomes [11–13]. *Pex11β* is expressed constitutively throughout the tissues, whereas α and γ isoforms are tissue specific and pronounced considerably in the heart, liver, and kidney as well as testis [10, 11]. In contrast to the knockout of *Pex11β*, which induces a phenotype similar to Zellweger syndrome and neonatal lethality, mice with a *Pex11α* KO display a mild phenotype and are viable after birth [9, 10], enabling investigations of the impact of peroxisomal defects on the lipid, metabolite, and protein composition of various organs (e.g., liver, heart, kidney, lung, and brain) and biological fluids (e.g., serum) in adult mice. Indeed, adult *Pex11α* knockout mice when treated with a high-fat diet develop nonalcoholic fatty liver disease [14].

In systems biology, concurrent extraction and investigation of various biomolecules (including proteins, peptides, lipids, and polar metabolites) and integration of mass spectrometry-guided multi-level molecular omics data (such as lipidomics, metabolomics, peptidomics, and proteomics) of the same sample has become a promising strategy to improve the understanding of complex biological cascades [15]. A series of recent studies has demonstrated one-step extraction protocols for serial-omics analyses from a single piece of sample and has been applied in cancer [16], cardiovascular [17], pulmonary [18], plant [19], and toxicological research [20].

In order to characterize the metabolic alterations occurring due to *Pex11*alpha deficiency, we investigated changes in the lipidome, metabolome, and proteome of different biological specimens (serum, liver, and heart) from *Pex11α* KO adult mice using a liquid–liquid extraction method combined with untargeted sequential omics approaches by ultra-high-performance liquid chromatography equipped with high-resolution tandem mass spectrometry (UHPLC-HRMS/MS). Our study provides extensive semi-quantitative molecular information on the metabolic alterations in *Pex11α* KO mice, which will complement the understanding of the molecular functions of *Pex11α* and underlying pathophysiological mechanisms of peroxisomal biogenesis disorders.

Materials and methods

Materials

Ammonium bicarbonate, ammonium formate, bovine serum albumin, dithiothreitol (DTT), iodoacetamide (IAA), methyl tert-butyl ether (MTBE), thiourea, and urea were purchased from Sigma-Aldrich (Steinheim, Germany). LC–MS grade solvents acetonitrile (ACN), methanol (MeOH), water (H_2O), 2-propanol/isopropyl alcohol (IPA), and formic acid were procured from Honeywell Riedel-de Haën (Seelze, Germany). The synthetic lipid internal standards were procured from Avanti Polar Lipids (Alabaster, AL, USA). Sequencing grade modified trypsin was obtained from Promega Corporation (Mannheim, Germany) and RapiGest SF surfactant from Waters Corporation (Milford, MA, USA). Bradford reagent was purchased from Bio-Rad Laboratories (CA, USA) and $ZipTip_{C18}$ from Merck Millipore (MA, USA).

Pre-analytics

Pathogen-free C57BL/6 J mice were obtained from the central animal facility of the Justus Liebig University Giessen, Germany. They were kept on a normal laboratory diet and water and maintained under standard environmental conditions. The generation, breeding, and basal characterization of *Pex11α* KO animals were described in details earlier [9]. Adult 3-month-old male mice (WT control and homozygous *Pex11α* KO) were narcotized using 3% isofluran and sacrificed by cervical dislocation. For the isolation of heart and liver, the animals were perfused with phosphate buffer saline through the left ventricle to remove the blood. Liver and heart tissues were dissected, snap-frozen immediately in liquid nitrogen, and stored at − 80 °C until further processing. Blood was extracted by cardiac puncture immediately following the cervical dislocation and left standing for 30 min at 37 °C to separate the serum from the red blood

cells. Then, the samples were spun for 10 min at 1500 × *g* at 4 °C, and serum was collected and stored at − 80 °C until further use.

The animal experiments were performed in accordance with the German Animal Welfare Law and recommendations of institutional animal welfare officers. All experiments were approved by the German Government Commission of Animal Care (Justus Liebig University internal classification: JLU-Nr.: 616_M, Project ID: 1016 Peroxisomen).

Liquid–liquid extraction

Ten milligrams of the snap-frozen liver and heart tissues from three biological replicates of WT control (*Pex11α*$^{+/+}$) and homozygous *Pex11α* KO (*Pex11α*$^{-/-}$) mice were homogenized in phosphate buffer saline solution (200 µl) using a tissue homogenizer (Retsch GmbH, Germany) with zirconia beads for 1 min at 20 Hz at 4 °C. 200 µl of liver or heart tissue homogenates and/or 80 µl of serum were transferred into respective glass vials and subjected to liquid–liquid extraction as reported earlier [16]. Briefly, 750 µl of ice-cold methanol (LC–MS grade) containing the following lipid standard mix: 56 pmol phosphatidylethanolamine (PE 17:0/14:1); 52.5 pmol phosphatidylglycerol (PG 17:0/14:1); 82.5 pmol phosphatidylinositol (PI 17:0/14:1); 90 pmol phosphatidylserine (PS 17:0/14:1); 56 pmol phosphatidylcholine (PC 17:0/14:1); 47.5 pmol lysophosphatidylcholine (LPC 17:1); 16.6 pmol lysophosphatidylinositol (LPI 17:1); 84.6 pmol lysophosphatidylserine (LPS 17:1); 50 pmol lysophosphatidylglycerol (LPG 17:1); 42.8 pmol lysophosphatidylethanolamine (LPE 17:1); 69.6 pmol sphingomyelin (SM d18:1/17:0); 50 pmol cholesteryl ester (ChE 19:0); 90.4 pmol ceramide (Cer d18:1/17:0); 77.6 pmol hexosylceramide (HexCer d18:1/12:0); 30 pmol triglyceride (TG 17:0/17:0/17:0) were added to the homogenate samples and vortexed vigorously for 1 min. After that, 2.5 ml of ice-cold MTBE (anhydrous, 99.8%) were added to each vial and vortexed for 1 h at room temperature. Later, 625 µl of ice-cold water (LC–MS grade) were added for phase separation, vortexed for 1 min, and centrifuged at 4,000 g for 15 min at 4 °C. After centrifugation, the upper non-polar (lipids) and lower polar (metabolites) phases were separately collected, transferred to fresh vials, dried out in vacufuge concentrator (ambient temperature), and stored at − 80 °C until further analysis. The lower sediment (protein) pellets were resuspended in 250 µl of lysis buffer containing 0.1% RapiGest, 1 M urea, 0.2 M thiourea, and 70 mM dithiothreitol in 50 mM of ammonium bicarbonate buffer solution. The resuspended solution was vortexed vigorously followed by centrifugation for 10 min at 14,000 g at 4 °C and the supernatants were collected and stored at − 80 °C until further processing.

Lipidomics (upper organic phase)

Dried lipid extracts were resuspended in 100 µl of ACN:IPA:H_2O buffer (65:30:5 v/v) and analyzed using a hybrid quadrupole orbital trapping mass spectrometer (Q Exactive; Thermo Fisher Scientific, Bremen, Germany). In brief, 10 µl of resuspended lipid extract were loaded on a reversed-phase ACQUITY UPLC HSS T3 (1.8 µm, 100 × 2.1 mm, Waters Corporation) column and separated using a Dionex UltiMate 3000 UHPLC system (Thermo Fisher Scientific), with a flow rate of 250 µl/min. The solvent system consisted of eluent A (H_2O:ACN, 40:60 v/v) and eluent B (IPA:ACN, 90:10 v/v) both with 10 mM ammonium formate and 0.1% formic acid. Lipids were separated with a 28 min multi-step linear gradient of 30 to 100% eluent B (electronic supplementary material, ESM Table S1). The column temperature was set to 50 °C and autosampler to 15 °C. Lipidomic datasets were acquired separately in positive- and negative-ion mode in a data-dependent manner using the top-15 method (Full MS/ddMS^2, Top15), modified from a previous study [21]. The optimized heated electrospray ionization (HESI-II) source and data-dependent acquisition (DDA) method parameters for lipidomics experiments in both ionization modes are provided in the ESM (Tables S2 and S3).

High-resolution and accurate mass lipidomic raw datasets were analyzed with LipidSearch (v4.2.23) software (Thermo Fisher Scientific) for identification and alignment [21, 22]. The precursor (MS) and product (MS/MS) mass tolerance was set to 5 ppm. The fragment match score (m-score) was set to 5 and the identification level (fragmentation grade) quality filters A, B, and/or C were considered. The optimized parameters used for lipid identification (independently in positive- and negative-ion mode) and alignment processes (to combine positive- and negative-ion mode search results) are indicated in the ESM (Table S4). Further, all lipid species identified/aligned using the LipidSearch software were filtered (filtering criteria described in the ESM Table S4 and Data file S1) to remove/minimize false positives, and inspected manually (accept, reject, or reassign) after computational analysis.

Metabolomics (lower aqueous phase)

Dried polar metabolite extracts were resuspended in 100 µl of 15% aqueous methanol and a 10 µl injection volume was used. The separation was performed using a reversed-phase ACQUITY UPLC HSS T3 (1.8 µm, 100 × 2.1 mm, Waters Corporation) column at a flow rate of 300 µl/min of a solvent system consisted of eluent A (100% water) and eluent B (100% acetonitrile) both with 0.1% formic acid. Polar metabolites were separated with a 20 min multi-step linear gradient of 1 to 99% eluent B (ESM Table S5). In the case of

serum metabolite analysis, eluent B was replaced by 100% methanol with 0.1% formic acid and a multi-step linear gradient of 1 to 95% in 14 min (ESM Table S6). The autosampler and column compartments were maintained at 4 °C and 40 °C, respectively. Metabolomic datasets were acquired using a hybrid quadrupole orbital trapping mass spectrometer (Q Exactive; Thermo Fisher Scientific, Bremen, Germany) individually in positive- and negative-ion mode in a data-dependent manner using the top-10 method (Full MS/ddMS^2, Top10), adopted from a previous study [23]. The optimized HESI-II ion source and DDA method parameters for metabolomics experiments in both ionization modes are provided in the ESM (Tables S7 and S8).

Positive- and negative-ion mode polar metabolomic raw datasets were processed independently using the Progenesis QI (v2.4) software (Waters Corporation) with default parameters. The untargeted workflow used for data processing and analysis includes retention time alignment, peak picking, deconvolution, compound annotation, normalization, and relative-quantification [23]. The ion adducts of each feature were deconvoluted and annotated primarily using an in-house developed metabolite database with MetaScope search plug-in of Progenesis QI and further verified with MassBank of North America (MoNA), mzCloud, and EMBL-MCF mass spectral libraries using precursor ion accurate mass (MS) and fragmentation (MS/MS) patterns.

Proteomics (lower solid phase)

Total protein concentrations in supernatants of resuspended pellets were measured with Bradford's reagent and subjected to in-solution tryptic digestion followed by label-free quantitative bottom-up proteomics experiments as described elsewhere [24, 25]. Briefly, an equal amount of protein (50 µg) from WT control and *Pex11α* KO mouse liver and/or heart tissues were solubilized in 50 mM ammonium bicarbonate buffer (50 µl) containing 0.1% RapiGest and denatured at 80 °C for 15 min. Then, the proteins were reduced and alkylated with 100 mM DTT at 56 °C for 30 min, 200 mM IAA at ambient temperature in the dark for 30 min, respectively. After that, the proteins were digested with trypsin (1:20 protease-to-protein ratio) at 37 °C for overnight. The tryptic digestion reaction was stopped by incubating with concentrated formic acid (2 µl) for 10 min at 37 °C. The peptide digests were desalted by ZipTip$_{C18}$, dried out using vacufuge concentrator, and reconstituted in 3% aqueous ACN with 0.1% formic acid for further MS analysis.

Peptide digests (2.5 µg) were loaded on a Kinetex C18 reversed-phase (2.6 µm, 100 × 2.1 mm, 100 A°, Phenomenex) column and separated using a Dionex UltiMate 3000 UHPLC system (Thermo Fisher Scientific), with a flow rate of 250 µl/min. The solvent system consisted of eluent A (100% water) and eluent B (100% acetonitrile) both with 0.1% formic acid. Peptides were separated with a 120 min multi-step linear gradient of 3 to 50% eluent B (ESM Table S9). The autosampler temperature was set to 4 °C and column at 40 °C. Proteomic datasets were acquired using a hybrid quadrupole orbital trapping mass spectrometer (Q Exactive; Thermo Fisher Scientific, Bremen, Germany) in positive-ion mode in a data-dependent manner using the top-10 method (Full MS/ddMS^2, Top10), with slight modifications from our previous study [25]. The optimized parameters of HESI-II ion source and DDA method for proteomics experiments are provided in the ESM (Tables S10 and S11).

Proteomic raw datasets were processed using untargeted label-free processing and consensus quantitative workflow (ESM Fig. S1) of Proteome Discoverer (v2.2.0.388) software (Thermo Fisher Scientific). MS data files were searched against UniProt *Mus musculus* protein database (dated 15th September 2019, containing 17,422 target sequences and 9,908,993 residues) using Sequest HT search algorithm. The search was performed with peptide precursor (MS) and fragment (MS/MS) mass tolerance of 10 ppm, 0.02 Da respectively and trypsin as a protease with two missed cleavages and a strict target false discovery rate value of 0.01 (1% FDR). Search criteria also comprised carbamidomethylation (cysteine) as static modification, oxidation (methionine) and acetylation (N-terminal) as dynamic modifications. Unique and razor peptides were considered, precursor abundance values were normalized with total peptide amount, and replicate-based resampling imputed missing values. Abundance ratios were calculated using the pairwise ratio method and significant values were obtained from ANOVA hypothesis test (based on the background population of proteins or peptides). The common external protein contaminant list (MaxQuant database) was used to mark contaminants in the result file. As regulated, only proteins with (i) master group, (ii) high confidence, (iii) at least two peptides, (iv) no contaminants, (v) p-value of ≤ 0.05, and (vi) an abundance ratio of ≤ 0.5 and/or ≥ 2 (equivalent to twofold regulation) were considered.

Bioinformatics analyses

Statistical analysis

Integrated chromatographic peak area values of the individual lipids and polar metabolites were exported as a matrix (samples in columns and features in rows) after manual curation, and statistical analyses were performed using freely accessible MetaboAnalyst (v4.0) [26]. Lipidomic datasets were normalized to the total lipid signal, as no true internal standards were added for all identified lipid species and/or lipid classes and some of the lipid classes were noted with very few lipid species identifications [27, 28]. Prior to the statistical and pathway analyses, both lipidomic and

polar metabolomic datasets were checked for data integrity, outliers removed, normalized (total sum), transformed (generalized logarithmic transformation), scaled (Pareto and/or Range), and imputed (features with > 50% missing values were removed, and remaining missing values were estimated with k-nearest neighbor algorithm). Univariate descriptive statistical methods including fold-change analysis (threshold less than or equal to 0.5 and/or greater than or equal to 2), *t*-test (FDR-adjusted *p*-value less than or equal to 0.05), and volcano plots (log2 fold changes versus -log10 FDR-adjusted *p*-values) were employed to select statistically significant lipids and/or polar metabolites. Lipid class levels (sum of the normalized relative abundance values of all measured lipid species in a particular lipid class) represented as mean ± standard deviation and two-tailed Student's *t*-test (GraphPad Prism v6.01) were used for statistical comparison between the groups.

Pathway analysis

Differentially abundant lipids and polar metabolites (HMDB v4.0, Human Metabolome Database IDs as input) were combined and explored by metabolic pathway analysis for the identification of altered pathways. The analyses were performed using MetPA module of the MetaboAnalyst (v4.0) [29]. "*Mus musculus*" pathway (KEGG, Kyoto Encyclopedia of Genes and Genomes) library, "hypergeometric test" for "over-representation analysis," and "relative-betweenness centrality" for "pathway topology analysis" were used to identify altered specific metabolic pathways.

PANTHER

Protein analysis through evolutionary relationships (PANTHER, v14.1) was used to sort proteins with differential abundance into diverse cellular components, molecular functions, biological processes, signalling pathways, and protein classes [30].

BiNGO

Gene ontology (GO) clustering analysis for the proteins displaying differential abundance was carried out using STRING (Search Tool for the Retrieval of Interacting Genes, v11.0) and later visualized in Cytoscape (v3.7.2) BiNGO (Biological Network Gene Ontology, v3.0.3) [31]. The significantly enriched functional categories (such as biological processes, molecular functions, and cellular components) from GO Slim_*Mus musculus* were uncovered by employing a hypergeometric test and multiple test correction to attain *p*-value ≤ 0.05 using the Benjamini–Hochberg FDR correction method inbuilt within the BiNGO plug-in [32].

Results and discussion

Overview of the study design

Peroxisomes are multifunctional dynamic organelles with heterogeneous protein/enzyme composition and abundance in distinct cell types and organs. PEX11 proteins (α, β, and γ isoforms) are involved in peroxisomal proliferation and division. However, their specific function in these processes and the underlying molecular mechanisms of pathological alterations due to their deficiency have not been completely clarified. To investigate the diverse molecular changes that occur due to *Pex11α* deficiency, we performed comprehensive semi-quantitative sequential omics analyses of serum, liver, and heart tissue specimens from WT control ($Pex11\alpha^{+/+}$) and untreated homozygous *Pex11α* KO ($Pex11\alpha^{-/-}$) adult mice (genotypes of animals were determined by polymerase chain reaction and results are shown in ESM Fig. S2).

First, we optimized an integrated workflow that can profile a broad spectrum of biomolecules (lipids, polar metabolites, and proteins) from a single piece of tissue and/or biological fluids (Fig. 1). Briefly, an ice-cold MeOH/MTBE/H_2O liquid–liquid extraction protocol was utilized for the concurrent extraction of lipids (upper organic layer), polar metabolites (lower aqueous layer), and proteins (lower precipitated pellet) [33, 34]. Extraction was carried out in glass vials in order to minimize the sample loss and contaminants caused by the interaction between organic solvents and plastic tubing [35]. After extraction, distinct fractions were collected and processed independently (detailed in "2" section), after which they were subjected to individual well-established omics analyses using UHPLC-HRMS/MS system. Specialized software tools were then used for identification, relative-quantification, and statistical analysis of lipids, polar metabolites, and proteins (Fig. 1). Taken together, over 93% of the identified lipids, polar metabolites, and proteins showed high technical reproducibility (area relative standard deviation values were less than 15%) across all replicates and tested biological specimens (ESM Fig. S3).

Global lipidomics analysis

Comprehensive lipidome coverage

Lipids can be identified in positive- and/or negative-ion mode based on their chemical complexity. For instance, the majority of the glycerophospholipids (GP) and sphingolipids (SP) are identified in both ionization modes with various charge carriers, whereas neutral lipids such as

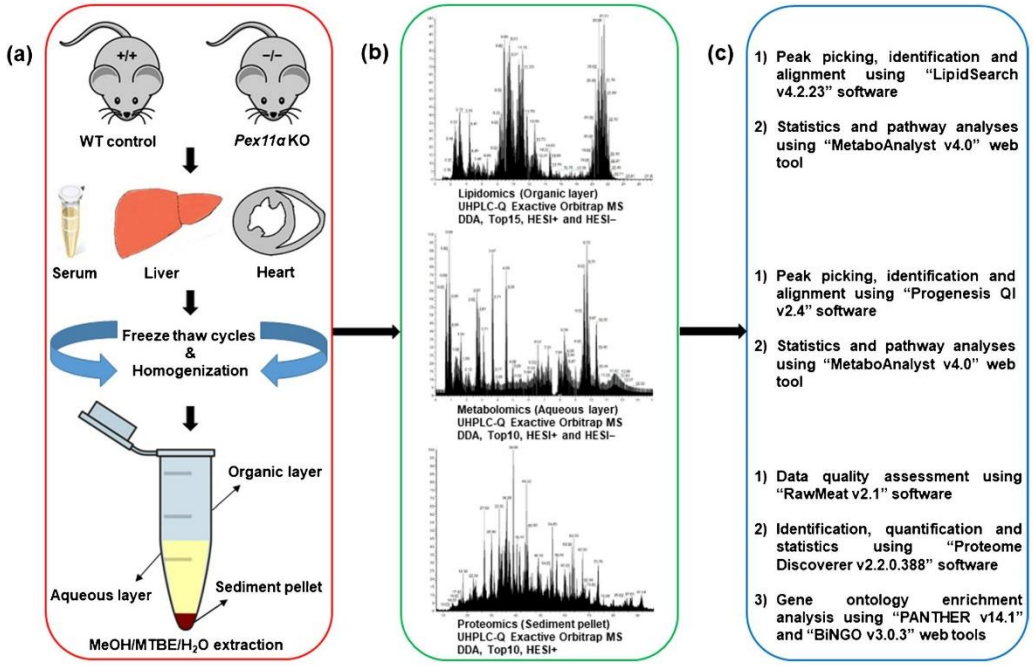

Fig. 1 Schematic representation of the experimental workflow for sequential omics analyses of serum, liver, and heart tissue specimens from wild type (WT; *Pex11α*$^{+/+}$) control and *Pex11α* knockout (KO; *Pex11α*$^{-/-}$) mice. **a** Sample collection, homogenization, and simultaneous extraction of lipids (organic layer), polar metabolites (aqueous layer), and proteins (sediment pellet) using MeOH/MTBE/H_2O liquid–liquid extraction. **b** Analytical workflow of multiple-molecular omics (lipidomics, metabolomics, and proteomics) data acquisition independently in positive- and negative-ion mode using ultra-high-performance liquid chromatography coupled with high-resolution tandem mass spectrometry (UHPLC-HRMS/MS). **c** Data processing, compound identification, statistics, and pathway analysis using dedicated bioinformatics tools

monoglyceride (MG), diglyceride (DG), triglyceride (TG), coenzyme (Co), cholesterol, fatty acyl esters of cholesterol (ChE), and carnitine (AcCa) are predominantly observed in positive-ion mode [36, 37]. With the aim of representing broader lipidome coverage, data were acquired independently in positive- and negative-ion mode (three biological replicates in technical triplicates). Base peak chromatograms obtained with serum, liver, and heart tissue homogenate lipid extracts unveiled a clear peak separation and characteristic lipid ion profiles in both positive- and negative-ion mode (ESM Fig. S4).

LipidSearch (LS) software, which includes a database of greater than 1.7 million lipids and corresponding predicted fragment ions, was used for the identification and alignment of lipid molecular species based on precursor ion accurate mass and characteristic fragment ion patterns [22]. After identification, positive- and negative-ion mode search results were aligned within a time window (0.25 min) and merged into a single report. On average, a total of 3000 lipid ion species belonging to several lipid classes were identified from mice serum (2867), liver (3808), and heart (3518) tissue homogenates (ESM Dataset S1, total count).

Even though lipids were identified based on accurate mass (≤ 5 ppm) and fragment ions (≤ 5 ppm), the aligned-results report comprised a huge number of false positives due to various reasons including fragment mismatch, peak tailing, and poor integration of the chromatographic peak. In order to remove/minimize false positives and to provide more confident lipid identifications, a series of predefined filtering criteria were applied (ESM Table S4). For instance, (i) Rejection (Rej parameter calculated by LS based on signal to noise ratio, intensity ratio, and number of data points thresholds of each peak group) equal to false (ESM Dataset S1, filtered count_1), (ii) deletion of low confidence lipid assignments on the basis of fragmentation grade, removal of recurring lipid annotations by selection of main ion adduct from multiple charge carriers (ESM Data file S1 and Dataset S1, filtered count_2), and

(iii) manual curation (ESM Dataset S1, filtered count_3). Throughout the manual curation, peak quality, fragmentation match score, area relative standard deviation, mass accuracy, isotopic profile, base retention time (as shown in ESM Fig. S4), and chromatographic peak integration for each precursor ion were carefully examined. Furthermore, a few ambiguous lipid assignments were ignored for final quantitation, which were possibly artifacts resulting from in-source fragmentation of corresponding precursor lipids. For instance, across all the identified samples, lysodimethylphosphatidylethanolamine (LdMePE) and dimethylphosphatidylethanolamine (dMePE) lipid species share the same retention time and approximately equivalent abundance ratio values with the identical acyl-chain compositions of LPC and PC lipid species, respectively (ESM Data file S1) [38]. Furthermore, low confidence free fatty acids were not considered by the LS software, due to the fact that the high confidence level identification with a diagnostic fragment ion ($[M-H-44]^-$, resulting from a loss of CO_2) requires relatively high collisional energies (NCE ˃ 40) [39]. Moreover, OAcyl(gamma-hydroxy) fatty acids (OAHFA), simple Glc series (CerG2GNAc), phosphatidylethanol (PEt), and phosphatidylmethanol (PMe) lipid species were also ignored for final quantitation due to insufficient diagnostic fragment ions for confident lipid identification.

After careful data evaluation and manual curation, a total of 690 (serum), 908 (liver), and 939 (heart) distinct lipid species were retained as unambiguous identifications (ESM Dataset S1, final count). Figure 2a–c summarizes an overview and distribution patterns of the identified unique lipid species, covering 22 different lipid classes belonging to three major lipid categories including glycerophospholipids (PC, LPC, PE, LPE, PG, LPG, PI, LPI, PS, LPS, and CL), glycerolipids (MG, DG, and TG), sphingolipids (SM, SPH, Cer, Hex1Cer, and Hex2Cer), and others (AcCa, ChE, and Co). In general, TGs were the most prominent class of lipid species identified among all the tested biological specimens (214, 220, and 271 TG species in serum, liver, and heart tissue homogenates, respectively), followed by PC (97 in serum, 121 in liver, and 146 in heart) and PE (79 in serum, 114 liver, and 134 in heart). A more detailed look into the distribution patterns of the lipid classes revealed (i) a reasonably high number of LPC, SM, and ChE, (ii) relatively lower number of AcCa, PC, PE, PG, PS, and DG, and (iii) no cardiolipin (CL) and LPS lipid species were identified in serum samples in comparison to the liver and heart tissue homogenates (Fig. 2a–c). Complete lipidomic dataset (final list of identified/aligned lipid species, their relative abundance values, differentially abundant lipids, and the associated statistical significance values) in a format that follows "LIPID MAPS consortium" and the "Lipidomics Standards Initiative" minimum reporting guidelines is provided as supplementary Microsoft Excel worksheets (ESM Dataset S1).

Relative-quantitative lipidomics

The generated global lipidome data were statistically evaluated using fold-change analysis, *t*-test, volcano plots, principal component analysis (PCA), and hierarchical clustering analysis (HCA; including dendrogram and heatmaps), to distinguish between the groups. As seen in ESM Fig. S6a-b, a clear separation (occupation of different space in the PCA score plots) and a high degree of dissimilarity (dendrogram) were observed in all the tested biological specimens of *Pex11α* KO and WT control mice. This is eventually visualized with two-dimensional hierarchical clustering heatmaps (Fig. 2d–f), where each column represents a biological sample and each row represents a significant lipid molecular species, ranked based on *t*-test. Furthermore, descriptive volcano plot analysis of all measured lipids revealed significant (FDR-adjusted p-value ≤ 0.05) changes in the abundance (ratio threshold ± 2) of 102 lipid species (64 increased, 38 decreased) in serum, of 145 lipid species (80 increased, 65 decreased) in liver, and 102 lipid species (12 increased, 90 decreased) in heart tissue homogenates of *Pex11α* KO mice, in comparison to those of WT controls (ESM Fig. S6c and Dataset S1_Quan). Moreover, we calculated and compared the individual lipid class levels (sum of the normalized relative abundance values of all analyzed lipid species within the class) among WT control and *Pex11α* KO mice (ESM Fig. S5a-c and Dataset S1_Lipid class). The various lipid classes and the individual lipid molecular species that were differentially abundant are discussed below.

Sphingolipids (SP) are an essential class of bioactive lipids with a sphingoid backbone. They are present as underivatized (e.g., sphingosine), or N-acetylated with fatty acids (e.g., Cer), or further derivatized by addition of charged, neutral, phosphorylated, and glycosylated head groups to form more complex SP (e.g., SM, CerP, CerPE, HexCer, and GalCer). Depending on the fatty acid conjugates and concentration, they play vital roles in proliferation, differentiation, apoptosis, senescence, and autophagy [40]. In the current study, numerous sphingolipid species (139 in serum, 138 in liver, and 123 in heart) covering SM, Cer, Hex1Cer, Hex2Cer, and SPH lipid classes were documented (Fig. 2a-c, ESM Dataset S1). Within the SP category, several ceramide and cerebroside (e.g., hexosylceramide) lipid species were markedly increased in serum (seven Cer, five Hex1Cer species) and liver (nine Cer, five Hex1Cer species) tissue homogenates of *Pex11α* KO mouse. Among them, two lipid species, namely Hex1Cer(d36:1; d18:1_18:0) and Hex1Cer(d43:2; d18:1_25:1), were found to be common and raised in both the liver tissue and serum. Similarly, 12 and one SM lipid species exhibited higher levels in *Pex11α*

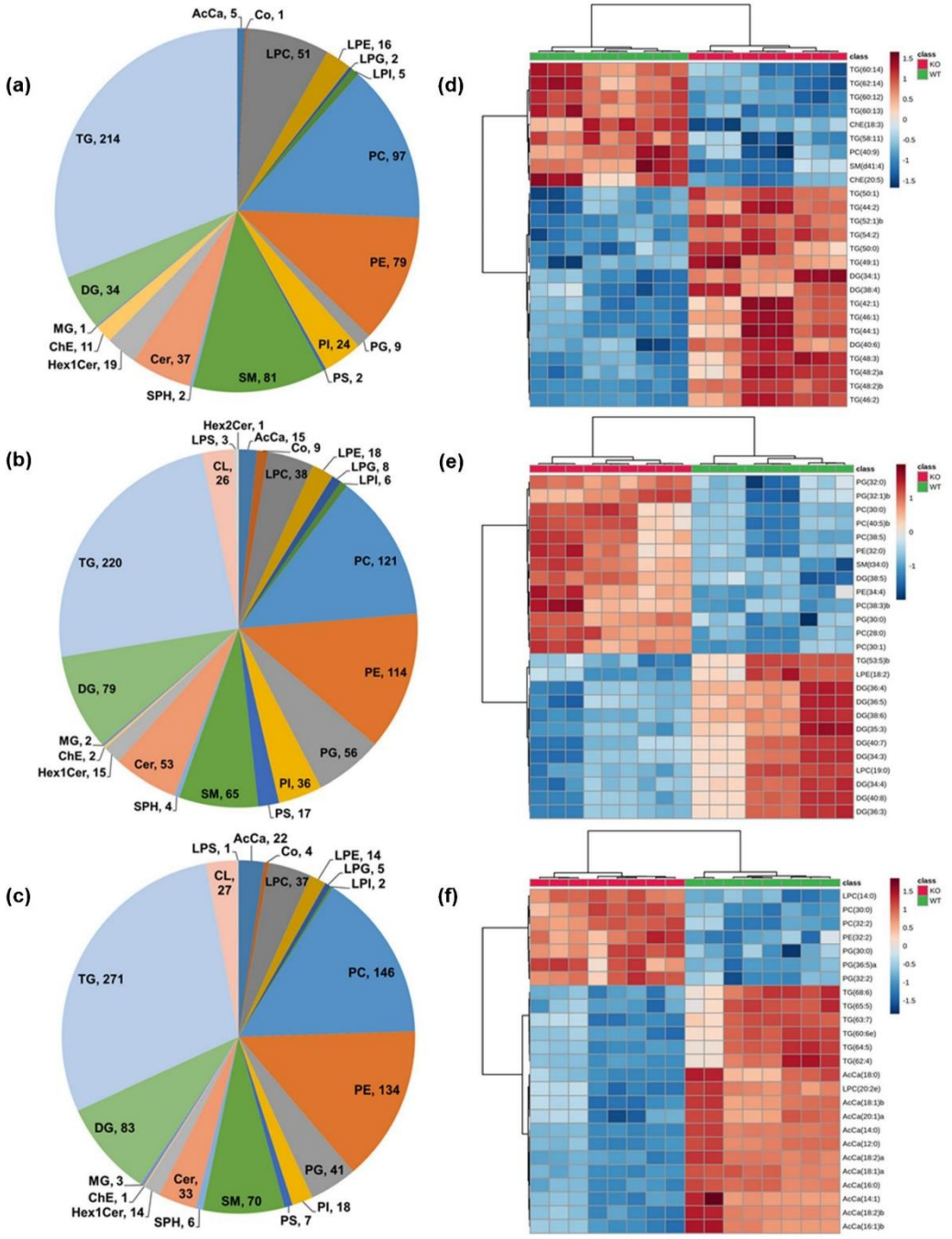
(a)
AcCa, 5
Co, 1
LPC, 51
LPE, 16
LPG, 2
LPI, 5
PC, 97
PE, 79
PI, 24
PG, 9
PS, 2
SM, 81
SPH, 2
Cer, 37
Hex1Cer, 19
ChE, 11
MG, 1
DG, 34
TG, 214
(b)
Hex2Cer, 1
LPS, 3
AcCa, 15
Co, 9
CL, 26
LPC, 38
LPE, 18
LPG, 8
LPI, 6
PC, 121
PE, 114
PG, 56
PI, 36
PS, 17
SM, 65
SPH, 4
Cer, 53
Hex1Cer, 15
ChE, 2
MG, 2
DG, 79
TG, 220
(c)
LPS, 1
AcCa, 22
Co, 4
CL, 27
LPC, 37
LPE, 14
LPG, 5
LPI, 2
PC, 146
PE, 134
PG, 41
PI, 18
PS, 7
SM, 70
SPH, 6
Cer, 33
Hex1Cer, 14
ChE, 1
MG, 3
DG, 83
TG, 271
(d)
(e)
(f)

◂**Fig. 2** Overview of the global lipidomics analysis. Pie charts depict the summary as well as distribution patterns of identified lipid species/classes among all the tested biological specimens **a** serum, **b** liver, and **c** heart tissue homogenates. The numbers in pie charts represent the number of lipid species confidently identified and quantified in a particular lipid class. Heatmap illustration of lipid species between *Pex11α* knockout (KO; $Pex11\alpha^{-/-}$) and wild type (WT; $Pex11\alpha^{+/+}$) control mouse **d** serum, **e** liver, and **f** heart tissue homogenates. Data in heatmaps is based on *z*-scores for the normalized, transformed, and scaled data. The top 25 differentially abundant lipid species (with lowest FDR-adjusted *p*-values) were ranked based on *t*-test, distance was measured using the Euclidean correlation, and clustering was performed using the Ward algorithm

KO mice liver and serum (while three species decreased) in comparison to the WT controls. In contrast, we did not notice statistically significant differences in the individual species and the total sphingolipid class levels of *Pex11α* KO mouse heart tissues (ESM Dataset S1 and Fig. S5). Pettus et al. observed increased levels of specific Cer and SM lipid species in brain and fibroblasts of newborn mice lacking *Pex5*, as well as in the fibroblasts of D-specific multifunctional protein 2 (MFP2) deficient mice [41]. Furthermore, similar observations were witnessed in fibroblasts derived from X-linked adrenoleukodystrophy (X-ALD) patients and proposed perturbations in $C_{26:1/0}$-ceramide lipid and ratio of $C_{26:1/0}$-ceramide/$C_{22:0}$-ceramide as possible potential diagnostic markers to study the peroxisomal disorders [41]. Likewise, other studies reported higher amounts of SM lipids with long-chain fatty acid moieties in liver [42] and cultured skin fibroblasts [43, 44], SM lipids with short-chain fatty acid moieties in cerebellum [42], and ceramide monohexoside in the cerebral gray matter but not in the white matter of ZS patients (e.g., *Pex1* and *Pex26* mutations) [45]. Moreover, increased levels of ceramide monohexoside were also observed in *Pex5*-mutated Chinese hamster ovary cells [46]. Remarkably, a recent metabolomic study disclosed unanticipated decreased levels of multiple SM lipid species in ZSD patient's plasma [47].

Glycerophospholipids (GP) are structural integral components of most cell and organelle membranes, which play crucial roles in various physiological and pathological processes. Within the GP category, we identified several lipid species (285 in serum, 443 in liver, and 432 in heart) spanning 11 different lipid classes (PC, LPC, PE, LPE, PG, LPG, PI, LPI, PS, LPS, and CL), which unveiled a wide diversity of quantitative trends between the tested biological specimens (Fig. 2, ESM Dataset S1 and Fig. S5). In detail, among phosphatidylcholines (the most abundant lipid class in GP), three PC species (PC 30:0, 30:1, and 37:5) in serum, seven species (PC 28:0, 30:0, 30:1, 38:3, 38:5, 40:5, and 42:9) in liver, and four species (PC 30:0, 32:2, 41:2, and 42:9) in heart were significantly increased in *Pex11α* KO mice. Among these, PC(30:0; 16:0_14:0) lipid showed higher levels in all the tested biological specimens of *Pex11α* KO mice, whereas PC(30:1; 16:1_14:0) and PC(42:9; 22:5_20:4) lipid species exhibited a similar rise in serum and liver, heart and liver tissue homogenates, respectively. Only one lipid species (PC 36:5) in liver, two lipid species including one ether-linked species (PC 36:6e, 41:5) in heart, and more interestingly five species (PC 40:9, 41:6, 42:6, 42:11, and 44:12) in serum, all comprising poly-unsaturated fatty acids (PUFA; C22:6) were significantly decreased in the *Pex11α* deficient mice. LPC species with a single fatty acyl chain ($C \leq 20$), derived from PC lipids, displayed comparatively lower levels in *Pex11α* deficient animals (LPC 19:0, 20:0, 20:2e in serum, LPC 19:0, 19:1, 20:1, 20:2 in liver, and LPC 20:2e in heart). In contrast, LPC 14:0 showed slightly higher levels in *Pex11α* KO mouse heart tissue homogenates. In phosphatidylethanolamine lipid class (the second-most abundant in GP), two species (PE 38:5, 40:4) in serum, one species (PE 32:2) in heart, and six lipid species (PE 32:0, 34:4, 38:4, 38:6e, 40:5p, 40:6e) in liver were significantly increased in *Pex11α* KO mice. Similar to PC, PE 36:5 and PUFA containing two species (PE 41:6, 42:8) were significantly decreased in *Pex11α* KO mouse liver. LysoPE lipids in the liver (eight species, ranging from LPE 18:2 to 22:6) followed the same pattern as of LPC but remained relatively constant in serum and heart. A number of PG lipid species (starting from PG 30:0 to 44:10) showed elevated levels in *Pex11α* KO mouse liver (nine species) and heart (four species) tissue homogenates. Among these, PG (30:0; 16:0_14:0) and PG (44:10; 22:5_22:5) lipids were found to be common and raised in both the liver and heart tissue homogenates. Nonetheless, individual PG lipid species in serum and total PG and LPG lipid species/class levels in all the tested biological specimens were not significantly changed. In addition to these phospholipid class alterations, we noted significantly increased levels of PI (16 species, starting from PI 34:1 to 40:7) and PS (four species including PS 34:2, 36:1, 38:4, and 42:7) lipid species in *Pex11α* KO mouse liver. On the contrary, three (PI 38:3, 40:4, and 40:5) and two (PI 39:4, 40:6) PI lipid species were decreased in serum and heart tissue homogenates. The remaining glycerophospholipid classes and their individual lipid molecular species did not show major differences in *Pex11α* deficient animals.

Cardiolipin (CL) is a dimeric phospholipid, which makes up to 20% (inner) and 3% (outer) of the total mitochondrial membrane lipid composition. While in peroxisomes, CL makes up to 2–4% of the total phospholipid pool [48]. In the present study, CL lipid species were identified in both liver (26 species) and heart (27 species) tissue homogenates, but not in serum (Fig. 2, ESM Dataset S1). Among these, five CL lipid species (CL 74:9, 76:12, 76:12, 78:14, and 78:15) were significantly elevated in *Pex11α* KO mouse liver, possibly due to mitochondrial proliferation [9, 10, 49]. Noticeably, the individual species and the total CL levels

remained relatively unchanged in the heart tissue homogenates. Abnormalities in the CL composition are known to be associated with severe metabolic disorders (e.g., Tangier disease and Barth syndrome) and are also linked with various pathological states [50]. In this regard, it is worth mentioning that decreased levels of several CL species were observed in the cultured skin fibroblasts derived from single PEDs and ZSDs patients [44, 51]. Nevertheless, the precise molecular mechanisms behind these phospholipid class (CL) alterations (positive/negative) in relation to peroxisomes and peroxisomal disorders are not clear yet, requiring further studies in this regard.

In the glycerolipid (GL) category, we spotted several lipid species (249 in serum, 301 in liver, and 357 in heart) belonging to MG, DG, and TG lipid classes (Fig. 2, ESM Dataset S1). In serum, 11 different lipid species ranging from DG 32:0 to 40:6 showed significantly higher levels in *Pex11α* KO mice. In contrast, DG lipid class levels and a wide variety of individual lipid species (starting from DG 32:3 to 44:9) including several PUFA containing species (for instance, DG 40:7, 40:8, 42:6, 42:7, 42:9, 42:10, and 44:7) were significantly decreased (except DG 38:5) in *Pex11α* KO mouse liver. However, no statistically significant changes were noted in heart tissues. TG lipids consist of a glycerol backbone esterified with three fatty acids. They are a vital source of energy during cellular metabolism. Among these, 55 TG lipid species (34 increased, 21 decreased) in serum, 14 species (10 decreased, four increased) in liver, and 65 lipid species (three increased, 62 decreased) in heart showed statistically significant differences in *Pex11α* KO mice when compared to the WT controls. Among the differentially abundant TGs, TG(60:13; 20:5_18:2_22:6) lipid showed reduced levels in all the tested biological specimens of *Pex11α* KO mice. Likewise, increased levels of TG(44:1; 16:1_14:0_14:0), and decreased levels of TG(56:10; 18:3_18:2_20:5) and TG(58:11; 18:3_18:2_22:6) lipid species were noted in the liver tissue and serum, whereas lower levels of TG(62:14; 18:2_22:6_22:6) lipid species were observed commonly in serum and heart tissue homogenates. Overall, the majority of the ether-linked and PUFA containing TG lipid species were significantly decreased in *Pex11α* KO mice (ESM Dataset S1). A minimal number of MG lipid species were identified in serum (one species), heart (three species), and liver (two species) tissue homogenates and they were statistically not as robust as the lipid classes with higher total numbers of species.

Notably, as stated earlier, a number of GP and GL lipid species containing long-chain fatty acid and poly-unsaturated fatty acid moieties showed significant variances (both positive and negative) in the biological specimens of *Pex11α* KO mice. Interestingly, fragmentation data (MS/MS) revealed that the majority of the lipid species with docosahexaenoic acid (DHA, C22:6) moieties were decreased (with few exceptions) in *Pex11α* deficient mice when compared to those of WT controls (ESM Dataset S1). DHA is an essential poly-unsaturated fatty acid, synthesized from the dietary fatty acid α-linoleic acid (ALA, C18:3) by successive elongation and desaturation reactions in the endoplasmic reticulum followed by peroxisomal β-oxidation [52]. Several studies have documented reduced levels of DHA and DHA-containing lipid species in different peroxisomal diseases [51–56]. Moreover, a previous study suggests that DHA enhances the peroxisomal division in a microtubule-independent manner [55].

In addition to the differences in SP, GP, and GL classes and specific lipid species, other lipid classes including fatty acyl esters of carnitine (AcCa), free and esterified cholesterol (ChE) species, and coenzyme (Co) were confidently identified and relatively quantified in all the tested biological specimens (Fig. 2, ESM Dataset S1). Concisely, among acylcarnitines (AcCa), AcCa 6:0 in serum and AcCa 10:0 in liver showed an increment, while the majority of the measured AcCa species were reduced in *Pex11α* KO mouse heart tissues. Two cholesteryl ester species (ChE 18:3, 20:5) showed relatively lower levels in *Pex11α* KO mouse serum.

Several studies employed both targeted and untargeted lipidomics approaches to study the functional consequences and to explore novel molecular biomarkers for a better understanding and diagnosis of peroxisomal disorders. To mention a few, differential lipidomic analyses were carried out in (i) cultured primary skin fibroblasts derived from PBDs (e.g., *Pex1*, *Pex13*, *Pex16*, and *Pex7* mutations) and single PEDs (e.g., ABCD1, ACOX1, DBP, and ACBD5 deficiencies) patients [43, 44, 51, 56–58], (ii) brain, liver, and fibroblasts from ZSDs patients (e.g., *Pex1*, *Pex26*, and *Pex5* mutations) [42], (iii) plasma from ZSDs (e.g., *Pex1* mutation), AMACR and DBP deficiency, Refsum disease, and RCDP type 1 or 5 patients [47, 59], (iv) brain, liver, kidney, and retina of peroxisomal disorder (e.g., ZS, NALD, X-ALD, BED, and AMN) patients [54], and also in mouse and cell culture models of several peroxisomal dysfunctions [41, 46, 56, 60]. The diversity and specimen-specific alterations in distinct lipid profiles reflect the heterogeneity and the widespread lipid-associated metabolic functions of peroxisomes in different cell types, organs, and whole organisms.

Global metabolomics analysis

Further, we investigated the polar metabolic changes and metabolic pathways modulated in different biological specimens due to *Pex11α* deficiency. To attain this, the lower aqueous phase containing polar metabolites was processed, untargeted metabolomic analysis was carried out (three biological replicates in technical triplicates), and obtained data were evaluated using the Progenesis QI. On average, global metabolomics data generated over 10,000 features across

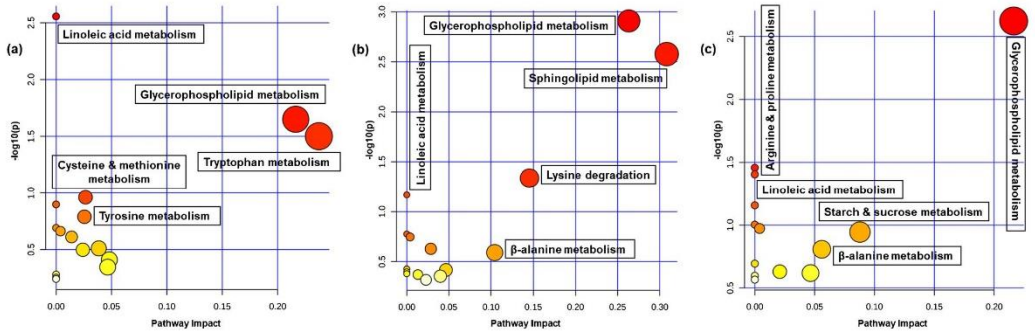

Fig. 3 Scatterplots of enriched KEGG pathways for combined lipidomic/metabolomic experiments when comparing *Pex11α* knockout (KO; $Pex11\alpha^{-/-}$) with wild type (WT; $Pex11\alpha^{+/+}$) control mice. Pathway topology analysis depicting the dysregulated metabolic pathways in **a** serum, **b** liver, and **c** heart tissue homogenates, respectively. Here, the *x*-axis represents the pathway impact, and the *y*-axis represents the pathway enrichment. Each node marks a pathway. The size (pathway impact value) and color (-log10 *p*-value) of the nodes represent the number of lipid/polar metabolite species and level of significance, respectively

all the tested biological specimens. Putative identification of metabolites was performed for the ions that had MS/MS data. Furthermore, compounds were manually filtered, based on their coefficient of variation, duplicates were removed, and misidentifications based on retention time, quality of peak shape, score, fragmentation match score, isotope similarity, and mass accuracy were deleted. After removal of false positives, by combining both positive- and negative-ion modes data collectively, 123, 98, and 80 metabolites were tentatively identified in serum, liver, and heart tissue homogenates, respectively. The identities of the metabolites (putatively annotated metabolites, their relative abundance values, differential abundances, and the associated statistical significance values) are provided as supplementary Microsoft Excel worksheets (ESM Dataset S2). Metabolites covering a broad spectrum of chemical classes, including amino acids, nucleotides, peptides, carbohydrates, bile acids, secondary lipid mediators, polyamines, vitamins, and cofactors, were identified. The majority of them were found to be shared between all the tested biological specimens.

Using PCA, HCA, and descriptive univariate statistical analysis, we observed a clear separation and significant changes between the *Pex11α* KO and WT control groups (ESM Fig. S7 and Dataset S2). To explore the metabolic pathways that were dysregulated in the *Pex11α* KO mice, differentially abundant polar metabolites (25 in serum, 12 in liver, 11 in heart) and lipid species (102 in serum, 145 in liver, 102 in heart) were combined (of these, collectively 82, 114, and 52 compounds of serum, liver, and heart were found in the HMDB database), and metabolic pathways analyses (KEGG, *Mus musculus* libraries) were performed using the MetPA module of MetaboAnalyst. Several pathways related to lipid metabolism (e.g., glycerophospholipid, sphingolipid, glycerolipid, linolenic acid, α-linolenic acid and arachidonic acid metabolism, and fatty acid degradation), amino acid metabolism (e.g., tryptophan, purine, tyrosine, cysteine and methionine metabolism, and lysine degradation), nucleotide metabolism, carbohydrate metabolism, and other metabolic pathways were found to be altered in *Pex11α* KO mice. The summary of pathway analysis is shown in Fig. 3 and is listed in detail in ESM Table S12. Many research articles can be found, focusing on alterations in lipid species, and the role of lipid metabolism is well established in several peroxisomal disorders. Nevertheless, a comprehensive polar metabolomic map and the metabolic pathways that are altered in various peroxisomal disorders (for instance with peroxisomal biogenesis gene mutants or single peroxisomal enzyme mutants) are still poorly understood. Recently, Wangler et al. performed untargeted metabolomics analysis and revealed alterations in known lipid pathways and unanticipated changes in carbohydrate metabolic processes including starch and sucrose metabolism, glycolysis, glycogen catabolism, and pentose phosphate pathway in *Pex16* and *Pex2* mutant *Drosophila melanogaster* (fruit flies) and *Pex5* deficient mouse liver [61].

Label-free quantitative proteomics analysis

Proteins play crucial roles in various cellular functions, and proteomics has emerged as a powerful tool to identify both pathophysiological mechanisms as well as potential biomarkers for various diseases. In order to identify alterations in the *Pex11α* KO mice, tissue protein relative abundance values were compared to those of WT control mice by relative-quantitative proteomics. At this level of the experiment, the remaining lower sediment pellets (possibly containing

stable and highly abundant proteins) were re-solubilized, and proteins extracted, digested with trypsin, and analyzed individually (three biological replicates in technical triplicates) by shotgun label-free quantitative (LFQ) proteomics. Prior to the quantitative proteome data analysis, data quality attributes (e.g., charge distributions and scan rates) and suitability of the sample complexity and applied method (e.g., Full MS/ddms^2, Top10) were inspected visually using RawMeat (v2.1, Vast Scientific) software (ESM Data file S2).

In total, the Proteome Discoverer software with Sequest HT search algorithm identified 1064 and 738 proteins from the sediment pellets of the liver and the heart tissue homogenates, respectively (ESM Dataset S3). Out of these, 626 and 399 master proteins in the liver and heart were quantified with two or more peptides and a strict target false discovery rate value of 0.01 (1% FDR). The corresponding list of identified and quantified proteins, as well as the data analysis output file including normalized abundance values, abundance ratios, and the corresponding statistical information, is presented as supplementary Microsoft Excel worksheets (ESM Dataset S3). Two-dimensional PCA score plots of the quantified proteome (normalized, log-transformed, and Pareto-scaled) showed that all the replicate acquisitions are clustered together and revealed a clear separation illustrating significant changes in the tissue proteome of *Pex11α* KO compared to WT controls (ESM Data file S2). In detail, the LFQ proteomics approach revealed significant (p-value threshold ≤ 0.05) changes in the abundance (ratio threshold ± 2) of 54 proteins (42 increased, 12 decreased) in the liver and 29 proteins (14 increased, 15 decreased) in the heart tissues of *Pex11α* KO in comparison to the WT control mouse (Fig. 4a-b, ESM Dataset S3). Interestingly, we noticed a downregulation of NUDT7 protein (peroxisomal coenzyme A diphosphatase) in the liver. NUDT7 eliminates toxic nucleotides (e.g., oxidized CoA) and nucleotide diphosphates (e.g., ADP-ribose, NAD+, and NADH) and regulates CoA and acyl-CoA levels in the peroxisomes in response to metabolic needs [62, 63]. Moreover, dysregulation of NUDT7 was also observed during senescence [64], and knockdown of NUDT7 resulted in the disruption of lipid homeostasis in chondrocytes [63]. In the heart, the small GTPase proteins from the Ras superfamily, which includes transforming protein RhoA, Ras-related protein Rap-1A, and Ras-related protein Rab-15 which regulates cytoskeletal reorganization, cell proliferation, and is associated with the peroxisomal membrane dynamics and biogenesis, were found to be downregulated in *Pex11α* KO [65, 66]. Likewise, other proteins including acyl-CoA-binding protein, fatty acid synthase, isocitrate dehydrogenase (NADP) cytoplasmic, isocitrate dehydrogenase (NADP) mitochondrial, aldehyde

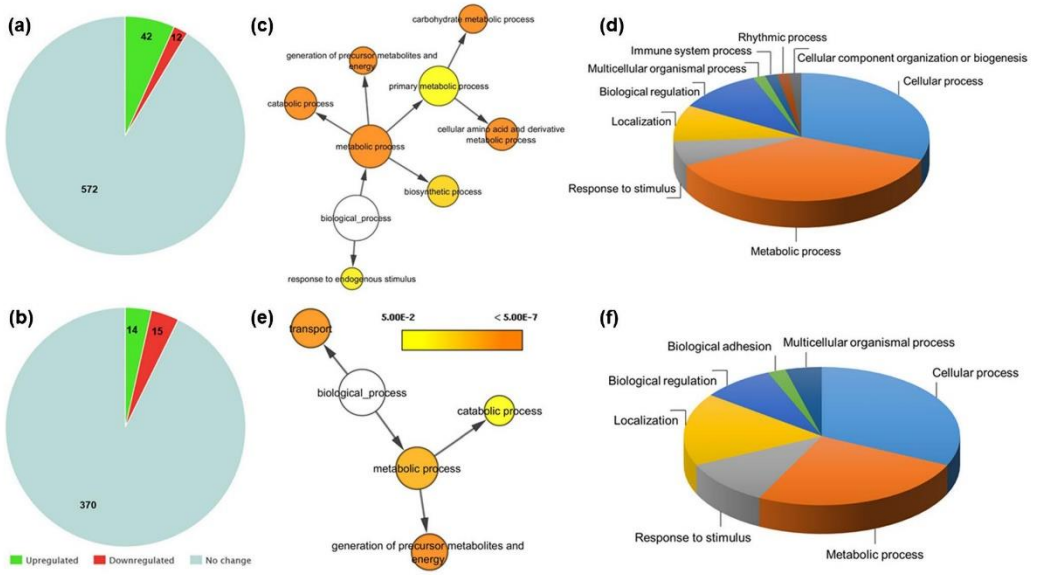

Fig. 4 Label-free quantitative proteomic analysis of *Pex11α* knockout (KO; *Pex11α*$^{-/-}$) and wild type (WT; *Pex11α*$^{+/+}$) control mice. Pie charts depict the number of quantified and differentially abundant proteins in **a** liver and **b** heart tissue homogenates. Biological processes of the differentially abundant proteins in (**c** and **d**) liver and (**e** and **f**) heart analyzed by Cytoscape and PANTHER. Color scale indicates the significance, and size of the circle indicates the number of proteins involved

dehydrogenase, carbonyl reductase, glutathione S-transferase, enoyl-CoA delta isomerase 2, glutathione peroxidase, and farnesyl pyrophosphate synthase, among other proteins, were differentially abundant in *Pex11α* KO in comparison to WT control mouse tissues. Seemingly, the relatively low number of total protein identifications from the whole-tissue homogenates (in comparison with the conventional proteomics workflow) might be ascribed to the one-step liquid–liquid extraction procedure (traditionally used for lipidomics) optimized for serial-omics analyses, from a single piece of biological sample. Also, the non-appearance of several important peroxisomal membrane proteins, matrix proteins, and peroxins might be ascribed to their low abundance and to the well-known difficulties associated with the extraction of labile hydrophobic proteins.

Furthermore, to elucidate the biological context of the differentially abundant proteins (DAPs), gene ontology enrichment analysis was carried out using PANTHER and Cytoscape (BiNGO plug-in) bioinformatics tools. Biological information such as molecular functions, biological processes, cellular components, signalling pathways involved, and protein classes of the DAPs was obtained as shown in Fig. 4c-f and ESM Data file S3. Taken together, in liver and heart tissues, we found that DAPs were involved in translation, protein folding, amino acid metabolism, nucleotide metabolism, fatty acid processing, carbohydrate metabolism, steroid biosynthesis, electron transport chain, and ROS metabolism (Fig. 4c-f, ESM Data file S3). Lastly, it is worth noting that many of these proteins (DAPs) are located within the mitochondrion, which suggests that knockout of *Pex11α* may induce major changes to mitochondrial metabolism.

Conclusion and future perspectives

In the present study, we utilized high-throughput mass spectrometry-guided sequential omics workflow and performed comprehensive semi-quantitative lipidomic, metabolomic, and proteomic analyses of different biological specimens (serum, liver, and heart) from *Pex11α* KO adult male animals. Complex lipids, polar metabolites, and proteins were simultaneously extracted via a single-step liquid–liquid (MeOH/MTBE/H_2O) extraction method, and the corresponding omics datasets were acquired using ultra-high-performance liquid chromatography coupled with high-resolution tandem mass spectrometry and processed with LipidSearch, Progenesis QI, and Proteome Discoverer, respectively. Primarily, we identified characteristic changes in the composition of several lipid species/classes, polar metabolites, metabolic pathways, and protein profiles of serum, liver, and heart tissue homogenates of *Pex11α* KO mice in comparison to the WT controls. Nevertheless, there are certain limitations in the current study that need to be mentioned. First, serial-omics analyses of distinct biological specimens were performed with a small sample size (three biological replicates in technical triplicates). Although stringent data analysis criteria were employed, a profound statistical evaluation is restricted due to the limited number of biological replicates, thereby, false positives and/or negatives may not be overruled at this stage. Complementary studies with an independent large sample size may be warranted to elucidate the panel of molecular signatures that were presented in this study and to demonstrate their potential as diagnostic biomarkers. Second, due to medium number of protein identifications, the present study did not allow us to integrate multi-layer omics data to fully capture and represent the complete molecular pathway changes occurring due to *Pex11α* deficiency. Despite these limitations, to the best of our knowledge, this is the first comprehensive serial-omics study to report the molecular alterations occurring in different biological specimens of *Pex11α* deficient mice. Further studies addressing changes in other biological specimens (e.g., fibroblasts, brain, kidney, and testis), the influence of diet (e.g., high-fat diet and DHA supplementation) on molecular alterations, and integrated analysis of multi-omics data with large cohort studies need to be investigated in the near future to gain deeper insights of *Pex11α* molecular functions and to uncover the pathophysiological mechanisms of peroxisomal disorders.

Supplementary Information The online version contains supplementary material available at https://doi.org/10.1007/s00216-021-03860-0.

Acknowledgements We thank Dr. David Peake (Thermo Fischer Scientific, USA) for assisting in lipidomics data analysis and Dr. Yashwant Kumar (DBT-THSTI, India) for assisting in metabolomics data analysis. We thank Andrea Textor and Bianca Pfeiffer for their technical support.

Author contribution Conceptualization and methodology: VG, CC, EBV, and BS; investigation: VG (sample preparation, omics data acquisition, and analysis) and CC (mouse breeding and tissue collection); writing — original draft: VG; writing — review and editing: all authors; resources, supervision, and funding acquisition: EBV and BS. All authors reviewed the whole work and edited and approved the manuscript.

Funding Open Access funding enabled and organized by Projekt DEAL. We thank the German Academic Exchange Service (DAAD) for granting the Graduate School Scholarship Programme "Lipids in Nutrition and Metabolism" (DAAD-GSSP-2015). VG is a holder of a doctoral fellowship within this programme (Personal reference no 91566181). In addition, financial support by the Deutsche Forschungsgemeinschaft DFG (Sp 314/13–1 and INST 162/500–1 FUGG), state of Hesse through LOEWE Center DRUID and LOM (Leistungsorientierte Mittel) performance-related resource allocation-funds of the Medical Faculty of the Justus Liebig University Giessen, Germany are gratefully acknowledged.

Data availability All relevant data and materials are within the manuscript and its electronic supplementary material. Raw MS data files have been deposited to the EMBL-EBI MetaboLights data respiratory with the unique identifier MTBLS1887.

Declarations

Animal welfare and ethics approval The animal experiments were performed in accordance with the German Animal Welfare Law and recommendations of institutional animal welfare officers. All experiments were approved by the German Government Commission of Animal Care (Justus Liebig University internal classification: JLU-Nr.: 616_M, Project ID: 1016 Peroxisomen).

Conflict of interest The authors declare no competing interests.

References

1. Wanders RJ. Metabolic functions of peroxisomes in health and disease. Biochimie. 2014;98:36–44. https://doi.org/10.1016/j.biochi.2013.08.022.
2. Schrader M, Fahimi HD. Peroxisomes and oxidative stress. Biochim Biophys Acta. 2006;1763(12):1755–66. https://doi.org/10.1016/j.bbamcr.2006.09.006.
3. Baumgart E. Application of in situ hybridization, cytochemical and immunocytochemical techniques for the investigation of peroxisomes. A review including novel data. Robert Feulgen Prize Lecture 1997. Histochem Cell Biol. 1997;108(3):185–210. https://doi.org/10.1007/s004180050160.
4. Karnati S, Baumgart-Vogt E. Peroxisomes in mouse and human lung: their involvement in pulmonary lipid metabolism. Histochem Cell Biol. 2008;130(4):719–40. https://doi.org/10.1007/s00418-008-0462-3.
5. Fidaleo M. Peroxisomes and peroxisomal disorders: the main facts. Exp Toxicol Pathol. 2010;62(6):615–25. https://doi.org/10.1016/j.etp.2009.08.008.
6. Fujiki Y, Okumoto K, Mukai S, Honsho M, Tamura S. Peroxisome biogenesis in mammalian cells. Front Physiol. 2014;5:307. https://doi.org/10.3389/fphys.2014.00307.
7. Waterham HR, Ferdinandusse S, Wanders RJ. Human disorders of peroxisome metabolism and biogenesis. Biochim Biophys Acta. 2016;1863(5):922–33. https://doi.org/10.1016/j.bbamcr.2015.11.015.
8. Braverman NE, D'Agostino MD, Maclean GE. Peroxisome biogenesis disorders: biological, clinical and pathophysiological perspectives. Dev Disabil Res Rev. 2013;17(3):187–96. https://doi.org/10.1002/ddrr.1113.
9. Li X, Baumgart E, Dong GX, Morrell JC, Jimenez-Sanchez G, Valle D, et al. PEX11alpha is required for peroxisome proliferation in response to 4-phenylbutyrate but is dispensable for peroxisome proliferator-activated receptor alpha-mediated peroxisome proliferation. Mol Cell Biol. 2002;22(23):8226–40. https://doi.org/10.1128/mcb.22.23.8226-8240.2002.
10. Li X, Baumgart E, Morrell JC, Jimenez-Sanchez G, Valle D, Gould SJ. PEX11 beta deficiency is lethal and impairs neuronal migration but does not abrogate peroxisome function. Mol Cell Biol. 2002;22(12):4358–65. https://doi.org/10.1128/mcb.22.12.4358-4365.2002.
11. Colasante C, Chen J, Ahlemeyer B, Baumgart-Vogt E. Peroxisomes in cardiomyocytes and the peroxisome / peroxisome proliferator-activated receptor-loop. Thromb Haemost. 2015;113(3):452–63. https://doi.org/10.1160/TH14-06-0497.
12. Anthonio EA, Brees C, Baumgart-Vogt E, Hongu T, Huybrechts SJ, Van Dijck P, et al. Small G proteins in peroxisome biogenesis: the potential involvement of ADP-ribosylation factor 6. BMC Cell Biol. 2009;10:58. https://doi.org/10.1186/1471-2121-10-58.
13. Kobayashi S, Tanaka A, Fujiki Y. Fis1, DLP1, and Pex11p coordinately regulate peroxisome morphogenesis. Exp Cell Res. 2007;313(8):1675–86. https://doi.org/10.1016/j.yexcr.2007.02.028.
14. Weng H, Ji X, Naito Y, Endo K, Ma X, Takahashi R, et al. Pex-11alpha deficiency impairs peroxisome elongation and division and contributes to nonalcoholic fatty liver in mice. Am J Physiol Endocrinol Metab. 2013;304(2):E187–96. https://doi.org/10.1152/ajpendo.00425.2012.
15. Kopczynski D, Coman C, Zahedi RP, Lorenz K, Sickmann A, Ahrends R. Multi-OMICS: a critical technical perspective on integrative lipidomics approaches. Biochim Biophys Acta Mol Cell Biol Lipids. 2017;1862(8):808–11. https://doi.org/10.1016/j.bbalip.2017.02.003.
16. Breitkopf SB, Taveira MO, Yuan M, Wulf GM, Asara JM. Serial-omics of P53-/-, Brca1-/- mouse breast tumor and normal mammary gland. Sci Rep. 2017;7(1):14503. https://doi.org/10.1038/s41598-017-15132-y.
17. Hendgen-Cotta UB, Esfeld S, Coman C, Ahrends R, Klein-Hitpass L, Flogel U, et al. A novel physiological role for cardiac myoglobin in lipid metabolism. Sci Rep. 2017;7:43219. https://doi.org/10.1038/srep43219.
18. Nakayasu ES, Nicora CD, Sims AC, Burnum-Johnson KE, Kim YM, Kyle JE et al. MPLEx: a robust and universal protocol for single-sample integrative proteomic, metabolomic, and lipidomic analyses. mSystems. 2016;1(3). https://doi.org/10.1128/mSystems.00043-16.
19. Salem MA, Juppner J, Bajdzienko K, Giavalisco P. Protocol: a fast, comprehensive and reproducible one-step extraction method for the rapid preparation of polar and semi-polar metabolites, lipids, proteins, starch and cell wall polymers from a single sample. Plant Methods. 2016;12:45. https://doi.org/10.1186/s13007-016-0146-2.
20. Zhao C, Zhu L, Li R, Wang H, Cai Z. Omics approach reveals metabolic disorders associated with the cytotoxicity of airborne particulate matter in human lung carcinoma cells. Environ Pollut. 2019;246:45–52. https://doi.org/10.1016/j.envpol.2018.11.108.
21. Li Z, Lai ZW, Christiano R, Gazos-Lopes F, Walther TC, Farese RV Jr. Global analyses of selective insulin resistance in hepatocytes caused by palmitate lipotoxicity. Mol Cell Proteomics. 2018;17(5):836–49. https://doi.org/10.1074/mcp.RA117.000560.
22. Breitkopf SB, Ricoult SJH, Yuan M, Xu Y, Peake DA, Manning BD et al. A relative quantitative positive/negative ion switching method for untargeted lipidomics via high resolution LC-MS/MS from any biological source. Metabolomics. 2017;13(3). https://doi.org/10.1007/s11306-016-1157-8.

23. Kumar Y, Dholakia BB, Panigrahi P, Kadoo NY, Giri AP, Gupta VS. Metabolic profiling of chickpea-Fusarium interaction identifies differential modulation of disease resistance pathways. Phytochemistry. 2015;116:120–9. https://doi.org/10.1016/j.phytochem.2015.04.001.
24. Korwar AM, Vannuruswamy G, Jagadeeshaprasad MG, Jayaramaiah RH, Bhat S, Regin BS, et al. Development of diagnostic fragment ion library for glycated peptides of human serum albumin: targeted quantification in prediabetic, diabetic, and microalbuminuria plasma by parallel reaction monitoring, SWATH, and MS^E. Mol Cell Proteomics. 2015;14(8):2150–9. https://doi.org/10.1074/mcp.M115.050518.
25. Koch A, Schlemmer T, Höfle L, Werner B, Preußer C, Hardt M et al. Host-induced gene silencing involves transfer of dsRNA-derived siRNA via extracellular vesicles. bioRxiv. 2020:2020.02.12.945154. https://doi.org/10.1101/2020.02.12.945154.
26. Chong J, Soufan O, Li C, Caraus I, Li S, Bourque G et al. MetaboAnalyst 4.0: towards more transparent and integrative metabolomics analysis. Nucleic Acids Res. 2018;46(W1):W486-W94. doi:https://doi.org/10.1093/nar/gky310.
27. Jha P, McDevitt MT, Halilbasic E, Williams EG, Quiros PM, Gariani K et al. Genetic regulation of plasma lipid species and their association with metabolic phenotypes. Cell Syst. 2018;6(6):709–21 e6. https://doi.org/10.1016/j.cels.2018.05.009.
28. Jha P, McDevitt MT, Gupta R, Quiros PM, Williams EG, Gariani K et al. Systems analyses reveal physiological roles and genetic regulators of liver lipid species. Cell Syst. 2018;6(6):722–33 e6. https://doi.org/10.1016/j.cels.2018.05.016.
29. Xia J, Wishart DS. MetPA: a web-based metabolomics tool for pathway analysis and visualization. Bioinformatics. 2010;26(18):2342–4. https://doi.org/10.1093/bioinformatics/btq418.
30. Mi H, Muruganujan A, Huang X, Ebert D, Mills C, Guo X et al. Protocol update for large-scale genome and gene function analysis with the PANTHER classification system (v.14.0). Nat Protoc. 2019;14(3):703–21. https://doi.org/10.1038/s41596-019-0128-8.
31. Maere S, Heymans K, Kuiper M. BiNGO: a Cytoscape plugin to assess overrepresentation of gene ontology categories in biological networks. Bioinformatics. 2005;21(16):3448–9. https://doi.org/10.1093/bioinformatics/bti551.
32. Kazi RS, Banarjee RM, Deshmukh AB, Patil GV, Jagadeeshaprasad MG, Kulkarni MJ. Glycation inhibitors extend yeast chronological lifespan by reducing advanced glycation end products and by back regulation of proteins involved in mitochondrial respiration. J Proteomics. 2017;156:104–12. https://doi.org/10.1016/j.jprot.2017.01.015.
33. Matyash V, Liebisch G, Kurzchalia TV, Shevchenko A, Schwudke D. Lipid extraction by methyl-tert-butyl ether for high-throughput lipidomics. J Lipid Res. 2008;49(5):1137–46. https://doi.org/10.1194/jlr.D700041-JLR200.
34. Coman C, Solari FA, Hentschel A, Sickmann A, Zahedi RP, Ahrends R. Simultaneous metabolite, protein, lipid extraction (SIMPLEX): a combinatorial multimolecular omics approach for systems biology. Mol Cell Proteomics. 2016;15(4):1453–66. https://doi.org/10.1074/mcp.M115.053702.
35. Yao CH, Liu GY, Yang K, Gross RW, Patti GJ. Inaccurate quantitation of palmitate in metabolomics and isotope tracer studies due to plastics. Metabolomics. 2016;12. doi:https://doi.org/10.1007/s11306-016-1081-y.
36. Garikapati V, Karnati S, Bhandari DR, Baumgart-Vogt E, Spengler B. High-resolution atmospheric-pressure MALDI mass spectrometry imaging workflow for lipidomic analysis of late fetal mouse lungs. Sci Rep. 2019;9(1):3192. https://doi.org/10.1038/s41598-019-39452-3.
37. Karnati S, Garikapati V, Liebisch G, Van Veldhoven PP, Spengler B, Schmitz G, et al. Quantitative lipidomic analysis of mouse lung during postnatal development by electrospray ionization tandem mass spectrometry. PLoS ONE. 2018;13(9): e0203464. https://doi.org/10.1371/journal.pone.0203464.
38. Xu LN, Wang XY, Jiao YP, Liu XH. Assessment of potential false positives via orbitrap-based untargeted lipidomics from rat tissues. Talanta. 2018;178:287–93.
39. Narvaez-Rivas M, Zhang QB. Comprehensive untargeted lipidomic analysis using core-shell C30 particle column and high field orbitrap mass spectrometer. J Chromatogr A. 2016;1440:123–34.
40. Merrill AH Jr. Sphingolipid and glycosphingolipid metabolic pathways in the era of sphingolipidomics. Chem Rev. 2011;111(10):6387–422. https://doi.org/10.1021/cr2002917.
41. Pettus BJ, Baes M, Busman M, Hannun YA, Van Veldhoven PP. Mass spectrometric analysis of ceramide perturbations in brain and fibroblasts of mice and human patients with peroxisomal disorders. Rapid Commun Mass Spectrom. 2004;18(14):1569–74. doi:https://doi.org/10.1002/rcm.1520.
42. Miyazaki C, Saitoh M, Itoh M, Yamashita S, Miyagishi M, Takashima S, et al. Altered phospholipid molecular species and glycolipid composition in brain, liver and fibroblasts of Zellweger syndrome. Neurosci Lett. 2013;552:71–5. https://doi.org/10.1016/j.neulet.2013.07.045.
43. Hama K, Nagai T, Nishizawa C, Ikeda K, Morita M, Satoh N, et al. Molecular species of phospholipids with very long chain fatty acids in skin fibroblasts of Zellweger syndrome. Lipids. 2013;48(12):1253–67. https://doi.org/10.1007/s11745-013-3848-5.
44. Herzog K, Pras-Raves ML, Vervaart MA, Luyf AC, van Kampen AH, Wanders RJ, et al. Lipidomic analysis of fibroblasts from Zellweger spectrum disorder patients identifies disease-specific phospholipid ratios. J Lipid Res. 2016;57(8):1447–54. https://doi.org/10.1194/jlr.M067470.
45. Saitoh M, Sakakihara Y, Mizuguchi M, Itoh M, Takashima S, Iwamori M, et al. Increase of ceramide monohexoside and dipalmitoyl glycerophospholipids in the brain of Zellweger syndrome. Neurosci Lett. 2007;417(2):165–70. https://doi.org/10.1016/j.neulet.2007.01.083.
46. Nagura M, Saito M, Iwamori M, Sakakihara Y, Igarashi T. Alterations of fatty acid metabolism and membrane fluidity in peroxisome-defective mutant ZP102 cells. Lipids. 2004;39(1):43–50. https://doi.org/10.1007/s11745-004-1200-z.
47. Wangler MF, Hubert L, Donti TR, Ventura MJ, Miller MJ, Braverman N, et al. A metabolomic map of Zellweger spectrum disorders reveals novel disease biomarkers. Genet Med. 2018;20(10):1274–83. https://doi.org/10.1038/gim.2017.262.
48. Dudek J. Role of cardiolipin in mitochondrial signaling pathways. Front Cell Dev Biol. 2017;5:90. https://doi.org/10.3389/fcell.2017.00090.
49. Baumgart E, Vanhorebeek I, Grabenbauer M, Borgers M, Declercq PE, Fahimi HD, et al. Mitochondrial alterations caused by defective peroxisomal biogenesis in a mouse model for Zellweger syndrome (PEX5 knockout mouse). Am J Pathol. 2001;159(4):1477–94. https://doi.org/10.1016/S0002-9440(10)62534-5.
50. Claypool SM, Koehler CM. The complexity of cardiolipin in health and disease. Trends Biochem Sci. 2012;37(1):32–41. https://doi.org/10.1016/j.tibs.2011.09.003.
51. Herzog K, Pras-Raves ML, Ferdinandusse S, Vervaart MAT, Luyf ACM, van Kampen AHC, et al. Functional characterisation of peroxisomal beta-oxidation disorders in fibroblasts using lipidomics. J Inherit Metab Dis. 2018;41(3):479–87. https://doi.org/10.1007/s10545-017-0076-9.
52. Ferdinandusse S, Denis S, Mooijer PA, Zhang Z, Reddy JK, Spector AA, et al. Identification of the peroxisomal beta-oxidation

enzymes involved in the biosynthesis of docosahexaenoic acid. J Lipid Res. 2001;42(12):1987–95.
53. Janssen A, Baes M, Gressens P, Mannaerts GP, Declercq P, Van Veldhoven PP. Docosahexaenoic acid deficit is not a major pathogenic factor in peroxisome-deficient mice. Lab Invest. 2000;80(1):31–5. doi:https://doi.org/10.1038/labinvest.3780005.
54. Martinez M. Abnormal profiles of polyunsaturated fatty acids in the brain, liver, kidney and retina of patients with peroxisomal disorders. Brain Res. 1992;583(1–2):171–82. https://doi.org/10.1016/s0006-8993(10)80021-6.
55. Itoyama A, Honsho M, Abe Y, Moser A, Yoshida Y, Fujiki Y. Docosahexaenoic acid mediates peroxisomal elongation, a prerequisite for peroxisome division. J Cell Sci. 2012;125(Pt 3):589–602. https://doi.org/10.1242/jcs.087452.
56. Abe Y, Honsho M, Nakanishi H, Taguchi R, Fujiki Y. Very-long-chain polyunsaturated fatty acids accumulate in phosphatidylcholine of fibroblasts from patients with Zellweger syndrome and acyl-CoA oxidase1 deficiency. Biochim Biophys Acta. 2014;1841(4):610–9. https://doi.org/10.1016/j.bbalip.2014.01.001.
57. Dorninger F, Brodde A, Braverman NE, Moser AB, Just WW, Forss-Petter S, et al. Homeostasis of phospholipids—the level of phosphatidylethanolamine tightly adapts to changes in ethanolamine plasmalogens. Biochim Biophys Acta Mol Cell Biol Lipids. 2015;1851(2):117–28. https://doi.org/10.1016/j.bbalip.2014.11.005.
58. Yagita Y, Shinohara K, Abe Y, Nakagawa K, Al-Owain M, Alkuraya FS, et al. Deficiency of a retinal dystrophy protein, acyl-CoA binding domain-containing 5 (ACBD5), impairs peroxisomal beta-oxidation of very-long-chain fatty acids. J Biol Chem. 2017;292(2):691–705. https://doi.org/10.1074/jbc.M116.760090.
59. Herzog K, Pras-Raves ML, Ferdinandusse S, Vervaart MAT, Luyf ACM, van Kampen AHC, et al. Plasma lipidomics as a diagnostic tool for peroxisomal disorders. J Inherit Metab Dis. 2018;41(3):489–98. https://doi.org/10.1007/s10545-017-0114-7.
60. Chen C, Wang H, Chen B, Chen D, Lu C, Li H, et al. Pex11a deficiency causes dyslipidaemia and obesity in mice. J Cell Mol Med. 2019;23(3):2020–31. https://doi.org/10.1111/jcmm.14108.
61. Wangler MF, Chao YH, Bayat V, Giagtzoglou N, Shinde AB, Putluri N, et al. Peroxisomal biogenesis is genetically and biochemically linked to carbohydrate metabolism in Drosophila and mouse. PLoS Genet. 2017;13(6): e1006825. https://doi.org/10.1371/journal.pgen.1006825.
62. Gasmi L, McLennan AG. The mouse Nudt7 gene encodes a peroxisomal nudix hydrolase specific for coenzyme A and its derivatives. Biochem J. 2001;357(Pt 1):33–8. https://doi.org/10.1042/0264-6021:3570033.
63. Song J, Baek IJ, Chun CH, Jin EJ. Dysregulation of the NUDT7-PGAM1 axis is responsible for chondrocyte death during osteoarthritis pathogenesis. Nat Commun. 2018;9(1):3427. https://doi.org/10.1038/s41467-018-05787-0.
64. Cho YM, Bae SH, Choi BK, Cho SY, Song CW, Yoo JK, et al. Differential expression of the liver proteome in senescence accelerated mice. Proteomics. 2003;3(10):1883–94. https://doi.org/10.1002/pmic.200300562.
65. Schollenberger L, Gronemeyer T, Huber CM, Lay D, Wiese S, Meyer HE, et al. RhoA regulates peroxisome association to microtubules and the actin cytoskeleton. PLoS ONE. 2010;5(11): e13886. https://doi.org/10.1371/journal.pone.0013886.
66. Marelli M, Smith JJ, Jung S, Yi E, Nesvizhskii AI, Christmas RH, et al. Quantitative mass spectrometry reveals a role for the GTPase Rho1p in actin organization on the peroxisome membrane. J Cell Biol. 2004;167(6):1099–112. https://doi.org/10.1083/jcb.200404119.

2.2 Supporting information related to publication 1

Table S4 Filters applied in LipidSearch software (v4.2.23) to remove/minimize false positives after the alignment process

Rej = false and ({MainGrade[c]}.in ("A", "B", "C") or {MainGrade[s1]}.in ("A", "B", "C") or {MainGrade[s2]}.in ("A", "B", "C")) and

((Class = "Cer"	and (MainIon = "+H" or MainIon = "+HCOO"))	or
(Class = "CerP"	and (MainIon = "+H" or MainIon = "+HCOO"))	or
(Class = "Hex1Cer"	and (MainIon = "+H" or MainIon = "+HCOO"))	or
(Class = "Hex2Cer"	and (MainIon = "+H" or MainIon = "+HCOO"))	or
(Class = "Hex3Cer"	and (MainIon = "+H" or MainIon = "+HCOO"))	or
(Class = "SPH"	and (MainIon = "+H" or MainIon = "+H-H_2O"))	or
(Class = "SPHP"	and (MainIon = "+H" or MainIon = "+H-H_2O"))	or
(Class = "ChE"	and (MainIon = "+NH_4" or MainIon = "+H-H_2O"))	or
(Class = "PIP"	and (MainIon = "+Na" or MainIon = "-H"))	or
(Class = "PIP2"	and (MainIon = "+Na" or MainIon = "-H"))	or
(Class = "SM"	and MainIon = "+H")	or
(Class = "MG"	and MainIon = "+H")	or
(Class = "AEA"	and MainIon = "+NH_4")	or
(Class = "CerG2GNAc1"	and (MainIon = "+H" or MainIon = "-H" or MainIon = "+H-H_2O"))	or
(Class = "OAHFA"	and MainIon = "-H")	or
(Class = "PEt"	and (MainIon = "+H" or MainIon = "-H"))	or
(Class = "PMe"	and (MainIon = "+H" or MainIon = "-H"))	or
(Class = "GM3"	and (MainIon = "+H" or MainIon = "-H"))	or
(Class = "GM2"	and (MainIon = "+H" or MainIon = "-H"))	or
(Class = "ST"	and (MainIon = "+H" or MainIon = "-H"))	or
(Class = "FA"	and MainIon = "-H"))	or

Rej = false and ({MainGrade[c]}.in ("A", "B") or {MainGrade[s1]}.in ("A", "B") or {MainGrade[s2]}.in ("A", "B")) and

((Class = "Co"	and (MainIon = "+NH_4" or MainIon = "+H"))	or
(Class = "DG"	and (MainIon = "+NH_4" or MainIon = "+Na"))	or

(Class = "TG"	and MainIon = "+NH_4")	or
(Class = "AcCa"	and MainIon = "+H")	or
(Class = "CL"	and MainIon = "-H")	or
(Class = "DLCL"	and MainIon = "-H")	or
(Class = "MLCL"	and MainIon = "-H")	or
(Class = "LPA"	and MainIon = "-H")	or
(Class = "PA"	and MainIon = "-H")	or
(Class = "LdMePE"	and (MainIon = "+H" or MainIon = "-H"))	or
(Class = "dMePE"	and (MainIon = "+H" or MainIon = "-H"))	or
(Class = "LPC"	and (MainIon = "+H" or MainIon = "+HCOO"))	or
(Class = "PC"	and (MainIon = "+H" or MainIon = "+HCOO"))	or
(Class = "LPE"	and (MainIon = "+H" or MainIon = "-H"))	or
(Class = "PE"	and (MainIon = "+H" or MainIon = "-H"))	or
(Class = "LPG"	and (MainIon = "+NH_4" or MainIon = "-H"))	or
(Class = "PG"	and (MainIon = "+NH_4" or MainIon = "-H"))	or
(Class = "LPI"	and (MainIon = "+NH_4" or MainIon = "-H"))	or
(Class = "PI"	and (MainIon = "+NH_4" or MainIon = "-H"))	or
(Class = "LPS"	and (MainIon = "+H" or MainIon = "-H"))	or
(Class = "PS"	and (MainIon = "+H" or MainIon = "-H")))	

LipidSearch software (v4.2.23) parameters

Search/Identification parameters

Database – General and HCD; Search Type – Product; Experiment Type – LC-MS; Parent Tolerance – 0.1 Da; NL/Prec Tol – 0.5 Da; Precursor Tolerance (MS) – 5.0 ppm; Product (MS/MS) Tolerance – 5.0 ppm; Merge Range (Min) – 0.0; Minimal Peak Width (min) – 0.0; Threshold Type – Relative; Product Ion – 1.0%; m-score threshold – 2.0; Recalculate Isotope – ON; R.T. Interval (min) – 0.0; Execute Quantitation – ON; *m/z* Tolerance – -5.0/+5.0; Tolerance Type – ppm; R.T. range (min) – -0.5/+0.5; Top rank filter – ON; Main Node Filter – Main Isomer Peak; m-Score Threshold (Display) – 5.0; C-Score Threshold (Display) – 2.0; Fatty Acid Priority (FA Priority) – ON; ID Quality Filter – (A, B, C, D); Adducts – (in positive-ion mode) +H, +NH_4, +Na, +K, +H-H_2O, +H-2H_2O, +2H; Adducts – (in negative-ion mode) -H, +HCOO, -CH_3, -2H

Alignment parameters

Search Type – Product; Experiment Type – LC-MS; Alignment Method – Mean; R.T. Tolerance – 0.25; Calculate Unassigned Peak Area – ON; Filter Type – New Filter; Top rank Filter – ON; Main Node Filter – All isomer peaks; m-score threshold – 5.0; ID Quality – A, B and/or C

Fragmentation grade/Identification level

Grade A: Lipid class and fatty acyl chains (FAs) were completely identified

Grade B: Lipid class and some FAs were identified

Grade C: Lipid class or FAs were identified

Grade D: Lipids identified based on neutral losses (e.g. H_2O)

Abbreviations

AEA: N-Acylethanolamine; AcCa: Acylcarnitines or Carnitine esters; CL: Cardiolipin; Cer: Ceramide; CerG2GNAc1, Hex1Cer, Hex2Cer and Hex3Cer: Simple Glc series; CerP: Ceramides phosphate; ChE: Cholesteryl esters and/or Cholesterol; Co: Coenzyme; DG: Diglyceride; DLCL: Cardiolipin (dilyso); FA: Fatty acid and/or Fatty acyl chain; GM2 and GM3: Gangliosides; LPA: Lysophosphatidic acid; LPC: Lysophosphatidylcholine; LPE: Lysophosphatidylethanolamine; LPG: Lysophosphatidylglycerol; LPI: Lysophosphatidylinositol; LPS: Lysophosphatidylserine; LdMePE: Lysodimethylphosphatidylethanolamine; MG: Monoglyceride; MLCL: Cardiolipin (monolyso); OAHFA: OAcyl-(gamma-hydroxy) fatty acid; PA: Phosphatidic acid; PC: Phosphatidylcholine; PE: Phosphatidylethanolamine; PEt: Phosphatidylethanol; PG: Phosphatidylglycerol; PI: Phosphatidylinositol; PIP: Phosphatidylinositol phosphate; PIP2: Phosphatidylinositol bisphosphate; PMe: Phosphatidylmethanol; PS: Phosphatidylserine; SM: Sphingomyelin; SPH: Sphingosine; SPHP: Sphingosine phosphate; ST: Sulfatide; TG: Triglyceride; dMePE: Dimethylphosphatidylethanolamine; C: Wild type control; S1: *Pex11α* knockout; S2: Pooled sample; Ion-adducts: +H, +Na, $+NH_4$, $+H-H_2O$, +HCOO and –H; m-score: Fragmentation match score; HCD: Higher-energy collisional dissociation; RT: Retention time

References

1. Peake DA et al., Processing of a complex lipid dataset for the NIST inter-laboratory comparison exercise for lipidomics measurements in human serum and plasma. ASMS 2015 Poster
2. Kiyonami R, Peake DA et al., Large scale lipid profiling of a human serum lipidome using a high-resolution accurate-mass LC/MS/MS approach. LIPID MAPS Annual Meeting 2015 Poster
3. Breitkopf SB, Ricoult SJH, Yuan M, Xu Y, Peake DA, Manning BD et al., A relative quantitative positive/negative ion switching method for untargeted lipidomics via high-resolution LC-MS/MS from any biological source. Metabolomics. 2017;13(3)
4. Li Z, Lai ZW, Christiano R, Gazos-Lopes F, Walther TC, Farese RV, Jr. Global analyses of selective insulin resistance in hepatocytes caused by palmitate lipotoxicity. Mol Cell Proteomics. 2018;17(5):836-49

Fig. S2 Genotypes of animals were determined by polymerase chain reaction as described previously[1]. Wild type (e.g. 88657) allele (*Pex11α*$^{+/+}$) is amplified by primer 10 (5′-AATCAGGGACCTGTGCAACCTG-3′) and primer 11 (5′-AGTACAGCGTGGCTAATGAAGAGAC-3′). Homozygous peroxisomal biogenesis factor 11α knockout (e.g. 88658 and 88659) allele (*Pex11α*$^{-/-}$) is amplified by primer 10 (5′-AATCAGGGACCTGTGCAACCTG-3′) and Neo primer (5′-ATATTGCTGAAGAGCTTGGCGGC-3′). Both bands (e.g. POSKTR) amplified for heterozygous animals (*Pex11α*$^{+/-}$)

Reference

1. Li X, Baumgart E, Dong GX, Morrell JC, Jimenez-Sanchez G, Valle D, et al., PEX11alpha is required for peroxisome proliferation in response to 4-phenylbutyrate but is dispensable for peroxisome proliferator-activated receptor alpha-mediated peroxisome proliferation. Mol Cell Biol. 2002;22(23):8226-40

(a) Lipidomics data

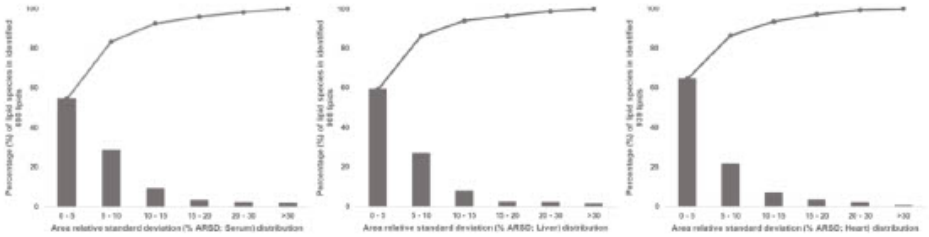

(b) Metabolomics data

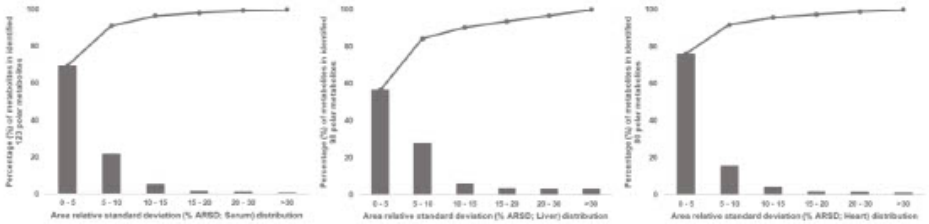

(c) Proteomics data

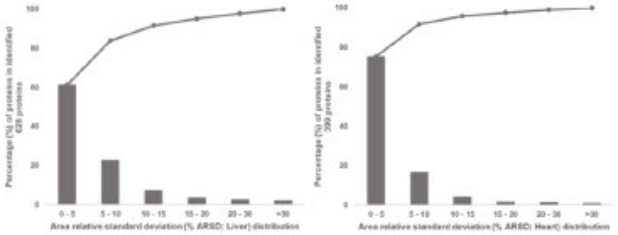

Fig. S3 The distributions of the area relative standard deviation (% ARSD) values for each identified lipid, polar metabolite and protein in serum, liver and heart tissue homogenates across all replicates

(a)

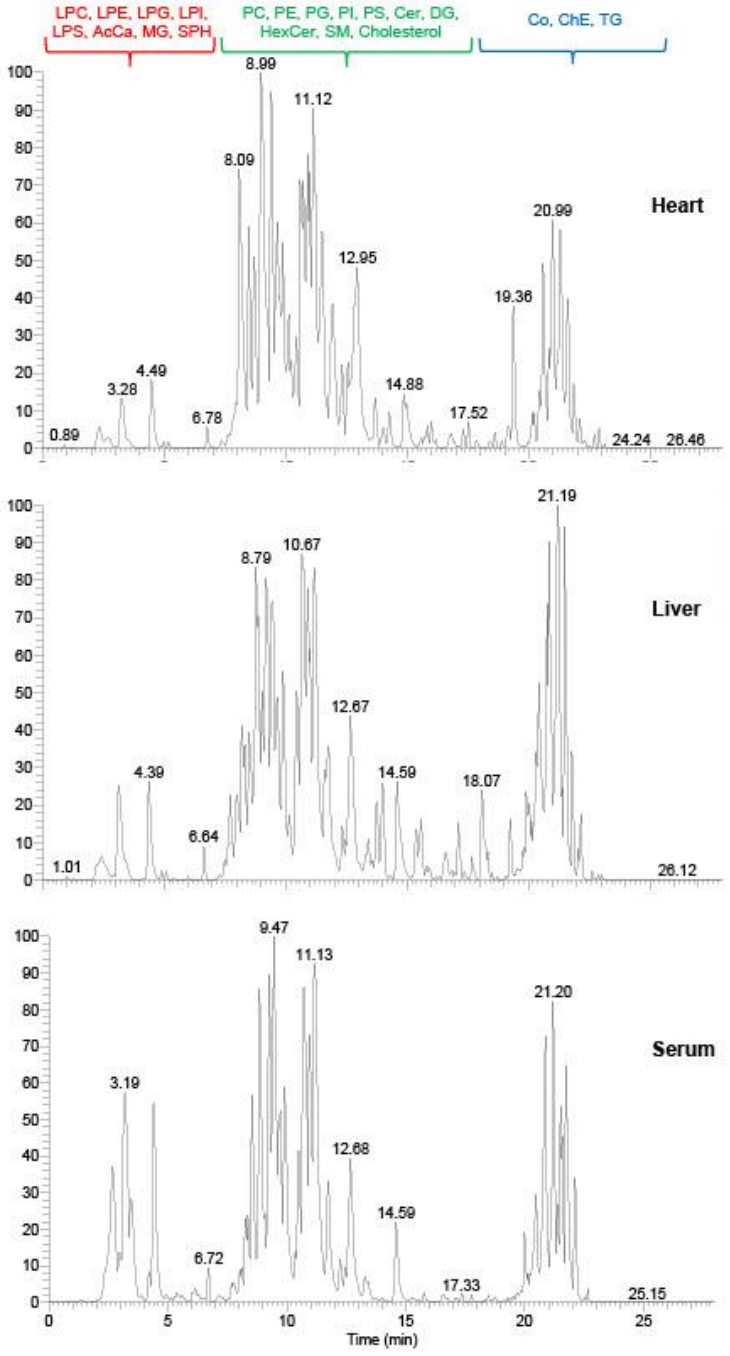

Fig. S4 a) Base peak chromatograms of the mouse heart, liver and serum lipidome extracted by MeOH/MTBE/H_2O liquid-liquid extraction method in positive-ion mode

(b)

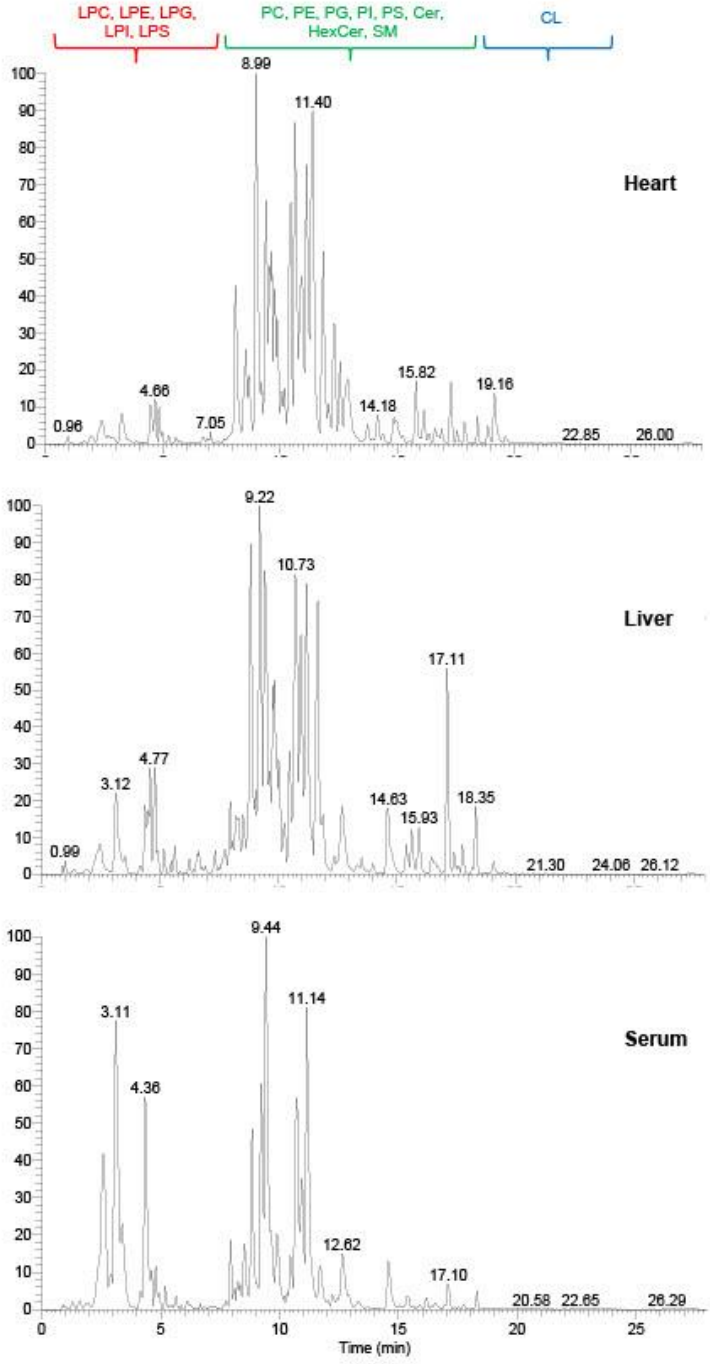

Fig. S4 b) Base peak chromatograms of the mouse heart, liver and serum lipidome extracted by MeOH/MTBE/H_2O liquid-liquid extraction method in negative-ion mode

Serum lipidome

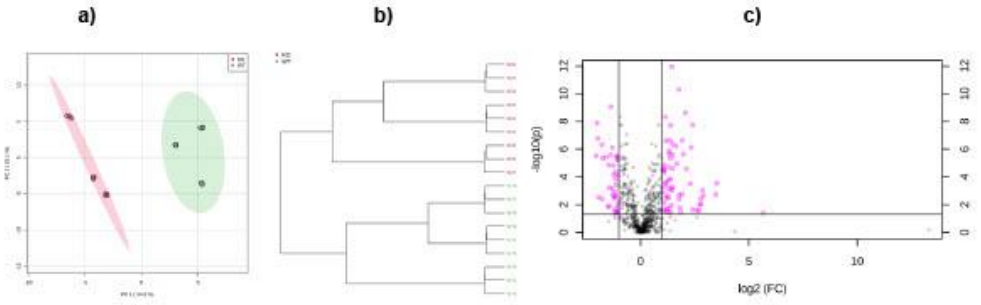

Heart lipidome

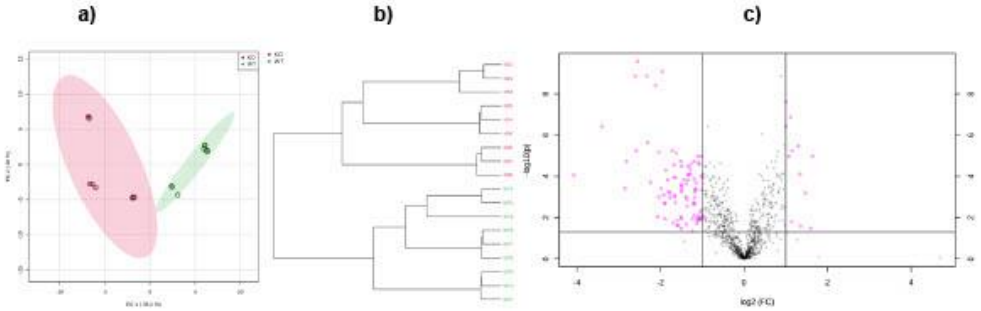

Liver lipidome

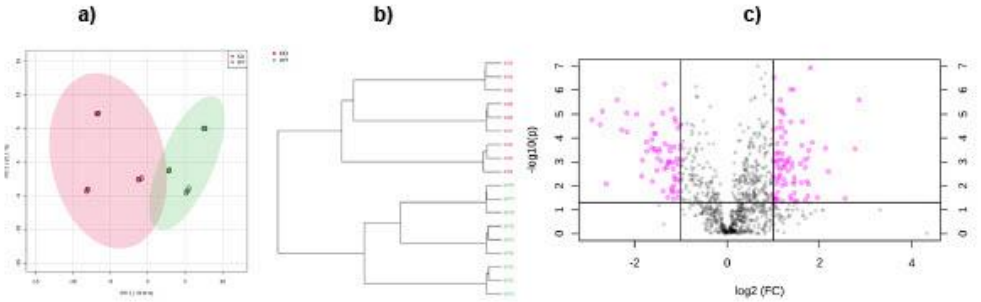

Fig. S6 a) Principal component analysis (PCA), b) hierarchical clustering analysis (HCA; dendrogram), and c) volcano plots (log2 fold changes versus -log10 FDR adjusted p-values) analyses of lipidomics data (combined positive- and negative-ion mode data from three biological replicates and technical triplicates) obtained from WT control and *Pex11α* KO mouse serum, heart and liver tissue homogenates

Serum metabolome

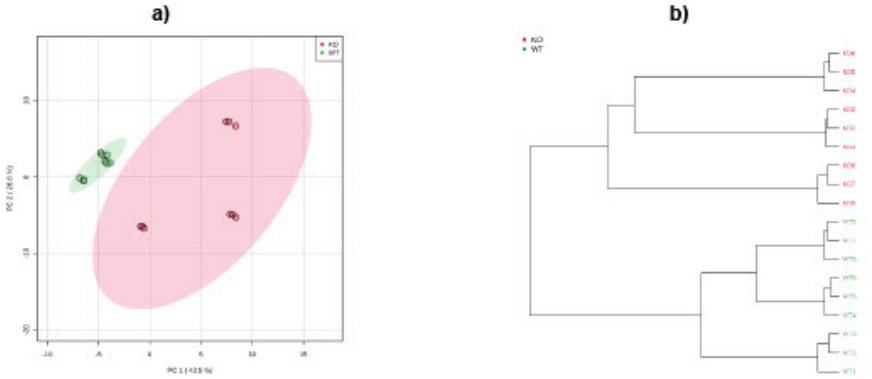

Liver metabolome

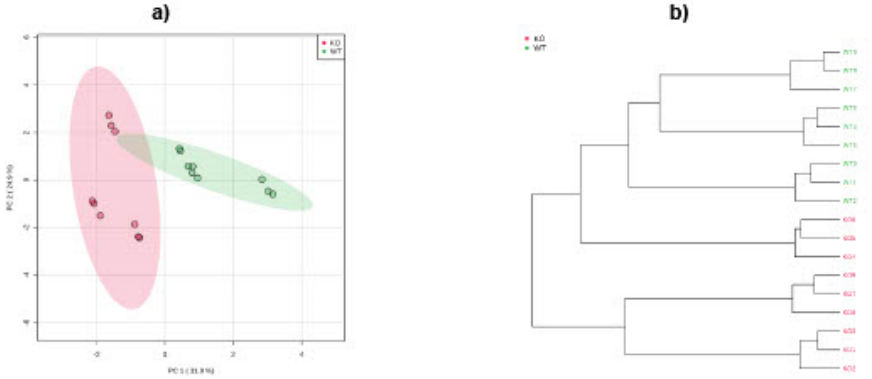

Heart metabolome

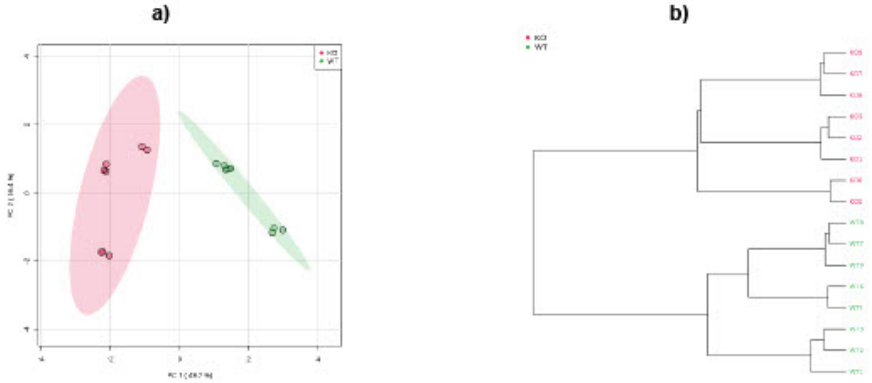

Fig. S7 a) Principal component analysis (PCA), b) hierarchical clustering analysis (HCA; dendrogram) of metabolomics data (combined positive- and negative-ion mode data from three biological replicates and technical triplicates) obtained from WT control and *Pex11α* KO mouse serum, liver and heart tissue homogenates

CHAPTER III

Publication 2

High-resolution atmospheric-pressure MALDI mass spectrometry imaging workflow for lipidomic analysis of late fetal mouse lungs

Vannuruswamy Garikapati, Srikanth Karnati, Dhaka Ram Bhandari, Eveline Baumgart-Vogt, Bernhard Spengler

Published in Scientific Reports, 2019;9(1):3192

DOI: 10.1038/s41598-019-39452-3

Supporting information: https://www.nature.com/articles/s41598-019-39452-3#Sec21

SCIENTIFIC REPORTS

OPEN

High-resolution atmospheric-pressure MALDI mass spectrometry imaging workflow for lipidomic analysis of late fetal mouse lungs

Received: 6 July 2018
Accepted: 17 January 2019
Published online: 28 February 2019

Vannuruswamy Garikapati[1,2], Srikanth Karnati[2,3], Dhaka Ram Bhandari[1], Eveline Baumgart-Vogt[2] & Bernhard Spengler[1]

Mass spectrometry imaging (MSI) provides label-free, non-targeted molecular and spatial information of the biomolecules within tissue. Lipids play important roles in lung biology, e.g. as surfactant, preventing alveolar collapse during normal and forced respiration. Lipidomic characterization of late fetal mouse lungs at day 19 of gestation (E19) has not been performed yet. In this study we employed high-resolution atmospheric pressure scanning microprobe matrix-assisted laser desorption/ionization MSI for the lipidomic analysis of E19 mouse lungs. Molecular species of different lipid classes were imaged in E19 lung sections at high spatial and mass resolution in positive- and negative-ion mode. Lipid species were characterized based on accurate mass and on-tissue tandem mass spectrometry. In addition, a dedicated sample preparation protocol, homogenous deposition of matrices on tissue surfaces and data processing parameters were optimized for the comparison of signal intensities of lipids between different tissue sections of E19 lungs of wild type and *Pex11β*-knockout mice. Our study provides lipid information of E19 mouse lungs, optimized experimental and data processing strategies for the direct comparison of signal intensities of metabolites (lipids) among the tissue sections from MSI experiments. To best of our knowledge, this is the first MSI and lipidomic study of E19 mouse lungs.

Lipids are versatile biologically active compounds involved in important physiological and pathological processes. Lipids are the structural integral components of the cell membranes, function as signalling molecules in various cellular cascades, and support energy homeostasis, based on a huge diversity of lipid species with unique physico-chemical properties[1,2]. Disruption or imbalance in lipid composition or metabolism lead to various metabolic disorders such as diabetes, obesity, atherosclerosis, or infectious and neurodegenerative diseases[3].

Lipid composition varies significantly from organ to organ and even differs within the various cells of an organ[4]. For example, the lung is composed of more than 40 different cell types and each cell shows a distinct lipid distribution pattern[5–7]. Furthermore, type-II pneumocytes - also called alveolar epithelial cells type II (AECII) - synthesize and secrete via exocytosis a complex mixture of lipids and proteins into the alveolar space, forming the pulmonary surfactant[8,9]. One of the major functions of the surfactant lipids is to reduce the surface tension at the air-liquid interface, and thereby decrease the tendency of alveolar collapse during end-expiration[9,10].

In fact, lipids account for up to 20% of dry weight of the lung tissue[4]. These lipids are vital in the lung and participate in many cellular functions. Especially, they (1) neutralize free radicals and reactive oxygen species[11], (2) protect lungs from inhaled particles and pathogenic micro-organisms[12], (3) act as a potent antiviral agent[13–15] and (4) are involved as biologically active secondary lipid messengers in the regulation of lung inflammation[16]. Indeed, abnormalities in pulmonary lipid/surfactant composition and/or metabolism are closely associated with various pulmonary diseases such as respiratory distress syndrome[17], hyaline membrane disease[18], asthma[19], chronic obstructive pulmonary disease[20], bronchiolitis[21], cystic fibrosis[22], pneumonia[23], interstitial lung diseases[24], lung injury[25] and cancer[26].

[1]Institute of Inorganic and Analytical Chemistry, Justus Liebig University Giessen, Giessen, Germany. [2]Institute for Anatomy and Cell Biology II, Division of Medical Cell Biology, Justus Liebig University Giessen, Giessen, Germany. [3]Present address: Institute for Anatomy and Cell Biology, Julius Maximilians University Würzburg, Würzburg, Germany. Correspondence and requests for materials should be addressed to B.S. (email: Bernhard.Spengler@anorg.chemie.uni-giessen.de)

Several studies have analyzed the pulmonary lipid composition of different mammalian species in normal and diseased states[4,6]. The most widely used methods for lipid analysis are hyphenated analytical techniques such as liquid chromatography or gas chromatography coupled to mass spectrometry. Matrix-assisted laser desorption/ionization mass spectrometry imaging (MALDI MSI) is a prominent, sensitive analytical tool, which provides molecular information and spatial distribution of the analytes directly from the biological specimens. MSI has received increasing attention, since (1) labelling is not necessary, (2) hundreds of molecules can be detected in a single measurement and (3) spatial distributions of biomolecules in biological tissues are provided[27]. From its introduction in 1994[28] until to date, this technique has been applied to visualize a broad spectrum of analytes such as lipids[29], proteins[30], peptides[31], metabolites[32], n-linked glycans[33], drugs[34] in various types of samples including mammalian tissues[35], cells[36], plant tissues[37], insects[38] and microbial cultures[39].

A large number of studies utilized MSI techniques in lung biology, to investigate the distribution and quantify drugs in different types of lung cancers[40], in tissues treated with several anti-tuberculosis drugs[41,42] and to molecularly characterize various lung cancers based on their proteomic profiles[43]. MSI has been applied to visualize the major surfactant lipid dipalmitoylphosphatidylcholine [DPPC, (PC32:0)] in human lung[44] and in xenografts from human lung cancer cells[45]. Berry and colleagues developed a modified optical cutting temperature compound as a new inflation and embedding material to map the major phospholipid species in adult mice[46] and in human lungs[7]. Carter and colleagues employed MALDI MSI as a tool for the detection of novel molecular biomarkers in radiation-induced lung injury[47]. In line with these technical developments, three-dimensional (3D) imaging workflows have been developed to visualize phosphatidylcholine (PC) and sphingomyelin (SM) lipid species in entire adult mouse lungs[48].

It is apparent that characterization of molecular information (lipids, metabolites and proteins, etc.) of the lungs in diseased states, during fetal and postnatal stages, is a key to understand the molecular alterations during lung development and the pathogenesis or pathophysiology of various pulmonary diseases, associated with these indispensable biomolecules[49,50]. We recently reported significant stage-specific differences in the individual lipid-species composition of mouse lung during postnatal pulmonary development processes[49]. However, so far no information is available on the lipidome of fetal mouse lungs, from either MSI or liquid chromatography-mass spectrometry.

In this study, high mass accuracy ($\leq$2 ppm), high-resolution in mass (140,000 @ m/z 200) and space (10 µm per pixel) atmospheric pressure scanning microprobe MALDI MSI (AP-SMALDI MSI) was used for the first time to characterize the lipid profile of late fetal mouse lungs at day 19 of gestation (E19) in positive- and negative-ion mode. An optimized sample preparation protocol and data analysis workflow were developed for the reliable and reproducible relative quantification of lipids and other cellular metabolites in different tissue sections. To demonstrate the power of our optimized method for relative comparisons of distinct lung sections with alterations in lipid content, knockout (KO) mice with a peroxisomal biogenesis defect (*Pex11β−/−*) were used in addition to wild type (WT) sections, as an experimental model.

Results and Discussion

MALDI MSI has become a fundamental qualitative and quantitative analytical tool for the analysis of a large variety of substances in biological specimens. The recent technological improvements in MSI such as incorporation of high-resolution accurate mass spectrometers (e.g. orbital trapping mass analyser), higher lateral resolution under close-to-physiological conditions (subcellular level, 1.4 µm spot size)[51], molecular and topographical analysis of 3D surfaces[52] has further advanced the field and its application value. Signal intensities of analytes in MSI depend on several critical parameters, such as sample handling and preparation, tissue thickness, matrix properties (choice of matrix, solvent, application method and local matrix concentration), intercomponent charge competition, spatial resolution, variance in the experimental, instrumental conditions and ion suppression effects[27]. Therefore, to achieve high quality reproducible information from MSI and to compare signal intensities of analytes in a set of tissue sections, a dedicated sample preparation and data analysis strategy within the imaging workflow is mandatory.

In the present study, we established a sample preparation protocol for optimal tissue processing, sectioning and lipid profiling of E19 mouse lungs using high-resolution AP-SMALDI MSI in positive- and negative-ion mode. A detailed data processing framework was optimized to compare the differential expression of cellular metabolites in distinct tissue sections to each other. As an experimental model to eventually show differences in the lipid composition between distinct lung tissue sections at late fetal stage, we analyzed and compared lipids in different lung sections of E19 WT and *Pex11β* KO mice. PEX11 proteins are peroxisomal membrane proteins which consist of three different isoforms (PEX11α, β and γ) in mammals and play an important role in peroxisomal proliferation[53]. *Pex11β* KO animals, which die immediately after birth (neonatal lethality), showed reduced numbers of peroxisomes and severe pathological features of Zellweger syndrome, such as developmental delay, hypotonia, neuronal migration defects and neuronal apoptosis[53,54]. The underlying molecular mechanisms of these pathological alterations in *Pex11β* KO animals are still poorly understood.

Optimized workflow for late fetal mouse lung lipidome using AP-SMALDI MSI. A scheme of an optimized workflow to characterize and compare lipid species directly from tissue sections of different E19 mouse lungs using high-resolution AP-SMALDI MSI is shown in Fig. 1. Briefly, sectioning of E19 mouse lungs, selection for section quality and ideal matching of section thickness, uniform deposition of matrix on tissue surfaces and MSI methodologies were optimized in positive- and negative-ion mode for comprehensive lipid mapping of E19 mouse lungs. E19 WT and *Pex11β* KO mouse lung MSI data sets were acquired individually under identical experimental and instrumental conditions. Thereafter, data sets (.raw) were converted to the common data format for MS imaging (imzML) using the in-house developed "RAW converter" version 1.1.0[55]. The converted WT and *Pex11β* KO imzML files were stitched together using "imzML converter" version 1.3[56], and a detailed data

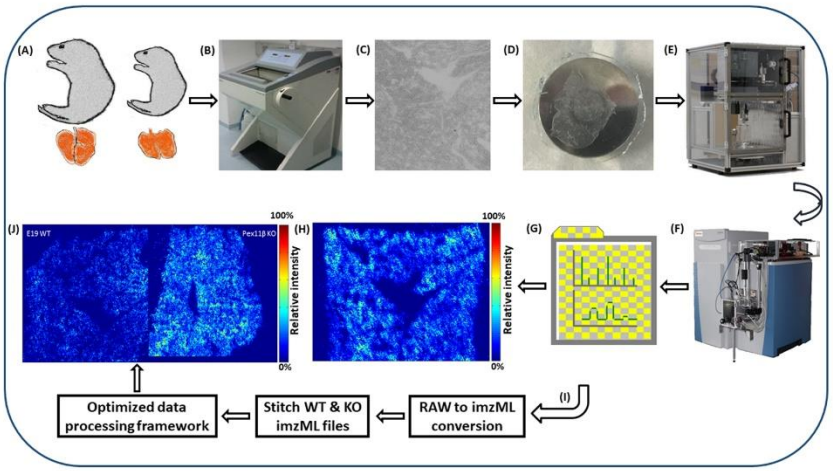

Figure 1. Optimized MSI workflow for characterization and comparative lipidomic analysis of late fetal mouse lung sections at day 19 of gestation (E19) using atmospheric-pressure scanning microprobe matrix-assisted laser desorption/ionization mass spectrometry imaging (AP-SMALDI MSI). (**A**) Breeding of WT and *Pex11β* KO E19 animals[53]. (**B**) Cryosectioning of fresh snap-frozen E19 mouse lung tissues for MSI experiments using a cryomicrotome. (**C**) Optical phase contrast image of a 12 µm thick section of E19 mouse lung and selection of optimal sections. (**D**) Tissue section fixed to the sample probe. (**E**) Homogenous deposition of matrices using an automatic pneumatic ultrafine sprayer ("SMALDIPrep"). (**F**) MSI data acquisition using an "AP-SMALDI10" ion source coupled to a Q Exactive mass spectrometer. (**G**) MSI data sets (.raw files). (**H**) Characterization of E19 (WT) mouse lung lipidome. (**I**) Optimization of the data analysis workflow for comparative lipidomic analysis. (**J**) Comparison of relative signal intensities of lipids between WT and *Pex11β* KO E19 lung tissue sections.

processing framework was optimized for comparative lipidomic analysis of E19 WT and *Pex11β* KO mouse lungs. The individual steps in the optimized workflow are described in the following.

Optimization of late fetal mouse lung tissue sectioning procedure for MSI. Sample preparation is the most crucial step in any MSI experiments. Initially, we obtained tissue sections from PFA-fixed OCT-embedded WT and KO E19 mouse lungs (Fig. S1A), which is the most-common tissue preparation method used for pulmonary histological studies. In general, OCT provides a smooth cutting surface and preserves the tissue architecture[57]. However, OCT contains benzalkonium salts as a preservative which suppress lipid ionization and form adducts with endogenous lipid species[46]. Furthermore, OCT contains polyethylene glycols and polyvinyl alcohol polymers, often causing ion suppression and strong background signals which can severely interfere with MS acquisition and data interpretation. OCT and other polymeric embedding materials are thus not compatible with imaging studies of small molecules (e.g. lipids, metabolites). Carter and colleagues recently demonstrated formalin-fixation via tracheal instillation and fixative inflation of the lung followed by gelatin embedding for lipidomic analysis of larger mammalian (monkey) lungs[58]. However, this method showed loss of phosphatidylethanolamine (PE) and reduced signal intensities of phosphatidylserine (PS) lipid species due to chemical crosslinking of primary amine groups[58,59]. Owing of drawbacks, these methods (e.g. formalin/PFA/agarose inflation and/or embedding with polymeric materials, etc.) are not appropriate to map the complete lipidome of lung tissues using MSI. Therefore, cryosectioning of tissue without using any embedding material is more suitable for MSI, which would aid to map a comprehensive lipidome and/or metabolome without any losses or chemical modifications.

The most challenging part in our approach was the preparation of E19 mouse lung cryosections for the lipid imaging studies. In order to detect all possible distinct lipid classes with less and/or no background signals, fresh frozen lung tissue was mounted with water on tissue holders for cryosectioning. 12 µm thick frozen sections were carefully cut and collected on a glass slide without embedding material. However, we frequently failed to obtain WT and KO tissue sections on a single objective slide for measuring both sections in a single experiment, a procedure which diminishes experimental artefacts in comparative analyses. Due to differences in lung tissue consistency of WT and KO sections, we often observed problems of different section quality on the same objective slide, WT sections sometimes containing a fold, or KO sections being broken several times in longitudinal direction (Fig. S1B). We therefore decided to mount WT and KO tissue sections on different glass slides to be able to select them according to their section quality and thickness. Even though always 12 µm were used as cutting thickness, we frequently observed variations in thickness of subsequent cryosections of the same tissue block of WT animals. These variations were even more pronounced due to the differences of tissue consistency

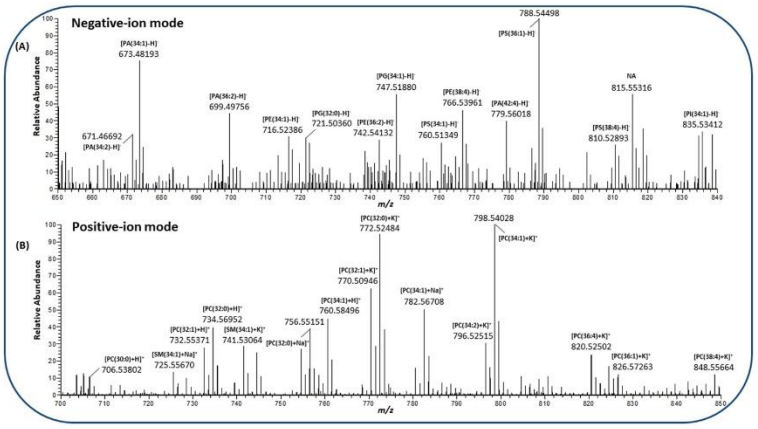

Figure 2. Single-pixel (10 µm) mass spectrum obtained from late fetal E19 mouse lung mass spectrometry imaging (MSI) experiments. (**A**) Negative-ion single-pixel mass spectrum for mass range *m/z* 650–850. (**B**) Positive-ion single-pixel mass spectrum for mass range *m/z* 700–850. Different classes of lipid species were identified based on high mass accuracy (≤2 ppm), labelled with measured mass and charge carrier.

between WT and KO animals (Fig. S1C,D). To check the effects of section thickness on MALDI imaging analysis we intentionally measured sections with distinct section thickness of WT animals. Indeed, we observed a drastic change in signal intensities of lipids between tissue (E19 WT) sections of varying thickness (Fig. S1E,F, data not shown). We therefore tried to develop a quick procedure to select for similar thickness of consecutive sections of WT and KO mice on different glass slides using water (ice) mounted tissue blocks (Fig. S1G,H). We optimized a quick photographic imaging procedure and digitally created full section phase-contrast images of all cut sections (see materials and methods). We then carefully compared grey values reflecting the section thickness and selected similar grey value images of WT and KO tissue sections with optimal tissue quality (criteria mentioned in Fig. S1) for preselection of the best region of interest in comparable tissue areas within images by avoiding tissue foldings and other sectioning artefacts.

Care was also taken that the same lung lobes were used for parallel comparisons, since development and alveolarization is different in apical or basal lung regions[60].

Lipidomic profiling of late fetal mouse lungs with high-resolution AP-SMALDI MSI. After optimization of the tissue sectioning and selection procedure, lipids were characterized by scanning the E19 (WT) lung tissue sections at a high mass resolution (140,000 @ *m/z* 200) and high spatial resolution (10 µm per pixel) using AP-SMALDI MSI. Figure 2A,B represent a single pixel (10 µm) mass spectrum of E19 mouse lungs for the selected *m/z* range in negative- and positive-ion mode. The negative-ion mode analysis of E19 mouse lungs resulted in detection of different classes of lipid deprotonated species (Fig. 2A), whereas in positive-ion mode, mainly PC and SM lipids were observed as protonated, sodiated, or potassiated species (Fig. 2B). In general, PC, SM and ceramide (Cer) lipid species are predominantly ionized and detected in positive-ion mode, due to their quaternary amine groups, suppressing the ionization of other lipid classes. Phosphatidylglycerol (PG), PE, PS, phosphatidic acid (PA) and phosphatidylinositol (PI), on the other hand, are dominant in negative-ion mode[61]. Therefore, to provide comprehensive lipid information of E19 mouse lungs, MSI experiments were performed in both ionization modes.

In positive-ion spectra (Fig. 2B) the most intense lipid signals were observed at *m/z* 772.52484, 798.54028 and annotated as potassiated PC. The signal at *m/z* 772.52484 with a mass error of 0.60 ppm corresponds to potassiated PC(32:0) lipid. PC(32:0) [DPPC; most probably a combination of two saturated palmitic acyl chains] is the major surface-active component (≈40–70% of total PC or ≈30–60% of total surfactant lipid) of the mammalian pulmonary lipidome and is responsible for generating a lower surface tension (close to zero mN/m) during respiration[10,62]. Protonated PC(32:0) at *m/z* 734.56952 (0.12 ppm) and its sodiated homologue at *m/z* 756.55151 (0.18 ppm) were also detected with very high mass accuracy. In addition to DPPC, di-saturated (30:0, 34:0) and mono-unsaturated (32:1, 34:1) PCs, which are the major PC lipid species of mammalian pulmonary surfactant were also observed as intense peaks and detected with three different charge carriers[63]. Sphingomyelins are essential constituents of plasma membranes and are involved in pathogenesis of various pulmonary diseases[64]. Among the sphingomyelins, SM(34:1) was found to be highly abundant and was detected with three different charge carriers (Fig. 2B). Similarly, other individual lipid species, in the low *m/z* range various lysophospholipids were detected with high mass accuracy.

In negative-ion mode (Fig. 2A), important acidic phospholipids such as PG (the second most abundant phospholipid class in lung surfactant), PE (abundant in whole lung tissue), other minor phospholipid classes (PA, PS, PI etc.), cholesterol sulfate and free fatty acids were detected and annotated based on high mass accuracy. For

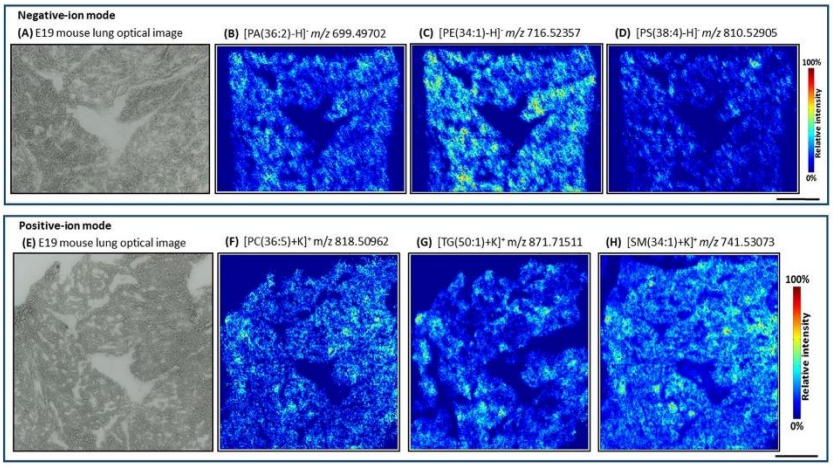

Figure 3. Characterization of late fetal E19 mouse lung lipidome using high-resolution AP-SMALDI mass spectrometry imaging experiments. (**A**,**E**) Microscopic images of E19 mouse lung. (**B**–**D**) Negative-ion MS images. (**B**) $[PA(36:2) - H]^-$, (**C**) $[PE(34:1) - H]^-$, (**D**) $[PS(38:4) - H]^-$. (**F**–**H**) Positive-ion MS images. (**F**) $[PC(36:5) + K]^+$, (**G**) $[TG(50:1) + K]^+$, (**H**) $[SM(34:1) + K]^+$. Scale bar 500 µm.

instance, intense signals at *m/z* 716.52386 (0.27 ppm), 760.51349 (0.13 ppm), 835.53412 (0.11 ppm), 747.51880 (0.80 ppm), 673.48193 (0.74 ppm) were annotated as 34:1 lipid molecular species of PE, PS, PI, PG and PA lipid classes respectively. PG and PI lipids are synthesized from the same precursor (CDP-glycerol) and constitute up to 8–15% of the total surfactant phospholipid pool[10]. They are known to enhance the adsorption and spreading of DPPC over the epithelial surface[63]. The most intense signal in Fig. 2A at *m/z* 788.54498 (0.35 ppm) corresponds to the deprotonated PS(36:1).

Late fetal E19 (WT) mouse lung lipid ion MS images were generated using MSiReader software (jet colour map, linear interpolation of zero order and no normalization). Figure 3 shows selected MS images in negative- and positive-ion mode. Figure 3B–D show negative-ion MS images corresponding to *m/z* 699.49702, 716.52386, 810.52905, annotated as $[PA(36:2) - H]^-$, $[PE(34:1) - H]^-$ and $[PS(38:4) - H]^-$ respectively. Similarly, Fig. 3F–H show positive-ion MS images of *m/z* 818.50962, 871.71511, 741.53064, annotated as $[PC(36:5) + K]^+$, $[TG(50:1) + K]^+$ and $[SM(34:1) + K]^+$. With our high-resolution MSI approach, various classes of phospholipids, glycerolipids, and sphingolipids were imaged and annotated based on accurate mass (RMSE $\leq$2 ppm, Tables S1 & S2, Fig. S2). The majority of the identified lipid species were ubiquitously distributed in the whole E19 mouse lung tissue sections. Due to the dense content of epithelial cells and typical fetal structure of the not yet air-inflated lung tissue, a homogenous lipid distribution pattern (mainly covering the peripheral region) was observed in the respiratory region of the E19 lung (later developing into the alveolar region of the adult lung).

On-tissue tandem mass spectrometry (MS/MS) experiments were performed to confirm the chosen lipid annotations. For instance, on-tissue MS/MS analysis of potassiated SM(34:1) at *m/z* 741.52910 ± 0.4 resulted in diagnostic fragment ions at *m/z* 682.45550 (neutral loss of trimethylamine, 59.0736), *m/z* 558.46357 (neutral loss of phosphocholine, 183.06553), *m/z* 162.95622 (potassiated cyclophosphate, a characteristic fragment ion for potassiated PC and SM), and *m/z* 184.07369 (phosphocholine). Similarly, HCD activation of sodiated SM(34:1) at *m/z* 725.55551 ± 0.4 yielded product ions at *m/z* 666.48207, *m/z* 542.48982 and *m/z* 184.07373. MS/MS analysis of protonated SM(34:1) at *m/z* 703.57337 ± 0.4 produced the predominant fragment ion at *m/z* 184.07373 (phosphocholine).

MS/MS analyses of lipid species in negative-ion mode allowed assignment of individual fatty acyl (FA) chains. For example, fragmentation of $[PE(34:1) - H]^-$ at *m/z* 716.52344 ± 0.4 produced fragment ions at *m/z* 255.23252 (16:0; palmitic acid) and *m/z* at 281.24821 (18:1; oleic acid). On-tissue MS/MS analysis of $[PA(36:2) - H]^-$ at *m/z* 699.49744 ± 0.4 showed an intense fragment ion at *m/z* 281.24843 (18:1; oleic acid). Similarly, different classes of lipid species showed diagnostic fragment ions for the individual lipid class (Table S3 and MS/MS spectra in Supplementary Data). For example, the most intense peak in Fig. 2A, PS(36:1) at *m/z* 788.54397 ± 0.4 yielded a fragment ion at *m/z* 701.51242 (loss of serine, 87.03155) which is characteristic for phosphatidylserine.

Taken together, our optimized method was able to detect and characterize all possible major lipid species from E19 mouse lungs, based on accurate mass and on-tissue MS/MS analysis in positive- and negative-ion mode. This lipidomic information may aid as a reference for the lung lipidome, for a better understanding of late stage fetal lung development and differentiation as well as of the molecular mechanisms of various pulmonary diseases associated with lipid alterations.

Optimization of data processing framework for comparative lipidomics. After lipidomic characterization of E19 (WT) mouse lungs, we optimized and established a data processing framework for the relative comparison of signal intensities of analytes in different tissue sections. A detailed scheme of the proposed data

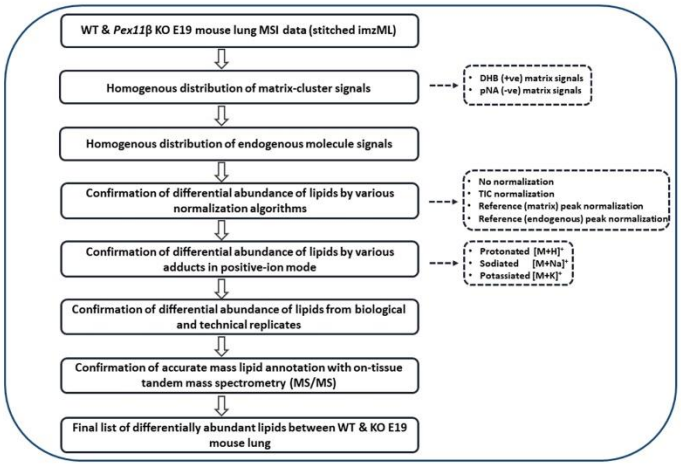

Figure 4. Scheme of the optimized data processing framework.

processing workflow is depicted in Fig. 4. Briefly, equally thick E19 WT and *Pex11β* KO lung tissue sections with optimal morphology were analyzed on consecutive days (biological and technical replicates) with identical sample preparation, experimental and instrumental conditions. The single MS raw files were converted to imzML files and stitched together. Data analysis and optimization of various parameters for the relative quantification of lipids using MALDI MSI is described in the following sections.

Homogenous deposition of matrix. In addition to the tissue quality and thickness of the tissue sections, matrix deposition is another critical parameter in MSI quantification. In order to compare signal intensities of analytes in two different tissue (WT and KO) sections, equal concentration and homogenous deposition of matrix on both tissue sections is necessary. In the present study, we obtained homogenously sprayed matrix crystals on tissue surfaces (crystal size $\leq$10 µm, Fig. S3) by optimizing the flow rate of the spray syringe (10 µl/min), nitrogen gas (1 bar), and rotation speed of the sample probe for pNA and DHB matrices using the SMALDIPrep system in negative- and positive-ion mode. No washing steps were performed before matrix deposition. Homogeneous distribution of pNA and DHB matrix in WT and KO E19 lung tissue sections in negative- and positive-ion mode are illustrated in Figs 5 & S4.

Figure 5A–C show the homogeneous distribution of pNA matrix clusters (A) *m/z* 547.13314 [4(pNA − H)$^-$], (B) *m/z* 427.10077 [3(pNA − H)$^-$ + H_2O] and (C) *m/z* 273.06293 [2(pNA − H)$^-$] between WT and KO tissue sections. Similarly, Fig. 5D–F demonstrate the homogeneous distribution of DHB matrix clusters (D) *m/z* 426.05815 [3DHB-2H_2O]$^-$, (E) *m/z* 755.06451 [5DHB-3H_2O + K]$^+$ and (F) *m/z* 870.15122 [6DHB-4H2O + NH4]$^+$ among WT and KO tissue sections. Uneven matrix deposition and crystallization creates artefacts in MSI, influencing signal intensities of analytes. Therefore, in our study we carefully optimized the matrix application to attain uniform deposition of matrix layers on both WT and KO tissue section surfaces. This enabled us to obtain high-quality and reproducible results from MSI for semi-quantification (relative quantification) of biomolecules. Recently, we showed that pneumatic spraying of matrix increases the lipid signal intensities 8-fold and 30-fold, compared to sublimation-recrystallization and sublimation, respectively[51]. In addition, reproducible MSI data (in terms of number and intensity of ion signals, pixel coverage and image quality) can be obtained from samples prepared by automated pneumatic spraying[51].

In addition to matrix signals, we also detected endogenous molecules that were distributed uniformly in E19 WT and KO lung tissue sections in negative- and positive-ion mode. For instance, Fig. 6A–C) show even distribution of PE-Cer(36:1), PE(32:0) and CerP(34:1) at *m/z* 687.54465, 690.50793 and 616.47115 in negative-ion mode. Similarly, Fig. 6D–F) show positive-ion MS images of *m/z* 780.49386, 762.50458, 738.50443, corresponding to potassiated PE(36:3), sodiated PE(36:4) and sodiated PE(34:2), respectively. Uniform distributions of these endogenous molecules in WT and KO were confirmed for all three charge carriers, H^+, Na^+ and K^+ in positive-ion mode. Homogenous distributions of the three differently charged PE(36:4) and PE(34:2) in WT and KO tissue sections are demonstrated in Fig. S5.

Differential abundance of lipid species between E19 WT and *Pex11β* KO mouse lungs. Our results showed a wide variety of lipid species and other cellular metabolites that were differentially expressed between WT and *Pex11β* KO E19 mouse lung tissue sections. For instance, in KO tissue sections, deprotonated PG(34:1) (*m/z* 747.51815) showed lower signal intensities in comparison to WT (Fig. 7). Phosphatidylglycerol (PG) is the second most abundant phospholipid in pulmonary surfactant, with PG(34:1) being the predominant lipid molecular species, playing a role in adsorption, alveolar stability and innate immunity of the lungs[9,10,14].

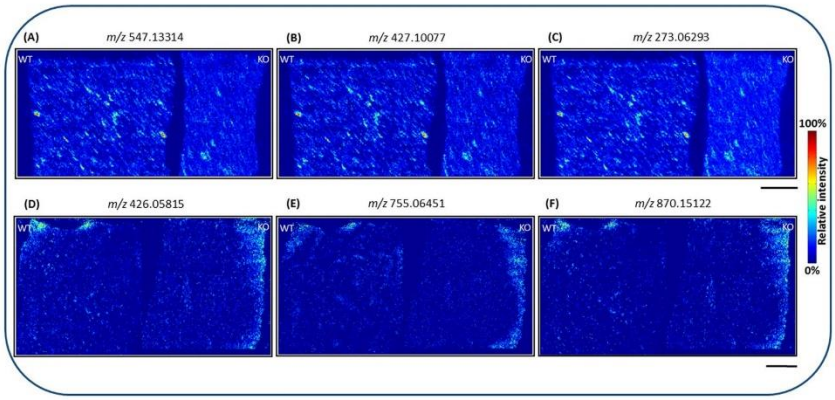

Figure 5. Distribution of matrix cluster signals in wild type (WT) and *Pex11β* knockout (KO) late fetal E19 mouse lung tissue sections from mass spectrometry imaging (MSI) experiments. (**A**–**C**) Evenly distributed 4-Nitroaniline (pNA) matrix cluster images in negative-ion mode. (**D**–**F**) Evenly distributed 2,5-Dihydroxybenzoic acid (DHB) matrix cluster images in positive-ion mode. Scale bar 500 µm.

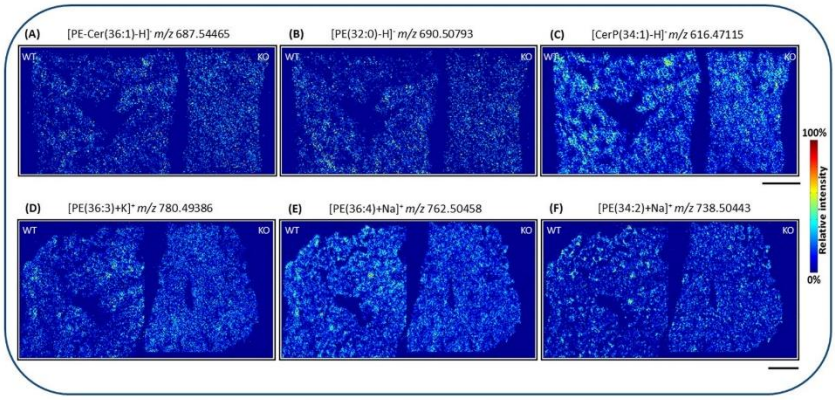

Figure 6. Homogenous distribution of endogenous compounds in wild type (WT) and *PEX11β* knockout (KO) late fetal E19 mouse lung tissue sections, measured by atmospheric-pressure MALDI MSI experiments. (A-C) Evenly distributed lipid species in negative-ion mode. (**A**) $[PE\text{-}Cer(36:1) - H]^-$, (**B**) $[PE(32:0) - H]^-$ and (**C**) $[CerP(34:1) - H]^-$. (**D**–**F**) Evenly distributed lipid species in positive-ion mode. (**D**) $[PE(36:3) + K]^-$, (**E**) $[PE(36:4) + Na]^+$ and (**F**) $[PE(34:2) + Na]^+$. Scale bar 500 µm.

Furthermore, recent studies demonstrated that PG(34:1) (palmitoyl-oleoyl-phosphatidylglycerol, POPG) acts as a potent antiviral agent against influenza A and respiratory syncytial viruses[13,15] as well as antagonizes the proinflammatory actions of mycoplasma pneumoniae[65]. In positive-ion mode, potassiated sulfatide lipid (SHexCer (t33:1), *m/z* 820.46415, based on MS1 annotation) showed differentially higher signal intensities in KO tissue sections compared to WT (Fig. 7). Sulfatides are multifunctional molecules, playing important roles in physiological processes of various organs. It has been shown that sulfatide (glycolipids) levels were elevated in many human cancer cells and tissues including pulmonary adenocarcinoma[66]. In our study, MS images clearly illustrate the differences in signal intensities between WT and KO lung tissues.

In addition to biological variations, several experimental and instrumental parameters may also cause variations in signal intensities across different imaging datasets. Therefore, to prove the correctness of observed biological variations from *Pex11β* E19 mouse lungs and to exclude technique-dependent differences between distinct cryosections, we applied several different normalization algorithms during image generation. In our study, MS images were generated (1) without normalization, (2) with normalization to total ion current (TIC), (3) with normalization to uniformly distributed matrix cluster signals, and (4) with normalization to uniformly distributed endogenous signals. Figure 7 shows MS images of differentially abundant lipid species in WT and *Pex11β*

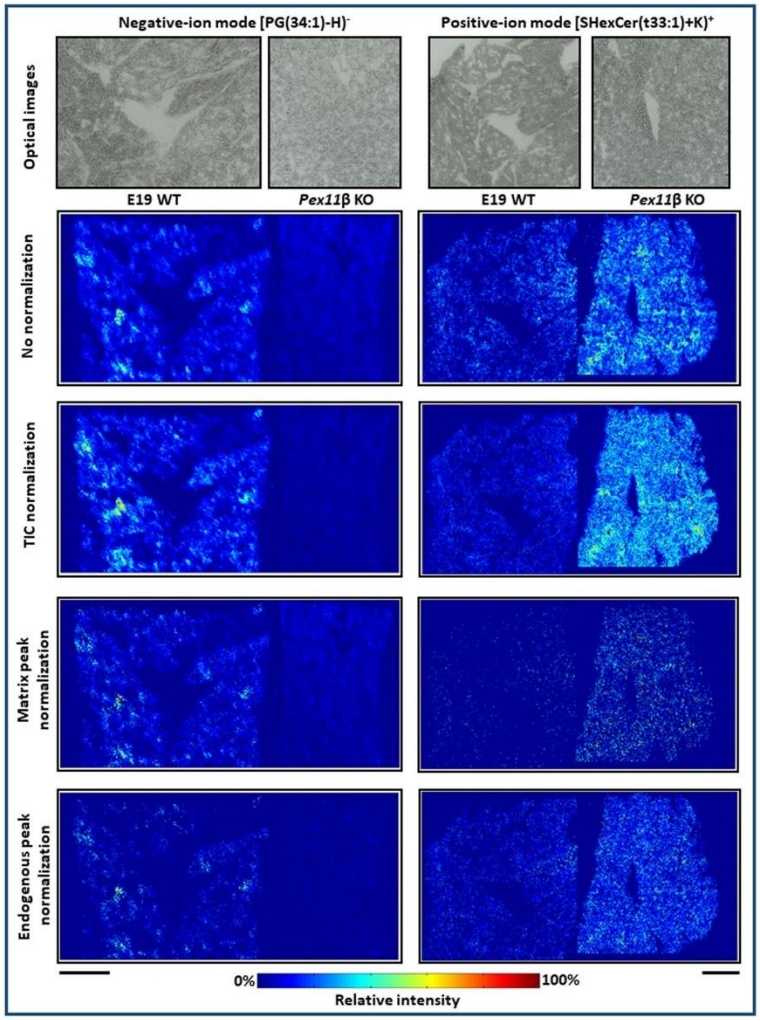

Figure 7. Differential abundance of lipid species in wild type (WT) and *Pex11β* knockout (KO) late fetal E19 mouse lung tissue sections in negative- and positive-ion mode. Downregulation of $[PG(34:1) - H]^-$ lipid (*m/z* 747.51815), upregulation of $[SHexCer(t33:1) + K]^+$ lipid (*m/z* 820.46415) in *Pex11β* KO E19 mouse lungs in negative- and positive-ion mode. The abundance comparisons between lipids in different cryosections were verified by applying various normalization algorithms: (i) no normalization, (ii) total ion count (TIC) normalization, (iii) normalization to homogenously distributed matrix signals and (iv) normalization to homogenously distributed endogenous signals. Scale bar 500 µm.

KO tissue sections, generated with various normalization algorithms. Regardless of the normalization method, our MSI data was found to be consistent, and normalization approaches did not induce significant changes in the determined differential abundance of lipid species in both ionization modes, proving the high quality of our optimized protocol used (Fig. 7 & Table S4).

Normalization is defined as a process of projecting all data to a common intensity scale for the comparison of spectra[67,68]. Many normalization strategies have been described in literature to correct the variations in signal intensities of MSI data such as TIC, root mean square (RMS), median intensity, vector normalization, normalization to matrix signals, endogenous signals, stable isotope standards, tissue-specific ionization efficiency coefficient and sliding window normalization, etc.[67–71]. Each strategy has its own limitations, a number of them are

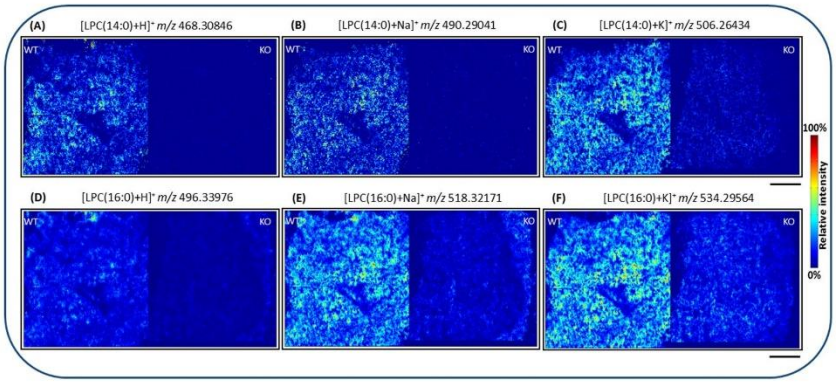

Figure 8. Confirmation of differential abundance of lipid species in wild type (WT) and *Pex11β* knockout (KO) late fetal E19 mouse lung tissue sections for various charge carriers in positive-ion mode. (**A**–**C**) Differential abundance of LPC(14:0) in WT and KO E19 mouse lung tissue. (**A**) $[LPC(14:0)+H]^+$, (**B**) $[LPC(14:0)+Na]^+$, (**C**) $[LPC(14:0)+K]^-$. (**D**–**F**) Differential abundance of LPC(16:0) in WT and KO E19 mouse lung tissue. (**D**) $[LPC(16:0)+H]^-$, (**E**) $[LPC(16:0)+Na]^+$, (**F**) $[LPC(16:0)+K]^-$. Scale bar 500 µm.

reviewed in detail in the context of quantification (relative and absolute) of low molecular weight compounds by MALDI MSI[71].

TIC normalization is the most common method, and several studies demonstrated uniformly distributed matrix cluster and/or endogenous signals as "internal-standard-like" normalization for semi-quantitative analysis by MALDI MSI[68]. In many cases, normalization, interpolation and other post-processing parameters influence signal intensities of analytes in MSI, which often leads to wrong interpretations of the data. In such cases, it is challenging to draw reliable biological conclusions from MSI data, especially in the case of biomarker studies and pharmaceutical applications (drug discovery). Therefore, we optimized the sample preparation, experimental and instrumental conditions, and our data processing framework very carefully to produce highly accurate and reproducible MSI data for a direct relative comparison of signal intensities of analytes.

The differential abundance of lipid species in WT and KO tissue sections was confirmed using biological replicates (Fig. S6). For instance, deprotonated PG (34:1) and potassiated SHexCer (t33:1) showed similar trends of differential abundance between WT and KO tissue sections of different animals (n = 3).

Confirmation of differential abundance of lipids with various ion adducts. Differential abundance of lipid species in WT and KO tissue sections was also confirmed based on various ionic species in positive-ion mode. For instance, the lysophosphatidylcholines LPC(14:0) and LPC(16:0) exhibited reduced signal intensities in KO lung tissue sections compared to WT. LPCs are lipid mediators produced from PCs by the action of phospholipase A2 (PLA2), and involved in various pro-inflammatory and pro-atherogenic activities[72]. The observed differential pattern was found to be consistent in protonated, sodiated and potassiated ionic state. Figure 8 shows MS images of LPC(14:0) [(A) 468.30846, (B) 490.29041 and (C) 506.26434] and LPC(16:0) [(D) 496.33976, (E) 518.32171 and (F) 534.29564], containing the three different charge carriers, respectively.

Structural confirmation of lipid species using on-tissue tandem mass spectrometry (MS/MS). The web-based "MetFrag" server was used to generate possible fragment ions of the lipid species[73]. The theoretical fragments generated by the software were identical to the fragments observed in our experiments. Annotation of differentially abundant lipids was further confirmed based on on-tissue tandem mass spectrometry experiments. For instance, deprotonated PG(34:1) (POPG) at m/z 747.51966 ± 0.4 was structurally confirmed with fragment ions at m/z 152.99460 (corresponding to the cyclic phosphate anion, red), m/z 255.23307 (corresponding to palmitic fatty acyl (FA 16:0), green), and m/z 281.24885 (corresponding to oleic fatty acyl (FA 18:1), blue) (Fig. 9A).

In positive-ion mode, protonated LPC(16:0) at m/z 496.34007 ± 0.4 was structurally confirmed using fragment ions at m/z 104.10758 (corresponding to choline, red), m/z 184.07364 (corresponding to phosphocholine head group, green), and m/z 478.32943 (corresponding to the loss of water $[M+H\text{-}H_2O]^+$, blue) (Fig. 9B). Similarly, sodiated and potassiated species were also confirmed with characteristic fragmentation patterns from both WT and KO tissue sections (Supplementary Data & Table S3).

Conclusion

We report a comprehensive lipid map of late fetal WT mouse lungs at day 19 of gestation (E19) using high-resolution accurate mass AP-SMALDI MSI. We demonstrated optimized experimental and instrumental conditions as well as a detailed data processing framework for comparative analysis of biomolecules in different tissue sections of WT and KO mice (using the *Pex11β* KO mouse here as a model system). The optimized workflow will be useful for relative (semi-) quantitative analyses of lipids and other cellular metabolites from different tissue sections using MALDI MSI. Highly specific and accurate lipidomic information of late fetal stage E19 mouse lungs may serve as

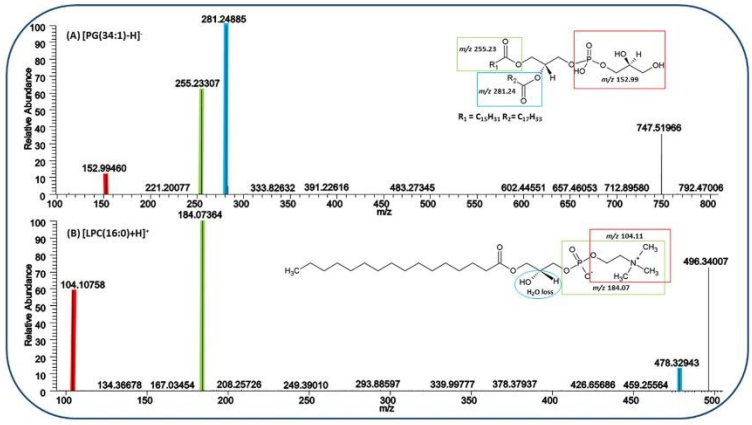

Figure 9. Structural confirmation of lipid annotations by on-tissue tandem mass spectrometry (MS/MS) in negative- and positive-ion mode, using high-energy collisional dissociation (HCD). (**A**) On-tissue HCD-MS/MS (averaged) spectrum of $[PG(34:1) - H]^-$ m/z 747.51966 ± 0.4. (**B**) On-tissue HCD-MS/MS (averaged) spectrum of $[LPC(16:0) + H]^+$ m/z 496.34007 ± 0.4.

a reference for better understanding of lung developmental processes (e.g. late fetal differentiation) or molecular mechanisms of various pulmonary diseases, associated with lipid alterations.

Materials and Methods

Materials. Trifluoroacetic acid (TFA, spectroscopy grade), 2,5-Dihydroxybenzoic acid (DHB, 98% purity) and acetone (spectroscopy grade) were purchased from Merck (Darmstadt, Germany). 4-Nitroaniline (pNA, ≥99% purity) and water (LC-MS grade) were procured from Sigma-Aldrich (Steinheim, Germany). Glass microscope slides (ground edges, SuperFrost) were obtained from R. Langenbrinck (Emmendingen, Germany). All other reagents used were of highest purity and analytical grade.

Animal experiments. Specific-pathogen-free (SPF) C57BL/6J mice were obtained from Charles River, Sulzfeld, Germany. Mice were kept on a regular laboratory diet and water *ad libitum* and housed in cages under standardized environmental conditions (12 hours light/dark cycle, 23 °C ± 1 °C and 55% ± 1% relative humidity). Generation and breeding of *Pex11β* knockout (KO) mice were described previously[53,54]. Pregnant dames with eventual *Pex11β* KO mice (autosomal-recessive inheritance with 25% WT, 50% *Pex11β* HTZ, and 25% *Pex11β* KO) were kept in the SPF central animal facility of Justus Liebig University Giessen, Germany. Pregnant dames were killed by cervical dislocation and the E19 fetus were killed by decapitation.

"Experiments were approved by the named animal welfare officers of the Justus Liebig University (administrative number M471) and performed according to the German and European animal welfare law".

Sample (E19 mouse lung tissue) preparation for MSI. For the perfusion of the E19 mouse lungs, the skin of the pups was opened, the right ventricle of the heart was punctured with an 18-size gauze needle. Thereafter, the left atrium was cut open and the animals were perfused via the right ventricle with 500 µl of saline. After the saline wash, lung tissues were perfused with 10 ml of a 4% paraformaldehyde (PFA) fixative in phosphate buffer saline (PBS), pH 7.4. Thereafter, the lungs were excised and further fixed from the outside by overnight immersion fixation. The PFA fixed lung tissues were embedded with the optimal cutting temperature (OCT) compound. Twelve µm thick cryosections were cut with a cryomicrotome (CM 3050 S cryostat, Leica Microsystems, Nussloch, Germany) and stored at −80 °C until further use.

Later, we optimized a sectioning procedure for fresh snap-frozen E19 mouse lung tissues without using any embedding material. For cryosectioning, fresh frozen E19 lung tissues were mounted directly on a sample holder of the cryotome, using deionized water (ice) as an adhesive. For MSI experiments, both WT and *Pex11β* KO E19 mouse lung tissue, serial sections were cut with an equal thickness of 12 µm at −20 °C with a cryomicrotome (CM 3050 S cryostat, Leica Microsystems, Nussloch, Germany). One section of a series was thaw-mounted on each glass microscope slide (ground edge, SuperFrost) and labelled with an appropriate number for later identification. For the purpose to get an overview on the quality and thickness of each entire cryosection, several overlapping images covering the whole tissue section were taken at a magnification of 40x with a Leica DMRD microscope (Leica, Bensheim, Germany) equipped with a Leica DC 480 camera (Leica, Bensheim, Germany) and thereafter stitched together with Image composite editor (Microsoft Research). Identical camera settings were used to be able to compare the darkness and grey values of all cut cryosections to optimize the selection procedure for high quality sections with similar section thicknesses. Care was taken to speed up the image taking procedure of each individual section. All other sections were stored in parallel prior to and after photographing in a slide box on dry ice.

The best and optimally matched lung cryosections of the appropriate WT and KO animals were either used directly for immediate MS imaging experiments or stored at −80 °C until further analysis on consecutive days for replicate measurements.

Matrix application. Prior to matrix application, the frozen lung tissue sections were brought to room temperature in a desiccator (about 15 minutes) to avoid condensation of humidity on the surface of the samples. DHB (30 mg mL^{-1} in acetone:water at 1:1 vol/vol, 0.1% TFA), and pNA (10 mg mL^{-1} in acetone:water at 1:1 vol/vol) solutions were prepared freshly for the matrix application. For positive-ion mode measurements, a volume of 120 µL of DHB, for negative-ion mode a volume of 50 µL of pNA matrix solution were deposited homogeneously on the tissue surfaces by using an automatic pneumatic ultrafine sprayer ("SMALDIPrep", TransMIT GmbH, Giessen, Germany)[74].

MALDI mass spectrometry imaging. Immediately after matrix application, MSI experiments were performed using a high-resolution atmospheric-pressure scanning microprobe matrix-assisted laser desorption/ionization ion source ("AP-SMALDI10", TransMIT GmbH, Giessen, Germany), coupled to a Fourier transform orbital trapping mass spectrometer (Q Exactive, Thermo Scientific GmbH, Bremen, Germany)[75]. Desorption and ionization of analytes were initiated by a nitrogen gas laser (LTB Lasertechnik GmbH, Berlin, Germany) with a wavelength of 337 nm, operating at a repetition rate of 60 Hz. The laser beam was focused coaxially with the ion beam by a centrally bored objective lens[76]. In all the MALDI MSI experiments, the E19 mouse lung tissue sections were measured with high resolution in mass (140,000 @ m/z 200) and space (10 µm per pixel). The step size of the sample stage was set to the desired pixel size (10 µm). The mass spectrometer was operated in positive- and negative-ion mode in the mass to charge number (m/z) range of m/z 250–1000 with a target voltage of +/−4.3 kV. Automatic gain control (AGC) was disabled, and the injection time (IT) was fixed at 500 ms (microscans = 1). The measurement speed in full scan mode (scan range m/z 250–1000) was about 0.8 pixels per second at a mass resolution of 140,000 (at m/z 200). Ions formed by 30 laser pulses per spot were accumulated in the C-trap before being sent to the orbitrap mass analyser for detection. Internal mass calibration was performed using known matrix ion signals as lock mass values (716.12462 and 409.09020 for positive- and negative-ion mode, respectively), which resulted in a mass accuracy better than 2 ppm root mean square error (RMSE) over the entire measurement.

Annotation of lipid species. Lipid species were annotated according to the proposal for shorthand notation of lipid structures derived from mass spectrometry[77]. For instance, phospholipid species (e.g. PC, PG, PI, etc.) were denoted as (X:Y), where X represents the total number of carbon atoms and Y represents the total number of double bonds in fatty acyl chains, without specifying the individual acyl chains attached to the glycerol or sphingosine backbone. In sphingolipids, "m", "d" and "t" represents the number of hydroxyl groups in sphingoid base (mono, di, and tri)[77].

Data processing and image generation. AP-SMALDI MSI data sets (.raw) were converted to centroid imzML files, and E19 mouse lung lipid ion MS images were generated using the open source software "MSiReader" version 0.09[78] with a m/z bin width of Δ $m/z = \pm 5$ ppm. No further (pre or post) data processing steps were applied for image generation in order to demonstrate the original data quality. The lipid species were annotated based on accurate ion mass (m/z) values, by using databases such as LIPID MAPS (www.lipidmaps.org), METLIN (www.metlin.scripps.edu) and Human Metabolite Database (www.hmdb.ca) within Δ $m/z = \pm 2$ ppm or 0.0005 Da. In negative-ion mode, deprotonated $[M-H]^-$, in positive-ion mode protonated $[M+H]^+$, sodiated $[M+Na]^+$ and potassiated $[M+K]^+$ species were considered for the annotation.

After characterization of the lipidome of E19 mouse lungs, signal intensities of lipid species were compared between E19 WT and *Pex11β* KO mouse lung tissue sections using the same software (MSiReader v0.09). Images were generated with a bin width of Δ $m/z = \pm 5$ ppm. Pre-processing steps, such as baseline correction, noise removal, smoothing or interpolation, were not applied during image generation. Normalization of signal intensities was performed in the following alternative ways: (1) no normalization, (2) total ion current (TIC) normalization, (3) normalization with ubiquitous matrix signals, (4) normalization with ubiquitous endogenous signals, or (5) specific strategies for comparison of relative ion abundances in WT and KO E19 lung tissue sections. These procedures are explained in detail in the results and discussion section.

On-tissue MS/MS analysis. Lipid annotation based on accurate ion mass (≤2 ppm) was further confirmed by on-tissue tandem mass spectrometry (MS/MS) analysis. MS/MS fragmentation was performed by using higher-energy collisional dissociation (HCD) with a precursor ion isolation window of 0.4 Da. Fragmentation of individual lipid species was obtained with normalized collision energy values (NCE) of 20–28% (averaged spectra from 20, 25 and 28 NCE) and 15–25% (averaged spectra from 15, 20 and 25 NCE) in positive- and negative-ion mode, respectively. The experimental fragmentation patterns of lipids were confirmed based on neutral losses, diagnostic fragment ions of the head groups[79], by matching with tandem MS spectra of standard lipid species available in databases (e.g. METLIN, HMDB, etc.), or by comparing with the in-silico fragmentation patterns using MetFrag web server[73].

References

1. Glatz, J. F. C. Lipids and lipid binding proteins: A perfect match. *Prostag Leukotr Ess* **93**, 45–49, https://doi.org/10.1016/j.plefa.2014.07.011 (2015).
2. Brugger, B. Lipidomics: analysis of the lipid composition of cells and subcellular organelles by electrospray ionization mass spectrometry. *Annual review of biochemistry* **83**, 79–98, https://doi.org/10.1146/annurev-biochem-060713-035324 (2014).
3. Lee, C. H., Olson, P. & Evans, R. M. Minireview: Lipid metabolism, metabolic diseases, and peroxisome proliferator-activated receptors. *Endocrinology* **144**, 2201–2207, https://doi.org/10.1210/en.2003-0288 (2003).

4. King, R. J. & Clements, J. A. In *Comprehensive Physiology* (John Wiley & Sons, Inc., 2011).
5. Karnati, S. & Baumgart-Vogt, E. Peroxisomes in mouse and human lung: their involvement in pulmonary lipid metabolism. *Histochem Cell Biol* **130**, 719–740, https://doi.org/10.1007/s00418-008-0462-3 (2008).
6. Fisher, A. B. In *Comparative Biology of the Normal Lung (Second Edition)* 423–466 (Academic Press, 2015).
7. Berry, K. A. Z., Murphy, R. C., Kosmider, B. & Mason, R. J. Lipidomic characterization and localization of phospholipids in the human lung. *J Lipid Res* **58**, 926–933, https://doi.org/10.1194/jlr.M074955 (2017).
8. Chakraborty, M. & Kotecha, S. Pulmonary surfactant in newborn infants and children. *Breathe* **9**, 476 (2013).
9. Agassandian, M. & Mallampalli, R. K. Surfactant phospholipid metabolism. *Bba-Mol Cell Biol L* **1831**, 612–625, https://doi.org/10.1016/j.bbalip.2012.09.010 (2013).
10. Veldhuizen, R., Nag, K., Orgeig, S. & Possmayer, F. The role of lipids in pulmonary surfactant. *Bba-Mol Basis Dis* **1408**, 90–108, https://doi.org/10.1016/S0925-4439(98)00061-1 (1998).
11. Glasser, J. R. & Mallampalli, R. K. Surfactant and its role in the pathobiology of pulmonary infection. *Microbes Infect* **14**, 17–25, https://doi.org/10.1016/j.micinf.2011.08.019 (2012).
12. Griese, M. Pulmonary surfactant in health and human lung diseases: state of the art. *Eur Respir J* **13**, 1455–1476, https://doi.org/10.1183/09031936.99.13614779 (1999).
13. Numata, M., Chu, H. W., Dakhama, A. & Voelker, D. R. Pulmonary surfactant phosphatidylglycerol inhibits respiratory syncytial virus-induced inflammation and infection. *P Natl Acad Sci USA* **107**, 320–325, https://doi.org/10.1073/pnas.0909361107 (2010).
14. Perino, J. *et al.* Lung surfactant DPPG phospholipid inhibits vaccinia virus infection. *Antivir Res* **89**, 89–97, https://doi.org/10.1016/j.antiviral.2010.11.009 (2011).
15. Numata, M. *et al.* Phosphatidylglycerol Suppresses Influenza A Virus Infection. *Am J Resp Cell Mol* **46**, 479–487, https://doi.org/10.1165/rcmb.2011-0194OC (2012).
16. Stables, M. J. & Gilroy, D. W. Old and new generation lipid mediators in acute inflammation and resolution. *Prog Lipid Res* **50**, 35–51, https://doi.org/10.1016/j.plipres.2010.07.005 (2011).
17. Gunther, A. *et al.* Surfactant alteration and replacement in acute respiratory distress syndrome. *Respir Res* **2**, 353–U352, https://doi.org/10.1186/Rr86 (2001).
18. Adams, F. H., Fujiwara, T., Emmanouilides, G. & Scudder, A. Surface Properties and Lipids from Lungs of Infants with Hyaline Membrane Disease. *J Pediatr-Us* **66**, 357−+, https://doi.org/10.1016/S0022-3476(65)80193-7 (1965).
19. Ackerman, S. J. *et al.* Polyunsaturated lysophosphatidic acid as a potential asthma biomarker. *Biomark Med* **10**, 123–135, https://doi.org/10.2217/bmm.15.93 (2016).
20. Telenga, E. D. *et al.* Untargeted Lipidomic Analysis in Chronic Obstructive Pulmonary Disease Uncovering Sphingolipids. *Am J Resp Crit Care* **190**, 155–164, https://doi.org/10.1164/rccm.201312-2210OC (2014).
21. Dargaville, P. A., South, M. & McDougall, P. N. Surfactant abnormalities in infants with severe viral bronchiolitis. *Arch Dis Child* **75**, 133–136 (1996).
22. Ollero, M. *et al.* Plasma lipidomics reveals potential prognostic signatures within a cohort of cystic fibrosis patients. *J Lipid Res* **52**, 1011–1022, https://doi.org/10.1194/jlr.P013722 (2011).
23. Gunther, A. *et al.* Surfactant alterations in severe pneumonia, acute respiratory distress syndrome, and cardiogenic lung edema. *Am J Resp Crit Care* **153**, 176–184 (1996).
24. Griese, M. *et al.* Surfactant lipidomics in healthy children and childhood interstitial lung disease. *Plos One* **10**, e0117985, https://doi.org/10.1371/journal.pone.0117985 (2015).
25. Lewis, J. F., Ikegami, M. & Jobe, A. H. Altered Surfactant Function and Metabolism in Rabbits with Acute Lung Injury. *J Appl Physiol* **69**, 2303–2310 (1990).
26. Marien, E. *et al.* Non-small cell lung cancer is characterized by dramatic changes in phospholipid profiles. *Int J Cancer* **137**, 1539–1548, https://doi.org/10.1002/ijc.29517 (2015).
27. Spengler, B. Mass Spectrometry Imaging of Biomolecular Information. *Analytical Chemistry* **87**, 64–82, https://doi.org/10.1021/ac504543v (2015).
28. Spengler, B., Hubert, M. & Kaufmann, R. In *Proceedings of the 42nd Annual Conference on Mass Spectrometry and Allied Topics* 1041 (Chicago, Illinois, 1994).
29. Jackson, S. N. *et al.* Imaging of lipids in rat heart by MALDI-MS with silver nanoparticles. *Anal Bioanal Chem* **406**, 1377–1386, https://doi.org/10.1007/s00216-013-7525-6 (2014).
30. Seeley, E. H. & Caprioli, R. M. Molecular imaging of proteins in tissues by mass spectrometry. *P Natl Acad Sci USA* **105**, 18126–18131, https://doi.org/10.1073/pnas.0801374105 (2008).
31. Schober, Y., Guenther, S., Spengler, B. & Rompp, A. High-resolution matrix-assisted laser desorption/ionization imaging of tryptic peptides from tissue. *Rapid Communications in Mass Spectrometry* **26**, 1141–1146, https://doi.org/10.1002/rcm.6192 (2012).
32. Bhandari, D. R., Schott, M., Rompp, A., Vilcinskas, A. & Spengler, B. Metabolite localization by atmospheric pressure high-resolution scanning microprobe matrix-assisted laser desorption/ionization mass spectrometry imaging in whole-body sections and individual organs of the rove beetle Paederus riparius. *Anal Bioanal Chem* **407**, 2189–2201, https://doi.org/10.1007/s00216-014-8327-1 (2015).
33. Everest-Dass, A. V. *et al.* N-glycan MALDI Imaging Mass Spectrometry on Formalin-Fixed Paraffin-Embedded Tissue Enables the Delineation of Ovarian Cancer Tissues. *Mol Cell Proteomics* **15**, 3003–3016, https://doi.org/10.1074/mcp.M116.059816 (2016).
34. Rompp, A., Guenther, S., Takats, Z. & Spengler, B. Mass spectrometry imaging with high resolution in mass and space (HR2 MSI) for reliable investigation of drug compound distributions on the cellular level. *Anal Bioanal Chem* **401**, 65–73, https://doi.org/10.1007/s00216-011-4990-7 (2011).
35. Rompp, A. *et al.* Histology by Mass Spectrometry: Label-Free Tissue Characterization Obtained from High-Accuracy Bioanalytical Imaging. *Angew Chem Int Edit* **49**, 3834–3838, https://doi.org/10.1002/anie.200905559 (2010).
36. Schober, Y., Guenther, S., Spengler, B. & Rompp, A. Single Cell Matrix-Assisted Laser Desorption/Ionization Mass Spectrometry Imaging. *Analytical Chemistry* **84**, 6293–6297, https://doi.org/10.1021/ac301337h (2012).
37. Bhandari, D. R. *et al.* High resolution mass spectrometry imaging of plant tissues: towards a plant metabolite atlas. *Analyst* **140**, 7696–7709, https://doi.org/10.1039/c5an01065a (2015).
38. Khalil, S. M., Rompp, A., Pretzel, J., Becker, K. & Spengler, B. Phospholipid Topography of Whole-Body Sections of the Anopheles stephensi Mosquito, Characterized by High-Resolution Atmospheric-Pressure Scanning Microprobe Matrix-Assisted Laser Desorption/Ionization Mass Spectrometry Imaging. *Analytical Chemistry* **87**, 11309–11316, https://doi.org/10.1021/acs.analchem.5602781 (2015).
39. Hoffmann, T. & Dorrestein, P. C. Homogeneous Matrix Deposition on Dried Agar for MALDI Imaging Mass Spectrometry of Microbial Cultures. *Journal of the American Society for Mass Spectrometry* **26**, 1959–1962, https://doi.org/10.1007/s13361-015-1241-8 (2015).
40. Marko-Varga, G. *et al.* Drug localization in different lung cancer phenotypes by MALDI mass spectrometry imaging. *J Proteomics* **74**, 982–992, https://doi.org/10.1016/j.jprot.2011.03.019 (2011).
41. Prideaux, B. *et al.* The association between sterilizing activity and drug distribution into tuberculosis lesions. *Nat Med* **21**, 1223−+, https://doi.org/10.1038/nm.3937 (2015).
42. Manier, M. L. *et al.* Reagent Precoated Targets for Rapid In-Tissue Derivatization of the Anti-Tuberculosis Drug Isoniazid Followed by MALDI Imaging Mass Spectrometry. *Journal of the American Society for Mass Spectrometry* **22**, 1409–1419, https://doi.org/10.1007/s13361-011-0150-8 (2011).

43. Yanagisawa, K. *et al.* Proteomic patterns of tumour subsets in non-small-cell lung cancer. *Lancet* **362**, 433–439, https://doi.org/10.1016/S0140-6736(03)14068-8 (2003).
44. Kurabe, N. *et al.* Visualization of phosphatidylcholine (16:0/16:0) in type II alveolar epithelial cells in the human lung using imaging mass spectrometry. *Pathol Int* **63**, 195–200, https://doi.org/10.1111/pin.12050 (2013).
45. Fernandez, R. *et al.* Analysis of the Lipidome of Xenografts Using MALDI-IMS and UHPLC-ESI-QTOF. *Journal of the American Society for Mass Spectrometry* **25**, 1237–1246, https://doi.org/10.1007/s13361-014-0882-3 (2014).
46. Berry, K. A. Z. *et al.* MALDI imaging MS of phospholipids in the mouse lung. *J Lipid Res* **52**, 1551–1560, https://doi.org/10.1194/jlr.M015750 (2011).
47. Carter, C. L. *et al.* A Maldi-Msi Approach to the Characterization of Radiation-Induced Lung Injury and Medical Countermeasure Development. *Health Phys* **109**, 466–478, https://doi.org/10.1097/Hp.0000000000000353 (2015).
48. Jones, E. E., Quiason, C., Dale, S. & Shahidi-Latham, S. K. Feasibility Assessment of a MALDI FTICR Imaging Approach for the 3D Reconstruction of a Mouse Lung. *Journal of the American Society for Mass Spectrometry* **28**, 1709–1715, https://doi.org/10.1007/s13361-017-1658-3 (2017).
49. Karnati, S. *et al.* Quantitative lipidomic analysis of mouse lung during postnatal development by electrospray ionization tandem mass spectrometry. *Plos One* **13**, e0203464, https://doi.org/10.1371/journal.pone.0203464 (2018).
50. Dautel, S. E. *et al.* Lipidomics reveals dramatic lipid compositional changes in the maturing postnatal lung. *Scientific reports* **7**, 40555, https://doi.org/10.1038/srep40555 (2017).
51. Kompauer, M., Heiles, S. & Spengler, B. Atmospheric pressure MALDI mass spectrometry imaging of tissues and cells at 1.4-mum lateral resolution. *Nature methods* **14**, 90–96, https://doi.org/10.1038/nmeth.4071 (2017).
52. Kompauer, M., Heiles, S. & Spengler, B. Autofocusing MALDI mass spectrometry imaging of tissue sections and 3D chemical topography of nonflat surfaces. *Nature methods* **14**, 1156–1158, https://doi.org/10.1038/nmeth.4433 (2017).
53. Li, X. *et al.* PEX11β Deficiency Is Lethal and Impairs Neuronal Migration but Does Not Abrogate Peroxisome Function. *Molecular and Cellular Biology* **22**, 4358–4365, https://doi.org/10.1128/MCB.22.12.4358-4365.2002 (2002).
54. Ahlemeyer, B., Gottwald, M. & Baumgart-Vogt, E. Deletion of a single allele of the Pex11β gene is sufficient to cause oxidative stress, delayed differentiation and neuronal death in mouse brain. *Disease Models & Mechanisms* **5**, 125 (2011).
55. Schramm, T. *et al.* imzML - A common data format for the flexible exchange and processing of mass spectrometry imaging data. *J Proteomics* **75**, 5106–5110, https://doi.org/10.1016/j.jprot.2012.07.026 (2012).
56. Race, A. M., Styles, I. B. & Bunch, J. Inclusive sharing of mass spectrometry imaging data requires a converter for all. *J Proteomics* **75**, 5111–5112, https://doi.org/10.1016/j.jprot.2012.05.035 (2012).
57. Schwartz, S. A., Reyzer, M. L. & Caprioli, R. M. Direct tissue analysis using matrix-assisted laser desorption/ionization mass spectrometry: practical aspects of sample preparation. *J Mass Spectrom* **38**, 699–708, https://doi.org/10.1002/jms.505 (2003).
58. Carter, C. L., Jones, J. W., Farese, A. M., MacVittie, T. J. & Kane, M. A. Inflation-Fixation Method for Lipidomic Mapping of Lung Biopsies by Matrix Assisted Laser Desorption/Ionization-Mass Spectrometry Imaging. *Analytical Chemistry* **88**, 4788–4794, https://doi.org/10.1021/acs.analchem.6b00165 (2016).
59. Gaudin, M. *et al.* Ultra performance liquid chromatography - mass spectrometry studies of formalin-induced alterations of human brain lipidome. *J Mass Spectrom* **49**, 1035–1042, https://doi.org/10.1002/jms.3424 (2014).
60. Schittny, J. C., Mund, S. I. & Stampanoni, M. Evidence and structural mechanism for late lung alveolarization. *American journal of physiology. Lung cellular and molecular physiology* **294**, L246–254, https://doi.org/10.1152/ajplung.00296.2007 (2008).
61. Kim, H., Ahn, E. & Moon, M. H. Profiling of human urinary phospholipids by nanoflow liquid chromatography/tandem mass spectrometry. *Analyst* **133**, 1656–1663, https://doi.org/10.1039/b804715d (2008).
62. Holm, B. A., Wang, Z., Egan, E. A. & Notter, R. H. Content of dipalmitoyl phosphatidylcholine in lung surfactant: ramifications for surface activity. *Pediatric research* **39**, 805–811, https://doi.org/10.1203/00006450-199605000-00010 (1996).
63. Postle, A. D., Heeley, E. L. & Wilton, D. C. A comparison of the molecular species compositions of mammalian lung surfactant phospholipids. *Comp Biochem Phys A* **129**, 65–73, https://doi.org/10.1016/S1095-6433(01)00306-3 (2001).
64. Uhlig, S. & Gulbins, E. Sphingolipids in the Lungs. *Am J Resp Crit Care* **178**, 1100–1114, https://doi.org/10.1164/rccm.200804-595SO (2008).
65. Kandasamy, P. *et al.* Pulmonary surfactant phosphatidylglycerol inhibits Mycoplasma pneumoniae-stimulated eicosanoid production from human and mouse macrophages. *The Journal of biological chemistry* **286**, 7841–7853, https://doi.org/10.1074/jbc.M110.170241 (2011).
66. Takahashi, T. & Suzuki, T. Role of sulfatide in normal and pathological cells and tissues. *J Lipid Res* **53**, 1437–1450, https://doi.org/10.1194/jlr.R026682 (2012).
67. Fonville, J. M. *et al.* Robust Data Processing and Normalization Strategy for MALDI Mass Spectrometric Imaging. *Analytical Chemistry* **84**, 1310–1319, https://doi.org/10.1021/ac201767g (2012).
68. Deininger, S. O. *et al.* Normalization in MALDI-TOF imaging datasets of proteins: practical considerations. *Anal Bioanal Chem* **401**, 167–181, https://doi.org/10.1007/s00216-011-4929-z (2011).
69. Wijetunge, C. D. *et al.* EXIMS: an improved data analysis pipeline based on a new peak picking method for EXploring Imaging Mass Spectrometry data. *Bioinformatics* **31**, 3198–3206, https://doi.org/10.1093/bioinformatics/btv356 (2015).
70. Jones, E. A., Deininger, S. O., Hogendoorn, P. C. W., Deelder, A. M. & McDonnell, L. A. Imaging mass spectrometry statistical analysis. *J Proteomics* **75**, 4962–4989, https://doi.org/10.1016/j.jprot.2012.06.014 (2012).
71. Rzagalinski, I. & Volmer, D. A. Quantification of low molecular weight compounds by MALDI imaging mass spectrometry - A tutorial review. *Bba-Proteins Proteom* **1865**, 726–739, https://doi.org/10.1016/j.bbapap.2016.12.011 (2017).
72. Yoder, M. *et al.* Bioactive lysophosphatidylcholine 16:0 and 18:0 are elevated in lungs of asthmatic subjects. *Allergy, asthma & immunology research* **6**, 61–65, https://doi.org/10.4168/aair.2014.6.1.61 (2014).
73. Wolf, S., Schmidt, S., Müller-Hannemann, M. & Neumann, S. In silico fragmentation for computer assisted identification of metabolite mass spectra. *BMC Bioinformatics* **11**, 148, https://doi.org/10.1186/1471-2105-11-148 (2010).
74. Bouschen, W., Schulz, O., Eikel, D. & Spengler, B. Matrix vapor deposition/recrystallization and dedicated spray preparation for high-resolution scanning microprobe matrix-assisted laser desorption/ionization imaging mass spectrometry (SMALDI-MS) of tissue and single cells. *Rapid Communications in Mass Spectrometry* **24**, 355–364, https://doi.org/10.1002/rcm.4401 (2010).
75. Koestler, M. *et al.* A high-resolution scanning microprobe matrix-assisted laser desorption/ionization ion source for imaging analysis on an ion trap/Fourier transform ion cyclotron resonance mass spectrometer. *Rapid Communications in Mass Spectrometry* **22**, 3275–3285, https://doi.org/10.1002/rcm.3733 (2008).
76. Guenther, S., Koestler, M., Schulz, O. & Spengler, B. Laser spot size and laser power dependence of ion formation in high resolution MALDI imaging. *International Journal of Mass Spectrometry* **294**, 7–15, https://doi.org/10.1016/j.ijms.2010.03.014 (2010).
77. Liebisch, G. *et al.* Shorthand notation for lipid structures derived from mass spectrometry. *J Lipid Res* **54**, 1523–1530, https://doi.org/10.1194/jlr.M033506 (2013).
78. Robichaud, G., Garrard, K. P., Barry, J. A. & Muddiman, D. C. MSiReader: An Open-Source Interface to View and Analyze High Resolving Power MS Imaging Files on Matlab Platform. *Journal of The American Society for Mass Spectrometry* **24**, 718–721, https://doi.org/10.1007/s13361-013-0607-z (2013).
79. Murphy, R. C. *Tandem Mass Spectrometry of Lipids: Molecular analysis of complex lipids* (Royal Society of Chemistry, 2014).

Acknowledgements

V.G. is grateful for a doctoral fellowship (DAAD-GSSP-2015, ID:91566181) of the German Academic Exchange Service (DAAD). This work was supported by grants from the Deutsche Forschungsgemeinschaft (DFG, Sp 314/13-1) and the Medical Faculty of Justus Liebig University Giessen, Germany. We thank Bianca Pfeiffer for excellent technical assistance.

Author Contributions

V.G., S.K., E.B.V. and B.S. designed the experiments. V.G., S.K. performed the experiments. V.G., S.K., D.R.B., E.B.V. and B.S. analyzed the data. E.B.V and B.S. supervised the research. V.G., S.K., D.R.B., E.B.V. and B.S. wrote the manuscript. All authors reviewed the whole work, and edited and approved the manuscript.

Additional Information

Supplementary information accompanies this paper at https://doi.org/10.1038/s41598-019-39452-3.

Competing Interests: B.S. is a consultant of TransMIT GmbH, Giessen, Germany. D.R.B. is a part-time employee of TransMIT GmbH, Giessen, Germany. The other authors declare no competing interests.

Publisher's note: Springer Nature remains neutral with regard to jurisdictional claims in published maps and institutional affiliations.

CHAPTER III

3.2 Supporting information related to publication 2

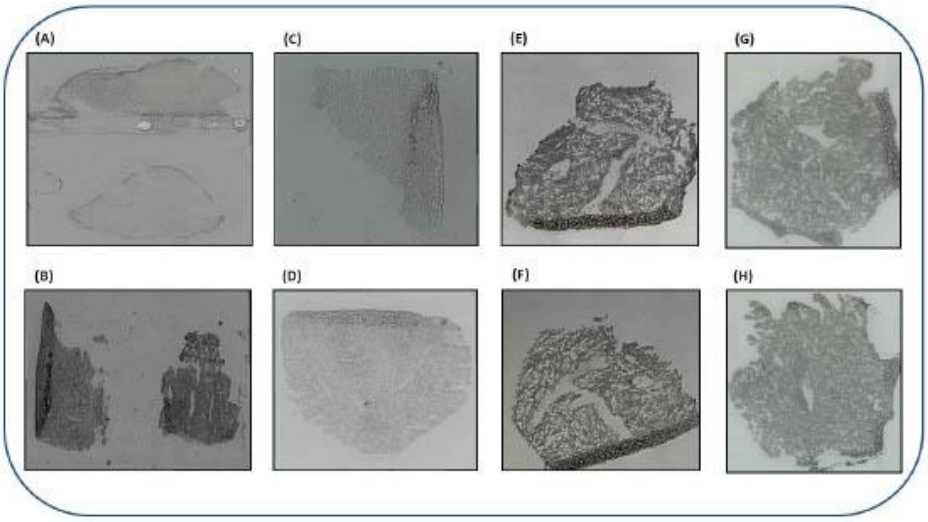

Fig. S1 Optimization of tissue sectioning procedure to obtain sections from fresh snap-frozen wild type (WT) and *Pex11β* knockout (KO) late fetal E19 mouse lungs for mass spectrometry imaging (MSI) experiments. A) Microscopic phase contrast image of paraformaldehyde (PFA)-fixed, optimal cutting temperature (OCT)-embedded WT and KO E19 lung tissue sections mounted on same glass slide. B) Microscopic image of WT and KO E19 lung tissue sections mounted on same glass slide without using any embedding material, problem of different section quality; WT section contains a fold on the left; the KO section on the right side is broken several times in longitudinal direction. C & D) Microscopic images of unequal thickness and folds in KO and WT E19 lung tissue sections mounted on different glass slides. E & F) Microscopic images of the unequal thickness of WT E19 lung tissue sections. G & H) Finally selected microscopic images of equal thickness (≈12 µm) of WT and KO E19 lung tissue sections mounted on different glass slides using deionized water (ice) as an adhesive. The small artefacts due to compression only at the rim can be omitted by choosing the region of interest in the measurement. The tissue sections, i) with no scratches and no broken parts, ii) no tissue foldings, iii) flat (same focal plane) and uniform thickness throughout the section, iv) no air bubbles and v) no other possible mechanical artefacts were considered as a good quality of sections and used for further MALDI MSI experiments.

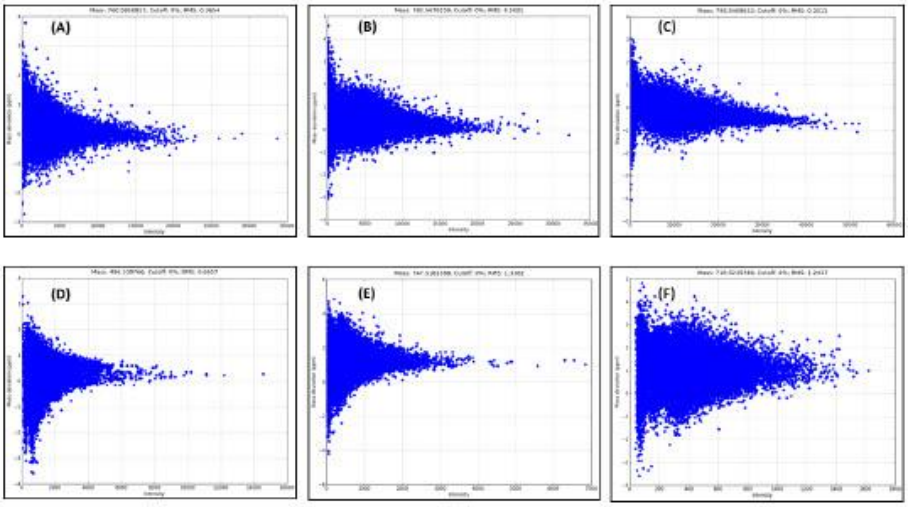

Fig. S2 High mass accuracy mass spectrometry imaging (MSI) data acquisition in positive- (A-D) and negative-ion mode (E-F). Mass deviation of lipid species as a function of intensities, root-mean-square error values (RMSE) of respective lipid species were represented in parts per million (RMSE ≤ 2ppm).

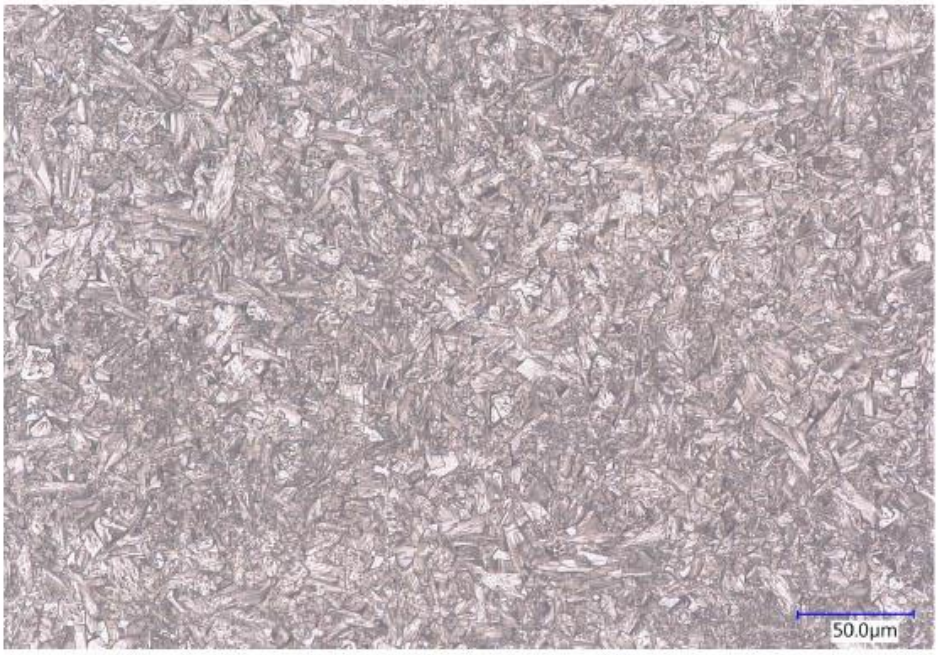

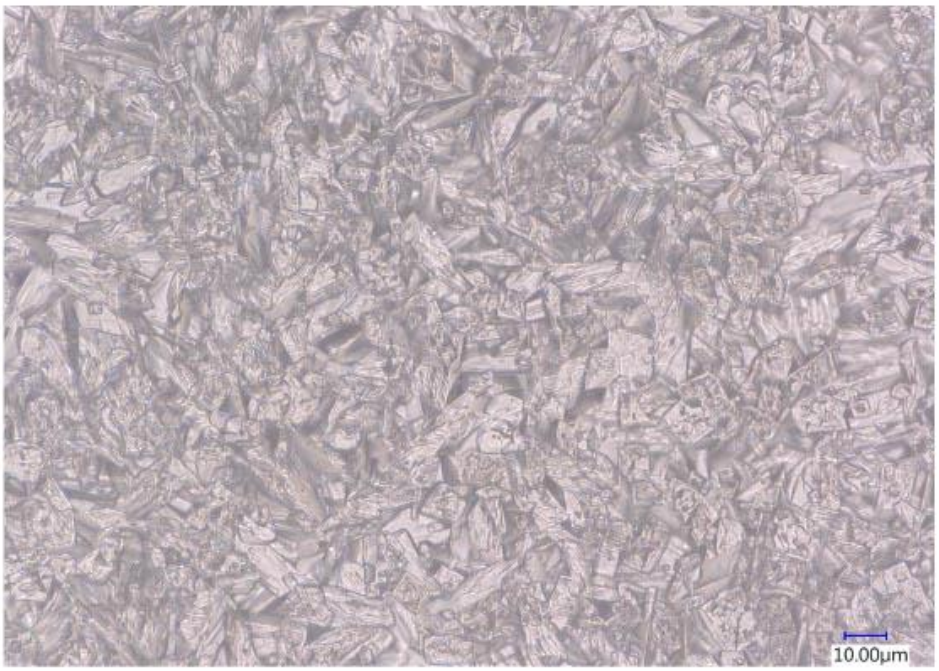

Fig. S3 Microscopic optical images of 2,5-dihydoxybenzoic acid (DHB) matrix crystals deposited on tissue surfaces using "SMALDIPrep" automatic pneumatic ultrafine matrix sprayer (TransMIT GmbH, Giessen, Germany). Optical images were obtained using a Keyence VHX-5000 digital microscope (Keyence Germany GmbH).

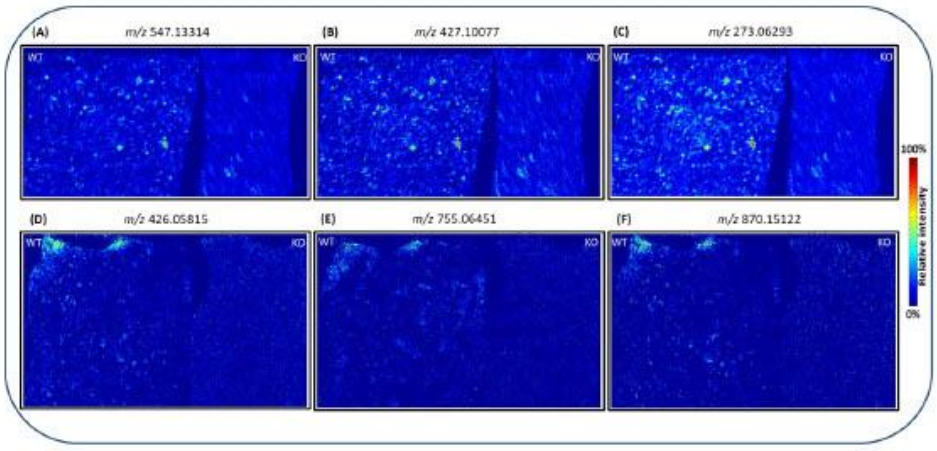

Fig. S4 Distribution of matrix cluster signals in replicate measurement samples of wild type (WT) and *Pex11β* knockout (KO) late fetal E19 mouse lung tissue sections. (A-C) Evenly distributed *para-*

nitroaniline (pNA) matrix cluster images in negative-ion mode. (D-F) Evenly distributed 2,5-dihydroxybenzoic acid (DHB) matrix cluster images in positive-ion mode.

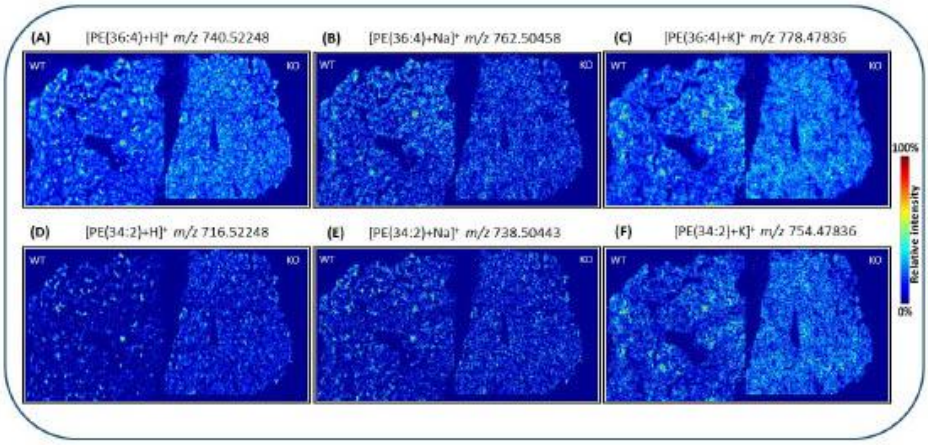

Fig. S5 Homogenous distribution of endogenous molecules with different charge carriers (H^+, Na^+, K^+) in wild type (WT) and *Pex11β* knockout (KO) late fetal E19 mouse lung tissue sections, measured by atmospheric-pressure MALDI mass spectrometry imaging (MSI) experiments. (A-C) Uniform distribution of PE(36:4) with different charge carriers, measured in positive-ion mode. (A) $[PE(36:4)+H]^+$, *m/z* 740.52248, (B) $[PE(36:4)+Na]^+$, *m/z* 762.50458 and (C) $[PE(36:4)+K]^+$,*m/z* 778.47836. (D-F) Uniform distribution of PE(34:2) with different charge carriers, measured in positive-ion mode. (D) $[PE(34:2)+H]^+$, *m/z* 716.52248 (E), $[PE(34:2)+Na]^+$, *m/z* 738.50443 and (F) $[PE(34:2)+K]^+$, *m/z* 754.47836.

Supplementary Table 4 Comparison of mean abundance values and ratios of lipid species between wild type (WT) and *Pex11β* knockout (KO) mice lung tissue sections using different normalization approaches in negative- and positive-ion mode.

Sample type	Mean abundance values and ratios		
	Without normalization	TIC normalization	Reference peak (matrix) normalization
Negative-ion mode, $[PG(34:1)-H]^-$, *m/z* 747.51815			
Wild type	526.23647	0.00156	1.07913
Knockout	279.68205	0.00036	0.67696
KO/WT	0.53	0.23	0.63
Positive-ion mode, $[SHexCer(t33:1)+K]^+$, *m/z* 820.46415			
Wild type	93.51792	0.00014	0.36839
Knockout	261.84857	0.00061	1.02317
KO/WT	2.80	4.36	2.78

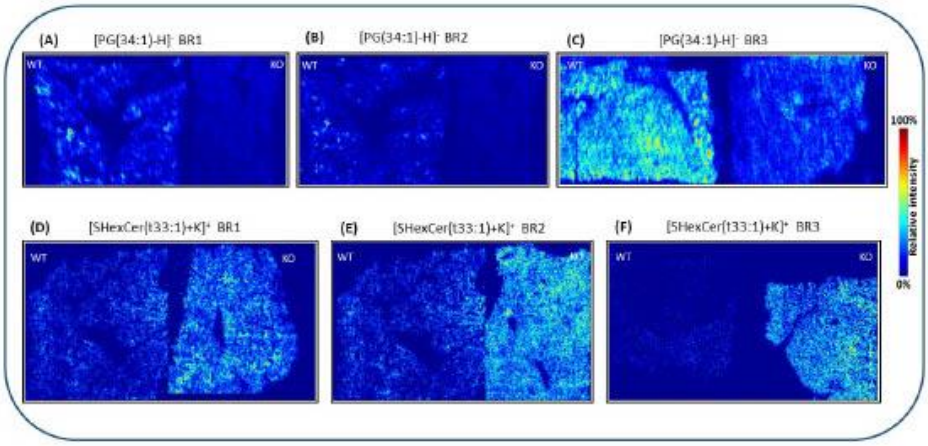

Fig. S6 Confirmation of differential abundance of lipid species in wild type (WT) and *Pex11β* knockout (KO) late fetal E19 mouse lung tissue sections from biological replicates (BR). (A-C) $[PG(34:1)-H]^-$, *m/z* 747.51815, (D-F) $[SHexCer\ (t33:1)+K]^+$, *m/z* 820.46415 differential expression, confirmed for biological replicates in negative- and positive-ion mode.

CHAPTER IV

Publication 3

Quantitative lipidomic analysis of mouse lung during postnatal development by electrospray ionization tandem mass spectrometry

Srikanth Karnati*, **Vannuruswamy Garikapati***, Gerhard Liebisch, Paul P Van Veldhoven, Bernhard Spengler, Gerd Schmitz, Eveline Baumgart-Vogt

(*Contributed equally to this work)

Published in PLoS ONE, 2018;13(9):e0203464

DOI: 10.1371/journal.pone.0203464

Supporting information: https://journals.plos.org/plosone/article?id=10.1371/journal.pone.0203464#sec023

PLOS ONE

RESEARCH ARTICLE

Quantitative lipidomic analysis of mouse lung during postnatal development by electrospray ionization tandem mass spectrometry

Srikanth Karnati[1☯¤]*, Vannuruswamy Garikapati[1,2☯], Gerhard Liebisch[3], Paul P. Van Veldhoven[4], Bernhard Spengler[2], Gerd Schmitz[3], Eveline Baumgart-Vogt[1]*

1 Institute for Anatomy and Cell Biology II, Division of Medical Cell Biology, Justus Liebig University Giessen, Giessen, Germany, **2** Institute of Inorganic and Analytical Chemistry, Justus Liebig University Giessen, Giessen, Germany, **3** Institute for Clinical Chemistry and Laboratory Medicine, University Hospital Regensburg, Regensburg, Germany, **4** Laboratory for Lipid Biochemistry and Protein Interactions, Campus Gasthuisberg, KU Leuven, Leuven, Belgium

☯ These authors contributed equally to this work.
¤ Current address: Institute for Anatomy and Cell Biology, Julius Maximilians University Würzburg, Würzburg, Germany
* Eveline.Baumgart-Vogt@anatomie.med.uni-giessen.de (EBV); Srikanth.Karnati@anatomie.med.uni-giessen.de, Srikanth.karnati@uni-wuerzburg.de (SK)

OPEN ACCESS

Citation: Karnati S, Garikapati V, Liebisch G, Van Veldhoven PP, Spengler B, Schmitz G, et al. (2018) Quantitative lipidomic analysis of mouse lung during postnatal development by electrospray ionization tandem mass spectrometry. PLoS ONE 13(9): e0203464. https://doi.org/10.1371/journal.pone.0203464

Editor: Harald Ehrhardt, Center of Pediatrics, GERMANY

Received: February 20, 2018

Accepted: August 21, 2018

Published: September 7, 2018

Data Availability Statement: All relevant data are within the paper and its Supporting Information files.

Funding: We thank German Academic Exchange Service (DAAD) for granting the Graduate School Scholarship Programme "Lipids in Nutrition and Metabolism" (DAAD-GSSP-2015). V.G. is a holder of a doctoral fellowship (DAAD-ID91566181) within this programme. Our study was supported also by LOM (Leistungsorientierte Mittel)

Abstract

Lipids play very important roles in lung biology, mainly reducing the alveolar surface tension at the air-liquid interface thereby preventing end-expiratory collapse of the alveoli. In the present study we performed an extensive quantitative lipidomic analysis of mouse lung to provide the i) total lipid quantity, ii) distribution pattern of the major lipid classes, iii) composition of individual lipid species and iv) glycerophospholipid distribution pattern according to carbon chain length (total number of carbon atoms) and degree of unsaturation (total number of double bonds). We analysed and quantified 160 glycerophospholipid species, 24 sphingolipid species, 18 cholesteryl esters and cholesterol from lungs of a) newborn (P1), b) 15-day-old (P15) and c) 12-week-old adult mice (P84) to understand the changes occurring during postnatal pulmonary development. Our results revealed an increase in total lipid quantity, correlation of lipid class distribution in lung tissue and significant changes in the individual lipid species composition during postnatal lung development. Interestingly, we observed significant stage-specific alterations during this process. Especially, P1 lungs showed high content of monounsaturated lipid species; P15 lungs exhibited myristic and palmitic acid containing lipid species, whereas adult lungs were enriched with polyunsaturated lipid species. Taken together, our study provides an extensive quantitative lipidome of the postnatal mouse lung development, which may serve as a reference for a better understanding of lipid alterations and their functions in lung development and respiratory diseases associated with lipids.

performance related resource allocation-funds of the Medical Faculty of the Justus Liebig University Giessen, Germany. Financial support by the Deutsche Forschungsgemeinschaft (DFG, Sp 314/13-1) is gratefully acknowledged. The research leading to these results also received funding from the European Community's Seventh Framework Programme (FP7/2007-2013) under grant agreement n° 202272, IP-Project LipidomicNet.

Competing interests: The authors declare that they have no conflict of interests in relation to the work described.

Abbreviations: PC, phosphatidylcholine; LPC, lysophosphatidylcholine; PC O, ether-phosphatidylcholine; PG, phosphatidylglycerol; PE, phosphatidylethanolamine; PE P, PE based plasmalogen; PI, phosphatidylinositol; PS, phosphatidylserine; SM, sphingomyelin; Cer, ceramide; HexCer, hexosylceramide; GP, glycerophospholipids; SP, sphingolipids; SL, sterol lipids; CE, cholesteryl esters; ESI, electrospray ionization; MS/MS, tandem mass spectrometry; P1, newborn mice; P15, 15-day-old mice; P84, 12-week-old adult mice.

Introduction

The lung is composed of more than 40 different pulmonary cell types, whose cellular membranes are enriched with lipids that perform a variety of functions including maintenance of the lung architecture [1–3]. In addition, alveolar epithelial type II cells of the pulmonary epithelium that are lining the alveolar surface synthesize and secrete surfactant into the alveolar space. Pulmonary surfactant is a complex mixture of lipids (phospholipids, triglycerides, fatty acids and cholesterol, etc.), surfactant proteins (A-D) and a small amount of carbohydrates. The majority of the pulmonary lipids comprise glycerophospholipids (GP) in which phosphatidylcholine (PC) is a predominant lipid class making up to 50% of the phospholipids. Phosphatidylethanolamine (PE) makes up to 20% of the lipids and phosphatidylserine (PS), phosphatidylinositol (PI) and phosphatidylglycerol (PG) constitute 12%-15% of the total phospholipid pool [4, 5].

Pulmonary lipids are important and diverse biomolecules that are involved in many biological processes. The thus far known functions of the major lung lipids include 1) prevention of alveolar collapse and preservation of bronchiolar patency [6], 2) improvement of mucociliary transport [7], 3) involvement in innate immunity and viral protection [8, 9], 4) action as potent intracellular signalling molecules in lung inflammation [10], 5) involvement of lipid mediators like leukotrienes, lipoxins and prostaglandins in specific reactions of inflammation and immunity [11, 12], 6) suppression of the proliferation, immunoglobulin production and cytotoxicity of lymphocytes [6]. In fact, alterations in whole lung lipid composition and/or deficiency of pulmonary surfactant lipids are closely associated with a) respiratory distress syndrome (RDS) [13], b) bronchopulmonary dysplasia (BPD) [13, 14], c) asthma [15], d) chronic obstructive pulmonary disease (COPD) [15, 16], e) cystic fibrosis [17], f) pneumonia [17, 18], g) lung injury [19], h) cancer [20] and in other lung diseases [6, 21].

High heterogeneity of lung tissue (e.g., bronchial versus alveolar regions) and differences in the lipid composition of individual pulmonary cell types create a complex mixture of lipid classes and molecular species associated with a set of potential complications. Despite these difficulties, several studies analyzed the lipid composition of lung tissue in different mammalian species such as in pig [22], rat [23], rabbit [24], monkey [24], dog [25], bovine [26], mice [27] and human [28] and also compared the lung lipid composition among different mammalian species [28, 29]. Actually, the major lipid classes were similar among different mammalian species and minor differences were observed only in the class of phospholipids. Interestingly, surfactant has proven to be highly diverse across species in its molecular design, especially in the concentration of individual surfactant proteins and its GP profile [30, 31]. Further, most of these studies focused on the analysis of PC, which are the prominent class of lipids in whole lung tissue and pulmonary surfactant. Furthermore, among the analyzed PC, dipalmitoylphosphatidylcholine (DPPC; PC 32:0), a species with two saturated acyl chains, is believed to be a major compound of the pulmonary surfactant [32]. However, recent studies on homeothermic/heterothermic mammalian species surfactant showed that DPPC is not the only major surfactant phospholipid component. In addition to major PC lipid molecular species, there are minor lipid classes such as PG and PI, which also play an important role in lung biology [33, 34].

Lung development in the majority of mammalian species (e.g., rat, mice and humans) continues postnatally. One important aspect of postnatal lung development is alveolarization, a process, in which the total number of terminal gas exchange units increase total size and surface area of the lung [35–37]. To address the lipidomic changes in the fetal and postnatal lung development, various studies were conducted in several mammalian species (e.g., rat, rabbit, lamb, pig and human) and in birds (e.g., duck and chicken) by using morphometric and biochemical approaches [35–41]. However, the existing lipidomic studies of postnatal lung

development primarily focused on the composition of surfactant PC and very few PG lipid species [31, 40, 41]. Dautel et al., recently reported postnatal developmental changes of mouse lung using a multi-omics approach [27]. These data are consistent with our results, but in comparison to their study (day7, day14 and 6–8 week old animals), we have used a wider time frame between birth (new born) and the 12^{th} week of life. Furthermore, the highly abundant cholesterol, as well as cholesteryl ester species were not analysed in the Dautel et al., study during postnatal development. Moreover, we performed direct infusion lipidomics using triple-quadrupole MS analytical setup and provided the quantitative information (nmol/mg wet weight) of individual lipid species of possible major lipid classes during postnatal development.

In our study, we employed electrospray ionization tandem mass spectrometry (ESI-MS/MS) to 1) investigate total lipid quantity and 2) to perform a detailed analysis of lipid classes (PC, LPC, PG, PS, PE, PE P, PI, SM, Cer, HexCer, CE, and cholesterol), and 3) the composition of individual lipid species (e.g. PC 32:0, PC 32:1 etc.), and 4) to analyse their distribution pattern based on the carbon chain length (total number of carbon atoms). Additionally, we analysed the degree of unsaturation (total number of double bonds) of whole lung homogenates in newborn, 15-day-old and 12-week-old adult mice in order to provide a detailed lipidomic information during the postnatal development. Our current study provides an extensive quantitative lipidome of mouse whole lung, which may serve as a reference for a better understanding of the development of lung and molecular mechanisms underlying various pulmonary diseases associated with the lipid alterations.

Materials and methods

Materials

Unless otherwise mentioned, all chemicals were procured from Sigma-Aldrich (Deisenhofen, Germany). Phospholipid standards were obtained from Avanti Polar Lipids (Alabaster, AL, USA). Cholesterol and cholesteryl ester standards of purity greater than 95% were obtained from Sigma (Taufkirchen, Germany). High purity cholesterol-(25, 26, 26, 26, 27, 27, 27-d7) was purchased from Cambridge Isotope Laboratories (Andover, MA, USA). HPLC grade solvents methanol and chloroform were obtained from Merck (Darmstadt, Germany). Analytical grade ammonium acetate and acetyl chloride were obtained from Sigma-Aldrich (Buchs, Switzerland). All other reagents used were of high purity and analytical grade.

Animal experiments

Twelve-week-old adult male mice, 15-day-old males and pregnant females of C57BL/6J genetic background were obtained from Charles River, Sulzfeld, Germany. Mice were kept on a normal laboratory diet and water *ad libitum* and housed in cages under standardized environmental conditions (12 hours light/dark cycle, 23˚C ± 1˚C and 55% ± 1% relative humidity) at the central animal facility of the Justus Liebig University Giessen, Germany. After delivery of the newborn pups in the morning, they were taken directly out of the animal facility. 15-day-old and 12-week-old adult mice were killed by cervical dislocation and the newborn pups were killed by decapitation. All experiments with laboratory mice were approved by the governmental ethics committee for animal welfare (Regierungspräsidium Giessen, Germany, permit number: V 54–19 C 20/15 c GI 20/23).

Lipid extraction and sample preparation

The newborn (P1), 15-day-old (P15) and 12-week-old adult (P84) male mice fur was vertically incised from the pelvis to the mandibles and removed to both sides. The abdomen was opened

and a bilateral pneumothorax was produced by puncturing the abdominal surface of the diaphragm. The sternum was cut in the middle and the thorax was opened with a thorax spanner. The lungs were isolated carefully and snap-frozen immediately.

Fresh snap-frozen lungs from P1, P15 and P84 male mice were homogenized with a Precellys homogenator (peQlab Biotech GmbH, Erlangen, Germany) at a concentration of 50 μg wet weight per μL. Homogenate corresponding to 2 mg wet weight was used for extraction, and lipids were extracted according to the procedure described by Bligh and Dyer [42]. Upon phase separation, the chloroform phase was transferred to a fresh tube and dried under a stream of nitrogen gas. For each lipid class (except for SM and PE P), two naturally not occurring lipid species were added as internal standards, to compensate for variations in sample preparation and ionization efficiency. PC 14:0/14:0 (28:0), PC 22:0/22:0 (44:0) for PC and SM, PE 14:0/14:0 (28:0), PE 20:0/20:0 (40:0) for PE and PE based plasmalogens (PE P), PS 14:0/14:0 (28:0), PS 20:0/20:0 (40:0), PG 14:0/14:0 (28:0), PG 20:0/20:0 (40:0), PI 16:0/16:0 (32:0), LPC 13:0, LPC 19:0, Cer 14:0, Cer 17:0 (d18:1/17:0), cholesterol-d7, CE 17:0 and CE 22:0 internal standards were added for the analysed lipid classes.

Mass spectrometric analysis of lipids

Lung homogenates were subjected to lipidome analysis by electrospray ionization-tandem mass spectrometry (ESI-MS/MS) in positive-ion mode as described [43–46]. Briefly, the samples were analyzed on a triple-quadrupole mass spectrometer (Quattro Ultima, Micromass, Manchester, UK) by direct flow injection analysis using an autosampler (HTS PAL, Zwingen, Switzerland) and a binary pump (Model 1100, Agilent, Waldbronn, Germany) with a solvent mixture of methanol containing 10 mM ammonium acetate and chloroform (3:1, v/v). A flow gradient was performed starting with a flow of 55 μL/min for 6 seconds followed by 30 μL/min for 1 minute and an increase to 250 μL/min for another 12 seconds. The mass spectrometer was equipped with electrospray ionization and operated in positive-ion mode using following tune parameters as capillary voltage, 3.5 kV; cone voltage, 110 V; collision energy, 30 V; collision gas, argon at a pressure of 0.13 Pa.

A precursor ion of *m/z* 184, which is specific for phosphocholine-containing lipids, was used for the analysis of phosphatidylcholine (PC), lysophosphatidylcholine (LPC) and sphingomyelin (SM) lipid species [43, 44]. Neutral loss scans of 141 and 185 were used for the phosphatidylethanolamine (PE) and phosphatidylserine (PS) respectively [47]. Fragment ions of *m/z* 364, 390, and 392 were used for the quantification of PE P-16:0, PE P-18:1 and PE P-18:0 plasmalogens according to Zemski et al. [48]. Neutral loss scans of 189 and 277 were used for the ammonium adducts of phosphatidylglycerol (PG) and phosphatidylinositol (PI) respectively [49]. Sphingosine (d18:1) based ceramides (Cer) were analysed using a fragment ion of *m/z* 264 [45]. Cholesterol and cholesteryl esters (CE) were quantified using a fragment ion of *m/z* 369 after selective derivatization of cholesterol using acetyl chloride [46].

After identification of relevant lipid species, selective ion monitoring analysis was performed to increase precision of the analysis of lipids. Quantification of different classes of lipid species was achieved by plotting the standard calibration curves of naturally occurring lipid species of PC 34:1, 36:2, 38:4, 40:0 and PC O-16:0/20:4; SM d18:1/16:0, 18:1, 18:0; LPC 16:0, 18:1, 18:0; PE 34:1, 36:2, 38:4, 40:6 and PE P-16:0/20:4; PS 34:1, 36:2, 38:4, 40:6; Cer d18:1/16:0, 18:0, 20:0, 24:1, 24:0; cholesterol, CE 16:0, 18:2, 18:1, 18:0. Correction of isotopic overlap of lipid species as well as data analysis were performed using self-programmed Excel Macros for all lipid classes according to principles described previously [43]. In brief, data analysis was performed with MassLynx software, which included the NeoLynx tool (Micromass) for averaging the scans at half peak height of the total ion count. NeoLynx generates centroid peak

data from the continuum spectra and allows selection of the intensities of certain peaks. Neolynx includes background subtraction and smoothing according to Savitzky Golay of the combined spectra. These NeoLynx results were exported to Excel spreadsheets and further processed by self-programmed Excel macros, which sort the results, correct for isotopic overlap, calculate the ratios to the internal standards, generate calibration curves, and calculate quantitative values [43].

Lipid species were annotated according to the proposal for shorthand notation of lipid structures derived from mass spectrometry [50]. Glycerophospholipid species annotation was based on the assumption of even numbered carbon chains only and presented as the sum of carbon chain length and degree of unsaturation, without specifying fatty acid location at the sn-1 or sn-2 position. SM species annotation was based on the assumption that sphingosine d18:1 is present [50]. Final quantities of lipid species and total lipid (sum of analysed lipid species) were calculated and expressed in nanomoles per milligram wet weight of tissue.

Statistics

All data are expressed as mean ± standard deviation (SD) with at least three mice (n = 3) for each group. Two-way analysis of variance (ANOVA) was calculated using GraphPad Prism Version 5.4 (GraphPad Software, San Diego, CA). Statistical comparisons among the groups were performed by Bonferroni post-test using the same software. A p-value of 0.05 or lower was considered as significant. Significance is indicated as **** $P < 0.0001$, *** $P < 0.001$, ** $P < 0.01$, $^{*}P < 0.05$.

Results

Overview and analysis of the pulmonary lipidome

The current study presents an extensive quantitative lipidome analysis of the total mouse lung homogenates during the postnatal development performed with the help of ESI-MS/MS. In total, we performed quantitative analysis of 160 GP, 24 SP, 18 CE species and cholesterol in different stages of the postnatal lung development (lungs of newborn, 15-day-old and 12-week-old adult mice). The glycerophospholipids consist of 35 PC, 15 LPC, 16 PG, 23 PE, 33 PE P, 15 PI and 23 PS lipid species. Sphingolipids consist of 15 SM, 7 Cer and 2 cerebroside (HexCer) lipid species. The overview of total lipid analyses from mouse lung homogenates during development is depicted in Fig 1A and 1B.

Total lipid quantitation during postnatal lung development

To evaluate the total lipid content in mouse lungs during the postnatal development, lipid quantity of phospholipids (sum of all analyzed GP classes), cholesteryl esters and cholesterol was calculated and expressed as nmol/mg wet weight (Fig 2). Total phospholipid content significantly increased during the development from P1 (28.26 ± 3.08 nmol/mg) to P84 (35.20 ± 1.42 nmol/mg) and from P15 (30.68 ± 0.85 nmol/mg) to P84 (35.20 ± 1.42 nmol/mg). However, we did not observe a statistically significant increase between P1 (28.26 ± 3.08 nmol/mg) and P15 (30.68 ± 0.85 nmol/mg). In contrast, cholesterol was significantly increased during progressing from P1 (7.9 ± 0.83 nmol/mg) to P15 (13.16 ± 0.70 nmol/mg) and a significant increase of the values was observed during the development from P1 (7.9 ± 0.83 nmol/mg) to adult lung (12.81 ± 0.55 nmol/mg). However, while developing from P15 to P84, cholesterol remained constant in P84 (12.81 ± 0.55 nmol/mg). The esterified cholesterol species remained at the level of <0.5 nmol/mg wet weight.

Individual lipid class (sum of the analysed lipid species) quantities are presented in S1 Table. For instance, the PC species gradually increased from the stage of P1 (16.47 ± 2.23

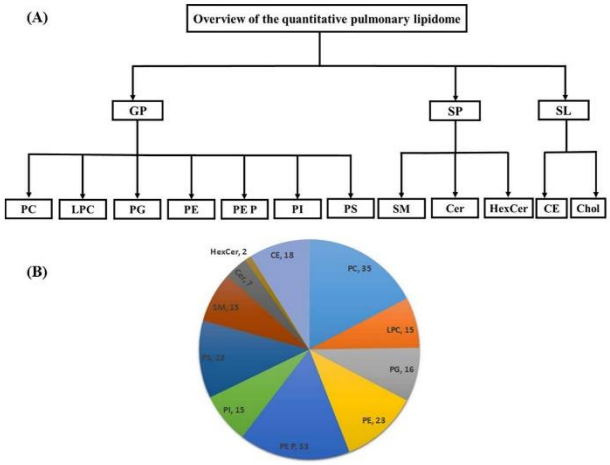

Fig 1. Overview of the quantitative lipidomic analyses of mouse lung homogenates during postnatal development by mass spectrometry. The numbers represent number of lipid species quantified for particular lipid class.

https://doi.org/10.1371/journal.pone.0203464.g001

nmol/mg) to P84 (18.03 ± 0.70 nmol/mg), but in P15 lung the PC species were lower (14.80 ± 0.57 nmol/mg) as compared to P1 and adult. In contrast, we observed a gradual increase in the total amount of PS, PI, PE, PE P, LPC and SM lipid classes during the postnatal development of the mouse lung. Among these, only PS (3.05 ± 0.19 to 5.35 ± 0.22 nmol/mg) and PE P (2.55 ± 0.23 to 3.82 ± 0.12 nmol/mg) showed statistical significance during the change from P1 to P84.

Individual lipid species analysis during postnatal lung development

To gain deeper insights into the postnatal developmental alterations, we evaluated the individual lipid species profile of respective lipid classes from mouse lung. The diacylglycerophospholipids were denoted with total number of carbon atoms and double bonds (C:D). LPC and CE species containing single fatty acids were denoted according to lipid species nomenclature.

Phosphatidylcholine species. In total, 35 different PC (24 PC, 11 PC O) species with different chain length and degree of unsaturation were documented in the lung extracts and their composition is depicted in Fig 3A and 3B. As expected, PC 32:0, PC 32:1, PC 30:0, PC 34:1 and PC 34:2 were the most abundant phosphatidylcholine species in the tested stages in the mouse lung. The predominant PC 32:0 increased significantly while progressing from P1 (4.11 ± 0.6 nmol/mg) to P84 (6.27 ± 0.2 nmol/mg). Similarly, PC 34:2, PC 36:4, PC 38:6, PC 38:4 and PC 40:6 lipid species were significantly elevated in P84 as compared to P1 (Fig 3A & 3B).

In contrast, monounsaturated lipid species (total number of double bonds = 1) PC 34:1 showed a significant reduction during the development from P1 (2.23 ± 0.23 nmol/mg) to P15 (1.73 ± 0.06 nmol/mg) and remained constant in P84 (1.79 ± 0.09 nmol/mg). Similarly, the values of PC 32:1 also significantly dropped during the maturation from P1 (4.08 ± 0.6 nmol/mg) to P15 (2.21 ± 0.19 nmol/mg) and thereafter slightly increased from the stage P15 to P84 (2.74 ± 0.11 nmol/mg). The monounsaturated lipid species (PC 30:1, 32:1, 34:1) were elevated in P1 lungs (Fig 3A).

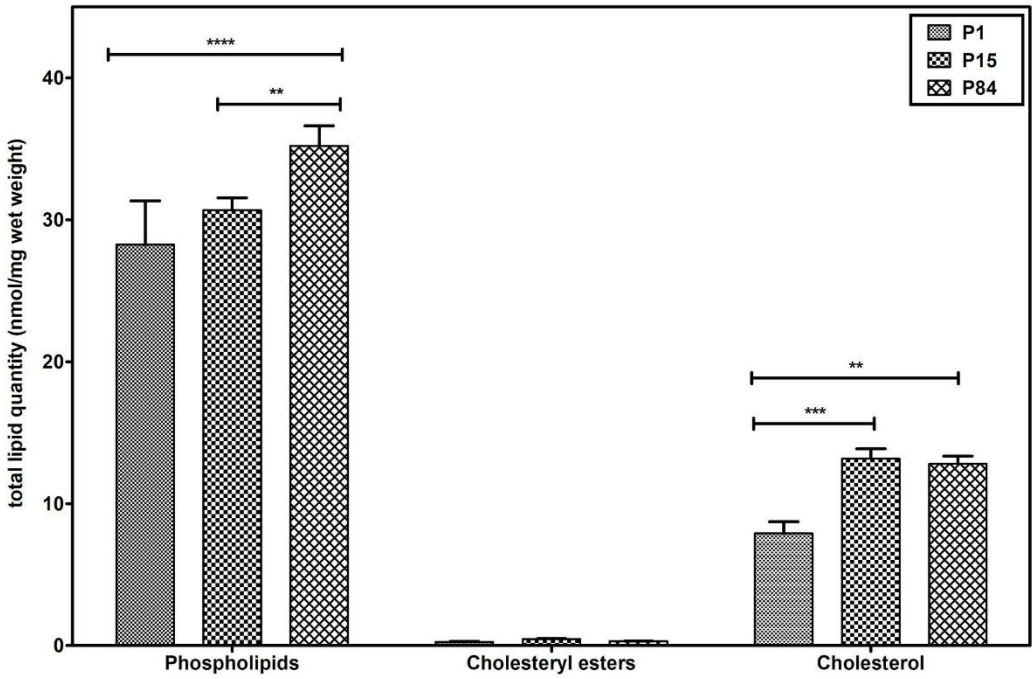

Fig 2. Total lipid quantity of phospholipids, cholesteryl esters and cholesterol in mouse lung during postnatal development. Displayed are nmol/mg wet weight of the lipid class of all analyzed lipid species. Values are represented as mean ± SD, p-value summary: **** $P < 0.0001$, *** $P < 0.001$, ** $P < 0.01$. Where significance is not mentioned, values are considered as being not significant. Phospholipids represents the sum of PC, LPC, PE, PE P, PG, PI, PS, and SM.

https://doi.org/10.1371/journal.pone.0203464.g002

The PC 30:0 gradually increased from the stage of P1 (1.3 ± 0.1 nmol/mg) to P15 (1.8 ± 0.07 nmol/mg) and then significantly decreased in P84 (0.91 ± 0.01 nmol/mg). Interestingly, higher levels of PC 30:0 were detected in P15 lungs in comparison to P1 and P84.

The analyzed ether-phosphatidylcholine (PC O) lipid species were present at low concentrations and their quantitative information during postnatal pulmonary development is showed in Fig 3B.

Lysophosphatidylcholine species. In total, 15 different lysophosphatidylcholine lipid species were analyzed and their composition pattern is depicted in Fig 4. The major LPC species detected were LPC 16:0 followed by 18:0, 18:1, 16:1, 18:2 and 20:4. The values of LPC 16:0 significantly increased during the maturation from P1 (0.103 ± 0.02 nmol/mg) to P15 (0.210 ± 0.01 nmol/mg) and P1 to P84 (0.212 ± 0.03 nmol/mg). Similarly, during development process from newborn to adult the amounts of all other LPC species including LPC 18:0, polyunsaturated LPC species 18:2 and 20:4 increased. Remaining LPC species occurred at lower concentrations and did not show any significant differences.

Phosphatidylglycerol species. We analyzed 16 individual lipid species of phosphatidylglycerol and their composition during the postnatal lung development is represented in Fig 5. As expected, PG 34:1, PG 34:2, PG 32:0 and PG 32:1 constituted highly abundant lipid species that were detected in all three groups. Interestingly, in contrast to PC 32:0, disaturated PG 32:0

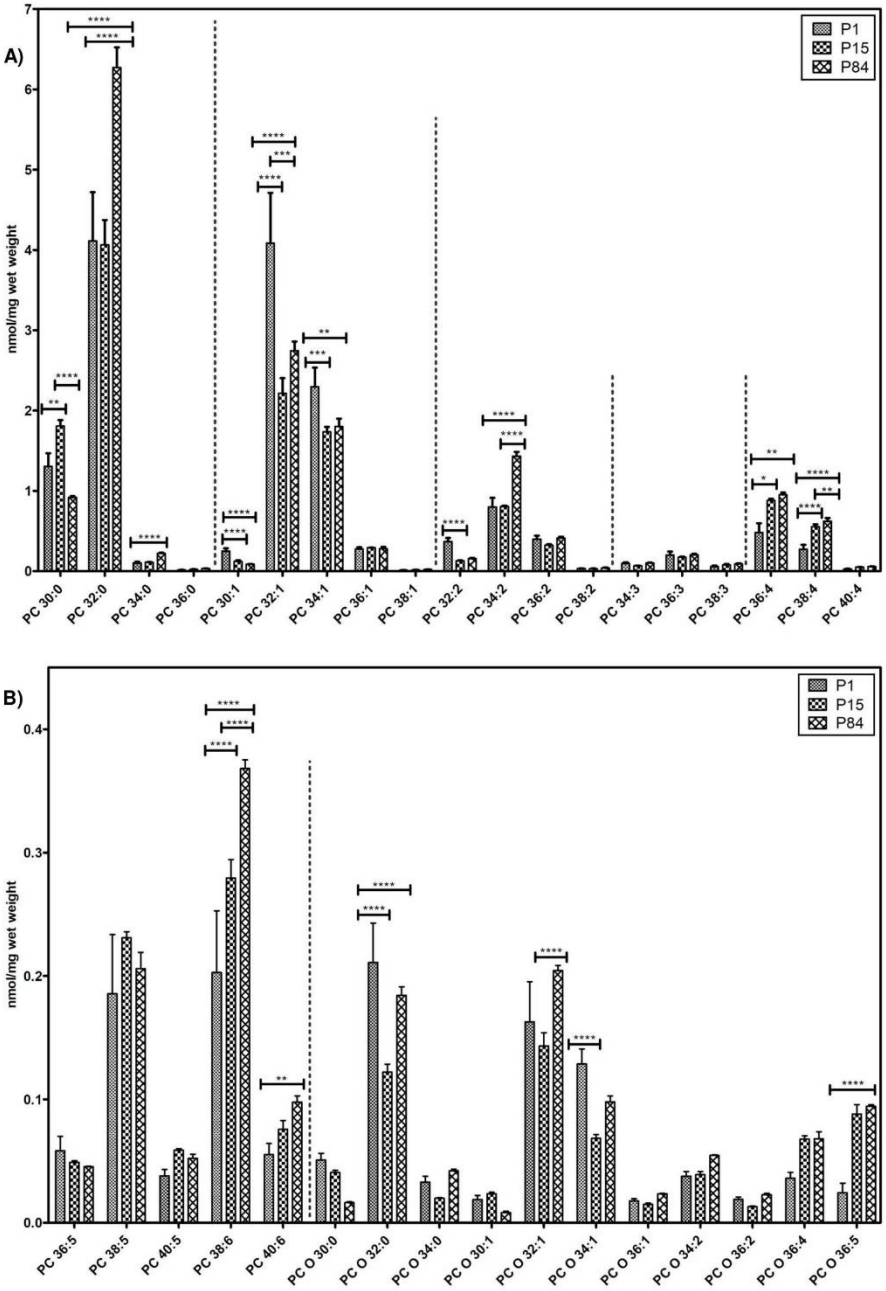
A)
P1
P15
P84
nmol/mg wet weight
PC 30:0
PC 32:0
PC 34:0
PC 36:0
PC 30:1
PC 32:1
PC 34:1
PC 36:1
PC 38:1
PC 32:2
PC 34:2
PC 36:2
PC 38:2
PC 34:3
PC 36:3
PC 38:3
PC 36:4
PC 38:4
PC 40:4
B)
P1
P15
P84
nmol/mg wet weight
PC 36:5
PC 38:5
PC 40:5
PC 38:6
PC 40:6
PC O 30:0
PC O 32:0
PC O 34:0
PC O 30:1
PC O 32:1
PC O 34:1
PC O 36:1
PC O 34:2
PC O 36:2
PC O 36:4
PC O 36:5

Fig 3. Composition of individual phosphatidylcholine (PC) and ether-phosphatidylcholine (PC O) lipid species during postnatal development of mouse lung. Values are represented as nmol/mg wet weight. A) PC B) PC and PC O. Values are mean ± SD, p-value summary: **** $P < 0.0001$, *** $P < 0.001$, ** $P < 0.01$, * $P < 0.05$. Where significance is not mentioned, values are considered as being not significant.

https://doi.org/10.1371/journal.pone.0203464.g003

decreased while progressing from P1 to P15. Notably, monounsaturated PG 32:1 significantly dropped in P84 (0.075 ± 0.002 nmol/mg) as compared to P1 (0.205 ± 0.04 nmol/mg). Similarly, the values of PG 34:1 dropped in P15 as compared to P1 and slightly increased while maturing from P15 to P84.

In contrast, diunsaturated (total number of double bonds = 2) PG 34:2 shows a significant increase during the development from P1 (0.117 ± 0.023 nmol/mg)) to P15 (0.173 ± 0.020 nmol/mg) and from P15 to P84 (0.367 ± 0.016 nmol/mg).

Similar to PC 30:0, the PG 30:0 was higher in P15 in comparison to P1 and P84. Interestingly, we detected higher levels of PG 36:4 in P15 lungs. Remaining PG lipid species did not show any statistically significant differences during development.

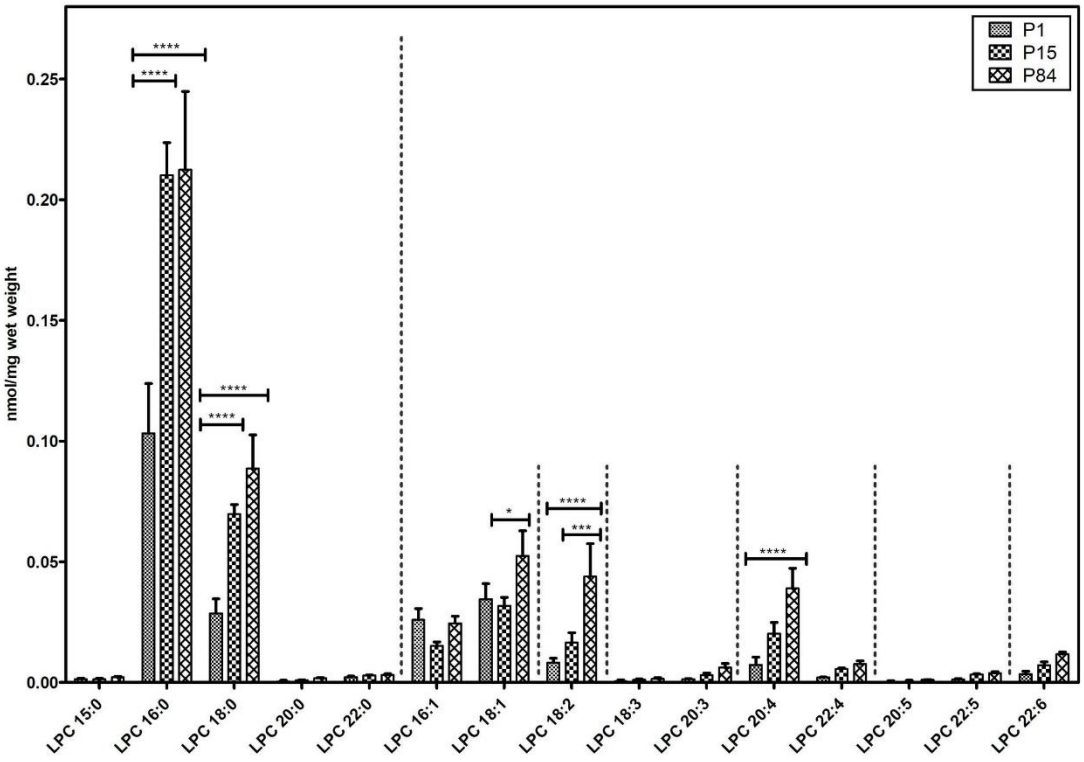

Fig 4. Composition of individual lysophosphatidylcholine (LPC) lipid species during postnatal development of mouse lung. Values are represented as nmol/mg wet weight. Values are mean ± SD, p-value summary: **** $P < 0.0001$, *** $P < 0.001$, ** $P < 0.01$, * $P < 0.05$. Where significance is not mentioned, values are considered as being not significant.

https://doi.org/10.1371/journal.pone.0203464.g004

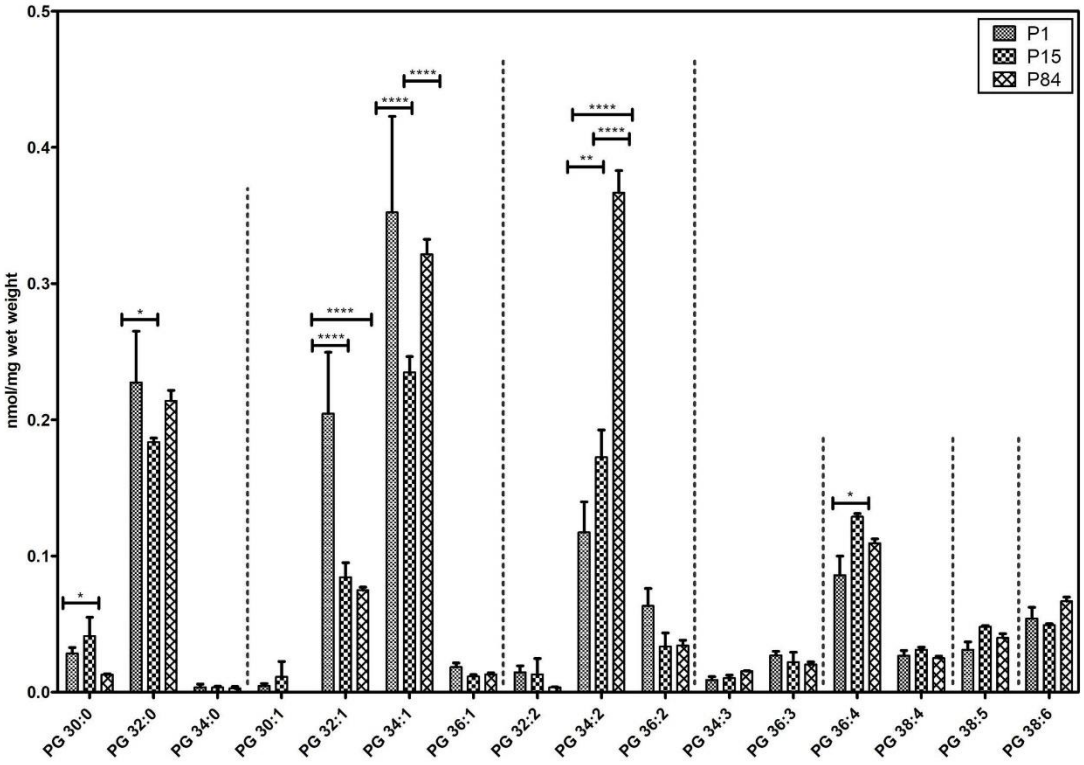

Fig 5. Composition of individual phosphatidylglycerol (PG) lipid species during postnatal development of mouse lung. Values are represented as nmol/mg wet weight. Values are mean ± SD, p-value summary: **** $P < 0.0001$, *** $P < 0.001$, ** $P < 0.01$, * $P < 0.05$. Where significance is not mentioned, values are considered as being not significant.

https://doi.org/10.1371/journal.pone.0203464.g005

Phosphatidylethanolamine species. Total 23 individual phosphatidylethanolamine lipid species were quantified and their composition is depicted in Fig 6. Interestingly, in comparison to the other lipid classes, PE lipids exhibited higher abundance of long chain polyunsaturated species. Strikingly, PE 38:4 showed higher abundance in all three groups in comparison to other PE species. Further, PE 38.4 significantly increased during maturation from P1 (0.50 ± 0.038 nmol/mg) to P15 (0.712 ± 0.046 nmol/mg) and remained constant in P84 (0.726 ± 0.066 nmol/mg). Similarly, PE 40:4, PE 40:5, PE 40:6 and PE 38:6 were relatively abundant in P84 and significantly increased during the development of the lung. In contrast, less abundant PE 34:1, 36:2 and 38:5 exhibited higher concentrations in P1 but then significantly decreased in P84. The concentration of other lipid species were low abundance and it did not show any significant differences in all three groups.

PE based plasmalogens. PE P-16:0, PE P-18:0 and PE P-18:1 (sn-1) individual plasmalogen compositions were calculated and their values have been displayed in Fig 7. Interestingly, PE P-16:0 (sn-1 substituent) plasmalogens are present in higher amounts in all three groups. Regardless of the alkenyl chain in sn-1, the plasmalogens containing PUFAs in sn-2 position

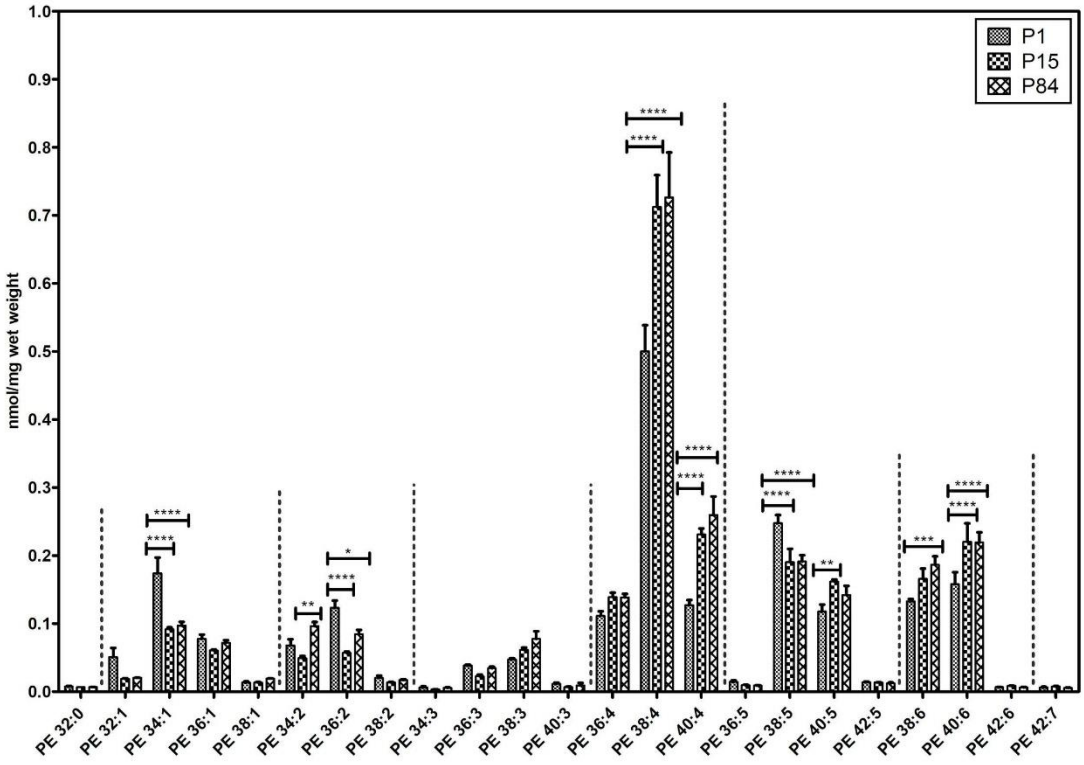

Fig 6. Composition of individual phosphatidylethanolamine (PE) lipid species during postnatal development of mouse lung. Values are represented as nmol/mg wet weight. Values are mean ± SD, p-value summary: **** $P < 0.0001$, *** $P < 0.001$, ** $P < 0.01$, * $P < 0.05$. Where significance is not mentioned, values are considered as being not significant.

https://doi.org/10.1371/journal.pone.0203464.g006

were the most abundant, represented mainly by 20:4 followed by 22:6, 22:4 and 22:5 in all tested groups.

The PE P-16:0/22:4 and PE P-16:0/22:6 significantly rose during the postnatal lung development (from P1 to P15 and P1 to P84). In contrast, the predominant PE P-16:0/20:4 and PE P-16:0/22:5 also rose during development from P1 to P15, however, a slight decrease from P15 to P84 was noted. Similarly, PE P-18:0 based 20:4, 22:4, 22:6 and PE P-16:0/18:1 lipid species increased significantly during the development process (P1 to P84). However, the values of low abundant PE P-16:0/16:1 were significantly lower in P84 as compared to P1. Other individual ethanolamine based plasmalogens were not significant during the postnatal lung development.

Phosphatidylinositol and phosphatidylserine species. The individual composition of 15 species of phosphatidylinositol and 23 species of phosphatidylserine is depicted in Fig 8A and 8B respectively. Similarly, to PE and PE based plasmalogens, both PI and PS were found to be highly enriched with polyunsaturated species. PI 38:4 was the most abundant during all developmental stages. PI 38:4 (0.806 ± 0.065 nmol/mg to 1.173 ± 0.027 nmol/mg), PI 36:4 were

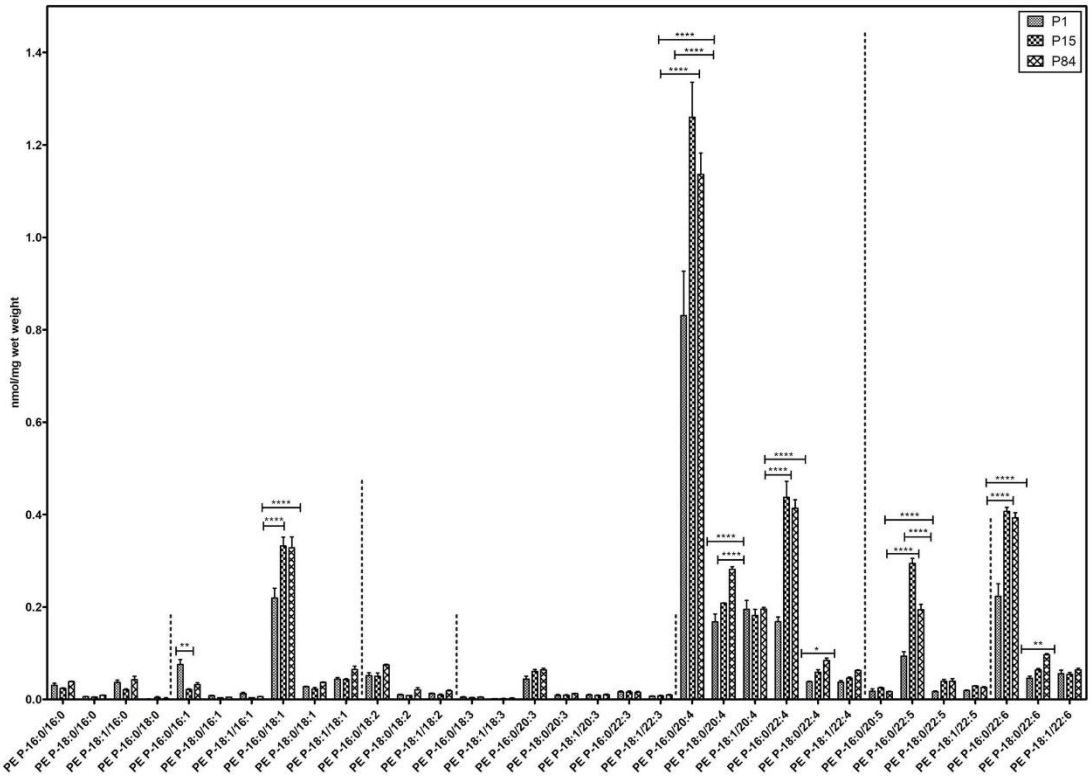

Fig 7. Composition of individual PE based plasmalogen (PE P) lipid species during postnatal development of mouse lung. Values are represented as nmol/mg wet weight. Values are mean ± SD, p-value summary: **** $P < 0.0001$, *** $P < 0.001$, ** $P < 0.01$, * $P < 0.05$. Where significance is not mentioned, values are considered as being not significant.

https://doi.org/10.1371/journal.pone.0203464.g007

significantly increasing while progressing from P1 to P84, whereas less abundant PI 36:2 and PI 38:5 species were higher in newborn and significantly gradually decreasing during the postnatal lung development (Fig 8A).

Among PS, polyunsaturated species (total number of double bonds >2) 40:4, 40:5, 40:6, 38:4 and the PS 36:1 were highly abundant in all stages of lung development. PS 40:4 was significantly gradually increasing from the phase of P1 (0.566 ± 0.04 nmol/mg) to P15 (1.218 ± 0.09) and from P15 to P84 (1.381 ± 0.06 nmol/mg). PS 38:4 and 36:1 species followed the same pattern (rise from P1 to P15 and P15 to P84). In addition, PS 36:2, 38:3 and 40:6 was detected in P1 and their increase was observed in P84. Among the PS species, PS 40:5 exhibited higher levels in P15 (0.827 ± 0.039 nmol/mg) as compared to P1 (0.335 ± 0.021 nmol/mg) and P84 (0.662 ± 0.031nmol/mg). The other analyzed PS species did not reach significance during lung development (Fig 8B).

Sphingomyelin and ceramide species. Within sphingolipids, individual 15 sphingomyelin, 7 ceramide and 2 cerebroside species compositions are depicted in Fig 9A and 9B respectively. SM 34:1 was the most dominant SM species in all developmental stages and gradually,

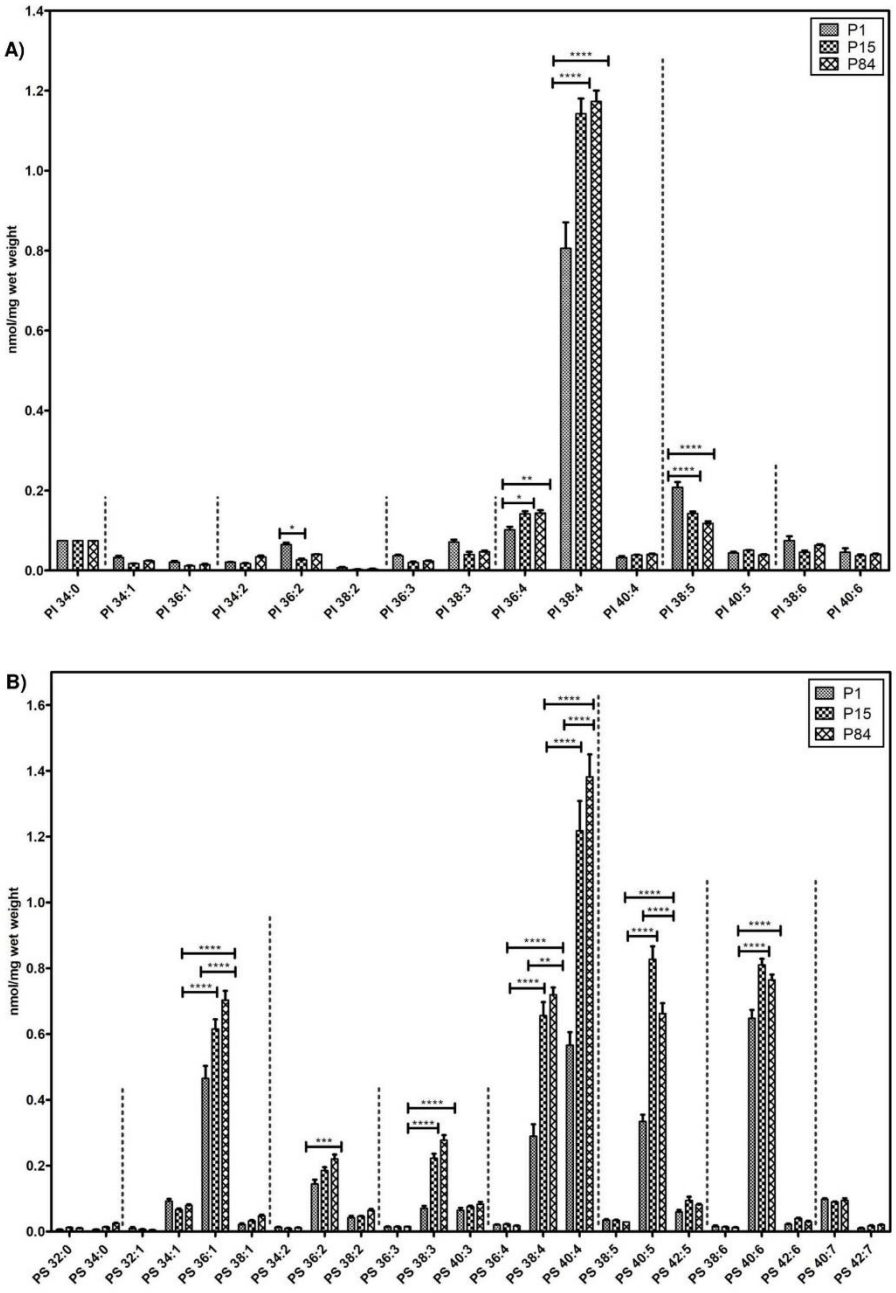
A)
P1
P15
P84
nmol/mg wet weight
PI 34:0
PI 34:1
PI 36:1
PI 34:2
PI 36:2
PI 38:2
PI 36:3
PI 38:3
PI 36:4
PI 38:4
PI 40:4
PI 38:5
PI 40:5
PI 38:6
PI 40:6
B)
P1
P15
P84
nmol/mg wet weight
PS 32:0
PS 34:0
PS 32:1
PS 34:1
PS 36:1
PS 38:1
PS 34:2
PS 36:2
PS 38:2
PS 36:3
PS 38:3
PS 40:3
PS 36:4
PS 38:4
PS 40:4
PS 38:5
PS 40:5
PS 42:5
PS 38:6
PS 40:6
PS 42:6
PS 40:7
PS 42:7

Fig 8. Composition of individual phosphatidylinositol (PI) and phosphatidylserine (PS) lipid species during postnatal development of mouse lung. Values are represented as nmol/mg wet weight. A) PI B) PS. Values are mean ± SD, p-value summary: "****" $P < 0.0001$, "***" $P < 0.001$, "**" $P < 0.01$, "*" $P < 0.05$. Where significance is not mentioned, values are considered as being not significant.

https://doi.org/10.1371/journal.pone.0203464.g008

but significantly increasing from the phase of P1 (0.46 ± 0.052 nmol/mg) to P15 (0.716 ± 0.05 nmol/mg), and thereafter slightly increasing from P15 to P84 (0.821 ± 0.057 nmol/mg). Similarly, SM 42:2 followed the same pattern during development.

The very long chain SM lipid species 40:1, 42:1and 42:3 were significantly rising during the postnatal lung development and their elevated levels were detected in P84 (Fig 9A).

Cer d18:1/16:0 was present in higher amounts in P15 lungs in comparison to P1 and P84. The very long chain fatty acid containing ceramide lipid species Cer d18:1/24:0 exhibited higher levels in P84. Interestingly, both of the analyzed HexCer d18:1/16:0 and HexCer d18:1/24:1 was present at higher levels in P1 and a significant gradual decrease was observed during the postnatal lung development up to the stage of P84 (Fig 9B).

Cholesteryl esters. Eighteen esterified forms of cholesterol were analysed and their composition is depicted in Fig 10. Similar to LPC, the myristic acid (14:0) and palmitic acid (16:0) containing CE species were significantly elevated in the phase of P15 in comparison to P1 and P84. Oleic (18:1), palmitoleic (16:1) containing CE species were more elevated in P1 and significantly lowered during development. In contrast, linoleic (18:2) and arachidonic (20:4) acid containing CE species were significantly gradually increasing from the stage of P1 and reached higher levels in P84.

Furthermore, the distribution pattern of GP according to their carbon chain length (total number of carbon atoms), degree of unsaturation (total number of double bonds) was elaborated and the results are shown in S2 Table, S1 Fig. Overall, the PC and PG comprised higher amounts of lipid species with carbon chain length $\leq$36. Whereas PE, PS and PI contained higher amount of lipid species with carbon chain length >36.

Discussion

Lipids constitute a diverse group of biomolecules, playing many roles in lung biology, especially in reducing the surface tension of alveoli to prevent the alveolar collapse and thereby stabilizing the lung parenchyma. The lung major lipid classes originating either from the pulmonary surfactant or from the bronchoalveolar lavage fluid (BALF) were already partly characterized, but a detailed distribution of total lipid classes and of their individual lipid molecular species composition in mouse lung during its postnatal development however, are not fully understood. In our current study, we used direct flow injection electrospray ionization tandem mass spectrometry to provide the total lipid quantity, and significant stage specific alterations of individual lipid species during the process of mouse postnatal pulmonary development. Furthermore, we showed the distribution pattern of lipid classes according to their carbon chain length and degree of unsaturation during development process.

In the present study, we analyzed and quantified total 202 lipid species (GP, SP, and CE) and cholesterol of the pulmonary lipidome from the mouse lung homogenates of the P1, P15 and adult lungs (Fig 1A & 1B and Fig 2 & S1 Table). In general, an increase in the total lipid quantity (nmol/mg wet weight) of pulmonary tissue is a characteristic change during the lung development process. Our results revealed increased levels of the total phospholipid and cholesterol content during development. Indeed, these results are in consistence with the findings of Williams and colleagues as well as of Hahn, et al. in which rat lung and other organ lipids were studied during maturation [51, 52].

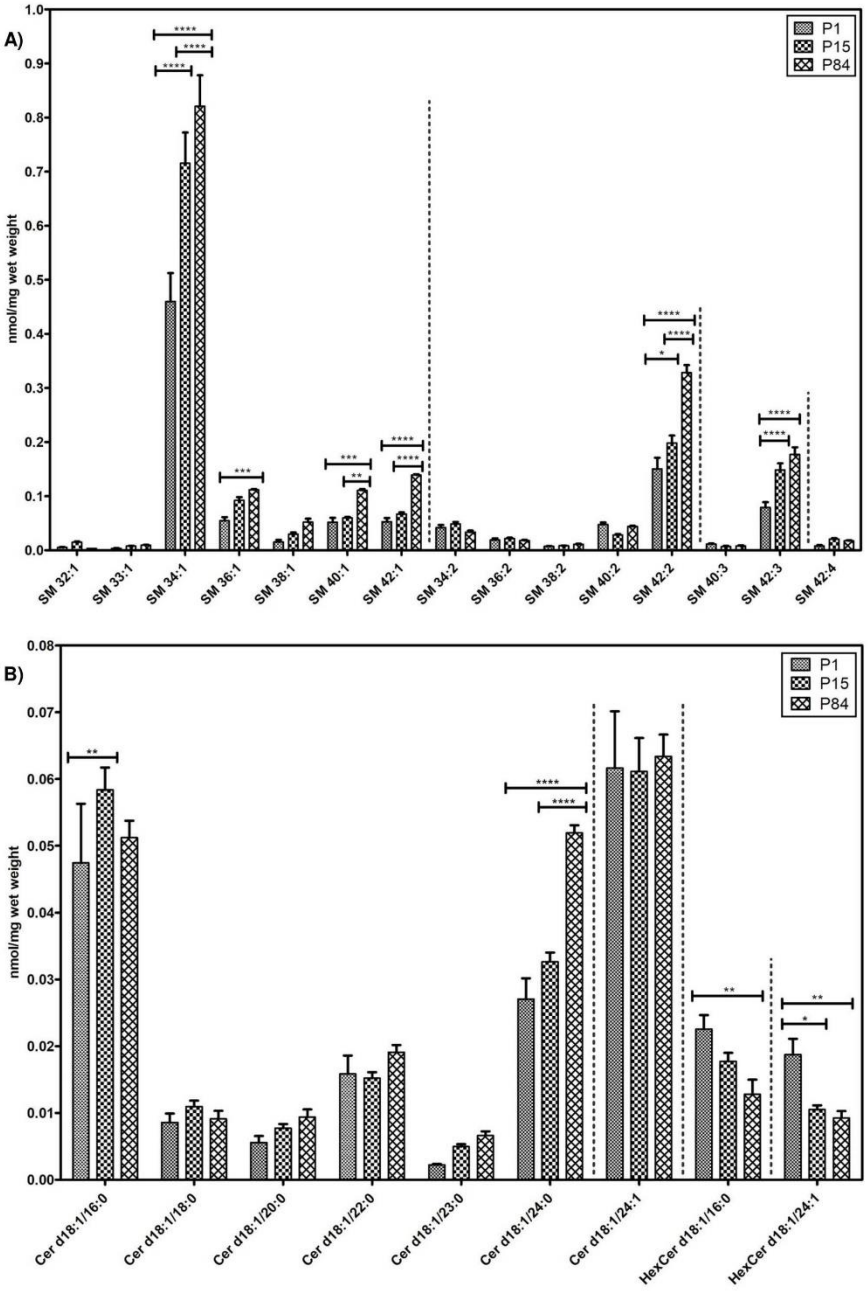
A)
P1
P15
P84
nmol/mg wet weight
SM 32:1
SM 33:1
SM 34:1
SM 36:1
SM 38:1
SM 40:1
SM 42:1
SM 34:2
SM 36:2
SM 38:2
SM 40:2
SM 42:2
SM 40:3
SM 42:3
SM 42:4
B)
P1
P15
P84
nmol/mg wet weight
Cer d18:1/16:0
Cer d18:1/18:0
Cer d18:1/20:0
Cer d18:1/22:0
Cer d18:1/23:0
Cer d18:1/24:0
Cer d18:1/24:1
HexCer d18:1/16:0
HexCer d18:1/24:1

Fig 9. Composition of individual sphingomyelin (SM) and ceramide (Cer) lipid species during postnatal development of mouse lung. Data are represented as nmol/mg wet weight. A) SM B) Cer. Values are mean ± SD, p-value summary: **** $P < 0.0001$, *** $P < 0.001$, ** $P < 0.01$, *$P < 0.05$. Where significance is not mentioned, values are considered as being not significant.

https://doi.org/10.1371/journal.pone.0203464.g009

Furthermore, pulmonary lipid distribution patterns of the whole lung tissue in comparison to the pulmonary surfactant lipid composition in different mammalian species were studied (see book chapters in ref) [3, 53]. In this context, it is important to mention that the distribution pattern of the lipids in the lung tissue is heterogeneous between distinct species. In general, PC's were the most predominant class of lipids of all tested species [32]. The second most abundant lipid class of the surfactant GP was PG, however, this lipid class was detected in lower amounts in the whole lung tissue. In contrast, PE represented the minor class of lipids in the surfactant but constituted second major lipid class following PC in the whole lung tissue. Similarly, SM and PS lipid classes were detected in lower amounts in the pulmonary surfactant, however, they also were described as being abundant in the whole lung tissue. In fact, our results of the lipid class distribution of the mouse lung homogenates are in agreement with these findings [3, 53]. Our data clearly indicate that PC and cholesterol occupy major parts of

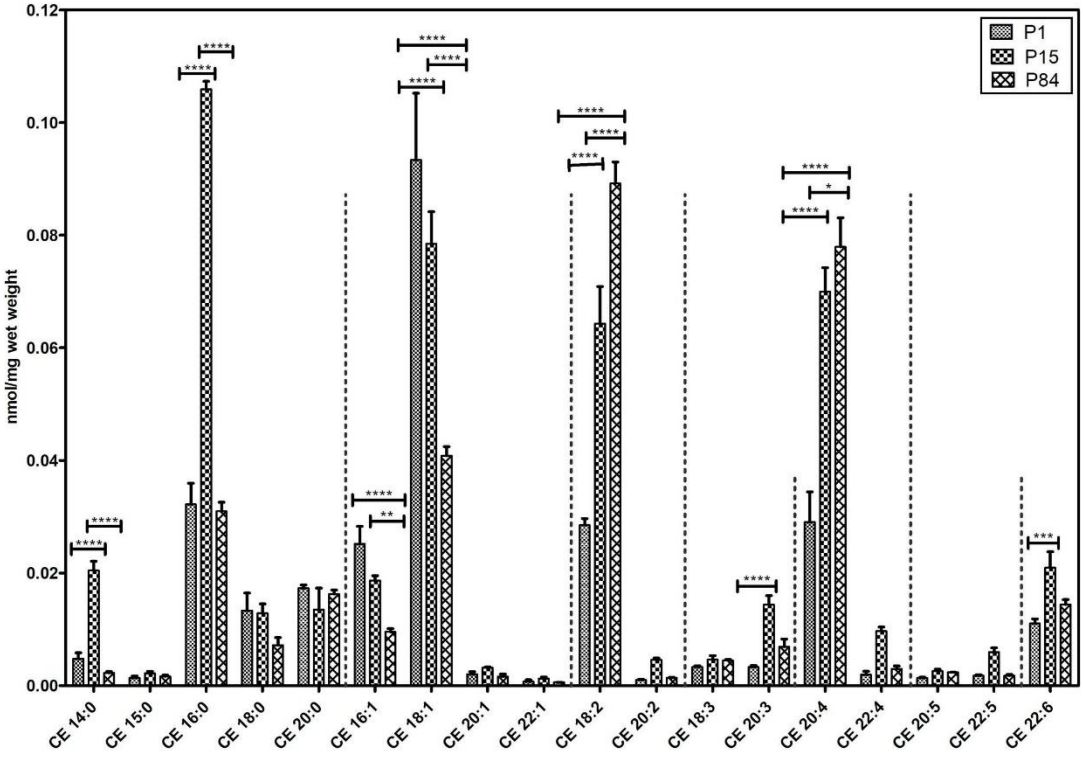

Fig 10. Composition of individual cholesteryl ester (CE) lipid species during postnatal development of mouse lung. Data are represented as nmol/mg wet weight. Values are mean ± SD, p-value summary: **** $P < 0.0001$, *** $P < 0.001$, ** $P < 0.01$, *$P < 0.05$. Where significance is not mentioned, values are considered as being not significant.

https://doi.org/10.1371/journal.pone.0203464.g010

the whole lung lipidome (Panel A in S2 Fig). Among the phospholipids, PC is the most dominant lipid class followed by PE (PE+PE P), PS, SM, PI and PG present during the postnatal mouse lung development (Panel B in S2 Fig). Based on these composition values, we calculated the molar ratios of lipid classes (S3 Table). For instance, the PC/LPC ratio is decreased from P1 to P15, and from P15 to P84. In contrast, SM/Cer molar ratio significantly increased from P1 to P15 and from P15 to P84.

Interestingly, we observed a significant increase in the concentration of cholesterol from the phase of newborn to P15 (Fig 2, S1 Table & Panel A in S2 Fig), suggesting that cholesterol may play an important role in the process of alveolarization. Cholesterol is an integral component of various cell membranes, involved in the maintenance of membrane fluidity, membrane functions and signal transduction. In fact, cholesterol is the major neutral lipid component of the lung and up to 80% of the cholesterol present in the lung is in surfactant [54], and it is considered as a protosurfactant in immature lungs, lungs with lack of septation and in saccular lungs [55]. Moreover, cholesterol enhances the adsorption of DPPC by increasing membrane fluidity and control the surface viscosity of the surfactant [56, 57].

In our study, we focused on the alterations of individual lipid species of mouse lungs during the postnatal development. Our results showed a significant increase in the abundance of PC 30:0 during the alveolarization (P1 to P15) (Fig 3A) process. These results are supported by previous observations on the postnatal development of the lung tissue and surfactant lipid analyses from 8-day-old mice and adult animals [41]. Bernhard and co-workers reported about significant alterations in the abundance of major PC lipid molecular species in the pulmonary surfactant of different mammalian species during lung development [31, 40, 41].

In contrast to PC findings of surfactant lipidome, we showed a significant gradual increase of PC 32:0 (most likely to be DPPC) during the postnatal lung development. DPPC is the primary surface-active material found in majority of the mammalian species pulmonary surfactant. Maintenance of adequate DPPC within air space is essential for normal lung function [58]. RDS is the major cause of mortality and morbidity in premature infants diagnosed with mainly DPPC deficiency in quantity and quality of pulmonary surfactant [59]. Currently, surfactant replacement therapy with added products of DPPC is an effective therapeutic strategy available for RDS management [60]. Interestingly, high contents of monounsaturated lipids of PC 32:1 and PC 34:1 was detected in P1 mice in comparison to P15 and adult lungs, suggesting that PC 32:1 might be involved in the establishment of the air-liquid interface in newborn animals. Furthermore, PC 34:1 is known to be crucial and plays an important role in the adsorption of DPPC immediately after birth [61, 62]. In contrast to mice, PC 30:0 is completely absent and PC 32:1 is minimal in nonalveolar species (birds), in which the lung contains capillaries instead of alveoli, suggesting that, PC 30:0 and PC 32:1 species are important and play an active dynamic role in the alveolarization process [30]. In this context, it is important to mention the recent findings that PC 30:0 inhibited macrophage-triggered proliferation of T-lymphocytes and decreased the production of reactive oxygen species (ROS) during alveolarization [63, 64]. Moreover, PC 30:0 was significantly reduced in the emphysema patients and infants with BPD as well as in the neonatal rat models of reduced alveolarization suggesting that PC 30:0 may serve as a diagnostic marker for alveolar size during diseases [65]. Similarly to these observations, in the pig model, PC 30:0 was found high in abundance in newborns and gradually decreased with age in adolescent pigs [31], whereas in humans and guinea pigs, PC 30:0 was increased during the lung development [41]. The specific functions of PC 30:0, PC 32:1 and PC 34:1 lipid species during postnatal lung development are not clear yet. Also, the molecular mechanism and alterations of lipid species during the lung development are not clear yet. These alterations may be specific for individual mammalian species, a supposition that requires further investigation.

Phosphatidylglycerol lipid concentrations are highly concentrated in the lung compared to other mammalian tissues [66]. It is well documented that PG lipids are involved in the adsorption and, spreading of surfactant over the epithelial surface, as well as influence innate immunity and protect against viral infections [9, 67, 68]. Interestingly, surfactant deficiency in premature infants and also in mouse models of BPD showed the complete absence of PG lipids [69]. Indeed, the presence of PG lipids in amniotic fluid is an indicator for the fetal lung maturity and PG lipids are known to be vital in the management of neonatal RDS and other obstetric conditions [70]. It is known that PG lipid species are crucial for the lung function. There are, however, no reports on the composition of PG 30:0 during the postnatal lung development. In fact, Bernhard and colleagues were not able to measure PG 30:0 from rat surfactant during the postnatal lung development [40]. Remarkably, in our study, we observed a significant increase in PG 30:0 abundance during alveolarization (P1 to P15), similar to PC 30:0, probably because of the high content of myristic acid during the postnatal lung development. In contrast to DPPC, we observed a significant decrease of abundance of DPPG during postnatal lung development. Recent findings suggest that DPPG interacts with vaccinia and variola virus strains and reduces the infection of pneumocytes in respiratory poxvirus infection [68]. Moreover, several reports demonstrated that PG 34:1 (palmitoyl-oleoyl-phosphatidylglycerol, POPG) acts as a potent antiviral lipid against influenza A and respiratory syncytial virus [9, 67]. Interestingly, we observed a high content of this antiviral lipid PG 34:1 (POPG) in the newborn mouse lungs in comparison to P15 and P84 (Fig 5), suggesting that they might improve the innate immunity against viruses during the perinatal period.

In addition to PC and PG, we measured other lipid species in the lung tissue such as PE, PI and PS (Figs 6, 8A & 8B). In contrast to PC and PG, we found that these lipid classes were found to be mostly enriched with long chain polyunsaturated species. Monounsaturated lipid species (PE 32:1) were found in high abundance in P1 in comparison to P15 and P84. In fact, long chain polyunsaturated species serve as substrates for the pro-inflammatory (leukotrienes, prostaglandins, etc.), as well as anti-inflammatory and pro-resolution (lipoxins, etc.) lipid mediators [71]. Furthermore, mass spectrometry imaging of adult mouse lungs showed that these long chain polyunsaturated lipids are highly abundant at the epithelial lining of airways [72]. We observed that 38:4 lipids were abundant in case of PE and PI lipid classes in all three age groups, which may serve as a source for arachidonic acid (AA) for the generation of lipid mediators. Proteomics data of a recent study revealed that proteins (cyclooxygenases, lipoxygenases, etc.) responsible for the generation of bioactive lipid mediators, are significantly upregulated in the adult mouse lungs, suggesting that these long chain polyunsaturated lipid species serve as a source for AA [27].

Quantitative information of less abundant species of these lipid classes would help to understand postnatal developmental alterations in detail. However, the mechanism of alterations of individual lipid species of these lipid classes during lung development needs to be further explored.

Plasmalogens are glycerophospholipids characterized by a vinyl ether linkage in sn-1 and an ester linkage in sn-2 position of the glycerol backbone. Plasmalogens are involved in the membrane dynamics, serve as an endogenous antioxidants, protect against ROS and prevent lipoprotein oxidation [73]. Plasmalogen biosynthesis starts in the peroxisomes and deficiency of plasmalogens is associated with various peroxisomal disorders [74] and other respiratory diseases like BPD [75], asthma and COPD [76]. We observed that PE-based plasmalogens are much higher abundant compared to ether-phosphatidylcholines (PC O) during the postnatal mouse lung development. In ethanolamine plasmalogens, PE P-16:0 plasmalogens comprised the highest amount, whereas, PE P-18:0 and PE P-18:1 made up a smaller amount (Fig 7). Interestingly, we observed a high content of 20:4, 22:6, 22:5 and 22:4 (most likely to be

arachidonic acid AA, docosahexaenoic acid DHA, docosapentaenoic acid DPA and adrenic acid)-rich plasmalogens (Fig 7). Further, the total quantities of plasmalogens (sum of all analyzed PE P species) were gradually increased from P1 to P84 during the postnatal lung development (S1 Table). These results are in consistent with the previous study, in which high abundance of PE P species were noted in adult mouse lungs during postnatal pulmonary developmental processes [27]. Arachidonic acid enriched plasmalogens seem to play an important role in immune defence and normal lung physiology [73]. Plasmalogens are reported to serve as a reservoir for the precursor molecules (e.g., AA, EPA, DHA, and DPA etc.) of eicosanoids, which are biologically active secondary lipid signalling messengers or for maresin and resolvins, lipid derivatives involved in the regulation of inflammation [77, 78]. Rüdiger and colleagues showed that addition of plasmalogens to surfactant-like phospholipid mixtures reduces surface tension [79] and high content of plasmalogens in tracheal aspirate of preterm infants reduces the risk of respiratory diseases [80]. Likewise, another study reported that high contents of plasmalogens protects the endothelial cells from hypoxia and ROS mediated stress [81].

Sphingolipids are primarily found in cell membranes and are involved in diverse biologic processes such as migration, proliferation, differentiation, senescence, cell death, autophagy, and efferocytosis [82]. In the lungs, sphingolipids are associated with cystic fibrosis, asthma, pulmonary edema, BPD, inflammation, lung injury and various types of lung cancers [83]. Ceramides show both proliferative and apoptotic effects depending on their concentration and chain length [84]. In analyzed SM lipid species, we detected that SM 34:1 lipid species as being predominant in all stages (Fig 9A). Both sphingomyelin 34:1 and ceramide species (Cer d18:1/16:0) showed high contents during alveolarization, especially in P15 (Fig 9A & 9B) mouse lungs, suggesting that, these lipid species are involved in the remodelling of tissue, also observed in the rat lung development [85]. In contrast to our findings (P1 to P15), a recent study on mouse lungs using LC-MS/MS approach showed no significant alterations in the Cer d18:1/16:0 levels from P7 to P14 [27]. The total content of sphingomyelin gradually increased with the age and the necessary transfer of biochemical substances across the semipermeable membranes (S1 Table).

So far, no reports are available about the developmental changes of less abundant cholesteryl ester species in the mouse lung. Saturated fatty acids such as myristic acid (14:0)- and, palmitic acid (16:0)-containing lysophosphatidylcholines (Fig 4) and cholesteryl esters (Fig 10) were found highly abundant during P15 in comparison to P1 and P84. Monounsaturated fatty acid (MUFA) containing CE species were elevated in the newborn, whereas polyunsaturated fatty acid (PUFA) containing CE species were elevated in adult lungs. Physicochemical properties of lipids depend on their chain length and their degree of unsaturation. In this aspect, we calculated the distribution patterns of glycerophospholipids according to their carbon chain length (number of carbon atoms). We observed that, PC and PG glycerophospholipids are highly abundant of lipid species with carbon chain length $C \leq 36$, whereas PE, PS and PI glycerophospholipids are highly abundant with long chain lipid species ($C > 36$). The majority of the monounsaturated glycerophospholipids were found to be highly abundant in newborns, whereas polyunsaturated lipid species were highly abundant in adult lungs (S1 Fig). In contrary, P15 lungs exhibited high contents of myristic (14:0)- and palmitic (16:0)-acid containing lipid species.

Limitations and weaknesses of the study

In the current study, we performed an extensive quantitative lipidomic analysis of P1, P15 and P84 mouse whole lung tissue homogenates to understand the changes occurring during

postnatal development. The data provides lipidomic alterations in mouse lung during developmental process. However, at this stage we are not able to discriminate the lipidomic changes occurring specifically at cellular (membrane or intracellular) and extracellular (alveolar) level. Comprehensive comparative (quantitative) lipidomic analysis of bronchoalveolar lavage fluid (BALF) and whole lung tissue homogenates in mice and other mammalian species in which alveolarization continues beyond extra-uterine life (e.g. rats) needs to be investigated in the near future, which can provide deeper insights for a better understanding of pulmonary developmental process at molecular and cellular level.

Conclusion

In our study, we have provided the total lipid quantity and given a detailed overview of lipid classes as well as absolute quantitative information on the individual lipid species and their distribution pattern according to carbon chain length and degree of unsaturation during postnatal mouse lung development using high-throughput tandem mass spectrometry. Our study provides an extensive quantitative lipidome of whole mouse lung tissue (including less abundant lipid species, neutral lipid components such as cholesterol and their esters), which may serve as reference for understanding the occurring lipid alterations, which in turn affect lung function during development or in pulmonary diseases.

Supporting information

S1 Table. Quantitative analyses of individual lipid classes in mouse lung during postnatal development. Values are expressed as nmol/mg wet weight and represented as mean ± SD.
(DOC)

S2 Table. Distribution of glycerophospholipids according to carbon chain length (total number of carbon atoms) and alkenyl chain (PE P) during postnatal development of mouse lung. Values are represented as nmol/mg wet weight.
(DOC)

S3 Table. Molar ratios of lipid classes. Displayed are the values of molar ratios of lipid classes. Values are represented as mean ± SD.
(DOC)

S1 Fig. Distribution of glycerophospholipids according to degree of unsaturation (total number of double bonds) during postnatal development of mouse lung. Saturated (total number of double bonds = 0), Monounsaturated (total number of double bonds = 1), Polyunsaturated (total number of double bonds $\geq$2) lipids.
(TIF)

S2 Fig. Total lipid composition of mouse lung during postnatal development. The displayed values are mol% of the respective lipid class of all analyzed lipids. Panel A) Glycerophospholipids (GP), sphingolipids (SP), cholesteryl esters (CE) and cholesterol. Panel B) only GP, SP without CE and cholesterol. Values are represented as mean ± SD, p-value summary: **** $P < 0.0001$, *** $P < 0.001$, ** $P < 0.01$, $^{*}P < 0.05$.
(TIF)

S1 File. Lipid profiling of mouse lung during postnatal development used in this study. The list of identified and quantified lipid molecules, experimental protocol, abbreviations and statistics.
(XLS)

Author Contributions

Formal analysis: Vannuruswamy Garikapati, Gerd Schmitz.

Investigation: Gerhard Liebisch.

Methodology: Gerhard Liebisch, Paul P. Van Veldhoven.

Supervision: Srikanth Karnati.

Validation: Bernhard Spengler, Eveline Baumgart-Vogt.

Visualization: Paul P. Van Veldhoven, Bernhard Spengler, Eveline Baumgart-Vogt.

Writing – review & editing: Srikanth Karnati, Vannuruswamy Garikapati.

References

1. Karnati S, Baumgart-Vogt E. Peroxisomes in mouse and human lung: their involvement in pulmonary lipid metabolism. Histochemistry and cell biology. 2008; 130(4):719–40. https://doi.org/10.1007/s00418-008-0462-3 PMID: 18665385.
2. Karnati S, Graulich T, Oruqaj G, Pfreimer S, Seimetz M, Stamme C, et al. Postnatal development of the bronchiolar club cells of distal airways in the mouse lung: stereological and molecular biological studies. Cell and tissue research. 2016; 364(3):543–57. https://doi.org/10.1007/s00441-015-2354-x PMID: 26796206.
3. Fisher AB. Chapter 22—Lung Lipid Composition and Surfactant Biology A2—Parent, Richard A. Comparative Biology of the Normal Lung (Second Edition). San Diego: Academic Press; 2015. p. 423–66.
4. Bernhard W, Haagsman HP, Tschernig T, Poets CF, Postle AD, van Eijk ME, et al. Conductive airway surfactant: surface-tension function, biochemical composition, and possible alveolar origin. American journal of respiratory cell and molecular biology. 1997; 17(1):41–50. https://doi.org/10.1165/ajrcmb.17.1.2594 PMID: 9224208.
5. Batenburg JJ. Surfactant phospholipids: synthesis and storage. The American journal of physiology. 1992; 262(4 Pt 1):L367–85. https://doi.org/10.1152/ajplung.1992.262.4.L367 PMID: 1566854.
6. Griese M. Pulmonary surfactant in health and human lung diseases: state of the art. Eur Respir J. 1999; 13(6):1455–76. https://doi.org/10.1183/09031936.99.13614779 PubMed PMID: WOS:000081775800036. PMID: 10445627
7. Blanco O, Perez-Gil J. Biochemical and pharmacological differences between preparations of exogenous natural surfactant used to treat Respiratory Distress Syndrome: Role of the different components in an efficient pulmonary surfactant. Eur J Pharmacol. 2007; 568(1–3):1–15. https://doi.org/10.1016/j.ejphar.2007.04.035 PubMed PMID: WOS:000248154800001. PMID: 17543939
8. Hallman M, Enhorning G, Possmayer F. Composition and Surface-Activity of Normal and Phosphatidylglycerol-Deficient Lung Surfactant. Pediatr Res. 1985; 19(3):286–92. https://doi.org/10.1203/00006450-198503000-00006 PubMed PMID: WOS:A1985ACJ2600006. PMID: 3838583
9. Numata M, Chu HW, Dakhama A, Voelker DR. Pulmonary surfactant phosphatidylglycerol inhibits respiratory syncytial virus-induced inflammation and infection. P Natl Acad Sci USA. 2010; 107(1):320–5. https://doi.org/10.1073/pnas.0909361107 PubMed PMID: WOS:000273559200056. PMID: 20080799
10. Stables MJ, Gilroy DW. Old and new generation lipid mediators in acute inflammation and resolution. Prog Lipid Res. 2011; 50(1):35–51. https://doi.org/10.1016/j.plipres.2010.07.005 PubMed PMID: WOS:000287059800004. PMID: 20655950
11. Samuelsson B, Dahlen SE, Lindgren JA, Rouzer CA, Serhan CN. Leukotrienes and Lipoxins—Structures, Biosynthesis, and Biological Effects. Science. 1987; 237(4819):1171–6. https://doi.org/10.1126/science.2820055 PubMed PMID: WOS:A1987J838900034. PMID: 2820055
12. Lewis RA, Austen KF, Soberman RJ. Leukotrienes and Other Products of the 5-Lipoxygenase Pathway—Biochemistry and Relation to Pathobiology in Human-Diseases. New Engl J Med. 1990; 323(10):645–55. PubMed PMID: WOS:A1990DW78700006. https://doi.org/10.1056/NEJM199009063231006 PMID: 2166915
13. Hallman M, Merritt TA, Pohjavuori M, Gluck L. Effect of surfactant substitution on lung effluent phospholipids in respiratory distress syndrome: evaluation of surfactant phospholipid turnover, pool size, and the relationship to severity of respiratory failure. Pediatr Res. 1986; 20(12):1228–35. https://doi.org/10.1203/00006450-198612000-00008 PMID: 3797115.

14. Clement A, Masliah J, Housset B, Just J, Garcia J, Grimfeld A, et al. Decreased phosphatidyl choline content in bronchoalveolar lavage fluids of children with bronchopulmonary dysplasia: a preliminary investigation. Pediatric pulmonology. 1987; 3(2):67–70. PMID: 3588058.

15. Yoder M, Zhuge Y, Yuan Y, Holian O, Kuo S, van Breemen R, et al. Bioactive lysophosphatidylcholine 16:0 and 18:0 are elevated in lungs of asthmatic subjects. Allergy, asthma & immunology research. 2014; 6(1):61–5. https://doi.org/10.4168/aair.2014.6.1.61 PMID: 24404395; PubMed Central PMCID: PMC3881403.

16. Hallman M, Spragg R, Harrell JH, Moser KM, Gluck L. Evidence of lung surfactant abnormality in respiratory failure. Study of bronchoalveolar lavage phospholipids, surface activity, phospholipase activity, and plasma myoinositol. The Journal of clinical investigation. 1982; 70(3):673–83. https://doi.org/10.1172/JCI110662 PMID: 6896715; PubMed Central PMCID: PMC370271.

17. Freedman SD, Katz MH, Parker EM, Laposata M, Urman MY, Alvarez JG. A membrane lipid imbalance plays a role in the phenotypic expression of cystic fibrosis in cftr(-/-) mice. Proc Natl Acad Sci U S A. 1999; 96(24):13995–4000. PMID: 10570187; PubMed Central PMCID: PMC24179.

18. Gunther A, Siebert C, Schmidt R, Ziegler S, Grimminger F, Yabut M, et al. Surfactant alterations in severe pneumonia, acute respiratory distress syndrome, and cardiogenic lung edema. American journal of respiratory and critical care medicine. 1996; 153(1):176–84. https://doi.org/10.1164/ajrccm.153.1.8542113 PMID: 8542113.

19. Lewis JF, Ikegami M, Jobe AH. Altered surfactant function and metabolism in rabbits with acute lung injury. Journal of applied physiology. 1990; 69(6):2303–10. https://doi.org/10.1152/jappl.1990.69.6.2303 PMID: 2077029.

20. Hakomori S. Tumor malignancy defined by aberrant glycosylation and sphingo(glyco)lipid metabolism. Cancer research. 1996; 56(23):5309–18. PMID: 8968075.

21. Griese M, Kirmeier HG, Liebisch G, Rauch D, Stuckler F, Schmitz G, et al. Surfactant lipidomics in healthy children and childhood interstitial lung disease. PloS one. 2015; 10(2):e0117985. https://doi.org/10.1371/journal.pone.0117985 PMID: 25692779; PubMed Central PMCID: PMC4333572.

22. Body DR. The phospholipid composition of pig lung surfactant. Lipids. 1971; 6(9):625–9. PMID: 4334827.

23. Godinez RI, Sanders RL, Longmore WJ. Phosphatidylglycerol in rat lung. I. Identification as a metabolically active phospholipid in isolated perfused rat lung. Biochemistry. 1975; 14(4):830–4. PMID: 1115773.

24. Rooney SA, Canavan PM, Motoyama EK. The identification of phosphatidylglycerol in the rat, rabbit, monkey and human lung. Biochimica et biophysica acta. 1974; 360(1):56–67. PMID: 4369311.

25. Pfleger RC, Thomas HG. Beagle Dog Pulmonary Surfactant Lipids—Lipid Composition of Pulmonary Tissue, Exfoliated Lining Cells, and Surfactant. Arch Intern Med. 1971; 127(5):863–&. https://doi.org/10.1001/archinte.127.5.863 PubMed PMID: WOS:A1971J354500006. PMID: 5109219

26. Yu S, Harding PGR, Smith N, Possmayer F. Bovine Pulmonary Surfactant—Chemical-Composition and Physical-Properties. Lipids. 1983; 18(8):522–9. https://doi.org/10.1007/Bf02535391 PubMed PMID: WOS:A1983RE05700004. PMID: 6688646

27. Dautel SE, Kyle JE, Clair G, Sontag RL, Weitz KK, Shukla AK, et al. Lipidomics reveals dramatic lipid compositional changes in the maturing postnatal lung. Scientific reports. 2017; 7:40555. https://doi.org/10.1038/srep40555 PMID: 28145528; PubMed Central PMCID: PMC5286405.

28. Clements JA, Nellenbogen J, Trahan HJ. Pulmonary surfactant and evolution of the lungs. Science. 1970; 169(3945):603–4. PMID: 5426782.

29. Postle AD, Heeley EL, Wilton DC. A comparison of the molecular species compositions of mammalian lung surfactant phospholipids. Comparative biochemistry and physiology Part A, Molecular & integrative physiology. 2001; 129(1):65–73. PMID: 11369534.

30. Bernhard W, Gebert A, Vieten G, Rau GA, Hohlfeld JM, Postle AD, et al. Pulmonary surfactant in birds: coping with surface tension in a tubular lung. American journal of physiology Regulatory, integrative and comparative physiology. 2001; 281(1):R327–37. https://doi.org/10.1152/ajpregu.2001.281.1.R327 PMID: 11404309.

31. Rau GA, Vieten G, Haitsma JJ, Freihorst J, Poets C, Ure BM, et al. Surfactant in newborn compared with adolescent pigs: adaptation to neonatal respiration. American journal of respiratory cell and molecular biology. 2004; 30(5):694–701. https://doi.org/10.1165/rcmb.2003-0351OC PMID: 14578213.

32. Veldhuizen R, Nag K, Orgeig S, Possmayer F. The role of lipids in pulmonary surfactant. Bba-Mol Basis Dis. 1998; 1408(2–3):90–108. https://doi.org/10.1016/S0925-4439(98)00061-1 PubMed PMID: WOS:000077203900003.

33. Lang CJ, Postle AD, Orgeig S, Possmayer F, Bernhard W, Panda AK, et al. Dipalmitoylphosphatidylcholine is not the major surfactant phospholipid species in all mammals. American journal of physiology

Regulatory, integrative and comparative physiology. 2005; 289(5):R1426–39. https://doi.org/10.1152/ajpregu.00496.2004 PMID: 16037124.

34. Egberts J, Beintema-Dubbeldam A, de Boers A. Phosphatidylinositol and not phosphatidylglycerol is the important minor phospholipid in rhesus-monkey surfactant. Biochimica et biophysica acta. 1987; 919(1):90–2. PMID: 3567218.

35. Burri PH, Dbaly J, Weibel ER. The postnatal growth of the rat lung. I. Morphometry. The Anatomical record. 1974; 178(4):711–30. https://doi.org/10.1002/ar.1091780405 PMID: 4592625.

36. Amy RW, Bowes D, Burri PH, Haines J, Thurlbeck WM. Postnatal growth of the mouse lung. Journal of anatomy. 1977; 124(Pt 1):131–51. PMID: 914698; PubMed Central PMCID: PMC1235518.

37. Zeltner TB, Burri PH. The postnatal development and growth of the human lung. II. Morphology. Respiration physiology. 1987; 67(3):269–82. PMID: 3575906.

38. Ricardo MJ Jr., Small GW, Myrvik QN, Kucera LS. Lipid composition of alveolar macrophage plasma membrane during postnatal development. Journal of immunology. 1986; 136(3):1054–60. PMID: 3001185.

39. Benson BJ, Kitterman JA, Clements JA, Mescher EJ, Tooley WH. Changes in phospholipid composition of lung surfactant during development in the fetal lamb. Biochimica et biophysica acta. 1983; 753 (1):83–8. PMID: 6688364.

40. Bernhard W, Schmiedl A, Koster G, Orgeig S, Acevedo C, Poets CF, et al. Developmental changes in rat surfactant lipidomics in the context of species variability. Pediatric pulmonology. 2007; 42(9):794–804. https://doi.org/10.1002/ppul.20657 PMID: 17659602.

41. Bernhard W, Hoffmann S, Dombrowsky H, Rau GA, Kamlage A, Kappler M, et al. Phosphatidylcholine molecular species in lung surfactant: composition in relation to respiratory rate and lung development. American journal of respiratory cell and molecular biology. 2001; 25(6):725–31. https://doi.org/10.1165/ajrcmb.25.6.4616 PMID: 11726398.

42. Bligh EG, Dyer WJ. A rapid method of total lipid extraction and purification. Canadian journal of biochemistry and physiology. 1959; 37(8):911–7. https://doi.org/10.1139/o59-099 PMID: 13671378.

43. Liebisch G, Lieser B, Rathenberg J, Drobnik W, Schmitz G. High-throughput quantification of phosphatidylcholine and sphingomyelin by electrospray ionization tandem mass spectrometry coupled with isotope correction algorithm. Biochimica et biophysica acta. 2004; 1686(1–2):108–17. https://doi.org/10.1016/j.bbalip.2004.09.003 PMID: 15522827.

44. Liebisch G, Drobnik W, Lieser B, Schmitz G. High-throughput quantification of lysophosphatidylcholine by electrospray ionization tandem mass spectrometry. Clinical chemistry. 2002; 48(12):2217–24. PMID: 12446479.

45. Liebisch G, Drobnik W, Reil M, Trumbach B, Arnecke R, Olgemoller B, et al. Quantitative measurement of different ceramide species from crude cellular extracts by electrospray ionization tandem mass spectrometry (ESI-MS/MS). Journal of lipid research. 1999; 40(8):1539–46. PMID: 10428992.

46. Liebisch G, Binder M, Schifferer R, Langmann T, Schulz B, Schmitz G. High throughput quantification of cholesterol and cholesteryl ester by electrospray ionization tandem mass spectrometry (ESI-MS/MS). Biochimica et biophysica acta. 2006; 1761(1):121–8. https://doi.org/10.1016/j.bbalip.2005.12.007 PMID: 16458590.

47. Brugger B, Erben G, Sandhoff R, Wieland FT, Lehmann WD. Quantitative analysis of biological membrane lipids at the low picomole level by nano-electrospray ionization tandem mass spectrometry. Proc Natl Acad Sci U S A. 1997; 94(6):2339–44. PMID: 9122196; PubMed Central PMCID: PMC20089.

48. Zemski Berry KA, Murphy RC. Electrospray ionization tandem mass spectrometry of glycerophosphoethanolamine plasmalogen phospholipids. Journal of the American Society for Mass Spectrometry. 2004; 15(10):1499–508. https://doi.org/10.1016/j.jasms.2004.07.009 PubMed PMID: 15465363. PMID: 15465363

49. Matyash V, Liebisch G, Kurzchalia TV, Shevchenko A, Schwudke D. Lipid extraction by methyl-tert-butyl ether for high-throughput lipidomics. Journal of lipid research. 2008; 49(5):1137–46. https://doi.org/10.1194/jlr.D700041-JLR200 PMID: 18281723; PubMed Central PMCID: PMC2311442.

50. Liebisch G, Vizcaino JA, Kofeler H, Trotzmuller M, Griffiths WJ, Schmitz G, et al. Shorthand notation for lipid structures derived from mass spectrometry. Journal of lipid research. 2013; 54(6):1523–30. https://doi.org/10.1194/jlr.M033506 PMID: 23549332; PubMed Central PMCID: PMC3646453.

51. Williams HH, Galbraith H, et al. The effect of growth on the lipid composition of rat tissues. The Journal of biological chemistry. 1945; 161:475–84. PMID: 21006930.

52. Hahn P. Lipid Synthesis in Various Organs of the Rat during Postnatal Development. Neonatology. 1986; 50(4):205–13.

53. King RJ, Clements JA. Lipid Synthesis and Surfactant Turnover in the Lungs. Comprehensive Physiology: John Wiley & Sons, Inc.; 2011.

54. Meaney S, Bonfield TL, Hansson M, Babiker A, Kavuru MS, Thomassen MJ. Serum cholestenoic acid as a potential marker of pulmonary cholesterol homeostasis: increased levels in patients with pulmonary alveolar proteinosis. Journal of lipid research. 2004; 45(12):2354–60. https://doi.org/10.1194/jlr.M400302-JLR200 PMID: 15466366.

55. Orgeig S, Daniels CB. The roles of cholesterol in pulmonary surfactant: insights from comparative and evolutionary studies. Comparative biochemistry and physiology Part A, Molecular & integrative physiology. 2001; 129(1):75–89. PMID: 11369535.

56. Notter RH, Tabak SA, Mavis RD. Surface properties of binary mixtures of some pulmonary surfactant components. Journal of lipid research. 1980; 21(1):10–22. PMID: 6892572.

57. Fleming BD, Keough KM. Surface respreading after collapse of monolayers containing major lipids of pulmonary surfactant. Chemistry and physics of lipids. 1988; 49(1–2):81–6. PMID: 3233714.

58. Nkadi PO, Merritt TA, Pillers DA. An overview of pulmonary surfactant in the neonate: genetics, metabolism, and the role of surfactant in health and disease. Molecular genetics and metabolism. 2009; 97 (2):95–101. https://doi.org/10.1016/j.ymgme.2009.01.015 PMID: 19299177; PubMed Central PMCID: PMC2880575.

59. Ma CC, Ma S. The role of surfactant in respiratory distress syndrome. The open respiratory medicine journal. 2012; 6:44–53. https://doi.org/10.2174/1874306401206010044 PMID: 22859930; PubMed Central PMCID: PMC3409350.

60. Polin RA, Carlo WA, Committee on F, Newborn, American Academy of P. Surfactant replacement therapy for preterm and term neonates with respiratory distress. Pediatrics. 2014; 133(1):156–63. https://doi.org/10.1542/peds.2013-3443 PMID: 24379227.

61. Yu SH, Possmayer F. Effect of pulmonary surfactant protein B (SP-B) and calcium on phospholipid adsorption and squeeze-out of phosphatidylglycerol from binary phospholipid monolayers containing dipalmitoylphosphatidylcholine. Biochimica et biophysica acta. 1992; 1126(1):26–34. PMID: 1606172.

62. Holm BA, Wang Z, Egan EA, Notter RH. Content of dipalmitoyl phosphatidylcholine in lung surfactant: ramifications for surface activity. Pediatr Res. 1996; 39(5):805–11. https://doi.org/10.1203/00006450-199605000-00010 PMID: 8726232.

63. Gille C, Spring B, Bernhard W, Gebhard C, Basile D, Lauber K, et al. Differential effect of surfactant and its saturated phosphatidylcholines on human blood macrophages. Journal of lipid research. 2007; 48 (2):307–17. https://doi.org/10.1194/jlr.M600451-JLR200 PMID: 17099186.

64. Bernhard W, Raith M, Pynn CJ, Gille C, Stichtenoth G, Stoll D, et al. Increased palmitoyl-myristoyl-phosphatidylcholine in neonatal rat surfactant is lung specific and correlates with oral myristic acid supply. Journal of applied physiology. 2011; 111(2):449–57. https://doi.org/10.1152/japplphysiol.00766.2010 PMID: 21636561.

65. Ridsdale R, Roth-Kleiner M, D'Ovidio F, Unger S, Yi M, Keshavjee S, et al. Surfactant palmitoylmyristoylphosphatidylcholine is a marker for alveolar size during disease. American journal of respiratory and critical care medicine. 2005; 172(2):225–32. https://doi.org/10.1164/rccm.200501-109OC PMID: 15879423.

66. Hamm H, Fabel H, Bartsch W. The Surfactant System of the Adult Lung—Physiology and Clinical Perspectives. Clin Investigator. 1992; 70(8):637–57. PubMed PMID: WOS:A1992JJ38400003.

67. Numata M, Kandasamy P, Nagashima Y, Posey J, Hartshorn K, Woodland D, et al. Phosphatidylglycerol suppresses influenza A virus infection. American journal of respiratory cell and molecular biology. 2012; 46(4):479–87. https://doi.org/10.1165/rcmb.2011-0194OC PMID: 22052877; PubMed Central PMCID: PMC3359948.

68. Perino J, Crouzier D, Spehner D, Debouzy JC, Garin D, Crance JM, et al. Lung surfactant DPPG phospholipid inhibits vaccinia virus infection. Antiviral research. 2011; 89(1):89–97. https://doi.org/10.1016/j.antiviral.2010.11.009 PMID: 21095206.

69. Haumont D, Rossle C, Clercx A, Spehl M, Biver A, Richelle M, et al. Modifications of surfactant phospholipid pattern in premature infants treated with curosurf: clinical and dietary correlations. Biology of the neonate. 1992; 61 Suppl 1:37–43. https://doi.org/10.1159/000243842 PMID: 1391264.

70. Whittle MJ, Wilson AI, Whitfield CR. Amniotic fluid phosphatidylglycerol: an early indicator of fetal lung maturity. British journal of obstetrics and gynaecology. 1983; 90(2):134–8. PMID: 6824613.

71. Serhan CN, Chiang N. Endogenous pro-resolving and anti-inflammatory lipid mediators: a new pharmacologic genus. British journal of pharmacology. 2008; 153 Suppl 1:S200–15. https://doi.org/10.1038/sj.bjp.0707489 PMID: 17965751; PubMed Central PMCID: PMC2268040.

72. Berry KA, Li B, Reynolds SD, Barkley RM, Gijon MA, Hankin JA, et al. MALDI imaging MS of phospholipids in the mouse lung. Journal of lipid research. 2011; 52(8):1551–60. https://doi.org/10.1194/jlr.M015750 PMID: 21508254; PubMed Central PMCID: PMC3137021.

73. Brites P, Waterham HR, Wanders RJ. Functions and biosynthesis of plasmalogens in health and disease. Biochimica et biophysica acta. 2004; 1636(2–3):219–31. https://doi.org/10.1016/j.bbalip.2003.12.010 PMID: 15164770.

74. Schrakamp G, Schutgens RB, Wanders RJ, Heymans HS, Tager JM, Van den Bosch H. The cerebrohepato-renal (Zellweger) syndrome. Impaired de novo biosynthesis of plasmalogens in cultured skin fibroblasts. Biochimica et biophysica acta. 1985; 833(1):170–4. PMID: 3967038.

75. Rudiger M, von Baehr A, Haupt R, Wauer RR, Rustow B. Preterm infants with high polyunsaturated fatty acid and plasmalogen content in tracheal aspirates develop bronchopulmonary dysplasia less often. Crit Care Med. 2000; 28(5):1572–7. PubMed PMID: WOS:000087167800052. PMID: 10834714

76. Wang-Sattler R, Yu Y, Mittelstrass K, Lattka E, Altmaier E, Gieger C, et al. Metabolic Profiling Reveals Distinct Variations Linked to Nicotine Consumption in Humans—First Results from the KORA Study. PloS one. 2008; 3(12). doi: ARTN e3863 https://doi.org/10.1371/journal.pone.0003863 PubMed PMID: WOS:000265452300005. PMID: 19057651

77. Braverman NE, Moser AB. Functions of plasmalogen lipids in health and disease. Biochimica et biophysica acta. 2012; 1822(9):1442–52. https://doi.org/10.1016/j.bbadis.2012.05.008 PMID: 22627108.

78. Wallner S, Grandl M, Konovalova T, Sigruner A, Kopf T, Peer M, et al. Monocyte to Macrophage Differentiation Goes along with Modulation of the Plasmalogen Pattern through Transcriptional Regulation. PloS one. 2014; 9(4). doi: ARTN e94102 https://doi.org/10.1371/journal.pone.0094102 PubMed PMID: WOS:000334160900083. PMID: 24714687

79. Rudiger M, Kolleck I, Putz G, Wauer RR, Stevens P, Rustow B. Plasmalogens effectively reduce the surface tension of surfactant-like phospholipid mixtures. The American journal of physiology. 1998; 274 (1 Pt 1):L143–8. PMID: 9458812.

80. Rudiger M, Tolle A, Meier W, Rustow B. Naturally derived commercial surfactants differ in composition of surfactant lipids and in surface viscosity. American journal of physiology Lung cellular and molecular physiology. 2005; 288(2):L379–83. https://doi.org/10.1152/ajplung.00176.2004 PMID: 15501950.

81. Zoeller RA, Grazia TJ, LaCamera P, Park J, Gaposchkin DP, Farber HW. Increasing plasmalogen levels protects human endothelial cells during hypoxia. American journal of physiology Heart and circulatory physiology. 2002; 283(2):H671–9. https://doi.org/10.1152/ajpheart.00524.2001 PMID: 12124215.

82. Hannun YA, Obeid LM. Principles of bioactive lipid signalling: lessons from sphingolipids. Nature reviews Molecular cell biology. 2008; 9(2):139–50. https://doi.org/10.1038/nrm2329 PMID: 18216770.

83. Uhlig S, Gulbins E. Sphingolipids in the lungs. American journal of respiratory and critical care medicine. 2008; 178(11):1100–14. https://doi.org/10.1164/rccm.200804-595SO PMID: 18755926.

84. Grosch S, Schiffmann S, Geisslinger G. Chain length-specific properties of ceramides. Prog Lipid Res. 2012; 51(1):50–62. https://doi.org/10.1016/j.plipres.2011.11.001 PMID: 22133871.

85. Longo CA, Tyler D, Mallampalli RK. Sphingomyelin metabolism is developmentally regulated in rat lung. American journal of respiratory cell and molecular biology. 1997; 16(5):605–12. https://doi.org/10.1165/ajrcmb.16.5.9160843 PMID: 9160843.

4.2 Supporting information related to publication 3

S1 Table Quantitative analyses of individual lipid classes in mouse lung during postnatal development. Values are expressed as nmol/mg wet weight and represented as mean ± SD.

Lipid class	P1	P15	P84
PC	16.47 ± 2.23	14.80 ± 0.57	18.03 ± 0.70
LPC	0.22 ± 0.05	0.39 ± 0.03	0.50 ± 0.09
PE	2.08 ± 0.09	2.27 ± 0.12	2.44 ± 0.19
PE P	2.55 ± 0.23	3.77 ± 0.18	3.82 ± 0.12
PG	1.27 ± 0.21	1.08 ± 0.10	1.32 ± 0.03
PI	1.58 ± 0.12	1.74 ± 0.06	1.81 ± 0.04
PS	3.05 ± 0.19	5.12 ± 0.26	5.35 ± 0.22
SM	1.05 ± 0.12	1.51 ± 0.11	1.94 ± 0.09
Phospholipids	28.26 ± 3.08	30.68 ± 0.85	35.20 ± 1.42
Cer	0.17 ± 0.02	0.19 ± 0.01	0.21 ± 0.01
HexCer	0.041 ± 0.004	0.028 ± 0.002	0.022 ± 0.003
CE	0.27 ± 0.02	0.45 ± 0.02	0.31 ± 0.00
Cholesterol	7.90 ± 0.83	13.16 ± 0.70	12.81 ± 0.55

S2 Table Distribution of glycerophospholipids according to carbon chain length (total number of carbon atoms) and alkenyl chain (PE P) during postnatal development of mouse lung. Values are represented as nmol/mg wet weight.

PC:

Postnatal stage	≤34	>34	≤36	>36
P1	13.41	2.31	14.84	0.88
P15	11.04	3.11	12.78	1.37
P84	13.73	3.47	15.65	1.55

PG:

Postnatal stage	≤34	>34	≤36	>36
P1	0.96	0.30	1.15	0.11
P15	0.75	0.32	0.95	0.12
P84	1.01	0.30	1.18	0.13

PE:

Postnatal stage	≤34	>34	≤36	>36
P1	0.31	1.77	0.67	1.40
P15	0.17	2.10	0.45	1.80
P84	0.23	2.21	0.56	1.87

PS:

Postnatal stage	≤34	>34	≤36	>36
P1	0.13	2.91	0.77	2.27
P15	0.11	5.01	0.94	4.17
P84	0.13	5.21	1.08	4.26

PI:

Postnatal stage	≤34	>34	≤36	>36
P1	0.13	1.51	0.35	1.29
P15	0.11	1.70	0.31	1.50
P84	0.13	1.74	0.35	1.52

PE P:

Postnatal stage	P 16:0	P 18:0	P 18:1
P1	1.77	0.32	0.43
P15	2.93	0.41	0.40
P84	2.71	0.58	0.50

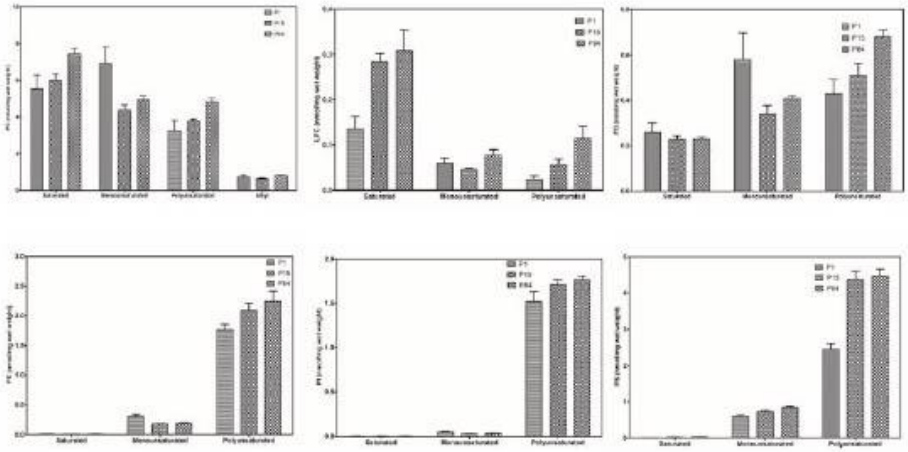

S1 Fig Distribution of glycerophospholipids according to degree of unsaturation (total number of double bonds) during postnatal development of mouse lung. Saturated (total number of double bonds = 0), Monounsaturated (total number of double bonds = 1), Polyunsaturated (total number of double bonds ≥2) lipids.

S3 Table Molar ratios of lipid classes. Displayed are the values of molar ratios of lipid classes. Values are represented as mean ± SD.

Molar ratio	P1	P15	P84
PC/LPC	75.43 ± 6.59	38.17 ± 3.71	36.63 ± 5.37
PC/PE	7.89 ± 0.80	6.54 ± 0.55	7.40 ± 0.29
PC/PS	5.39 ± 0.43	2.89 ± 0.04	3.37 ± 0.05
PC/PI	10.42 ± 0.70	8.51 ± 0.56	9.95 ± 0.20
PE/PS	0.69 ± 0.02	0.44 ± 0.04	0.45 ± 0.02
PC/Cholesterol	2.08 ± 0.07	1.13 ± 0.02	1.41 ± 0.02
PC/total cholesterol	2.01 ± 0.08	1.09 ± 0.02	1.37 ± 0.01
SM/Cer	6.25 ± 0.26	7.93 ± 0.81	9.21 ± 0.76

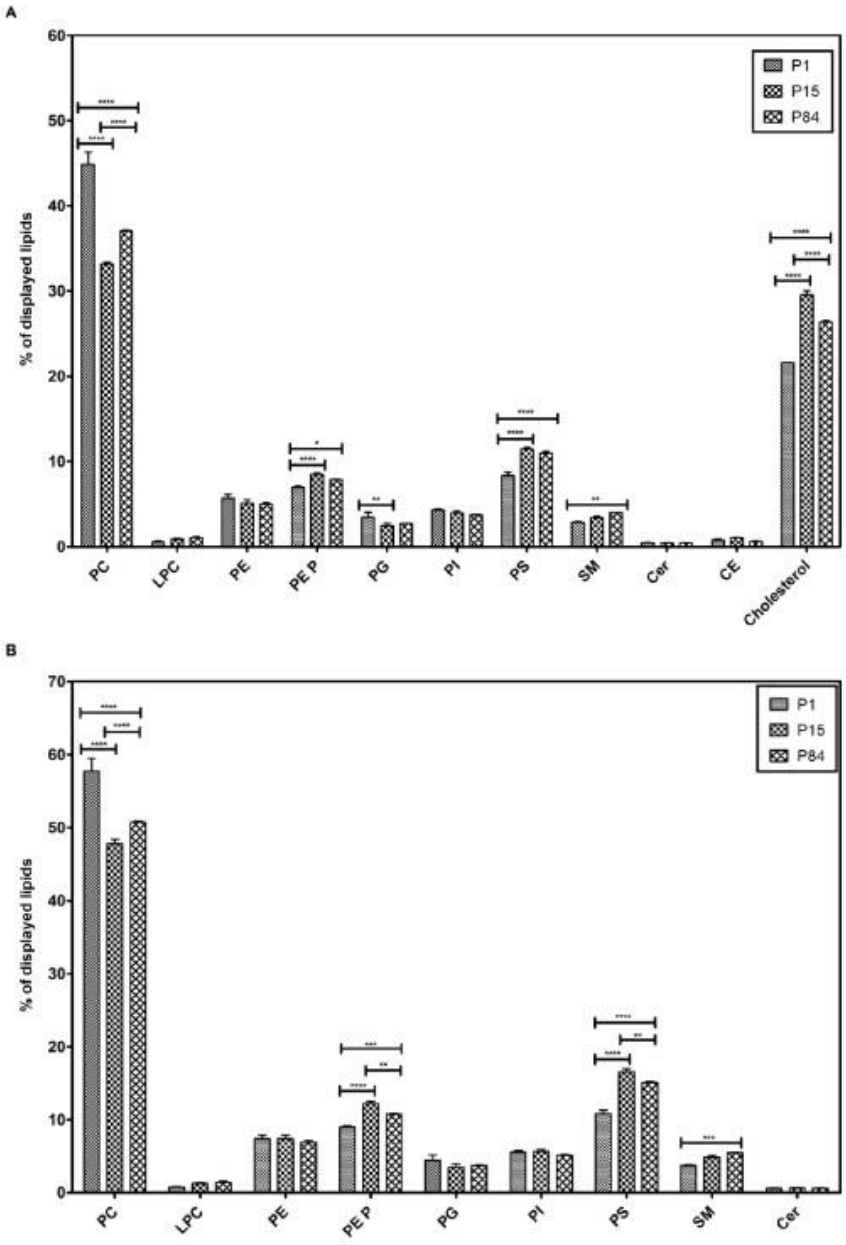

S2 Fig Total lipid composition of mouse lung during postnatal development. The displayed values are mol% of the respective lipid class of all analyzed lipids. Panel A) Glycerophospholipids (GP), sphingolipids (SP), cholesteryl esters (CE) and cholesterol. Panel B) only GP, SP without CE and cholesterol. Values are represented as mean ± SD, p-value summary: **** $P < 0.0001$, *** $P < 0.001$, ** $P < 0.01$, *$P < 0.05$.

CURRICULUM VITAE

Der Lebenslauf wurde aus der elektronischen Version der Arbeit entfernt

The curriculam vitae was removed from the electronic version of the paper

PUBLICATIONS

1. Kasarla SS, **Garikapati V**, Kumar Y, Dodoala S. Interplay of vitamin D and *CYP3A4* polymorphisms in endocrine disorders and cancer. Endocrinology and Metabolism. 2022;37(3):392-407.
2. **Garikapati V**, Colasante C, Baumgart-Vogt E, Spengler B. Sequential lipidomic, metabolomic, and proteomic analyses of serum, liver, and heart tissue specimens from peroxisomal biogenesis factor 11α knockout mice. Analytical and Bioanalytical Chemistry. 2022;414(6):2235-2250.

3. Ghezellou P, Albuquerque W, **Garikapati V**, Casewell N, Kazemi SM, Ghassempour A, Spengler B. Integrating top-down and bottom-up mass spectrometric strategies for proteomic profiling of Iranian saw-scaled viper, *Echis carinatus sochureki*, venom. Journal of Proteome Research. 2021;20(1):895-908.
4. Koch A, Schlemmer T, Höfle L, Werner BT, Presusser C, Hardt M, Möbus A, Biedenkopf D, Claar M, Perlet C, Jelonek L, Goesmann A, **Garikapati V**, Spengler B, Busche T, Kalinowski J, Kogel KH. Host-induced gene silencing involves transfer of dsRNA-derived siRNA via extracellular vesicles. bioRxiv, 2020. DOI: 10.1101/2020.02.12.945154.
5. Ghezellou P, **Garikapati V**, Kazemi SM, Strupat K, Ghassempour A, Spengler B. A perspective view of top-down proteomics in snake venom research. Rapid Communications in Mass Spectrometry. 2019;33:20-27.
6. **Garikapati V**, Karnati S, Bhandari DR, Baumgart-Vogt E, Spengler B. High-resolution atmospheric pressure MALDI mass spectrometry imaging workflow for lipidomic analysis of late fetal mouse lungs. Scientific Reports. 2019;9(1):3192.
7. Karnati S*, **Garikapati V***, Liebisch G, Van Veldhoven PP, Spengler B, Schmitz G, Baumgart-Vogt E. Quantitative lipidomic analysis of mouse lung during postnatal development by electrospray ionization tandem mass spectrometry. PLoS ONE. 2018;13(9):e0203464.
8. Ding X, **Garikapati V**, Spengler B, Heiles S. Analysis of ketone-based neurosteroids by reactive low temperature plasma mass spectrometry. Rapid Communications in Mass Spectrometry. 2018;32:1439-50.
9. Vijayan V, Srinu T, Karnati S, **Garikapati V**, Linke M, Kamalyan L, Mali SR, Sudan K, Kollas A, Schmid T, Schulz S, Spengler B, Weichhart T, Immenschuh S, Baumgart-Vogt E. A new immunomodulatory role for peroxisomes in macrophages activated by the TLR4 ligand lipopolysaccharide. Journal of Immunology. 2017;198(6):2414-25.
10. **Vannuruswamy G**, Korwar AM, Jagadeeshaprasad MG, Kulkarni MJ. Targeted quantification of the glycated peptides of human serum albumin. Serum/Plasma Proteomics. Methods in Molecular Biology. 2017;vol 1619. Humana Press, New York.
11. Gajbhiye A, Dhabhi R, Taunk K, **Vannuruswamy G**, Choudhury SR, Adhav R, Seal S, Mane A, Santhakumari B, Santra MK, Chaudhury K, Rapole S. Urinary proteome alterations in HER2 enriched breast cancer revealed by multipronged quantitative proteomics. Proteomics. 2016;16(17):2403-18.
12. **Vannuruswamy G**, Jagadeeshaprasad MG, Kashinath K, Kesavan SK, Bhat S, Korwar AM, Chougale AD, Boppana R, Reddy DS, Kulkarni MJ. Molecules with O-acetyl group protect protein glycation by acetylating lysine residues. RSC Advances. 2016;6(70):65572-8.

13. Singh P, Jayaramaiah RH, Agawane SB, **Vannuruswamy G**, Korwar AM, Anand A, Dhaygude VS, Shaikh ML, Joshi RS, Boppana R, Kulkarni MJ, Thulasiram HV, Giri AP. Potential dual role of eugenol in inhibiting advanced glycation end products in diabetes: proteomic and mechanistic insights. Scientific Reports. 2016;6:18798.
14. Korwar AM, **Vannuruswamy G**, Jagadeeshaprasad MG, Jayaramaiah RH, Bhat S, Regin BS, Ramaswamy S, Giri AP, Mohan V, Balasubramanyam M, Kulkarni MJ. Development of diagnostic fragment ion library for glycated peptides of human serum albumin: targeted quantification in prediabetic, diabetic, and microalbuminuria plasma by PRM, SWATH, and MS^E. Molecular & Cellular Proteomics. 2015;14(8):2150-9.
15. **Vannuruswamy G**, Rathna GVN, Gadgil BST, Gadad AP. Blends of shellac as nanofiber formulations for wound healing. Journal of Bioactive and Compatible Polymers: Biomedical Applications. 2015;30(5):472-89.
16. Kolekar YM, **Vannuruswamy G**, Bansode SB, Santhakumari B, Thulasiram HV, Kulkarni MJ. Investigation of antiglycation activity of isoprenaline. RSC Advances. 2015;5(32):25051-8.
17. Mohammad N, Malvi, P, Meena, AS, Singh SV, Chaube B, **Vannuruswamy G**, Kulkarni MJ, Bhat MK. Cholesterol depletion by methyl-β-cyclodextrin augments tamoxifen induced cell death by enhancing its uptake in melanoma. Molecular Cancer. 2014;13(1):204.

MANUSCRIPTS

18. Colasante C, Chen J, **Garikapati V**, Spengler B, Schlüter K-D, Baumgart-Vogt E. Heart recovery after ischemia/reperfusion injury is impaired by a mild peroxisome biogenesis defect induced by the knockout of the peroxin PEX11α.
19. Boateng E, Bonilla-Martinez R, Ahlemeyer B, **Garikapati V**, Alam MR, Trompak O, Oruqaj G, El-Merhie N, Seimetz M, Ruppert C, Günther A, Spengler B, Karnati S, Baumgart-Vogt E. Role of peroxisome proliferator-activated receptor beta/delta and catalase in pulmonary fibrosis.
20. Pflieger FJ, **Garikapati V**, Bhandari DR, Bredehöft J, Peek V, Roeb E, Roderfeld M, Hernandez J, Schulz S, Culmsee C, Laye S, Mayer K, Roth J, Spengler B, Rummel C. Combined lipidomics in a multimodal pathway analysis revealed alterations of brain lipid mediator metabolism during the progression of LPS-induced systemic inflammation in wild type and fat-1 mice.

AFFILIATIONS

2015 – Present	German Society for Mass Spectrometry (DGMS)
2018 – Present	American Society for Mass Spectrometry (ASMS)
2022 – Present	International Lipidomics Society (ILS)
Lifetime member	Proteomics Society of India (PSI)